Non-Newtonian coupled field analysis of blood flow in normal and stenosed carotid artery with varying haemodynamic parameters

Nitesh Kumar

Internal Supervisor 1: Professor Panicos Kyriacou

Internal Supervisor 2 : Professor Sanowar Khan

Research Centre for Biomedical Engineering

External Supervisor: Professor Raghuvir Pai

Department of Mechanical and Manufacturing Engineering

Manipal Institute of Technology

Manipal Academy of Higher Education, Manipal

This dissertation is submitted for the degree of

Doctor of Philosophy

City, University of London

October 2020

Dedicated to my parents, wife and daughter

Abstract

Atherosclerosis is a chronic disease affecting millions worldwide by leading to heart attack and stroke. It usually develops in regions with disturbed flow like the carotid artery, aorta, and coronary arteries. The major cause of atherosclerosis development is the deposition of lipids under the endothelial layer of the artery leading to plaque build-up. Also, evidence that the plaque formation occurs mainly near the bifurcations or curvatures had led to the hypothesis that irregular flow conditions plays a major role in development and progression of atherosclerosis. In vivo and in vitro studies at the cellular level and macroscopic levels shows the importance of understanding the local haemodynamics in atherosclerosis prone regions. Although diagnostic techniques such as Computed Tomography (CT) and Magnetic Resonance Imaging (MRI) provides detailed anatomic information non-invasively, local haemodynamics can be studied at patient specific models using computational techniques like Computational Fluid Dynamics (CFD) and Fluid Structure Interaction (FSI). Therefore, it is very important to reconstruct anatomical models using CT or MRI images to gain accurate results in CFD or FSI analysis. The flow behaviour in large arteries is complex and it is influenced by the elasticity of the artery. Apart from this, the blood pressure changes during day to day activities. This interesting phenomenon of variation of blood pressure is studied by numerical simulation of blood flow in the normal and stenosed carotid artery.

In this work, a three-dimensional (3D) Fluid Structure Interaction (FSI) study was carried out for a normal and stenosed patient specific carotid artery models. By considering physiological conditions, first the normal and then with hypertension disease, haemodynamic parameters were evaluated to better understand the genesis and progression of atherosclerotic plaques in the carotid artery bifurcation. Two-way FSI was

performed by applying a fully implicit second-order backward Euler differencing scheme using commercial software ANSYS and ANSYS CFX (version 19.0). Arbitrary Lagrangian–Eulerian (ALE) formulation was employed to calculate the arterial response by using the temporal blood response. Due to arterial bifurcation, obvious velocity reduction and backflow formation were observed which decreased shear stress and made it oscillatory at the starting point of the internal carotid artery near the carotid sinus, which resulted in low shear stress. Oscillatory shear index (OSI) signifies oscillatory behaviour of artery wall shear stress. Comparison of the results of this study with those in the published literature showed that the regions with low wall shear stress and with OSI value greater than 0.3 pose potential risk to the development of plaques. It was observed that haemodynamics of the carotid artery was very much affected by the geometry and flow conditions. Furthermore, regions of relatively low wall shear stress were observed post stenosis, which is a known cause of plaque development and progression. The results were compared between Newtonian and Carreau – Yasuda blood viscosity models. Critical haemodynamic parameters such as wall shear stress (WSS) and Oscillatory Shear Index (OSI) were examined. Simulated hemodynamic parameters were able to capture the disturbed flow conditions in a normal and a stenosed carotid artery bifurcation, which play an important role in the development of local atherosclerotic plaques. Computational simulations based on diagnostic tools such as Ultrasound might help improving diagnostic and treatment management of carotid atherosclerosis.

Table of Contents

List of Figures

List of Tables

Nomenclature

Abbreviations

CCA	Common Carotid Artery
CFD	Computational Fluid Dynamics
CIMT	Carotid intima media thickness
DSE	Digitized Shape Editor
ECA	External Carotid Artery
FSI	Fluid Structure Interaction
ICA	Internal Carotid Artery
NO	Nitric oxide
PIV	Particle image velocimetry
PSV	Peak systolic velocity
WSS	Wall Shear Stress
TIA	Transient Ischemic Attack

Greek nomenclature

ρ	Density of fluid (kg/m3)
v	Velocity (m/s)
P	Pressure (Pa)
τ	Deviatoric stress tensor
μ	Dynamic viscosity (N-s/m^s)
γ	Strain rate

v_b	Grid velocity
b	Body force at time t
∂S	Solid domain
$\partial \Omega$	Fluid domain
δ	Displacement relative to previous mesh locations
ϕ	Dependent variable
Γ_{disp}	Mesh stiffness
Γ_{ϕ}	Diffusion coefficient for ϕ
S_{ϕ}	Source term
n_i	Cartesian component of the outward normal surface vector

Symbols

M	Structural mass matrix
C	Structural damping matrix
K	Structural stiffness matrix
F^a	Applied load vector
U	Acceleration vector
U	Velocity vector
U	Displacement vector
A_m	Mean Pressure/Velocity

A_n	Fourier coefficient
B_n	Fourier coefficient
N	Number of harmonics
ω	Fundamental frequency

List of publications

Journal Publications

- Kumar N, Khader SA, Pai R, Khan SH, Kyriacou PA. Fluid structure interaction study of stenosed carotid artery considering the effects of blood pressure. International Journal of Engineering Science. 2020 Sep 1;154:103341.
  doi: 10.1016/j.ijengsci.2020.103341
- Kumar N, Khader A, Pai R, Kyriacou P, Khan S, Koteshwara P. Computational fluid dynamic study on effect of Carreau-Yasuda and Newtonian blood viscosity models on hemodynamic parameters. Journal of Computational Methods in Sciences and Engineering. 2019 Jan 1;19(2):465-77.
  doi: 10.3233/JCM-181004

International conferences

- Kumar N, Khader SA, Pai R, Kyriacou PA, December 2015, A Review of Application of CFD in Blood Flow Modelling, In International conference on computational methods in engineering and health sciences 2015, UPM, Malaysia. (accepted for presentation)
- Kumar N, Khader SA, Pai R, Kyriacou PA, December 2016, Non Newtonian blood flow in arteries, In International conference on computational methods in engineering and health sciences 2016, Tobata Campus, Kyushu Institute of Technology, Japan. (accepted for presentation)
- Kumar N, Khader SA, Pai R, Khan SH, Kyriacou PA, Numerical Investigation on the effect of Blood pressure on Wall Shear Stress and Vorticity, In the 14 th

International Symposium in Biomechanics in Vascular Biology and Cardiovascular Disease, 2019. Imperial College, London (poster presentation).

Acknowledgements

I am truly grateful to the lord almighty for giving me strength and confidence in this journey. My sincere gratitude to my supervisor Prof. Raghuvir Pai, Department of Mechanical and Manufacturing Engineering, Manipal Academy of Higher Education for providing me an opportunity and introducing me to Prof. Panicos Kyriacou to pursue my doctoral studies at City, University of London. I am grateful to him for being an excellent advisor and taking valuable time from his hectic schedule to supervise my work and for giving me expert guidance and moral support throughout. My heartfelt thanks go out to both my supervisors at City, University of London, Prof. Panicos Kyriacou, and Prof. Sanowar Khan. I thank Prof. Kyriacou for being a generous mentor, teacher, and supervisor. I am deeply indebted to him for allowing me to be a part of his team and for his support and advice in completing this research. I am grateful to Prof. Sanowar Khan for being there for me during my visit to City and for his critical advice throughout. I have learned many valuable lessons from him.

A special thanks to my dear friend Dr. S M Abdul Khader for his help provided during this work. He has given me very valuable advice on FSI analysis. I owe him a huge debt of gratitude for supporting my work and encouraging me to overcome the difficulties in this research.

Dr. Prakashini K, for encouraging and helping me to find the biological and clinical applications of the methods developed in this thesis. She has always been able to find time for me in her busy schedule at the KMC Hospital.

Dr. Manjunath M S, for his help, support, and friendship during all these years. Working with him has been very exciting and productive.

My friends at RCBE lab at City, University of London, Karthik, Tomas, Subhashree, Nystha, Michelle, James, and Abdullah for making me feel at home during my visits. Special thanks to Karthik and Tomas for always being there and all the fun moments we shared.

I express my sincere gratitude to Bharath, Sakthivel, and Sidhartha from Coreel technologies for their technical help to solve FSI problems in Ansys.

I am always indebted to my dearest teachers, Dr. Raviraja, Dr. B Satish Shenoy, Dr. Raghunandana, for their support and encouragement.

I owe my sincere gratitude to Dr. Dinesha P and Dr. Shivakumar for their help and support in writing articles and sharing their knowledge and motivating me to push forward in this journey.

My gratitude also extends to Dr. Srikanth Rao, Director, MIT, Dr. B.H.V Pai, Joint Director, MIT, Dr. Divakara Shetty, Dr. S. S Sharma, H.O.D, Department of Mechanical and Mfg., Engineering, MIT Manipal and CAD – Lab support staff for providing the support and permitting me to avail the lab facilities.

Finally, I owe, by far, the greatest gratitude to my family, my parents, my wife, and my daughter. They have taught me the most valuable life lessons, more than any academic learning. They have supported me with endless love, and have managed to make me feel them very close every day.

Declaration

I hereby declare that the work presented in this thesis is my own work. Any idea, result, or illustration originating from other subject's work has been acknowledged in the text by citing the original author. This thesis has never been published or submitted elsewhere for obtaining an academic degree or professional qualification. This dissertation is my own work and contains nothing which is the outcome of work done in collaboration with others, except as specified in the text and acknowledgements.

I grant power of discretion to the Librarian at City, University of London to allow the thesis to be copied in whole or in part without further reference. This permission covers only single copies made for study purposes, subject to normal conditions of acknowledgement.

Nitesh Kumar

October 2020

Chapter 1 Introduction

1.1 Background

Atherosclerosis affects millions of people all over the world, resulting in heart attack and stroke [1]. It usually develops in the regions where the flow is disturbed, like bifurcations, and regions with high curvature[2]. It begins when an element such as cholesterol, calcium, and macrophages are deposited under the endothelium layer of the artery (Plaque). Sometimes, the growth of plaque can reach a significant level and can cause severe problems to an individual, like occlusion, which may lead to life-threatening situations like myocardial infraction. The plaque may even rupture at extreme circumstances, causing the accumulation of platelets at the affected area to form a clot leading to stroke.

The artery is made of multi-layered muscle cells and tissues which helps in the flow of blood (*Figure 1-1*). The artery typically consists of three layers: Intima, Media, and Adventitia. The internal wall is lined with smooth endothelial cells to minimize the resistance to flow. Any damage to this layer could lead to arterial disease.

Atherosclerosis is a process of thickening and hardening of the wall of the artery caused by the continuous build-up of thrombus, lipids, cholesterol, and fatty deposits. It occurs in the major arteries and is one of the major causes of Transient Ischemic Attack (TIA), stroke, and heart attack. In such disease, the artery wall is stiffened due to the build-up of plaque underneath the endothelial layer leading to the narrowed lumen (*Figure 1-2*). The earliest step of lesion development is the adherence of monocytes to the endothelium.

When a monocyte enters the junction between the arterial wall and endothelial layer, it consumes Low-density lipoproteins (LDL) present in excess in the arterial wall and then transforms into macrophages.

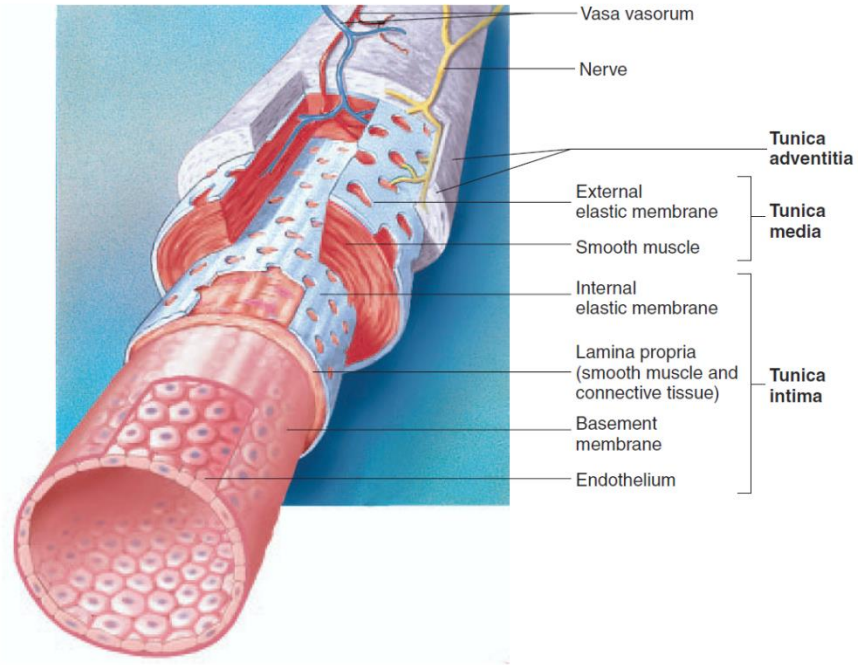

Figure 1-1: Dissected view of multi-layered tissues constituting the artery [3].

The macrophages are oxidized by consuming more LDL to form foam cells. The permeability of the arterial wall is increased by damage caused by the accumulation of foam cells, which leads to plaque build-up [4]. When the plaque gets ruptured and thrombus blocks the smooth flow of blood, the tissue experiences lack of oxygen resulting in myocardial ischemia and leads to a heart attack or chest pain from ischemia.

Cardiovascular disease (CVD) is a major cause of concern in modern society, hence the understanding and development of currently available clinical therapies are of prime importance. To facilitate the available clinical techniques, there is an increasing demand for computational tools to help diagnose CVD and assist the clinicians to diagnose pre and post-surgical treatments. In this thesis, it is shown that computational tools can help better visualize and the flow dynamics in atherosclerotic arteries.

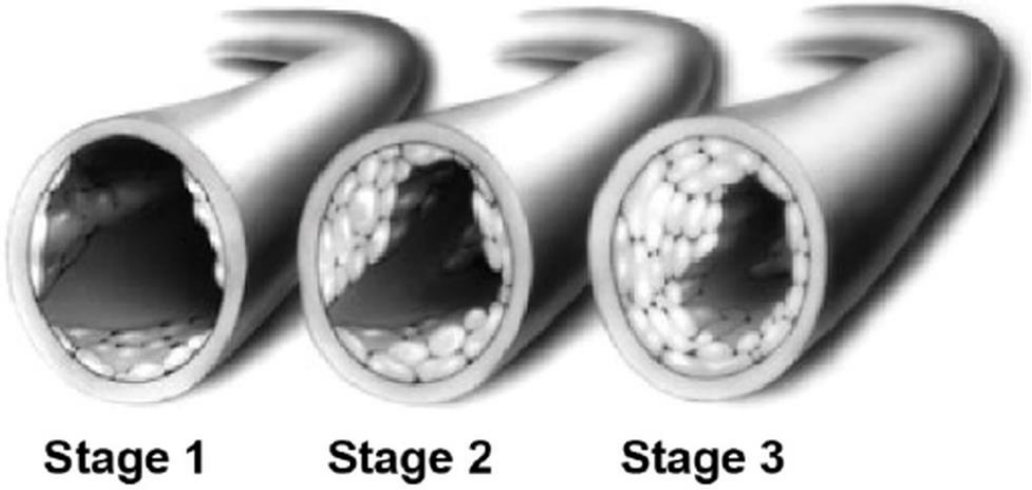

Figure 1-2: Narrowed lumen due to the build-up of plaque over time [5].

Hypertension is another major cause of stroke. Many studies were performed on the effect of hypertension on aneurysms and stenosed arteries. Researchers observed that hypertension increases the Wall shear stress (WSS) and deformation in aneurysm regions, which is initiated by extreme stress-strain conditions [6], whereas Milad et al [7] experimentally elucidated that the increase in stenosis severity in the carotid artery. This leads to increased negative WSS and oscillatory shear in the post stenosis region and increased angular phase difference between WSS and circumferential stress waves at the throat of the stenosis. All the parameters help predict the potential plaque growth locations and these results helped in studying the plaque growth and arterial remodelling [8]. To understand the effect of arterial compliance, a two-way fluid-structure interaction study was performed on a hypertensive case to understand the progression of atherosclerotic plaque in an arterial bifurcation [7], [9]. The effect of hypertension on the atherosclerotic arteries was studied as it poses a major risk in the rupture of the plaque [10]. A significant correlation between carotid strain parameters and peak and mean WSS in hypertension was also observed [11]. Also, the intima-media thickness in the common carotid artery and the carotid bulb is related to the blood pressure [12]. Corrada et al showed that the

deformation of the wall was significantly influenced by hypertension and it is a risk factor based on FSI results. Blood pressure was classified into four stages, normal (120/80 mm Hg), prehypertension (120-139/80-89), stage 1 hypertension (140-159/90-99 mm Hg), stage 2 hypertension (≥ 160/ ≥ 100 mm Hg) [13].

Blood is a shear-thinning fluid and the general Newtonian model will not capture the haemodynamics at critical locations [14]. Johnston et al. [15] studied blood flow through coronary arteries using different non-Newtonian blood viscosity models and concluded that Carreau-Yasuda models give a better approximation of the WSS at low shear to the mid shear range. Chen and Lu [16] investigated the non-Newtonian flow in a bifurcation model to solve the governing equations in which the shear thinning behaviour was incorporated by using the Carreau-Yasuda model and investigated its influence on the flow phenomena. He found significant differences between Newtonian and the Carreau-Yasuda model and determined that non-Newtonian properties of blood was an important factor in haemodynamics and played a very important role in vascular biology [16], [17].

1.2 Motivation and Objectives.

This research was motivated by an intention to better understand the haemodynamics of the carotid artery under different blood pressure conditions and to explore the computational models as a tool to diagnose and treat a diseased atherosclerotic carotid artery. Carotid artery is a highly focused domain to study the hemodynamics. Since past decades research was focused on understanding the flow dynamics and the effect arterial distensibility on hemodynamic flow variables. However, the research on the physio – social factors like anxiety, mental stress and exercise where the blood pressure may increase momentarily is scarce.

In the past two decades, researchers have intensively studied the initiation and development of atherosclerosis both experimentally[18]–[20] and computationally[21]–[23]. The literature review discussed in Chapter 2 surveys the available numerical studies to identify the research gaps. The objectives addressing the research gaps are:

- To develop an anatomically realistic carotid artery model using CT/MRI data
- To perform a numerical simulation of blood flow in a patient-specific normal and stenosed carotid artery model considering non – Newtonian viscosity model using computational fluid dynamics
- Two-way Fluid-structure interaction study of non – Newtonian flow in a patient-specific normal and stenosed carotid artery and compare with the Newtonian flow
- A computational fluid dynamic study using a non – Newtonian blood viscosity model in a normal and stenosed carotid artery and different blood pressure conditions
- To study the difference between Newtonian and non – Newtonian blood rheology on the haemodynamic parameters like WSS, Flow separation, Oscillatory Shear Index, and Velocity

1.3 Research Overview

Anatomically realistic arterial models obtained by medical image reconstruction have been developed by many researchers. With modern imaging techniques, especially MRI and CT, subject-specific geometries can be obtained and reconstructed[24]–[26]. The relationship between haemodynamics and prediction of atherosclerosis is then studied using CFD[27], [28].

This thesis presents a systematic numerical approach to investigate the haemodynamics of a stenosed carotid artery subjected to different blood pressures using Fluid-Structure

Interaction (FSI). The difference between Newtonian and non – Newtonian blood rheology is also investigated, including the relationship between the mechanical forces and haemodynamic parameters.

In summary, numerical simulation results were used as clinical indicators, to provide more important suggestions to clinicians to assist in clinical diagnosis. FSI simulations of carotid artery bifurcation models with different blood pressure conditions, the influence of blood rheology on the initiation of atherosclerosis was analysed. Combining with haemodynamic and mechanical results, the region of flow recirculation at the carotid sinus and post stenosis near the bifurcation was found to be more susceptible to develop atherosclerosis.

Chapter 2 Literature Review

This chapter reviews the relevant physiology and pathology of atherosclerosis, with a focus on the carotid artery, and presents the current state of the art of computational studies in this field.

2.1 Endothelial Biology

Cardiovascular diseases like atherosclerosis and stroke are the leading risk factors for deaths around the world. The prevalence of stroke was as high as 6.5 million as per the statistics from the American Heart Association, and each year millions of cardiac patients experience new or recurrent stroke [29]. Of all strokes, 87% of cases are due to ischemic stroke, where 10% is due to intracerebral haemorrhage, and 3% due to subarachnoid haemorrhage. Most of the ischemic stroke usually occurs in the carotid artery [30], [31]. Arterial disease is characterized by the deposition of fatty tissues, lipids, and calcification deposition on the inner wall of the artery. This will lead to thrombus formation or complete occlusion leading to stroke. The treatments include carotid endarterectomy and carotid stenting.

The haemodynamics in the carotid artery is directly linked to the formation of atherosclerosis. Large arteries like the carotid artery, aortic arch, and abdominal artery observe flow disturbance caused by bifurcation or curvature and are atherosclerosis prone regions in the vasculature [32].

The endothelial cells form a layer of cells on the inner wall of the artery. These one-cell thick layers of cells are key players in the formation of atherosclerosis. The endothelial cells respond to pathological variations and play a pivotal role in the development of atherosclerosis [33]. A healthy endothelial layer is aligned optimally and will respond to

the chemical and physical stimulus which regulates vascular tone, cellular adhesion, thrombo-resistance, smooth muscle cell proliferation, and vessel wall inflammation [34], [35]. The resting endothelial cells (quiescent phenotype), switch to pro-coagulant/pro-thrombotic phenotype leading to several pathogenic risk factors [36], and in this process, the vasodilator Nitric Oxide (NO) plays an important role as it shows "atheroprotective genes" in the endothelial layer [37]. The NO activity and the endothelial dysfunction share a very strong relationship, including the increased response of vasoconstrictors, an increase in vascular adhesion molecules, the simulation of growth factors causing the propagation of underlying smooth muscle cells, and the permeability of the endothelial layer to low-density lipoprotein (LDL). As a result, the endothelial layer becomes dysfunctional and also lose its integrity and detach into the circulatory system [38].

The cause of endothelial dysfunction is still not very clear, however, several cardiovascular risk factors such as obesity, diabetes, high blood cholesterol, chronic infections, hypertension, smoking, and alcohol are assumed to be closely involved. Moreover, haemodynamic environment is closely associated with endothelial dysfunction, which controls the WSS - activated NO release [39]. Hence, a detailed understanding of haemodynamics provides information on susceptible locations for endothelial dysfunction, which will be useful for clinicians to identify areas prone to atherosclerosis [40].

2.2 Anatomy of the carotid artery

The carotid arteries are the major blood vessels carrying blood rich in oxygen to the face and brain located on each side of the neck. The carotid artery originates from the aortic arch as the common carotid artery and bifurcates into internal and external carotid arteries. *Figure 2-1 (a)* shows a schematic diagram representing the position of the carotid

bifurcation and *Figure 2-1 (b)* shows the positions of all the arteries originating from the aortic arch. The right common carotid artery originates from the brachiocephalic artery and extends to the right side of the neck. The left carotid artery originates from the aorta and extends till the left side of the neck. Each common carotid artery (CCA) branches into the internal carotid artery (ICA) and external carotid artery (ECA). The ICA supplies blood to the brain and eyes. The origin of the ICA progresses through several curvatures, through the base of the skull into the Circle of Willis. Unlike ECA, there are no branches until it passes through the base of the skull. At the base of the brain, the ICA gives rise to anterior and middle cerebral arteries and this location is referred to as carotid siphon. The location where the ICA emerges from the CCA, i.e., immediately after branching, the ICA widen a bit, known as carotid sinus or carotid bulb. Its shape, length, and width vary from one subject to another. The ECA branches from the CCA to supply oxygen-rich blood to the throat, neck, and face.

2.3 Effect of haemodynamic forces on atherosclerosis

The flow of blood varies from laminar fully developed flow to disturbed flow with flow reversals [41]–[43]. The disturbed flow generally occurs near bifurcations and curvatures usually related to the early occurrence and progression of atherosclerosis. The unbranched portions of the artery are generally not susceptible to atherosclerosis due to the uniform flow of blood.

Figure 2.2 shows three types of haemodynamic forces generated due to pulsatile blood flow through arterial vasculature. These forces are (a) wall shear stress (WSS), a force caused by blood viscosity, (b) pressure gradient across the wall known as transmural pressure, and (c) radial deformation. The endothelial layer senses the forces and secretes different vaso - active constituents to maintain a normal and stable equilibrium.

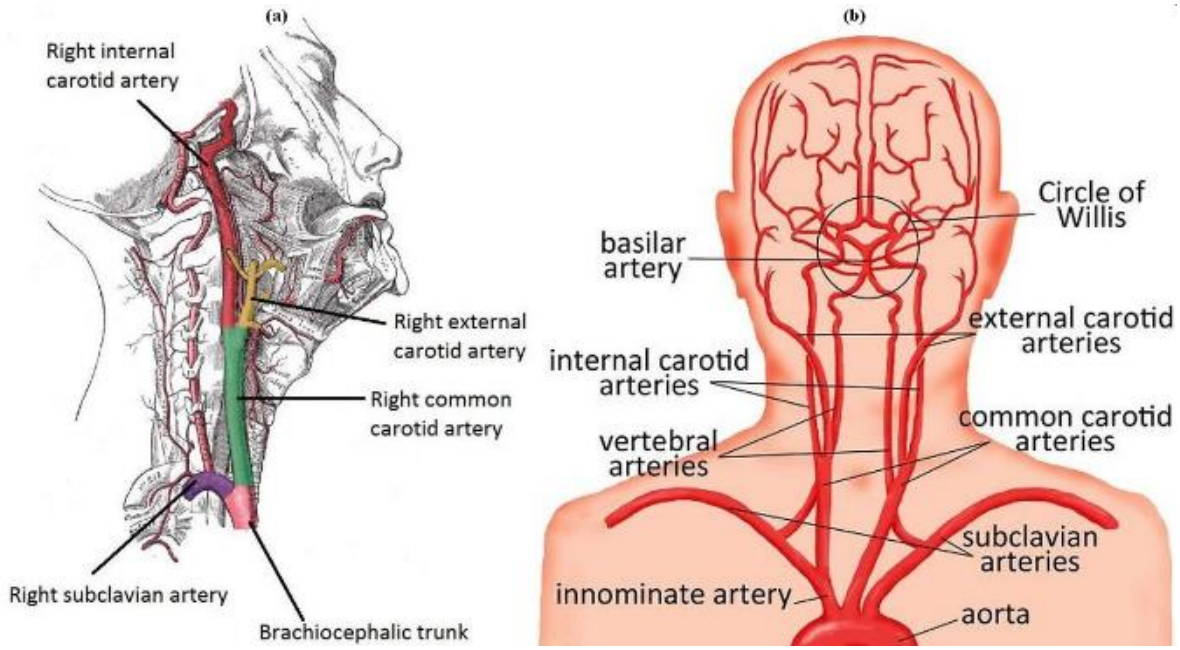

Figure 2-1: Schematic description of the carotid bifurcation, (b) carotid artery origin description

Among these forces, the major influence on the development of atherosclerosis is by WSS, which is extensively investigated and well understood [44]–[46]. The variations in WSS regulates the secretion of many factors including vasodilators such as Nitric oxide and prostacyclin [47], [48], vasoconstrictors like endothelin – 1 [49], and other growth factors [50], [51]. Although recent research has clarified the effects of mechanical deformation on endothelial cells [52]–[61], its role in the pathogenesis of atherosclerosis is not clearly understood. Clinical studies show that the bifurcation and bends in the human vasculature are subjected to higher arterial dilation compared to straight sections [62]. Further, the increase in vascular dilation due to hypertension is a common risk factor in atherosclerosis [63]. These observations suggest that arterial dilation plays a very important role in the pathogenesis of atherosclerosis.

In summary, the pathogenesis of atherosclerosis as shown in *Figure 2-3* is a very complex process of injury of the vascular wall leading to the formation of plaque due to local haemodynamic and systemic factors [64].

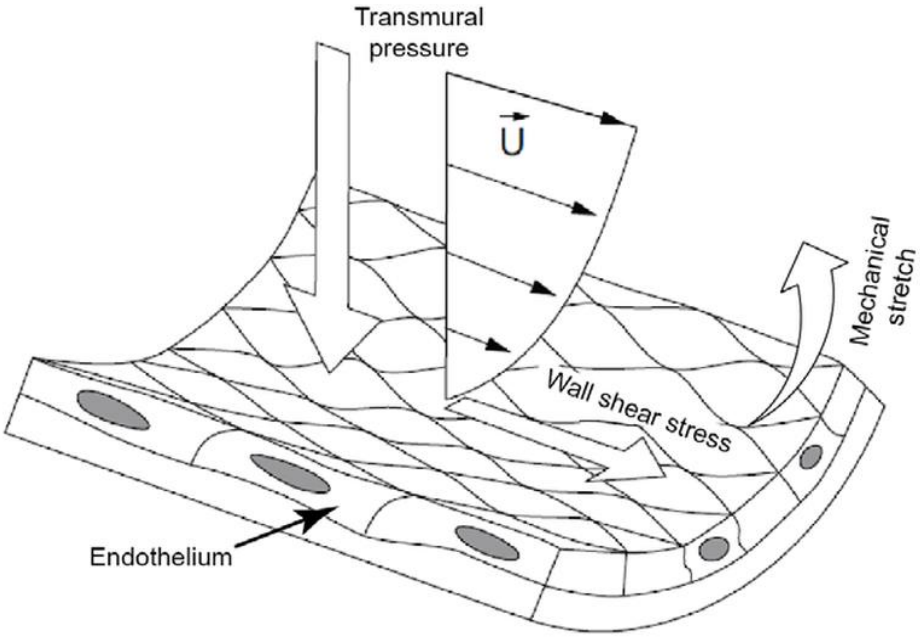

Figure 2-2: Arterial walls are subjected to haemodynamic forces [65]

WSS plays a very significant role in the development of atherosclerosis, where the flow gets disturbed with oscillating or low shear stress. Moreover, many factors such as high blood pressure, diabetes, etc. have an impact on endothelial dysfunction and damage the flow-mediated vascular dilation [66]. The combination of altered haemodynamics near and around the probable atherosclerotic sites like bifurcations and curvatures, where the secondary flows happen, and the risk factors accelerate atherosclerotic lesion and development of plaque.

2.4 Flow measurement

Research on the measurement of blood flow started around the mid-19th century using an airtight U tube of a known volume which was connected to a blood vessel to measure the arterial blood flow rate according to the Poiseuille Formula [67]. After many decades of study, many techniques were routinely employed to study cardiac output.

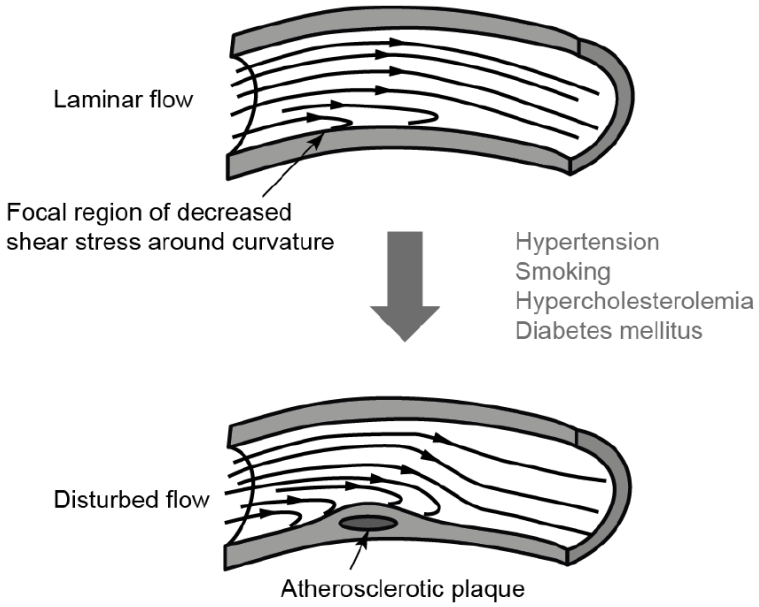

Figure 2-3: Early progression and development of atherosclerotic plaque [64]

At present, Doppler is the most widely used technique for in – vivo measurement of blood flow [68], [69], along with Magnetic resonance imaging (MRI) [70], [71] and ultrasonic transit-time flow sensors [72], [73]. Measurement of flow in a blood vessel requires a probe or a sensor that is accurate enough and linear over the flow range in the vessel where the flow is measured. In – vivo techniques provides more realistic data related to flow dynamics and they offer spatial and temporal results with limited resolution [74], [75], limiting the quality of actual physiological parameters such as anatomical geometry of the vessel, blood, and tissues.

Particle image velocimetry (PIV) experiments using representative models of required arterial models can be an alternative for in – vivo measurements. These models are generated either by using patient-specific data or by averaging the obtained data and build the model using transparent materials. Therefore, the experiments could be of varying complexities, including steady [76], [77] and pulsatile conditions [26], [45], idealised [78] and patient-specific geometries [79].

A large number of in – vitro experimental studies have been performed, many of which focused on velocity measurements, while WSS is a most important haemodynamic parameter due to the low spatial resolution of the visualised flow field. Although some effort has been made to produce WSS [80], the present experimental study of spatial and temporal WSS is challenging to capture and susceptible to uncertainties.

2.5 Numerical Modelling of Blood Flow

2.5.1 Computational Fluid Dynamics

Computational Fluid Dynamics (CFD) is an emerging tool whose progress is adopted by the research community as a potent technique for the numerical study of arterial haemodynamics. CFD offers many hemodynamic parameters like WSS, Oscillatory shear index, etc. which is challenging to access through experiments. The critical relationship between low WSS and development of lesion [45], [81], [82] makes the WSS as one of the most intensively studied parameters in arterial CFD modelling. Perktold et al [83] examined the geometrical effects such as carotid sinus, bifurcation angle under pulsatile conditions. It was established that the most physiologically relevant flow parameter is WSS and its time-based variation is in close agreement with in – vitro results. Many studies were conducted in varieties of arterial models, mostly bends and bifurcations. These comprise of WSS studies [84], [85], oscillatory shear index [86], WSS gradients (WSSG) [87], [88] and particle residence time [89], [90].

While several numerical studies have been carried out to formulate the parameters leading to the onset of atherosclerosis, their limitation remains. Firstly, the domain of interest is truncated in image-based carotid artery simulations, and the whole circulatory system is ignored. The application of boundary conditions at the inlet and outlet affect the accuracy of the study significantly. Therefore, the application of patient-specific inlet and outlet

parameters acquired from techniques such as MRI or Ultrasound was preferred [91]–[93]. However, for applications such as to predict surgical interventions, the flow or pressure waveforms are unknown, and the requirement of accurate boundary conditions is critical.

Secondly, many researchers have focused on studying the flow near the stenotic region by using many modelling assumptions such as steady flow [94], pulsatile flow [95], [96], rigid artery [97], elastic artery [98], Newtonian flow [99], non – Newtonian flow [100]. However, the effect of the existence of plaque on blood flow transportation is not significantly examined, which is of critical clinical significance as it is considered as a key marker to suggest appropriate clinical treatment [101].

Lastly, as atherosclerosis is a very complex pathology with many underlying factors, early researchers study this phenomenon by only looking this from the hemodynamic point of view [102], [103], and by also considering the elasticity of the artery which is not enough [104], [105]. Tang et al [106] performed complex computational modelling of a stenotic artery, however, the effect of arterial bifurcation was ignored. Therefore, the study on the effects of hoop stretch in patient-specific models was scarce.

2.5.2 Fluid-Structure interaction

Hemodynamic investigations of arteries considering the artery as rigid will not be physiologically realistic as the flow of blood is significantly influenced by the arterial wall behaviour. Many Fluid-Structure Interaction (FSI) simulations were conducted to understand the complex and altered flow behaviour in the areas surrounding the stenosis. Barbara et al [107] performed a numerical study of anatomically accurate 3D geometric model with rigid wall conditions considering blood as a non – Newtonian fluid under pulsatile flow conditions was performed. It demonstrated that arterial compliance consideration changed with reduced flow field and WSS when compared with rigid wall

results. A similar analysis was performed by Perktold and Rappitsch [108] and observed realistic wall deformation by considering revised non – linear shell assumptions. The change in the flow behaviour due to the elasticity of the artery during the pulsatile flow was observed in critical sites such as the carotid sinus. Using MRI data, a model of the normal, stenosed carotid artery was generated. The results were validated using experimental results [109] and concluded that the image-based numerical models are useful to investigate the haemodynamics in elastic arteries. The change in flow patterns across the idealized stenosed common carotid under steady and pulsatile conditions were studied and a mild flow disturbance in the post stenotic region was observed and its effect on the elastic wall was also presented by Lee et al [110]. A healthy carotid bifurcation was subjected to pulsatile flow conditions and the effect of WSS and circumferential stress and strain at the carotid sinus which is highly prone to atherosclerotic plaque deposition was discussed by Tada et al [111]. Most of the boundary conditions applied either are unknown, assumed or those obtained from MRI and a Doppler scan. In an attempt to apply pulsatile inlet and outlet boundary conditions, a 1D model of the arterial tree was coupled with a 3D fluid-structure interaction model by Urquiza et al [112] and the observations were acceptable with clinically observed flow patterns. The application of synthetic grafts and the existence of intimal hyperplasia during bypass surgery were analysed by Shaik et al [113]. The consideration of Newtonian and non – Newtonian fluid rheology demonstrated good agreement with experimental studies and clinical observation. It was also observed that the geometry of the arterial model played a very crucial role in predicting the location of severe wall shear stress, which are vulnerable to progression of atherosclerosis.

Varying degree of stenosis was investigated by Li et al [114] and revealed that extreme stenosis restricts the motion of the arterial wall, which results in higher velocities and

maximum wall shear stress and concentration of stress leading to progression and rupture of plaques. Cho et al [115] considering blood as a non – Newtonian fluid studied the effect of different elastic modulus of the artery on the blood flow and periodic and transient changes in the blood flow characteristics were observed. It was observed that as the elasticity of the arterial wall is increased, the temporal frame of velocity, pressure, and wall shear stress gets longer, and a reduced flow separation zone is observed. In addition to this, severe transient flow changes are caused due to higher deformation of the artery wall. Many available software codes have difficulty in developing coupling algorithms due to classical iterative processes involved in solving the mathematical equations. To overcome this a semi-implicit method was proposed by Quaini et al [116]. It was numerically verified through computer simulations of pulse pressure progression in idealized carotid artery bifurcation and observed that the solution remained stable for a wide range of discretization and physical parameters. In strongly coupled field problems, problems associated with partitioned couplings were studied by Degroote et al [117], and the existing algorithms like IBQN – LS coupling techniques were analysed and compared and new algorithms were developed. These simulations show that the developed algorithms were able to solve complex fluid-structure interaction problems in a partitioned method with black-box solvers. Lee et al [118] performed a simple study on carotid bifurcation with wave propagation validation and demonstrated a strongly skewed velocity and flow separation in the carotid bulb with low wall shear stress.

Fluid-Structure Interaction simulations predict a larger recirculation zone near the carotid bulb and a reduced wall shear stress, and a small backflow zone compared to the rigid model. Consideration of Pulse wave propagation is also equally important compared to pulsatile flow boundary conditions [119]. The pulse wave propagation is generally studied to check the capability of the coupled field solvers. Multiscale approaches are suitable for

absorbing the outgoing pressure waves which describe the flow of blood in the arterial system [120], [121]. The effect of pulse wave on wall shear stress was studied by Fukui et al [122] and suggested that propagating waves reduces the flow speed of blood and reduces the wall shear stress. Wave propagation through 3D elastic tubes was studied by Degroote et al [123] by developing a partitioned quasi Newtonian technique that is capable of solving coupled field problems through partitioned and monolithic ways and verified by applying a short pressure pulse at the inlet of a 3D elastic tube. These techniques were useful in coupling the commercial finite element flow and structural solvers. A revised algorithm of interface quasi–newton technique with an approximation for the inverted Jacobian from least square model and showed the importance of coupling algorithms, which are known as black box through pulse pressure propagation in an elastic tube.

The regions of high wall shear stress and atherosclerotic plaque development were studied by Robert et al [124]. The carotid artery model was studied by data obtained by in – vivo measurements like MRI, ultrasound, and angiogram. With these data, two anatomical 2D finite element models were created to find the localized stress concentration that occurs at the bifurcation. The role played by wall shear stress in the formation of the atherosclerotic lesion and high structural stress at the inner surface can cause damage to the endothelial layer [125], [126]. The study of blood flow in the realistic arterial model was studied by Deschamps et al [127] wherein the anatomical surfaces were obtained by Level – sets method which can accurately model the complex and varying surfaces of stenosis. The obtained surfaces were defined at a sub-pixel level where they interconnect the Cartesian lattice of the image. Therefore, surrounded boundary representation is constructed on the same lattice and further discretized to solve the Navier – stokes equation for compressible fluids. Juan et al [128] emphasized the use of accurate models of patient-specific data obtained from medical images for large clinical studies. An isosurface deformable model

was used for arteries with stenosis where the image was first smoothed by convolution with a Gaussian kernel and voxel intensities. The final model was generated by adopting the region-growing approach. Finally, a non-shrinking algorithm is used to smooth the model and extruded to minimize the influence of boundary conditions on the region of interest. Further, these models are solved numerically to study the haemodynamics at critical locations. A 3D Realistic model of the abdominal aorta was analysed by Rinderu et al [129] obtained from an MRI scan. The image slices from MRI are stacked precisely and the segmentation of the lumen area is performed for each slice by which the entire set is fitted with Bezier curves. The obtained 3D model is solved for steady and laminar flow of an incompressible non – Newtonian fluid and obtained results agreed well with Doppler anemometry results. Tabor et al [130] developed techniques to generate computational mesh from MRI/CT scan data, which allows the easy model generation of the flow domain. In this technique, CAD models were inserted into original scan data using Scan CAD thereby enhancing the capability to modify the geometry. Flow simulations before and after surgery were compared to understand the variations in the haemodynamics at critical sites. Alberto Figueroa [131] developed a new robust monolithic coupled momentum method and discussed different outlet boundary conditions such as constant pressure, impedance, and resistance boundary conditions influencing the physiological flow. Outflow boundary conditions were also discussed by Irene et al [132] suggesting that blood flow in large arteries is dependent on the applied boundary conditions. In situations where the flow distributions and pressure boundary conditions are not known, a multidomain approach with upstream regions of interest coupled to reduced order such as 0D or 1D models of downstream vessels is implemented. This method was adopted by Jarvinen et al [133] in addition to the artificial compressibility method to simulate tightly coupled simulation of blood flow in the deformable artery which shoed robust

convergence. Kim et al [134] also discussed this concept by using the augmented lagrangian method. This technique does not include any restrictions on the velocity profiles nor the pressure at the interface. Reymond [135] developed a 1D arterial tree with systemic arteries which was later extended to patient-specific models to predict better pressure and flow waveform closely related to in – vivo measurements.

FSI simulations showed inter-individual variations in haemodynamics and arterial mechanics and its effect on atherosclerosis [136] and observed that atherosclerosis is dependent on many factors not just on mechanical factors. A novel FSI technique based on DSD/SST known as stabilized space-time fluid-structure interaction (SSTFST) was used on arterial models considering membrane and continuum element approach separately for arterial wall [137]. The damping effect caused by surrounding tissue was also considered by adding mass – proportional damping. Similar studies were carried out for different cases of aneurysms [138], [139]. It is well demonstrated that SSTFSI is an economical alternative computationally to a fully coupled FSI approach in arterial fluid mechanics by adding more flexibility [140]. In addition to this, a non – Newtonian assumption was used to study the feasibility of strong coupling outflow boundary conditions with 1D and 0D by Toma et al on carotid bifurcation [141].

Hsu et al [142] discussed the significance of prestressing the models to avoid the discrepancies between the data obtained from imaging techniques and the computational model caused due to over-inflation of the artery caused by intramural pressure. The possibility of accurate prediction of flow phenomenon compared to the non-pre-stress model was demonstrated in this study. Different combinations of arterial wall thickness were studied to understand the importance of low wall shear stress in post plaque dilated region of carotid bifurcation [118]. Tang et al [143] discussed the assumption of non – Newtonian blood rheology and the changes in the flow caused by geometric factors with

adverse flow conditions leading to the growth of atherosclerotic plaque in detail. The components of atherosclerotic plaque and the arterial wall were modelled and found that large lipid pools and thin plaque caps were associated with high-stress strain conditions. This was numerically supported and found that favourable conditions for plaque growth depend on the structural stress of the artery [144]. This observation was supported by Kock et al [145] and suggested that maximum stress is located in the upstream and downstream shoulder regions of the fibrous cap, which is used to assess the vulnerability of the plaque cap and improve risk stratification. The plaques with prior episodes of ruptures are associated with higher critical plaque stress compared to non-ruptured plaque [146].

Accurate assessment of vulnerable plaque based on computational modelling and comparing it with in-vivo intravascular ultrasound imaging and angiography was discussed by Yang et al [147]. MATLAB was used to anatomically generate the contours of the lumen, vessel outer boundary, and components of the plaque enabled with a smoothing filter. Further, the 3D computational model is analysed to assess plaque vulnerability.

Leach et al [148] reported the rupture of the plaque due to excessive wall shear stress and elevated structural stress and noted that significant impact on altered predicted stress fields due to misrepresentation of features of the plaque which are smaller than the current in – vivo imaging resolution limits. The significant difference in plaque stress between symptomatic and asymptomatic patients showed plaque stress as one of the most important factors of vulnerable plaque assessment [149]. Besides, the stress levels in the plaque based on MRI in – vivo images are associated with the thickness of the fibrous cap, the size of the lipid core, and the surface of the fibrous cap. In 3D multicomponent carotid plaque numerical models with and without rupture, critical plaque stresses are associated with plaque rupture and predict the plaque rupture location.

2.6 Image acquisition and geometric modelling

To predict the behaviour of the arteries under physiological loading conditions it is necessary to model the stenosed region in the artery. Many computational techniques were developed to solve model reconstruction problems like segmentation. The discretization of 3D anatomically realistic models of the vasculature was presented by Aristokleous et al [150]. In this approach, attention was given to minimize human intervention and maximize reproducibility by producing accurate results and the introduction of geometric and fluid dynamics analysis of normal and stenosed arteries [151]. Anatomically realistic models were also used to study the pulsatile flow in human carotid bifurcation where the difference in the flow between normal and stenosed arteries is enumerated [152]. The parallel imaging technique was used to obtain a phase-locked image which leads to a high-resolution description of the vessel geometry at one single-phase and classical imaging techniques can be applied to this image set to produce the corresponding wall surface [81]. A High-resolution MRI of a stenosed carotid bifurcation obtained and an automated detection algorithm was then applied to the images. Segmentation of stenosed carotid bifurcation was generated using a 2D watershed transform form applied to each slice and a high-resolution 3D model was generated [153]. The lumen boundary extraction from the vascular anatomy images was the most important step in image-based modelling. Many researchers have focused on this process with studies depending upon manual or computer-based segmentation of image slices which is coupled to any number of reconstruction techniques [150], [154]. With fast and central graphics processing units and large scale improvements in the quality of images, performing 3D lumen extraction is much easier [155]. Lumen segmentation using a rapid technique and surface reconstruction using MR images reduces the time required to produce finite element meshes. It is done by using a computerized virtual balloon which when placed inside the

lumen geometry generated from MR images is inflated to concurrently segment and reconstruct the lumen and this surface of the lumen is filled with finite elements [156]. 3D realistic models were constructed using MR images which are manually segmented and the reconstructed 3D lumen surface was processed using the Vascular Modelling Toolkit which is a set of libraries and tools for image-based modelling of blood vessels [157]. Images that have well-defined vessel wall boundaries such as images obtained from CT or contrast-enhanced MRA, segmentation of the 3D images are preferred [158]. However, the 3D surface obtained from this technique is difficult to edit, hence 2D segmentation is preferred for low contrast structures like artery walls, thrombus, or stenosed locations [150] especially for Intravascular Ultrasound (IVUS) images [159]. It is very straightforward to loft the wall rings together for non-branching segments, but branches has its challenges [160]. The availability of open-source toolkits for image visualization, processing, and vascular modelling is a very significant development in image-based modelling [160], [161] which enables normalization of vascular model construction. Quality volumetric meshes are mostly in the scope of commercial mesh generators although there are open source codes available. The meshes are mostly over or under resolved relative to the solution requirements for which adaptive mesh technique is adopted to obtain an acceptable prediction of wall shear stress [162], [163]. The adaptive mesh strategy which produces anisotropic and boundary layer elements are preferable since the arteries have long tubular structures and the velocity of the blood is greater in radial than in a longitudinal direction. Sahni et al [164] generated a novel finite element mesh of vascular models incorporating anisotropic adaptivity and boundary layer meshing. Anisotropic meshing can yield mesh independent results for image-based modeling of blood flow with few elements when compared to isotropic adaptive mesh refinement models [165]. CT MRI was taken from volunteers and a 3D artery was

generated using the 2D slices obtained from the CT MRI by using a spline curve to connect the slices [166]. 2D slices obtained from a CT scan [164] was used to reconstruct a 3D model of an aortic aneurysm of a patient by importing the CT data into MIMICS, an image processing software [167]. Although 3D reconstruction of arteries is abundant, the mean carotid artery geometry is not characterized systematically. Such geometry on patients with carotid artery disease and the results of CTA were used to study the cross-sectional images using a semi-automated segmentation algorithm. The data extracted were used to reconstruct the mean 3D geometry and to determine the average values of various geometrical parameters [168].

2.7 Non – Newtonian blood rheology

From a clinical perspective, it is a known fact that the specific locations in the arterial network are sensitive to atherosclerosis development. Local haemodynamics plays a very important role in the progression of atherosclerotic lesions mainly at the carotid sinus [81], [169], [170]. The rheological properties of blood play a major role in local haemodynamics along with the pressure pulse and arterial geometry.

Bharadwaj et al [78] and many other researchers [171]–[174] studied the flow dynamics in carotid bifurcation. The blood was modelled as a Newtonian fluid and the viscoelastic nature was ignored, as the shear rates were predominantly high. The viscosity was taken as high shear - rate limit viscosity of blood (3.5×10^{-3} Pa s). Studies show that it is not necessary to consider the effect of shear-thinning properties of blood in large arteries [175], [176]. Other studies found that there is a significant effect of the shear-thinning property of blood [177], or scaling procedures were used while comparing Newtonian and non – Newtonian models [178], [179]. The influence of the viscoelastic behaviour of blood was analysed experimentally and a significant influence was observed [180], [181] on the

velocity distribution, and in large arteries, and its dependence on the variation of shear rate [94]. The non – Newtonian viscosity model also has a significant influence on the oscillatory shear index (OSI) and mean wall shear stress. Based on the momentum equation, a mathematical non-dimensional model was formulated for a modified Casson's fluid by Hernan et al [182]. The results obtained showed that the Newtonian model underestimated the hemodynamic parameters when compared to Casson's model.

Various blood viscosity models were studied to compare and suggest the best model to be used in hemodynamic simulations. At mid-range to high shear, the Newtonian model is certainly a good choice. But at low shear, which is biologically significant, it underestimates the key hemodynamic parameters [107]. The power-law model overestimates WSS at low inlet velocities and underestimates at high inlet velocities. Walburn – Schneck model underestimates WSS at high inlet velocities [175], [183]. The Casson's model takes hematocrit into account but yields a limiting viscosity at a shear rate slightly above 100 s^{-1} [184]. Barbara et al [15] suggested the use of the Generalized Power-law model which approximates WSS better than the Newtonian model for low velocities and low shear regions and effectively Newtonian at mid-range. The Carreau – Yasuda model fits the experimental data well and is a suitable model for hemodynamic analysis [12], [175].

Large Eddy Simulation (LES) is a mathematical model for the turbulent simulation used in Computation modelling. Using a 3D model of arterial stenosis, physiological pulsatile transition to turbulent non – Newtonian study using five different non – Newtonian viscosity model showed a maximum shear rate lies within 100 s^{-1}. This indicates the necessity of using non – Newtonian model in the computational simulations [185]. This observation is supported by experimental studies using particle image velocimetry technique and path - line flow visualization [186].

Wall shear stress was calculated in vessels by Kefayati et al with varying plaque severity [187] subjected to pulsatile flow using stereoscopic and tomographic PIV in combination with computed tomography of a phantom vessel [188]. A Newtonian viscosity blood analogue was used to address spatial and temporal velocity and WSS variations, but the varying shear direction was not studied. Conventionally, numerical and experimental studies of blood flow have considered blood as a Newtonian fluid with constant viscosity approximated at the high shear limit. However, the characterization of blood viscosity has shown that accumulation of red blood cells into long structures called rouleaux, which increases the viscosity in low shear regions, and shear-thinning behaviour is observed. Considering blood as a Newtonian fluid may be acceptable at the high shear rate and in large arteries. However, it may lead to inaccurate WSS measurements in the region of low shear particularly in post stenotic regions and regions of the unstable flow. Many numerical studies have shown that non – Newtonian viscosity models generate flattened velocity profiles and large recirculation zones when compared to the Newtonian model. An assumption of Newtonian viscosity underestimates WSS at low shear regions due to a lack of shear-thinning behaviour [16], [189], [190]. Multi-directional WSS calculated with viscosity fit to a cross model [191] and results compared to Newtonian blood analogue fluid showed exaggerated disturbed flow and underestimated shear stress when shear thinning is neglected [192]. It was also observed that the importance of rheology is specific to the degree of disease progression and studies investigating the impact of rheology should include a range of geometries including different levels of flow disturbances [193].

Many non – Newtonian models like Power-law [175], Carreau [175], Carreau – Yasuda [194], Modified – Casson [184], Generalized Power-law [179], and Walburn – Schneck model [195] were studied and compared to understand its effect on hemodynamic parameters and to suggest the suitable simulation model. WSS and radial velocity results

showed the same trend for both Newtonian and non – Newtonian viscosity models. However, there will be a significant quantitative difference between the models at low inlet velocities, and in the case of power-law and Walburn – Schneck model even for high velocities. Except for these two models, at mid-range velocities, i.e., between 12 cm/s to 16 cm/s, there are no significant differences. The power-law model overestimates the non – Newtonian behaviour as it predicts higher viscosities compared to Newtonian viscosity at both low and high shear rates and hence not recommended. Generalized power law and Modified Casson also underestimates the non – Newtonian behaviour, whereas Carreau and Carreau – Yasuda model is most suitable to mimic the blood viscosity at both low and high shear rates [196]. Although shear thinning behaviour of blood is not significant in large arteries [175], [176], at locations with acute curvatures like U type ICA [197], the shear thing must be considered. Experimental results demonstrated by Gijsen et al [94] showed that the Carreau – Yasuda model suitably predicts the non-Newtonian behaviour of blood in the artery. Carreau – Yasuda model is a generalized version of the power law. It can effectively fit most viscosity versus shear rate data and the parameters of this model have significant effects on the shape of the predicted curve. The relaxation time is a parameter in the model, which can be related to molecular structure and can be used to analyse molecular insight of the fluid [198].

2.8 Effect of Hypertension on atherosclerosis

Pulse Wave Velocity (PWV) is a robust parameter to predict cardiovascular events [199]and is regarded as a marker for asymptomatic organ damage in the European Society of Hypertension and European Society of Cardiology guidelines for arterial hypertension management [200]. Elevated levels of blood pressure have been associated with PWV in many studies [201]–[203] and has been assumed that severe alterations in the arterial wall due to hypertension causes stiffening of the arteries [204], [205]. However, a recent

statement from the American Heart Association [205] supports the hypothesis that the stiffening of the artery represents a cause rather than a consequence of hypertension. This evidence includes the concept that PWV predicts the increase in blood pressure and the beginning of hypertension in middle-aged and older individuals [206]–[208]. Also, PWV is directly and independently associated with blood pressure progression and incident hypertension in young adults [209]. It is also commonly accepted that plaque development is associated with low – density lipoproteins (LDL) and is enhanced by hypertension [210].

Many studies on primates have shown that hypertension accelerates and intensifies atherosclerosis. [211], [212]. A new entity "prehypertension" was defined by The Seventh Report of the Joint National Committee on Prevention, Detection, Evaluation, and treatment of high Blood Pressure (JNC – 7). Evidence that systolic blood pressure (SBP) ranging from 120 – 139 mm Hg and Diastolic Blood pressure (DBP) ranging from 80 – 89 mm Hg are associated with increased cardiovascular risk was highlighted [213]. It was also estimated that an additional 30% of adult individuals belong in this category [214]. However, clinical trials of patients with blood pressure in the prehypertensive range are scarce. Therefore, the therapeutic BP target remained at <140/90 mm Hg. Although some researchers studied the relationship between hypertension and coronary artery disease and extended these observations to the "prehypertension" range [215], there are no existing data regarding the effect of pre-hypertension, hypertension, and normal blood pressure on the progression of atherosclerosis.

Atherosclerosis preferentially develops at sites with low or oscillating shear stress [216], [217], and at regions of non-disturbed and steady flow, mid and high shear rate show resistance to the development of atherosclerosis. Moreover, high wall shear stress is found at the proximal side of the plaque linked to plaque vulnerability. Recently, it was observed

that the shear directionality of endothelial cells due to flow plays a key role in inflammatory endothelial cell responses [218], [219]. This regional wall shear stress variation is more often quantified in the numerical and experimental analysis by using oscillatory shear index (OSI) which was first proposed by Ku et al [45] to study the changes in the time-averaged stress vector under pulsatile flow. However, due to a lack of definitive evidence for oscillatory and low WSS hypothesis [82], [220] new metrics to quantify the multi–directionality of WSS were developed[221]–[223]. The traditional OSI parameter is unclear in distinguishing between uniaxial reversing shear and multi-directional shear stress. A new metric called transverse wall shear stress (transWSS) was proposed by Peiffer et al [82] which showed qualitative relation between transWSS obtained using CFD studies and lipid deposits in rabbit aorta. Other shear metrics that incorporate axial and orthogonal projections of WSS [221], [222], as well as normalized instantaneous transWSS components [220], have also been explored.

Chapter 3 3D computational model generation

3.1 Introduction

This chapter will describe the underlying theory and techniques of reconstructing a 3D model of a vessel, followed by a detailed description of the process employed in this research in reconstructing a 3D model of a vessel that will be used for the various computations investigations.

The different stages of a computational model generation of human vasculature are – image acquisition, conversion of obtained image data, image segmentation, and reconstruction of the surface. The first step of model generation is medical imaging of the subject from resources like Computed Tomography (CT) or Magnetic Resonance Imaging (MRI). This includes 2D or 3D matrices of volume elements known as voxels, where different regions like soft and hard tissues are differentiated by the differences in greyscales. The 2D image slice contains pixel data, wherein voxel is a 3D equivalence of a pixel where the additional third dimension is the distance between each slice.

3.2 Medical imaging

The geometry of the arterial system was identified by using various imaging technologies like MRI and CT. MRI uses radio waves and magnetic fields to obtain the images of any section of the human body. The scanning process involves passing an electric current pass through the coil, which generates a magnetic field. The protons of water in the body generally spins in arbitrary directions, and are aligned with the magnetic field. When the protons are aligned, a small surge of radio waves is passed through, causing variation in the quantum state of the protons for a short moment (flips the spin of protons). When the radio waves are stopped, the proton returns to its original orientation and reflects its radio

signal, which is detected by the scanner and decodes into images. Different tissues produce different pulse sequences, which leads to changes in contrast to several tissue markers. Besides, physiological and anatomical variations between subjects require different pulse sequences to obtain accurate contrast.

CT scan uses x-ray data obtained at multiple cross-sections targeted at any region of interest. The sensors collect the information at each cross-section and redirect it to a computer to combine into a single image. The images obtained by CT scans are similar to MRI images, however, contrast obtained by soft tissues are better in MRI. Since CT scan uses x – rays, its exposure for a long duration has unavoidable associated risks, and hence, CT scans are used only where benefits of the examination are greater than any potential risks. Although both MRI and CT are non – invasive, a dye was injected sometimes via one of the veins referred to as CT or MR angiography. The contrast dye highlights the circulatory system and helps to detect the arteries of interest on the x-ray. This procedure is known as angiography.

The obtained images are a set of greyscale values of different tissues and the value represents a measure of radiodensity in MRI. Hounsfield scale (HU) is used in medical imaging on a scale of 0 to 255 where 0 represents black and 255 represent white as shown in *Figure 3-1*.

3.3 Image Segmentation

Image segmentation is a process of partitioning images of different regions for processing. In this process, a label is assigned to the pixels to form a continuous region. The pixels which are not related to the region of interest will be seen as a pixel value outside the required criterion. Segmentation could be manual by individually selecting the pixels or

could be automated. The process of manual segmentation was time-consuming and produces variability while selecting pixels between the slices.

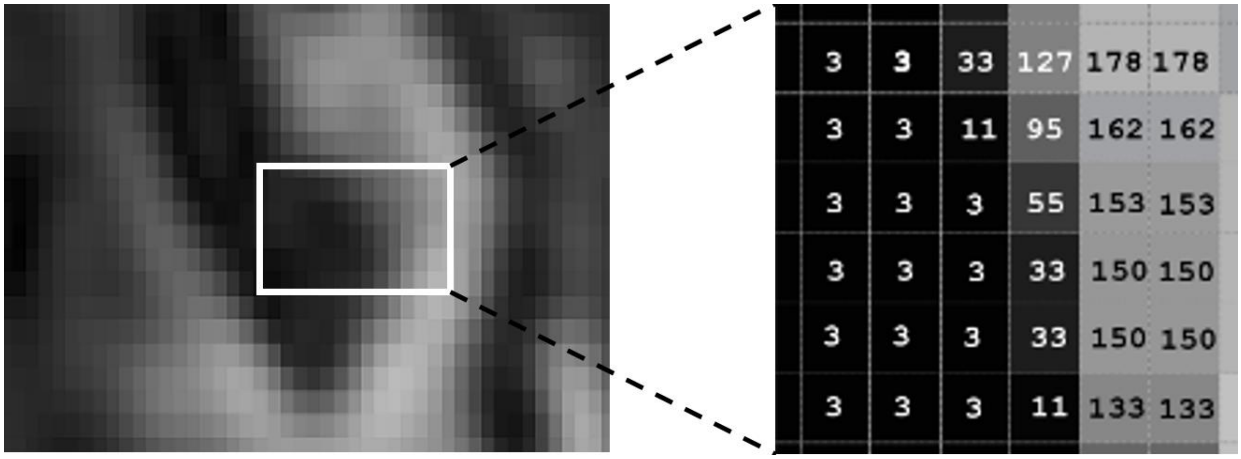

Figure 3-1: Digital representation of a greyscale image

Automated or semi-automated segmentation was dependent on the greyscale values where the discontinuities at an edge can be recognized by observing sudden changes in the greyscale intensity. Similar intensity regions can be used to extract regions showing similar properties as per a predefined criterion.

Many researchers have explored different segmentation procedures over the years. It is a challenging task where the user should overcome an increased range of changes within the images, artefacts such as motion blur, noise, and partial volume effects. Therefore, a single algorithm could not generate images that produce acceptable results for all kinds of medical images [224].

3.4 Segmentation methodology

The region of interest is generally defined by its greyscale strength, interior, or its boundary. Therefore, the segmentation procedure is classified into threshold-based, edge-based, and region-based. In the threshold-based method, each pixel was measured depending on the greyscale value that represents the intensity of the obtained scans. The

edge-based approach identifies the edge pixels and forms a boundary enclosing the area of interest. The region-based approach uses the greyscale values from the neighbouring pixels called region growing. Although the pixel-based approach was the simplest procedure, they do not contain background information and fail in high inhomogeneous scans. The edge-based method was the next simplest method and was effective on clearly defined scans of the anatomical structures such as arteries. However, noise or occlusions can lead to false or can miss edge perception. Also, the region-growing technique will be useful in noisy scan images where edge detection is challenging to detect. In this study, scan data obtained from CT was segmented using image processing software MIMICS 19.

The images obtained from CT or MRI consists of greyscale information. Anatomical models can be created in Mimics based on the greyscale values (Hounsfield units in CT images) within these images. A greyscale value is a number related to a pixel defining the shade of white, grey, or black. There is a direct relation between the density of the material of the scanned object and the greyscale value assigned to each pixel in the image. This gives the user flexibility to create models from any geometry which are distinguishable within the data. By grouping identical greyscale values, the image can be segmented, and models are created. This method of segmentation is called thresholding and results in inaccurate models. Using the segmentation tool and with information on the size of the pixel and the distance between the slices, a 3D model was generated. Further details on step by step procedure of image segmentation can be obtained from the Mimics user manual [225].

3.5 Surface and volume reconstruction

A general flow chart of the anatomical model generation is shown in *Figure 3-2*. After the segmentation process, a CFD meshing software directly reads the output. After the

segmentation process, the CFD meshing software can directly read the output file or some topographical data could be added in the model. The main purpose of adding the topographical data is due to its compatibility with the CFD software. While adding the topographical details, for simple integration into a CFD mesh program, the geometry can be mathematically represented with a Non – uniform Rational B – Spline (NURBS). This procedure includes overlaying a watertight surface, which keeps together data such as points, lines, and surface data that are interconnected.

3.6 Example of model reconstruction

The basic segmentation and reconstruction in this study are described in this section, using a patient-specific artery as an example. A patient-specific CT image data was obtained, and the region of interest was chosen and imported to MIMICS. The MIMICS window shows four different views i.e., coronal, sagittal, axial, and 3D as shown in *Figure 3-3*.

The 3D rendering tool in MIMICS was used to visualize the developed 3D anatomical model as shown in *Figure 3-4*. Using these tools user can examine and ensure the suitability of the selected threshold and confirm the anatomical accuracy of the physical carotid model.

Later, smoothing operation was performed by adopting enough iterations to remove sharp edges and corners and perform surface rendering operations. The model was verified for the suitability, it was exported as a stereolithographic file (.stl) into CATIA to generate a solid model. The stereolithography file format obtained from MIMICS was exported into CATIA, a CAD software package. As the FSI consists of structural and fluid models representing blood and elastic artery, the 3D models of fluid and artery were generated separately. The procedure of the generation of the 3D model is explained below. 3D model of the arterial wall was generated in a similar fashion considering a uniform wall thickness

of 0.7 mm representing the elastic artery [226]–[228]. The usual range of the Carotid Intima-Media Thickness (CIMT) is in the range of 0.6 – 0.8 mm and within this range was used in this study to model the arterial wall. The Digitized Shape Editor (DSE) module of CATIA was used to generate the surface. DSE was used as a reverse engineering tool, which provides tools for operations on imported data. The STL file was edited until a smooth surface was obtained. The surface patch was automatically generated by wrapping the refined surface using a quick surface reconstruction module.

The mean surface deviation was maintained at a lower value in the range of 0.01 – 0.005. The surface detail was maintained at a higher range of 8000 – 12000 to obtain a refined surface patch. The refined surface model was converted into a solid model by exporting it into the generative shape design module. The generated 3D models at their different stages are shown in *Figure 3-5*. A computational mesh is several elements that represent the computational domain. Generally, a series of fluid and structural equations were applied on each grid. By solving these equations, the interpolations between the cells were determined to find variables such as pressure, wall shear stress, velocity, and deformation. The strategy used in meshing was to generate an initial topology of coarse mesh, which gives a quick solution, depending on which the model can be refined. By incorporating a suitable coarse mesh, several test runs can be carried out to assess the convergence of the numerical solutions and the physical models.

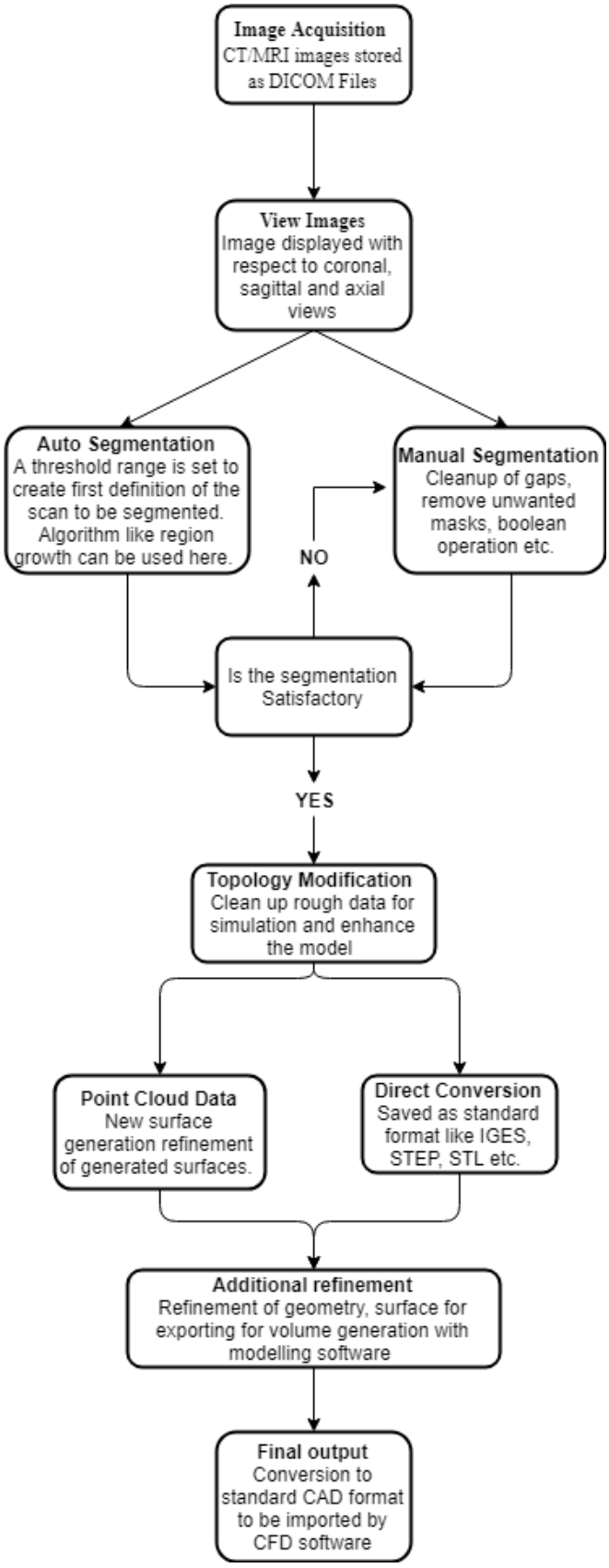

Figure 3-2: Flow chart of the segmentation process and generation of the 3D computational model.

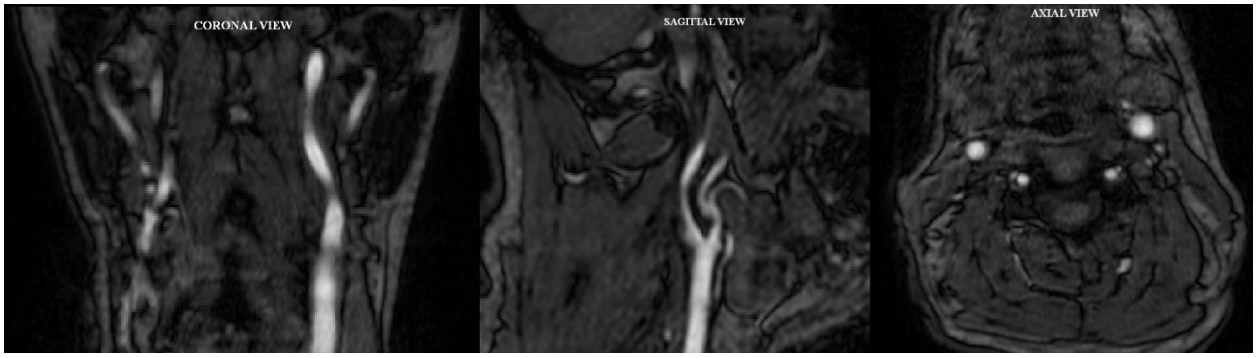

Figure 3-3: Different views of CT image data

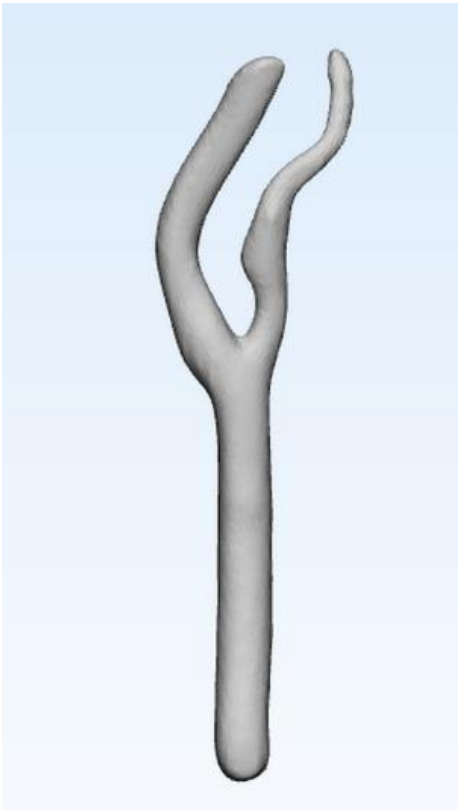

Figure 3-4: Generated 3D mask in .stl format to be imported to CATIA

When the applied numerical setup was acceptable with a converging solution, the mesh can be refined to get more accurate solution. If the solution was not converging, the mesh or the model was repaired for inaccuracy. Some probable causes of errors could be human errors, modelling errors, or errors in the numerical setup [5].

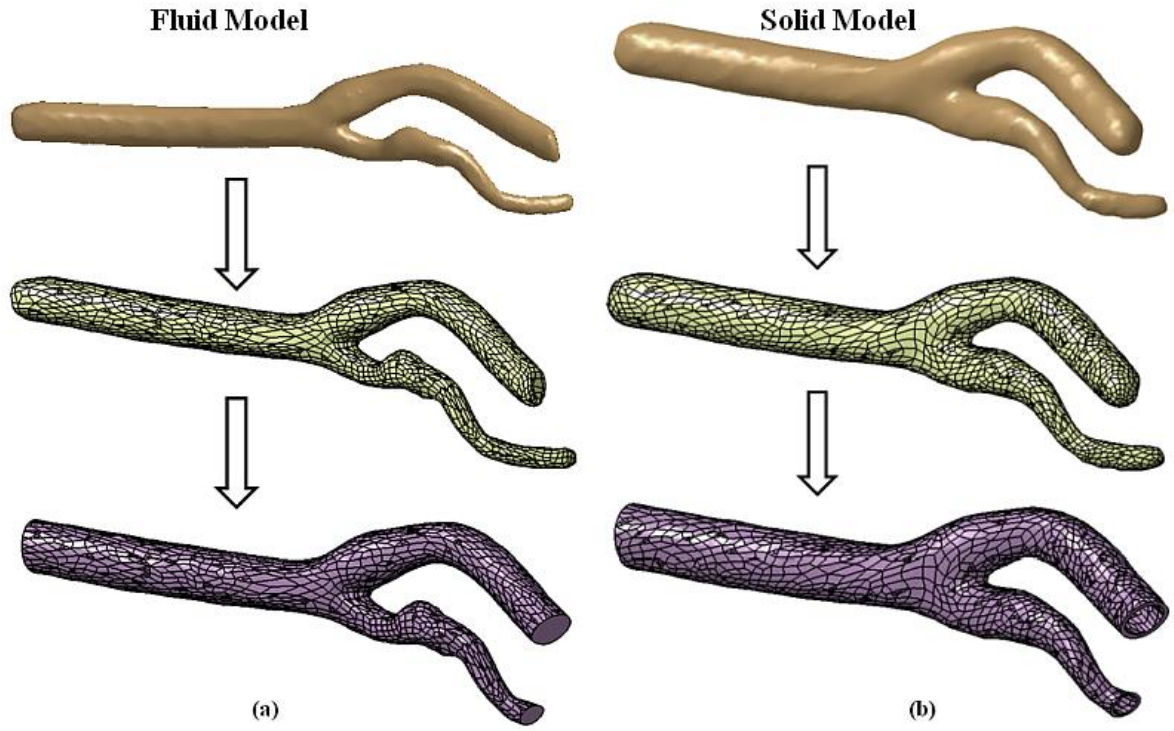

Figure 3-5: Step by step model generation of carotid bifurcation using CATIA

In an unstructured grid, there were no constraints on using a mesh type, a hybrid mesh blends various types of elements that can fit suitable mesh with boundary surfaces and allocates elements of different types in regions of complex flows. For circular domains, the quality of the grid is improved by placing quadrilateral or prism elements to resolve viscous boundary layers to capture near walls effects while tetrahedral elements are used for the rest of the domains.

The anatomical fluid and solid models of the carotid bifurcation were imported into Ansys Workbench in STEP formal (.step). Before performing the analysis of the CAD models, the surface patches present initially on the CAD model are merged to form a single surface using Virtual Topology. This aids in reducing the number of elements in the model, simplifies small features out of the model, and simplifies load abstraction. Both fluid and solid mesh are discretized using 10 noded tetrahedral mesh [229] as shown in *Figure 3-6*.

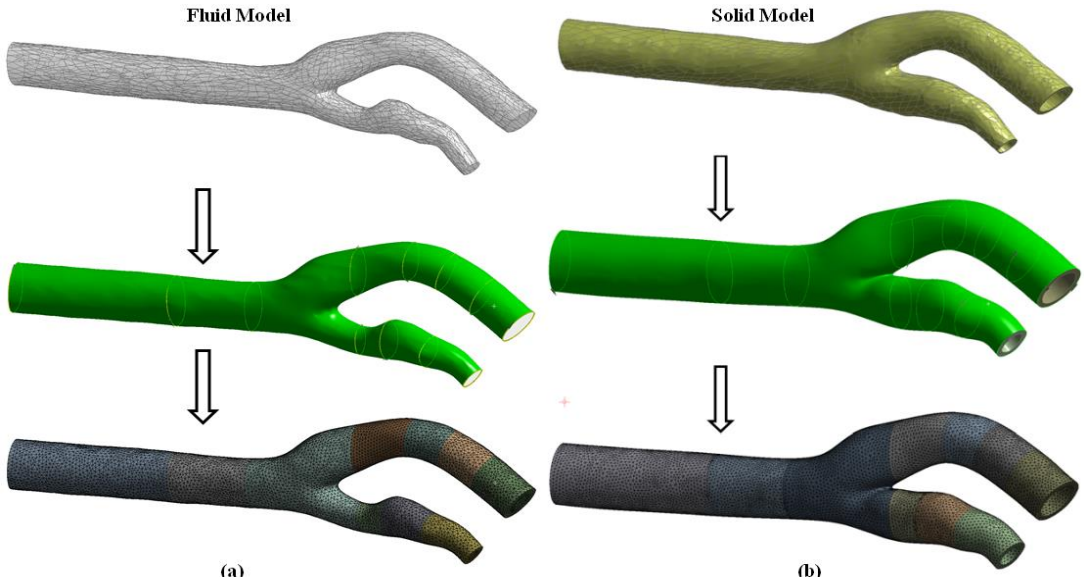

Figure 3-6: Steps to obtain 3D carotid bifurcation fluid and structural computation model.

This chapter highlighted the steps involved in generating a computational model for haemodynamic analysis using anatomical data. Numerical methods are applied to these models to solved using CFD (rigid wall) and FSI technique which is explained in detail in the coming chapters.

Chapter 4 Basic equations of Computational Fluid Dynamics and Fluid Structure Interaction.

The flow through the arterial is governed by conservation laws, and the arterial model is governed by law of conservation of linear momentum. This chapter will describe the numerical techniques used to solve the fluid and structural governing equations used in the study along with the dynamic and kinematic conditions necessary for coupling the fluid and structural domain.

4.1 Computational Fluid Dynamics

Equations of fluid dynamics are a set of equations representing conservation laws. The equations are law of conservation of mass, conservation of momentum and conservation of energy.

4.1.1 Conservation of mass

The conservation of mass is balance between mass entering a surface of a control volume and mass leaving a surface of the same control volume. This is summarized as shown below

$$\frac{D\rho}{Dt} + \rho\nabla.V = 0 \tag{4.1}$$

Where ρ is fluid density, t is total cycle time and V is the fluid velocity.

The above continuity equation is rewritten in Arbitrary Lagrange Eulerian (ALE) framework as

$$\frac{\partial \rho}{\partial t} + \nabla \cdot \rho(v - v_c) = 0 \quad (4.2)$$

Where v_c is grid velocity.

In human vasculature, there are many arteries which bifurcates into smaller branches like carotid artery and aortic arch. Here the mass flow is divided due to flow division. The flow rate in each branch is dependent on the flow resistance offered and it can be determined by the considering the lumen diameters of the branches and its bifurcation angle. However, the mass flow must be conserved in the entire arterial network.

4.1.2 Conservation of momentum

The momentum conservation principle was obtained from Newton's second law, $\sum F = ma$, where $\sum F$ is the sum of all forces on a control volume. The two types of forces action on the control volume are surface force and body force. For an incompressible flow,

$$\rho \frac{DU}{Dt} = Body\ force + Surface\ force \quad (4.2)$$

Where $\frac{DU}{Dt}$ is the acceleration.

Body forces like gravity, centrifugal forces etc. act on the entire domain and its effects are incorporated by including them in the momentum equation. The surface forces acts on the fluid surface and deforms the fluid. Therefore, the momentum equation can be written as

$$\rho \frac{\partial v}{\partial t} + \rho(v \cdot \nabla)v = \nabla \cdot (\rho \Upsilon \nabla v) \quad (4.3)$$

Where Υ is diffusivity

The above momentum equation is rewritten in ALE framework as

$$\rho \frac{\partial v}{\partial t} + \rho([v - v_c] \cdot \nabla)v = \nabla \cdot (\rho \Upsilon \nabla v) \quad (4.4)$$

4.2 Governing Equations of Solid

The governing equation for the solid domain is written in Lagrangian reference as

$$M\ddot{d} + C\dot{d} + Kd = F \tag{4.5}$$

Where d is the displacement, M is mass, C is damping, K is stiffness and F is force.

4.3 Discretization of governing equations

The governing equation of fluid in ALE framework is written as

$$\underbrace{\frac{\partial \rho \emptyset}{\partial t}}_{Temporal\ term} + \underbrace{\nabla \cdot (\rho[v - v_c]\phi)}_{Convection\ term} - \underbrace{\nabla \cdot \left(\rho \Upsilon_\phi \nabla \emptyset\right)}_{Diffusion\ term} = \underbrace{S_\emptyset(\emptyset)}_{Source\ term} \tag{4.6}$$

Where $\emptyset$ is transport variable, Υ_ϕ is diffusivity, $S_\emptyset$ is the source term.

The governing equations in the finite volume method must satisfy over the control volume V_P around point P. therefore writing the above equation in integral form,

$$\int_t^{t+\Delta t} \left\{ \underbrace{\frac{\partial}{\partial t}\int \rho \emptyset dV_P}_{Temporal\ term} + \underbrace{\int \nabla \cdot (\rho[v - v_c]\emptyset dV_P)}_{Convection\ term} - \underbrace{\int \nabla \cdot \left(\rho \Upsilon_\phi \nabla \emptyset\right) dV_P}_{Diffusion\ term} \right\} =$$

$$\int_t^{t+\Delta t} \left\{ \underbrace{\int S_\emptyset(\emptyset) dV_P}_{Source\ term} \right\} \tag{4.7}$$

Discretization of temporal term

- **First order backward Euler scheme:**

  Here the temporal form is discretized as

  $$\frac{\partial}{\partial t}\int \rho \emptyset dV_P = V_P \left(\frac{\rho^{n+1}\emptyset^{n+1} - \rho^n \emptyset^n}{\Delta t}\right) \tag{4.8}$$

  Where n and n+1 are time intervals.

- **Second order backward Euler scheme**

Here the temporal term is discretized as

$$\frac{\partial}{\partial t}\int \rho \emptyset dV_P = V_P\left(\frac{3\left(\rho^{n+1}\emptyset^{n+1}\right)-4(\rho^n\emptyset^n)+\left(\rho^{n-1}\emptyset^{n-1}\right)}{2\Delta t}\right) \tag{4.9}$$

Discretization of convection term

The convection term can be discretized by using Gauss theorem as

$$\begin{aligned}\int \nabla\cdot(\rho[v-v_c]\phi)dV_P &= \sum_{f_c} S_c(\rho[v-v_c]\phi)_{f_c}\\ &= \sum_{f_c} S_c(\rho[v-v_c])_{f_c}\emptyset_{f_c}\\ &= \sum_{f_c} F_c\phi_{f_c}\end{aligned} \tag{4.10}$$

F_c and S_c are mass flux and face area vector pointing outwards through the face of the element. If the flux value on the surface element is known, the convection term can be determined by interpolation. Subscript f_c is the element face. The primary aim of the convection differencing scheme is to calculate $\emptyset_{f_c}$ by using value of ϕ at the center of the elements. The following convection differencing schemes are available in CFX

- **First order upwind differencing scheme**

$$\phi_{f_c} = \begin{cases}\phi_{f_c} = \phi_P \; if \; F_c \geq 0\\ \phi_{f_c} = \phi_P \; if \; F_c < 0\end{cases} \tag{4.11}$$

- **Central differencing scheme**

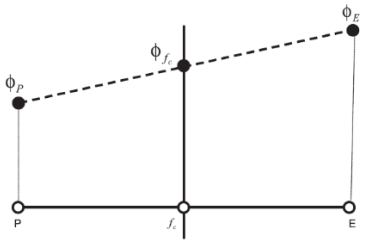

$$\phi_{f_c} = f_{intp}\phi_P + \left(1-f_{intp}\right)\phi_E \tag{4.12}$$

Where f_{intp} is the interpolation factor which can be estimated as

$$f_{intp} = \frac{f_c E}{PE} \tag{4.13}$$

- **High resolution scheme**

$$\emptyset_{f_c} = (1-\eta)\left(\phi_{f_c}\right)_{UD} + \eta\left(\phi_{f_c}\right)_{CD} \tag{4.14}$$

The values of $\left(\phi_{f_c}\right)_{UD}$ and $\left(\phi_{f_c}\right)_{CD}$ are calculated by upwind and central differencing scheme respectively. The upwind scheme is stable, however, the accuracy is low because of the numerical diffusion introduced in the system by the biased nature of the scheme. The central - differencing scheme is less biased and provides a second order accuracy but not stable. Therefore, high-resolution scheme is used to preserve stability and accuracy of the solution. It is a combination of upwind and central differencing scheme, the contribution of the two schemes are determined by η. This scheme reduces to upwind difference scheme when η is zero and reduces to central difference scheme when η is unity.

Discretization of diffusion term

The diffusion term is discretized by using gauss theorem as

$$\int \nabla \cdot \left(\rho \Upsilon_\phi \nabla \emptyset\right) dV_P = \sum_{f_c} S_c \left(\rho \Upsilon_\phi \nabla \emptyset\right)_{f_c}$$

$$= \sum_{f_c} \left(\rho \Upsilon_\phi\right)_{f_c} S_c (\nabla \emptyset)_{f_c} \tag{4.15}$$

$(\nabla \emptyset)_{f_c}$ must be correctly estimated to calculate the diffusion term, here

$$(\nabla \emptyset)_{f_c} = \left(\frac{\partial \emptyset}{\partial x}\right)_{f_c} + \left(\frac{\partial \emptyset}{\partial y}\right)_{f_c} + \left(\frac{\partial \emptyset}{\partial z}\right)_{f_c} \tag{4.16}$$

$\left(\frac{\partial \emptyset}{\partial x}\right)_{f_c} = \sum_n \left(\frac{\partial N_n}{\partial x}\right)_{f_c} \emptyset_n,$

$$\left(\frac{\partial \emptyset}{\partial y}\right)_{f_c} = \sum_n \left(\frac{\partial N_n}{\partial y}\right)_{f_c} \emptyset_n,$$

$$\left(\frac{\partial \emptyset}{\partial z}\right)_{f_c} = \sum_n \left(\frac{\partial N_n}{\partial z}\right)_{f_c} \emptyset_n,$$

Formula for shape function N_n depends on the element chosen during calculation [230].

Discretization of source term

By applying linearization, the source term is discretized in the fluid transport equation as suggested by Patankar et al [231],

$$\int S_\emptyset(\emptyset) dV_P = S_u V_P + S_P V_{P\emptyset_P} \tag{4.17}$$

4.4 FSI coupling methodology

Wang et al [232] suggested that the dynamic and kinematic conditions are necessary to perform FSI analysis. The kinematic condition maintains the displacement compatibility across the interface, which can be written as

$$d_\Gamma^f = d_\Gamma^s \tag{4.18}$$

Where d is the displacement, d_Γ^f and d_Γ^s are fluid and solid displacements respectively. This gives a relationship between fluid velocity v_Γ and rate of change of displacement written as

$$\hat{n} \cdot v_\Gamma = \hat{n} \cdot \dot{d}_\Gamma^s \tag{4.19}$$

Where $\hat{n}$ is normal vector on the interface.

The dynamic condition maintains the traction across the interface when no – slip condition is defines at the fluid interface given as

$$\hat{n} \cdot \sigma_\Gamma^s = \hat{n} \cdot \sigma_\Gamma^f \tag{4.20}$$

Where σ_Γ represent the interface stress.

These conditions were used in the FSI codes by adopting partitioned approach. The nodes on the fluid interface were modified according to the corresponding solid nodes by following the kinematic condition. The stress equilibrium on the FSI interface was ensured by following dynamic conditions and the fluid pressure was integrated into the fluid force used when applying to the solid interface nodes. This procedure is illustrated as shown in *Figure 4-1*.

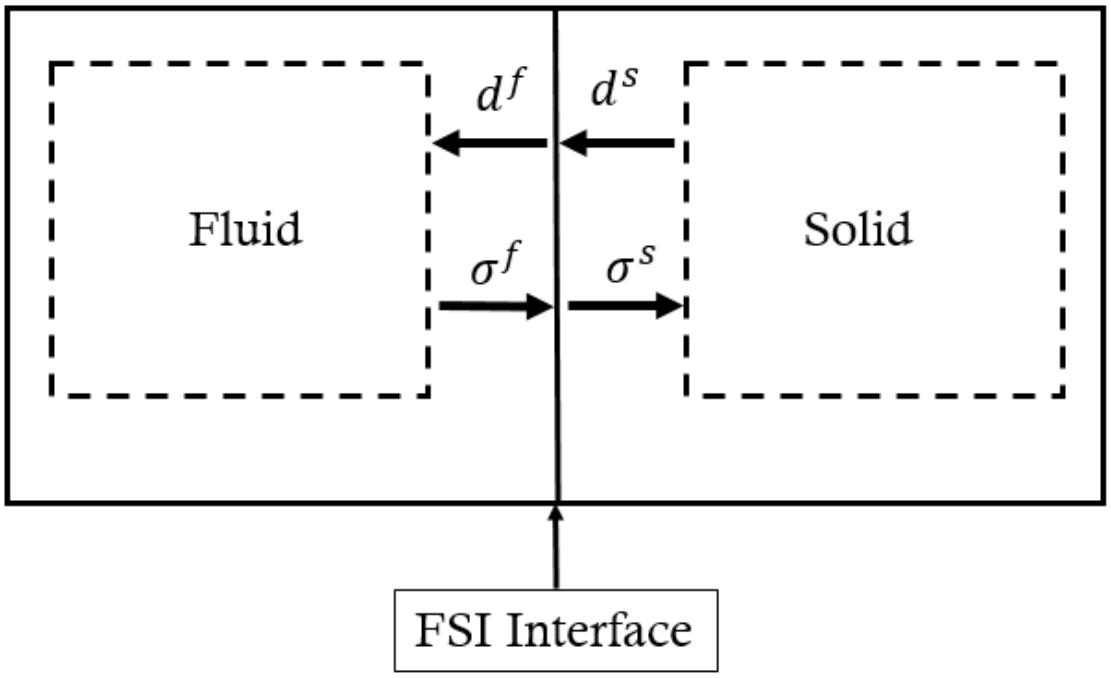

Figure 4-1: Diagrammatic representation of fluid structure interface coupling

4.5 Calculation procedure

The iterative method used by Ansys CFX for FSI coupling solution is Dirichlet/Neumann approach. It means, the fluid equation was imposed with Dirichlet boundary condition like displacement and velocity at the interface. At the same time, Neumann boundary conditions such as force was applied to solid equation. The standard procedure of

calculation in FSI problem is summarized in *Figure 4-2*. Similar work has been performed by Kamakoti et al and Wall et al [233], [234]. Information from the previous time step is used to compute the initial configuration of the fluid domain. If d^n is the information of first coupling step of level n+1, else information previous coupling iteration, i.e., d_m^{m+1} is used. That is

$$\tilde{d}_{m+1}^{n+1} = \begin{cases} d^n \, if \; m = 0 \\ d_m^{n+1} if \; m \neq 0 \end{cases} \tag{4.21}$$

Where $\tilde{d}$ is estimated displacement.

Next step is to solve the flow field to get

$$\tilde{P}_{m+1}^{n+1} = F\left(\tilde{d}_{m+1}^{n+1}\right) \tag{4.22}$$

Where P is the fluid pressure and F is fluid force term.

The obtained fluid load was transferred to structural solver and corresponding load to be applied to structural solver is estimated

$$\tilde{P}_{m+1}^{n+1} = \omega\left(\tilde{P}_{m+1}^{n+1}\right) \tag{4.23}$$

Where ω is applied under –relaxation factor.

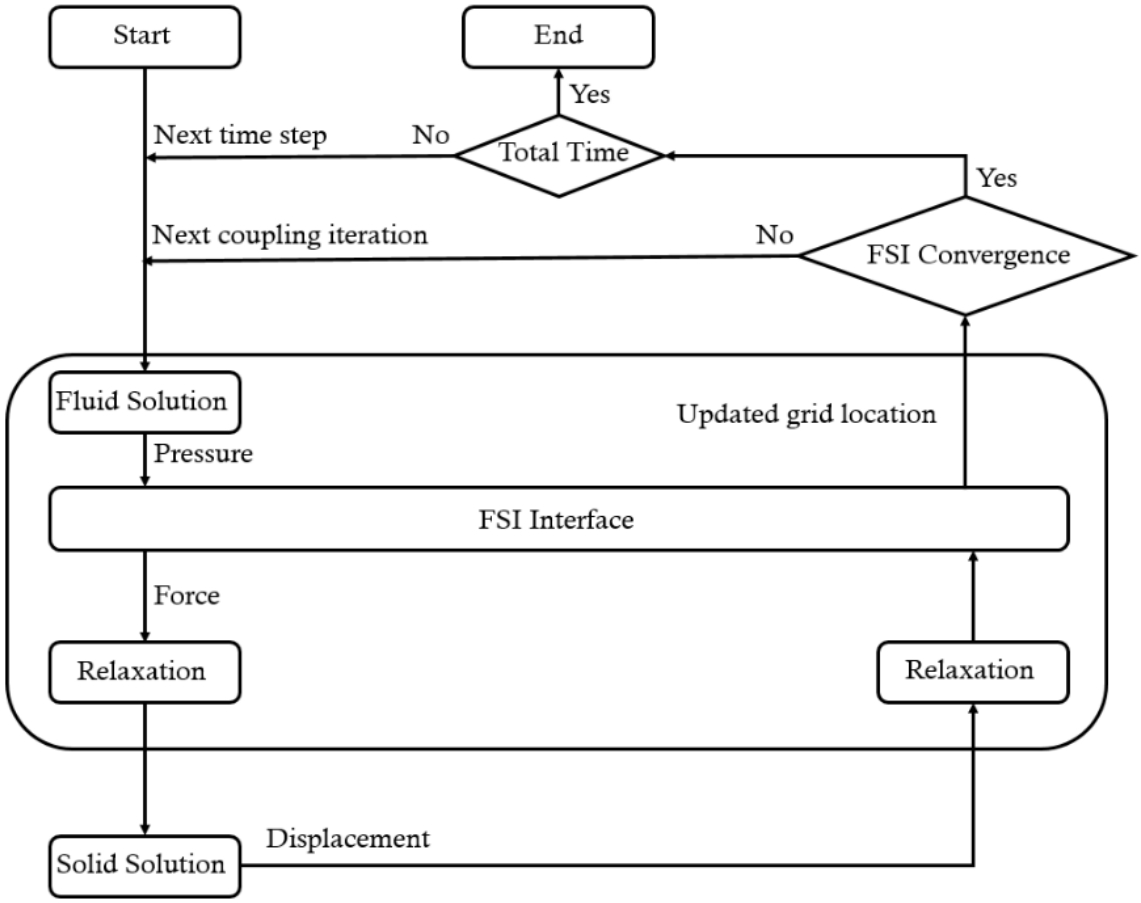

Figure 4-2: Flow chart showing standard FSI solution procedure

The solid governing equation is solved to get

$$\tilde{d}_{m+1}^{n+1} = S\left(\tilde{P}_{m+1}^{n+1}\right) \tag{4.24}$$

Where S represent solid calculation.

The fluid deformation is estimated which corresponds to structural solution obtained from previous time step given as

$$d_{m+1}^{n+1} = (1-\omega)\tilde{d}_{m+1}^{n+1} + \omega d_{m+1}^{n+1} \tag{4.25}$$

It should be noted that $\tilde{d}_{m+1}^{n+1}$ is not the final solution but only an estimated solution for fluid calculation at coupling level m+1.

The solution is converged if the following condition is satisfied

$$r^{n+1,s} < \varepsilon_0, r^{n+1,s} = d_{m+1}^{n+1} - d_m^{n+1} \tag{4.26}$$

$$r^{n+1,f} < \varepsilon_0, r^{n+1,f} = P_{m+1}^{n+1} - P_m^{n+1} \tag{4.27}$$

Where r is the residual, ε_0 is the convergence tolerance. *f* and *s* denote fluid and solid respectively.

The criteria to determine the convergence of the FSI solution is given as [230]

$$Convergence = \frac{log\left(\frac{\epsilon_x}{\epsilon_{min}}\right)}{log\left(\frac{\epsilon max}{\epsilon_{min}}\right)} \tag{4.28}$$

Where ϵ_x is the norm of interface quantities transferred between two domains, ϵ_{min} is the convergence criteria specified in the coupling setup, ϵ_{max} is the divergence limit. If $\epsilon_x < \epsilon_{min}$ then the solution is converged.

Chapter 5 Computational hemodynamic study of atherosclerotic carotid artery

5.1 Introduction

The flow in stenosed carotid arteries are subjected to disturbances like recirculation, oscillating shear etc. in post stenotic region which leads to thrombus formation. Hence, the assessment of flow disturbance was a very important factor in diagnosing carotid artery atherosclerosis. In this chapter, computational fluid dynamic simulation of patient specific carotid artery model with and without stenosis was performed by considering rigid wall.

To validate the accuracy of the numerical model, CFD simulations was performed on a carotid artery model was compared with PIV measurements [235] and the flow patterns near the bifurcation of the carotid artery was studied. Haemodynamic parameters such as WSS, Velocity, and Oscillatory shear index (OSI) was analysed.

5.2 Numerical validation

5.2.1 Validation model

A tuning fork shaped carotid artery model was proposed by Ding et al [236]. The model was defined as a parametric stereolithographic (STL) model and was scaled up to 3.2 times the original model. Similar model was used by Buchman [235] by using prototypes of the model manufactured by 3D printing. The fluid used in the study was glycerine solution with dynamic viscosity of 11.7 x 10^{-3} Pa. s and fluid density of 1150 kg m^{-3}. For validation of numerical model, a study was performed on a computational model shown in *Figure 5-1* and the dimensions are highlighted in *Table 5-1*.

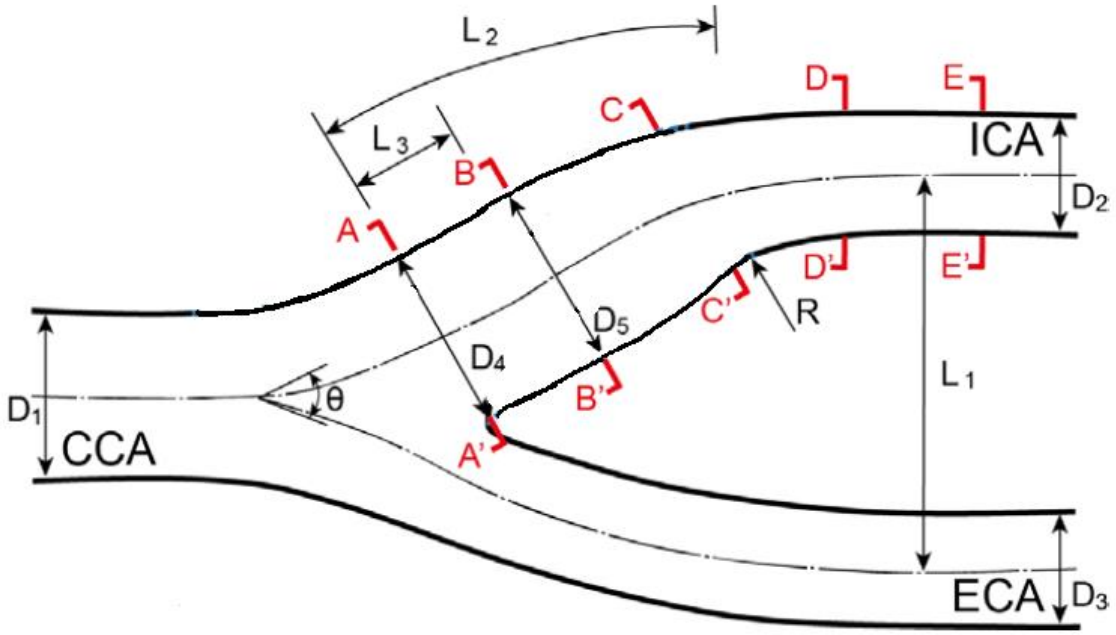

Figure 5-1: Representation of carotid artery model used in the study.

Table 5-1: Dimensions of the carotid artery model (mm), θ = 50°.

Location	D1	D2	D3	D4	D5	L1	L2	L3	R
Normalized Values	1	0.72	0.69	1.04	1.11	2.4	3.0	0.9	4.1

The computational model was modelled in CATIA V5 (3D modelling software) and imported into Ansys CFX (version 19.0) and meshed with 10 node tetrahedral elements. To capture near wall quantities, inflation with 12-point refinement with smooth transition were imposed. Meshed model is shown in *Figure 5-2*.

The field variables were solved iteratively using continuity and momentum equations as given by Eq. 5.1 and Eq. 5.2 respectively

$$\nabla \cdot u = 0 \tag{5.1}$$

$$\rho(u \cdot \nabla u) = -\nabla p + \mu \nabla^2 u + \rho g \tag{5.2}$$

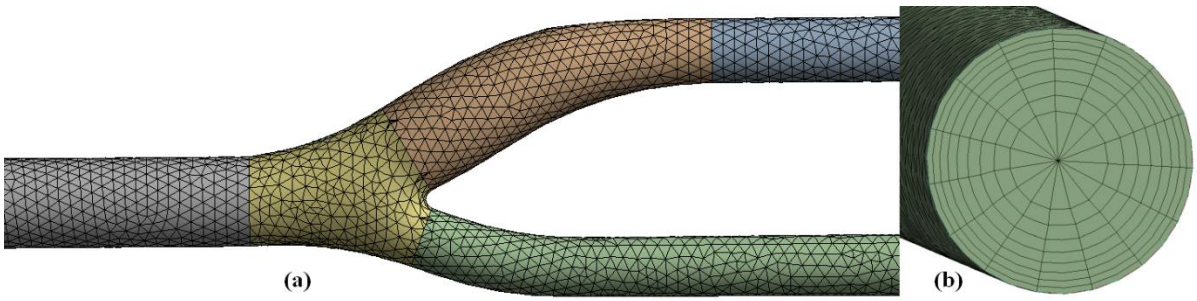

Figure 5-2: (a) Tetrahedral mesh used in the study, (b) 12 layer inflation used near boundary using smooth transition method.

Where u is the velocity vector, p is the blood pressure, ρ is the density, and μ is the viscosity. The governing equations were solved using high resolution advection scheme to calculate the advection terms in the discrete finite volume equations. The residual target is maintained at 0.0001. The wall was assumed to be rigid and stationery, and no – slip condition was defined at the wall. At the inlet, a fully developed Poiseuille flow was defined. Reynolds number of 400 and 800 were applied representing mean and peak systole velocities. This provided a detailed understanding on different inlet conditions and its effect on flow recirculation, secondary flows and WSS variations.

5.2.2 Validation results

Grid independence study

Grid independence study was performed to choose ideal mesh size for CFD study. An ideal mesh size of 149399 elements was chosen in the study. *Figure 5-3* shows the variation of average WSS with number of elements.

Figure 5-4 shows the comparison of velocity vectors between numerical and experimental measurements at the central plane of a health idealized carotid artery model. The velocity values were normalized with the maximum value at the centre line of the CCA inlet.

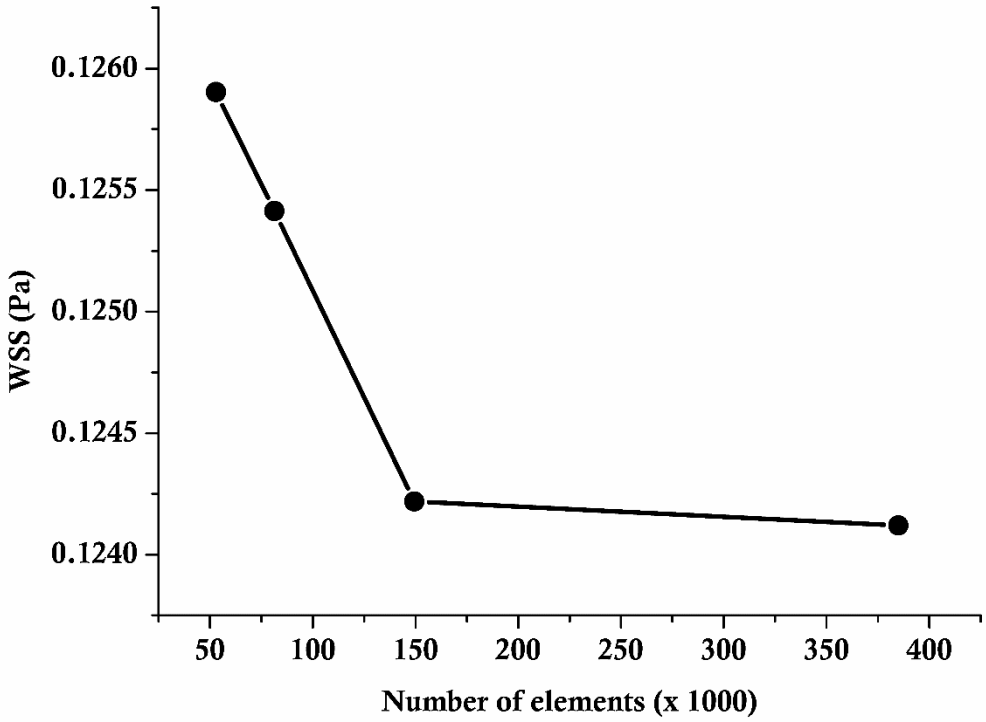

Figure 5-3: Grid independence study

Due to the shape of the model, the flow remains laminar and hence the laminar model was used in the study. Results obtained for both Reynolds numbers were in good agreement with the literature. Velocity profiles were slightly increased at the inner wall of ICA within the carotid sinus. This was due to flow division at the bifurcation apex, leading to flow concentration near the inner wall. At the outer wall, flow recirculation was observed due to pressure gradient. The low velocity zone was occupied by at least 50% of the lumen. The profile gets uniformly distributed with blunt profiles at the downstream where the vessel was straight. In conclusion, the flow patterns agree with the measured data [235]. Compared to PIV data, flow separation due to change in cross section at the carotid sinus at the ICA were successfully predicted using laminar model.

Flow experiences a sudden increase in the cross sectiona area causing rapid decrease in WSS to values close to or below zero at proximal sinus. WSS remains low at the sinus and increase again at the distal end of the sinus due to reduction in the cross sectional area.

As shown in *Figure 5-5*, for low Re, i.e., Re = 400, a single detached flow region exist along the carotid sinus with flow sepaeration and reattachment occurring at proximal and distal regions. This trend is also seen in higher Re, but magnitude of negative WSS increases with increasing Re.

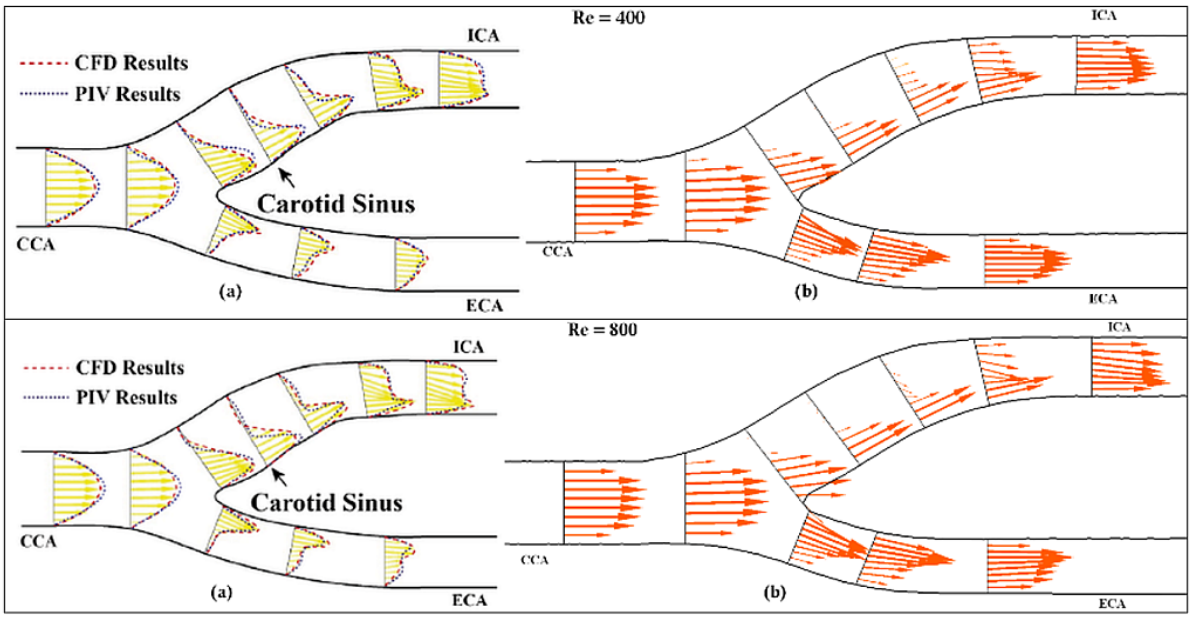

Figure 5-4: Comparison of velocity vectors at different locations in the carotid artery branches subjected to different Reynolds number. (a) Literature [5], [235], (b) present study.

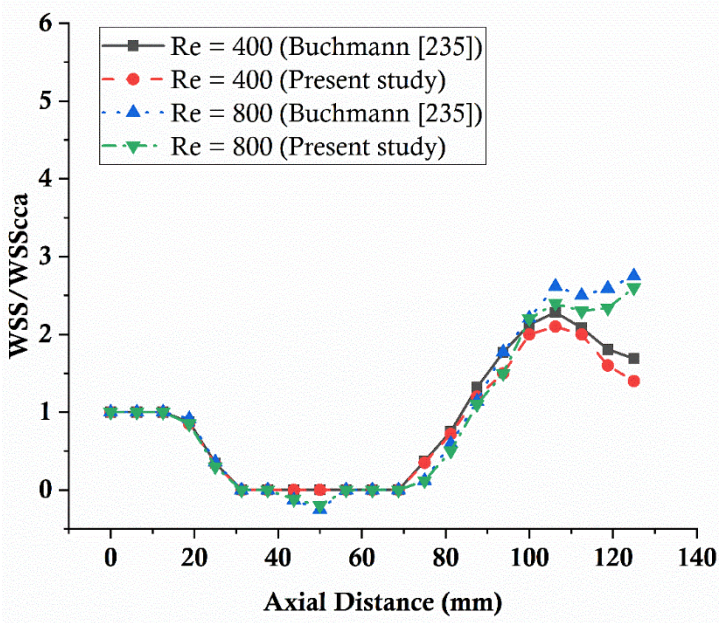

Figure 5-5: WSS plotted along the outer sinus wall for Reynolds numbers, Re = 400; 800; Data are normalised by their corresponding value in the common carotid artery

5.3 Computational Fluid Dynamic analysis of patient specific normal and stenosed carotid artery

The carotid bifurcation is an ideal location for non – invasive imaging and many extensive researches has been conducted during the past decades, and many image-based haemodynamics of carotid bifurcation has been performed from experimental and numerical aspects. In image based CFD studies, the domain of interest of the arterial model is always truncated. The applied flow conditions significantly effects the accuracy of the numerical simulation. Hence, the application of the inlet and outlet conditions based on the MRI or Ultrasound measurement was usually preferred [93], [237], [238]. In this research a computational fluid dynamic study on two patient specific carotid artery model (normal and stenosed) was studied under the effect of different blood pressures (Normal – NBP, pre - hypertension – HBP 1, hypertension stage 1 - HBP 2 and hypertension stage 2 – HBP 3) as discussed in section 2.8, and various hemodynamic parameters such as WSS, velocity streamlines and oscillatory shear index (OSI) are enumerated.

5.3.1 Carotid artery reconstruction

The general procedure to develop a 3D anatomical model of carotid artery involves selection of CT/MRI data and converting the 2D images into a 3D mask using medical image software like MIMICS 21(Materialise, Leuven, Belgium). The generated mask was then imported into a CAD tool such as CATIA V6 (Dassault Systems SE). In this study, patient specific anatomical model was developed using CT scan images with MIMICS 21. To avoid stair step effect which appears on curved surfaces, the slice thickness was maintained less than 2 mm. The developed model has more than 300 slices each in coronal, sagittal and axial planes.

5.3.2 Conversion of 2D CT scan images to 3D model.

MIMICS 21 is a tool which is used to edit the 2D images obtained from CT/MRI to generate a 3D anatomical model accurately. The images were segmented by taking accurate measurements to generate a 3D model which could be exported to various applications such as FEA, surgical simulation, additive manufacturing etc. The CT/MRI data usually is in DICOM (*.dcm) format in three different sections (axial, sagittal and coronal) which was compressed and merged into a single volume based on similar pixel size value. Further, 3D reconstruction of the model was performed by applying appropriate threshold value to identify the carotid bifurcation region. The segmentation process was performed by defining a range of threshold values to create a segmentation mask. The threshold value for artery segmentation was in the range of soft tissues which varies depending on the case ranging from -150 to 450 HU. HU (Hounsfield Units) is a measure of the density of the tissue. Therefore, proper threshold value helps differentiate the hard tissues like bones.

The segmentation was a trial process. Noise was introduced during the scanning process because of various factors like device limitations, image reconstruction algorithms, and other factors. The noise was reduced considerably by optimum threshold value. In this study, an optimum threshold value of 150 – 550 HU was selected. After segmentation, an automatic region growing tool was used to reconstruct the carotid bifurcation region consisting of the common carotid artery, internal and external artery. The automatic region growing eliminates the noise by removing the floating pixels and splits the unconnected domains. One of the major issues with this procedure was the pixel leaking into the surrounding tissues. This was because the vessel wall separating the lumen and the surrounding tissues was relatively thin. At some regions, the pixels grow through the wall, which resulted in large regions falsely defined as the vessel of interest. In such cases,

manual segmentation must be performed. Some regions were manually segmented to edit the mask to avoid unwanted regions which do not constitute the carotid artery region. Finally, the 3D model was generated as explained in section 3.6. *Figure 5-6* shows the generated 3D masks of normal and stenosed carotid artery. *Figure 5-7* shows the meshed carotid artery model used in the study. Both the models were meshed using ten node tetrahedral element. Inflation was used to capture near wall effects.

5.4 Newtonian and Non-Newtonian blood viscosity model

Newtonian behaviour was assumed in arteries whose lumen diameter is more than 1 mm and flows with shear strain rate greater than 100 s^{-1} [239]. In this study, for Newtonian model, flow was assumed to be laminar due to low Reynolds number and incompressible with density of 1060 kg/m^3, and dynamic viscosity of 0.004 Pa s.

Use of non – Newtonian rheological model in cardiovascular CFD was becoming more attractive due availability of robust computational tools. Steinman et al [240] enumerated the assumptions in blood flow modelling and performed analysis on its impact on computational haemodynamics. He highlighted the assumptions with respect to the constitutive properties of blood flow and artery wall and suggested the use of Newtonian model with adjustments to apparent viscosity depending on the size of the vessel.

This appears to be a rather bold statement since literature suggests otherwise, some of which are more detailed [250], which maintains that blood is a complex non – Newtonian fluid and it must be considered in computational studies.

The most popular non – Newtonian model was suggested by de Waele [241]. In this study, an empirical definition of a non – Newtonian fluid is suggested for the first time. The model was an extension of the Newtonian fluid by relating shear stress to shear strain rate given as

$$\tau = K\gamma n = (K\gamma^{n-1})\gamma \quad (5.3)$$

Where γ is the apparent viscosity, K is the consistency index, which is a measure of consistency of the fluid, n is a measure of divergence from Newtonian behaviour (n=1). When n > 1, the equation describes shear thickening fluid and when n<1 the equation describes shear thinning fluid. Since blood is a shear thinning fluid [240], [242] the index value less than 1 must be considered. The shear thinning effect of blood was because of aggregation, deformation and alignment of red blood cells which determine the rheological behaviour.

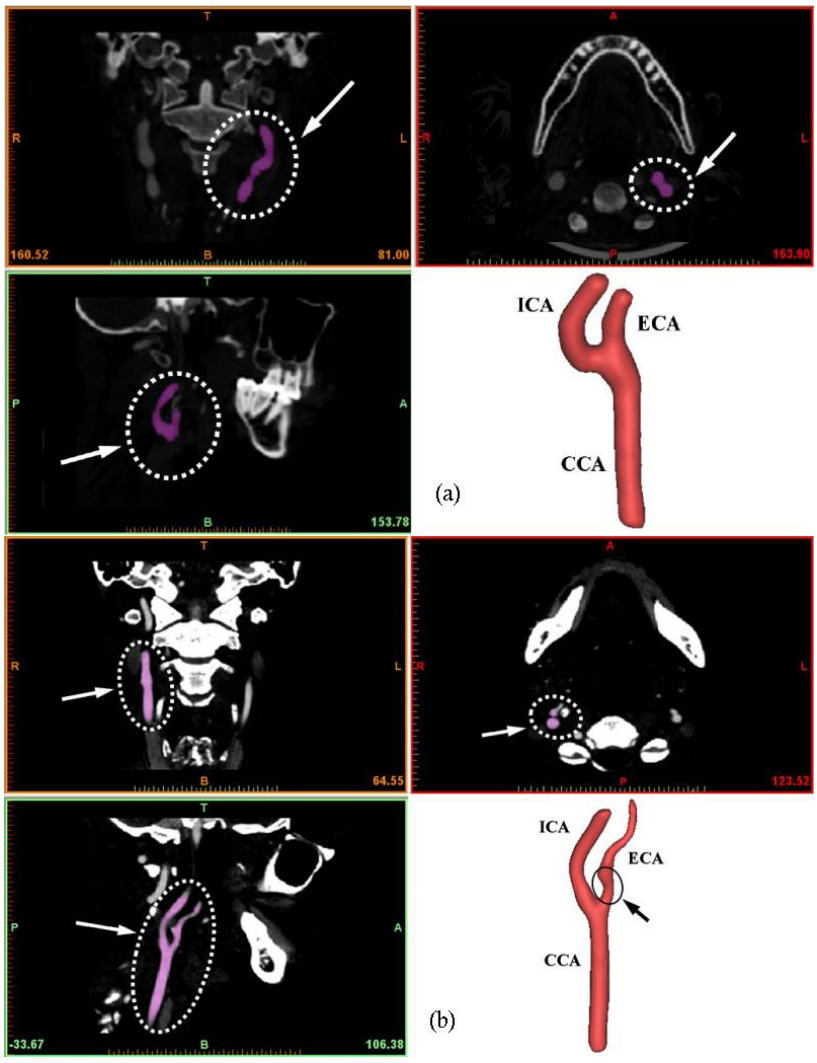

Figure 5-6: CT images of stenosed carotid artery from different planes and generated 3D model. (a) normal carotid artery, (b) stenosed carotid artery. The highlighted regions indicate a single slice image of the carotid artery in different planes.

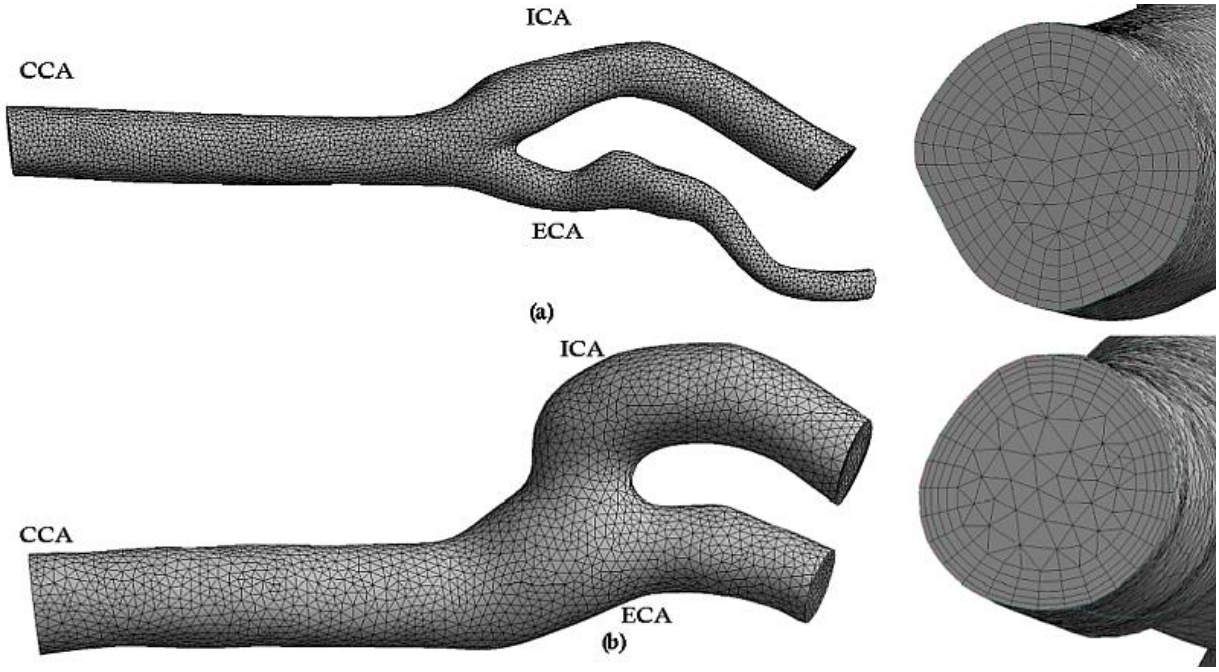

Figure 5-7: Meshed computational model of (a) stenosed, (b) normal carotid artery used in the study.

Cross [243] proposed a non – Newtonian blood viscosity model which was completely dedicated to shear thinning behaviour. In this equation, apparent viscosity was defined as

$$\frac{\mu - \mu_\infty}{\mu_0} = [1 + (\lambda\gamma)^2]^{\frac{(n-1)}{2}} \tag{5.4}$$

Where μ_0 is low shear viscosity, μ_∞ is high shear viscosity, λ is the time constant, n is the power law index. This allows for a constant low shear viscosity but was unrealistic at high shear rates as the viscosity tends to zero. It could be used to describe pseudoplastics which were in some ways analogous to blood.

The above shortcomings are overcome by Bird – Carreau and Carreau – Yasuda models which allows for limiting behaviour at high shear viscosities, which was more widely observed in cardiovascular flows. Bird – Carreau model was an extension of Cross model given as

$$\frac{\mu - \mu_\infty}{\mu_0 - \mu_\infty} = [1 + (\lambda\gamma)^2]^{\frac{(n-1)}{2}} \tag{5.5}$$

A generalized form of the above equation was obtained by replacing 2 and ½ with a and 1/a to get Carreau – Yasuda model given as

$$\frac{\mu - \mu_\infty}{\mu_0 - \mu} = [1 + (\lambda\gamma)^a]^{\frac{(n-1)}{a}} \tag{5.6}$$

Where a is Yasuda exponent [244]. In both Bird – Carreau and Carreau – Yasuda models, it could be noted that these models behave as Newtonian fluid when stress was directly proportional to strain – rate, when time constant was zero, i.e., when the viscosity was constant with time. Gijsen et al [94] showed that the shear thinning effect controls the non – Newtonian behaviour of the blood flow. In this study, shear thinning effect was modelled using Carreau – Yasuda model, where $\mu_\infty = 0.0022\ Pa\ s, \mu_0 = 0.022\ Pa\ s,\ \lambda = 0.1105\ s, n = 0.392\ and\ a = 0.644$ [94].

5.5 Boundary conditions and numerical setup

In this study, CFD analysis in a stenosed and normal human carotid artery subjected to different blood pressure was performed. The focus was to study the haemodynamics in stenosed and bifurcated regions, hence the ends of the inlets and outlets were considered sufficiently away from the regions of interest to avoid the afferent and efferent fluid dynamic effects. The inlet velocity was obtained from the Ultrasound Doppler scan and applied as inlet velocity boundary condition. *Figure 5-8* shows the velocity profile in the Ultrasound Doppler scan and corresponding inlet velocity profile. At the outlets, different boundary conditions like constant outlet pressure, Impedance and resistance boundary conditions were investigated [131], [132] for both stenosed and normal models. Similar studies were also performed on subject specific cases [245]–[249], where use of resistance boundary conditions was recommended.

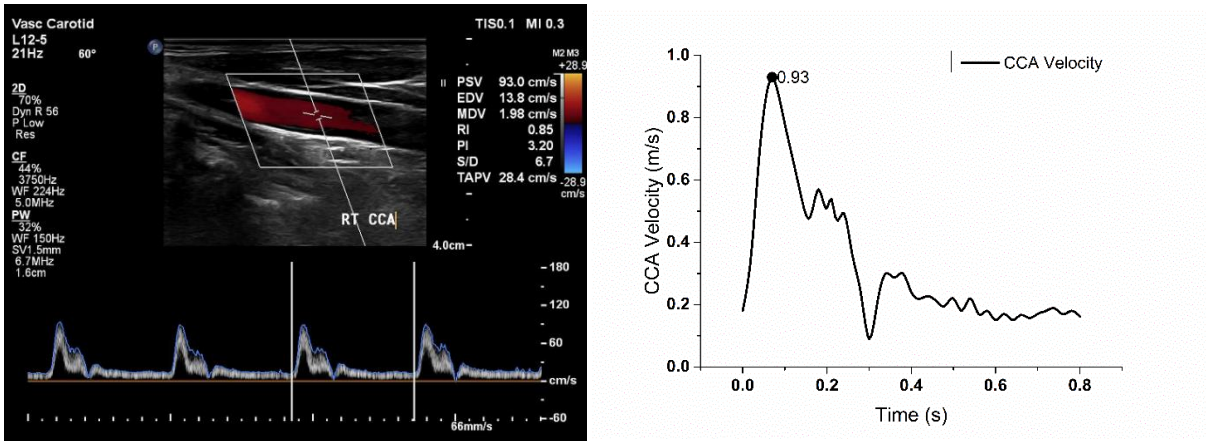

Figure 5-8: Ultrasound Doppler image to acquire the velocity at the common carotid artery inlet (CCA inlet) and corresponding velocity profile

Therefore, in this study, resistance boundary condition was applied to consider the peripheral resistance encountered by the downstream arteries [250]. A pulsatile pressure waveform as shown in *Figure 5-9* was applied at the outlets. Temporal velocity values are extracted from the Ultrasound Doppler data points, which are used to generate a polynomial equation and this data obtained was used in the Fourier series equation to generate the required pulse wave. Equation 5.7 shows the Fourier series approach which was adopted to obtain the time varying velocity and pressure waveform from initial waveforms approximated using six harmonics which was found to be enough to generate the desired waveform.

$$F(t) = A_m + \sum_{n=1}^{N} \left(A_n cos(n\omega t) + B_n sin(n\omega t)\right) \tag{5.7}$$

The Fourier equation was numerically derived using Microsoft Excel and the constants obtained were used in the CFD Expression Language (CEL) in Ansys CFX. A no – slip boundary condition was defined at the wall. In this study, high resolution advection scheme was used to solve the governing equations with second order backward Euler transient scheme.

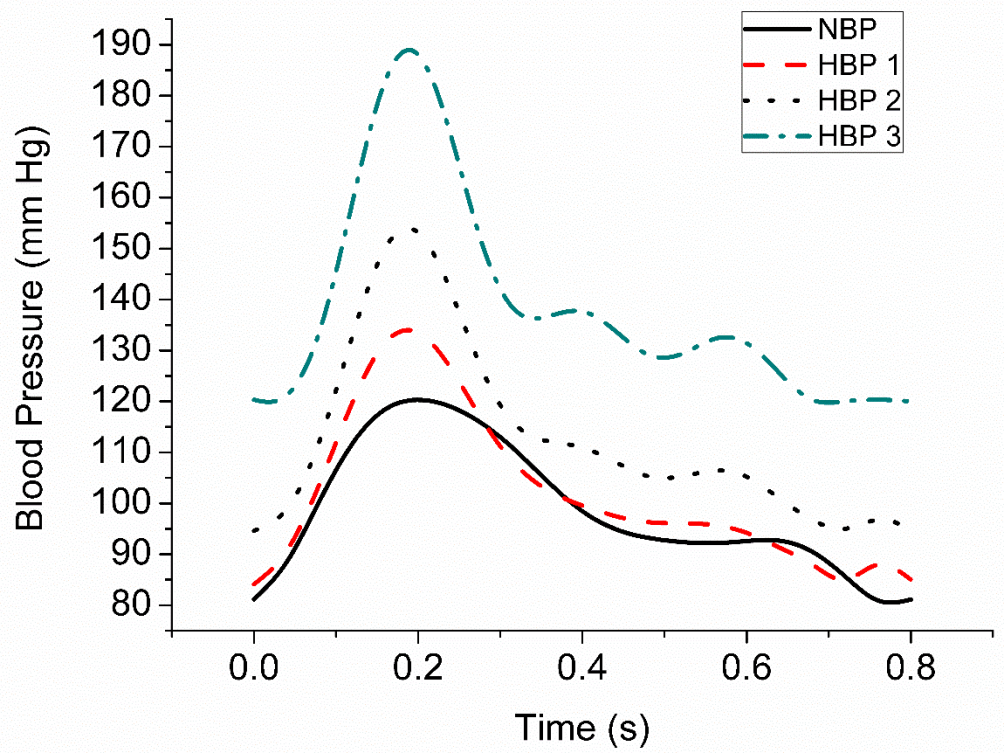

Figure 5-9: Representation of pulsatile pressure at the outlet

The convergence criteria for residuals of dependent variables was set 0.00001 to ensure convergence of every time step. Here, three cardiac cycles were necessary to damp the initial transients. Therefore, the last cycle was used to acquire the data.

5.6 Time step sensitivity test and Grid independence test.

Time step sensitivity test was carried out for a total time of 2.4 seconds and an optimum time step was obtained during the transient analysis. The last cycle of the three cardiac cycle was to capture the hemodynamic parameters like WSS and Velocity [251]. The computational model of both stenosed and normal carotid artery was subjected to time step sensitivity test. Time step size sensitivity based on step size of 50, 100, 125, 160 and 200 for both stenosed and normal carotid artery were performed for normal blood pressure. *Figure 5-10* shows the time step sensitivity results and based on this, an ideal time step of 100, i.e., 0.008s was chosen to perform the analysis.

Grid independence study was performed depending on the element size of 1mm, 0.8mm, 0.6mm 0.4mm and 0.3mm to choose the optimum mesh size for the simulation. *Figure 5-11* shows the variation of average WSS at the wall and average velocity in the fluid domain for different mesh size. Optimum mesh size of 55626 and 68090 was chosen for stenosed and normal carotid artery respectively.

5.7 Results and Discussion

The variation in flow pattern during different blood pressure ranges was investigated by considering critical hemodynamic parameters such as WSS and velocity. Major changes have been observed during peak systole, therefore this instant in the pulse cycle was considered to show the comparison of stenosed and normal carotid artery model.

5.7.1 Wall Shear Stress

Wall shear stress contours were compared between two carotid artery model, normal and stenosed by considering Newtonian and Carreau – Yasuda blood viscosity models subjected to different blood pressures. *Figure 5-12* to *Figure 5-15* shows the WSS contours of normal carotid artery subjected to different blood pressures by considering blood as Newtonian fluid. In all cases, maximum WSS was located at the bifurcation tip, where the flow was divided.

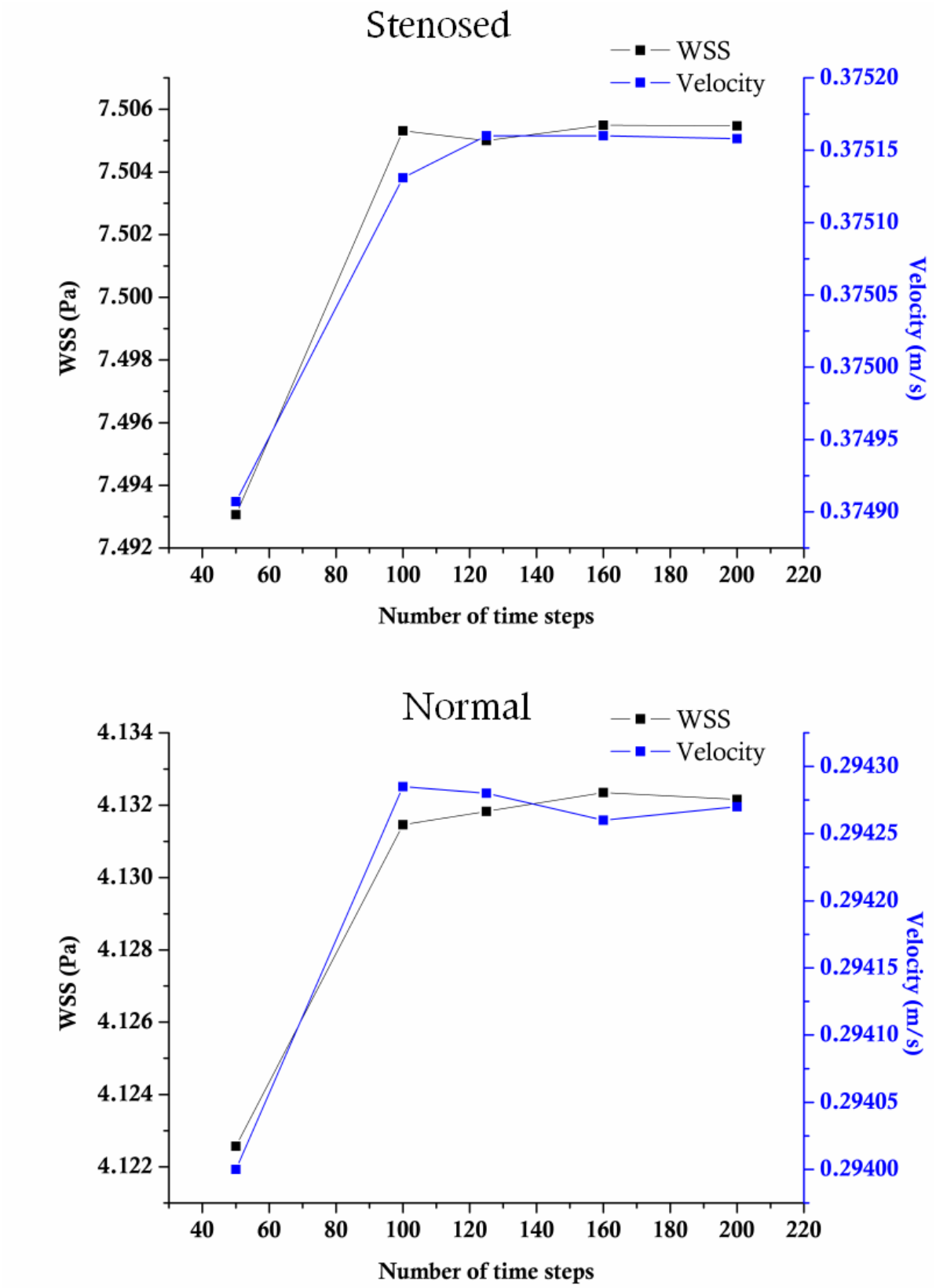

Figure 5-10: Time step sensitivity test

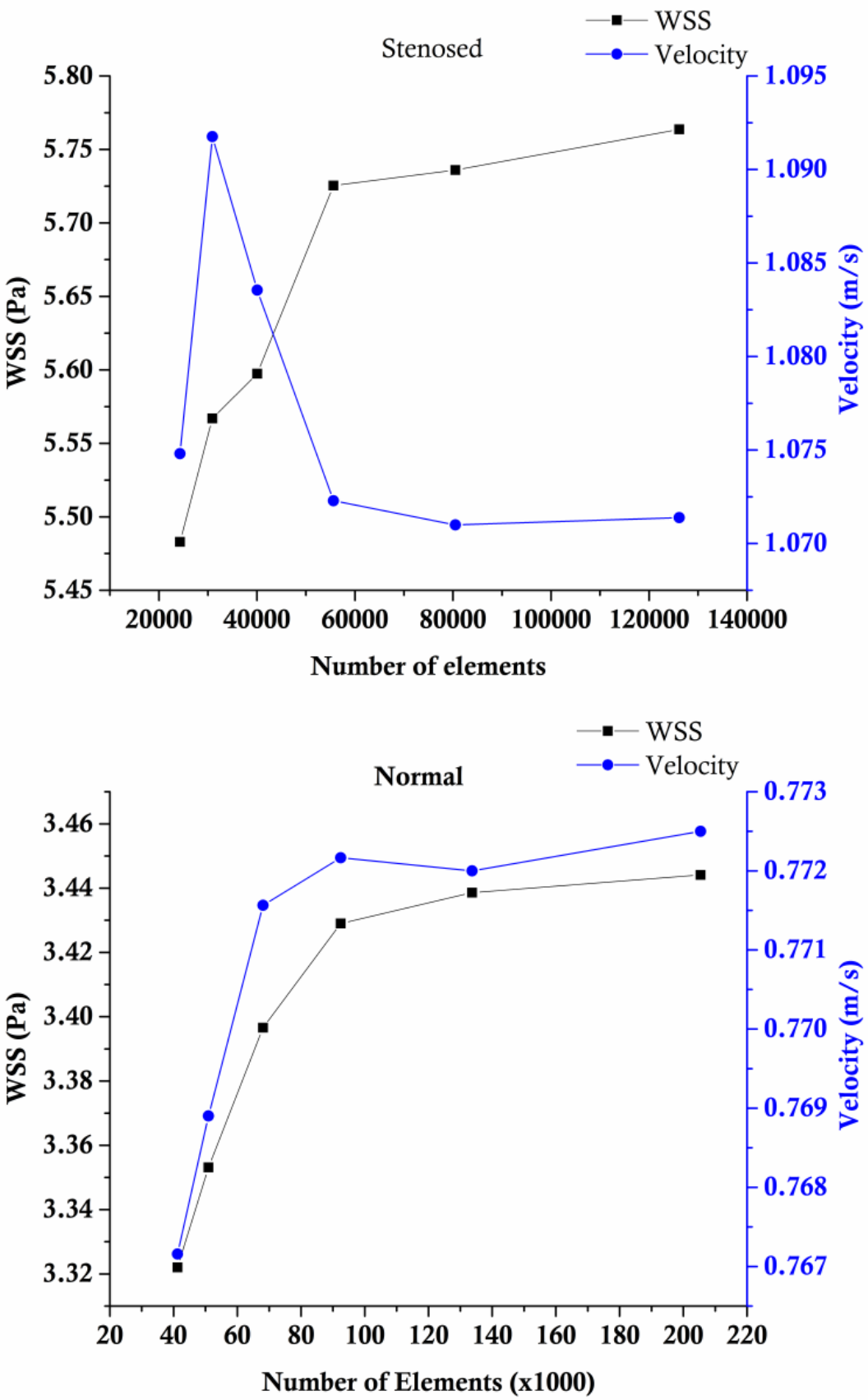

Figure 5-11: Grid Independence test

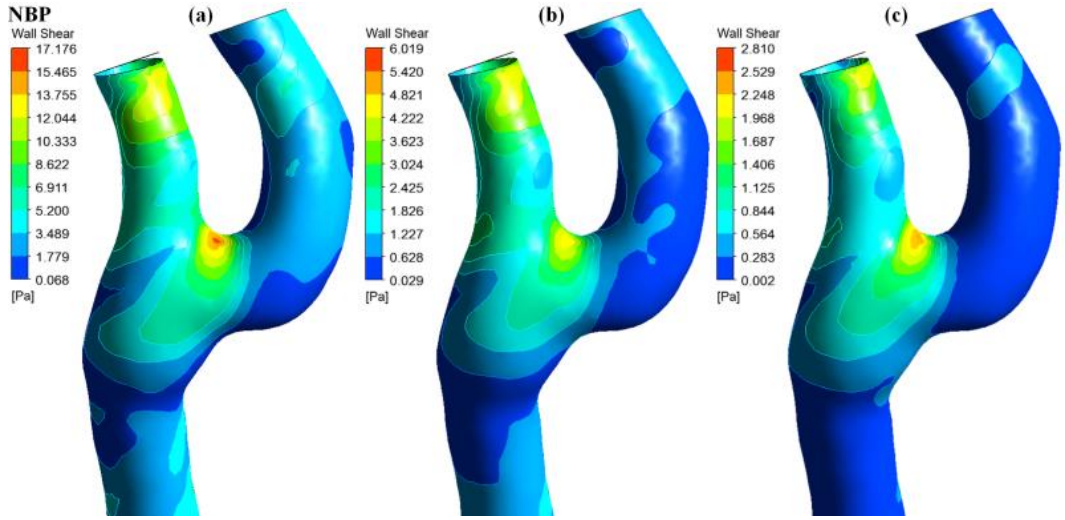

Figure 5-12: WSS contour in normal carotid artery subjected to NBP considering Newtonian model, (a) Peak systole, (b) Early diastole, (c) Late diastole.

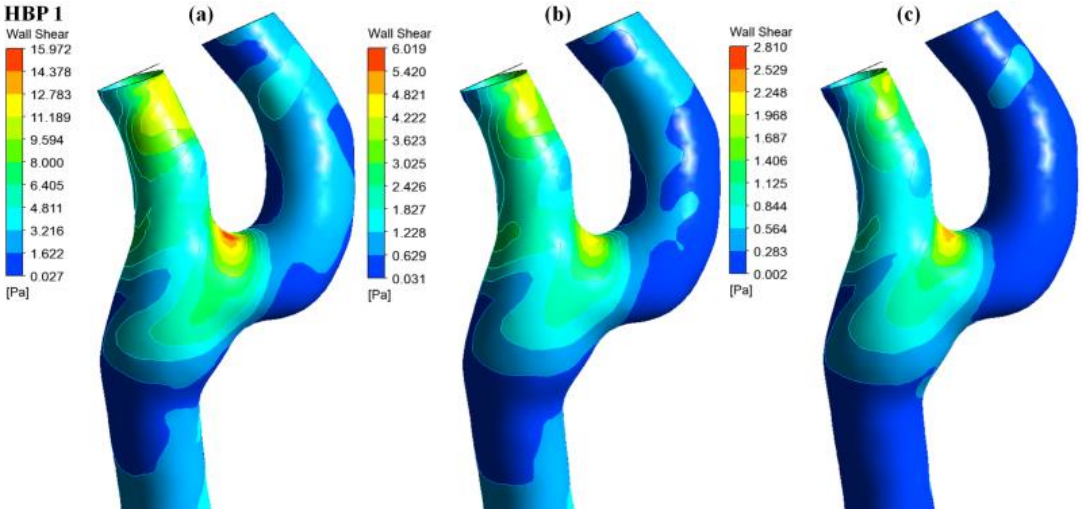

Figure 5-13: WSS contour in normal carotid artery subjected to HBP 1 considering Newtonian model, (a) Peak systole, (b) Early diastole, (c) Late diastole.

The maximum WSS at NBP, HBP 1, HBP 2, HBP 3 was 17.176 Pa, 15.972 Pa, 15.972 Pa, and 15.688 Pa respectively by considering the Newtonian model.

The Carreau - Yasuda model shows similar WSS patterns as Newtonian model, however, the WSS magnitude was overestimated in Newtonian model as compared to Carreau – Yasuda model. *Figure 5-16* to *Figure 5-19* shows the WSS contours of normal carotid artery by considering the Carreau – Yasuda model.

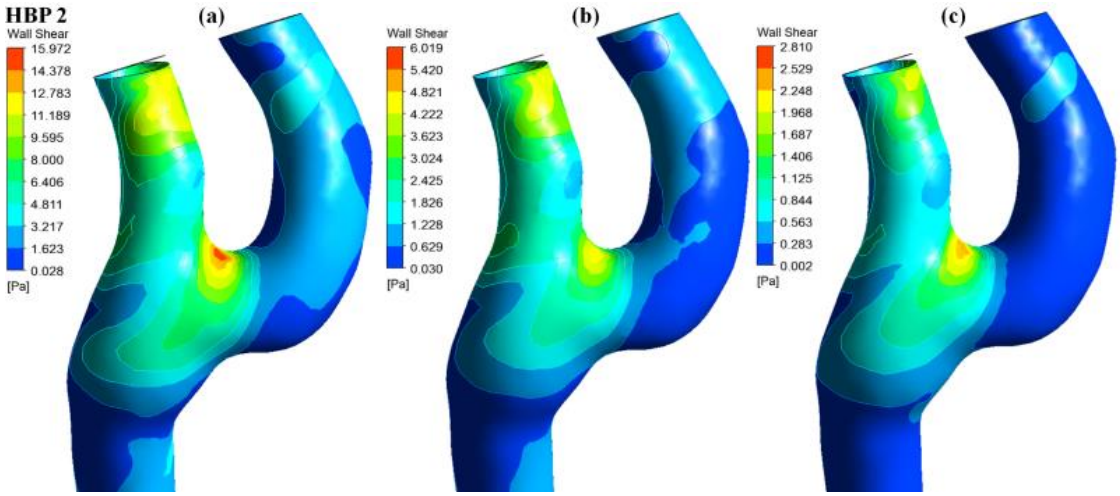

Figure 5-14: WSS contour in normal carotid artery subjected to HBP 2 considering Newtonian model, (a) Peak systole, (b) Early diastole, (c) Late diastole.

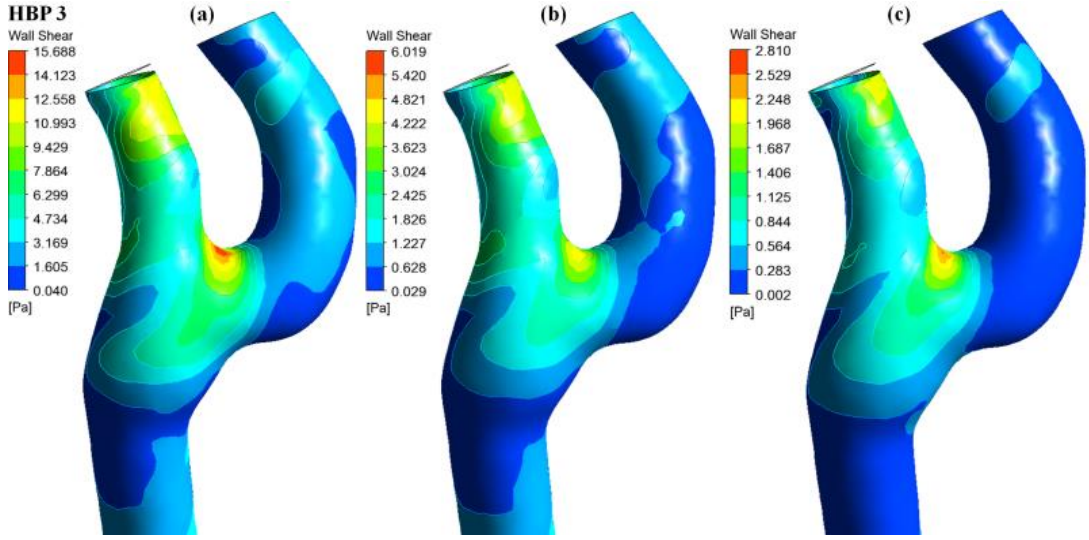

Figure 5-15: WSS contour in normal carotid artery subjected to HBP 3 considering Newtonian model, (a) Peak systole, (b) Early diastole, (c) Late diastole.

Maximum WSS was located at the bifurcation tip and the low WSS was restricted to a region above the carotid bulb in the base of the ICA at late diastole. This was the location more prone to atherosclerosis development due to high flow recirculation leading to lower viscosity of the blood which was more actively captured by the Carreau – Yasuda model as it considered the shear thinning behaviour of blood. However, at the CCA there was no qualitative difference in the WSS between the two blood viscosity models. *Figure 5-28* shows the difference in the maximum WSS between the rheological models, and it can be

observed there is 15% decrease in WSS compared to Newtonian model. Also, the Newtonian model exaggerates the low WSS region in the ICA when compared to the Carreau – Yasuda model.

Figure 5-20 to *Figure 5-27* shows the WSS contours of stenosed carotid artery model where blood is considered as Newtonian and Carreau – Yasuda model. As observed in the normal carotid artery model, WSS is overestimated by 25% by the Newtonian model as compared to the Carreau – Yasuda model, as shown in *Figure 5-29*. Peak WSS was observed at the bifurcation tip, and WSS increased in the stenosed region at the base of the ECA and post stenosis, flow recirculation was observed, leading to low WSS region. The magnitude of WSS between different blood pressure had no significant difference quantitatively. But the Newtonian model overestimates the low WSS region compared to the Carreau – Yasuda model.

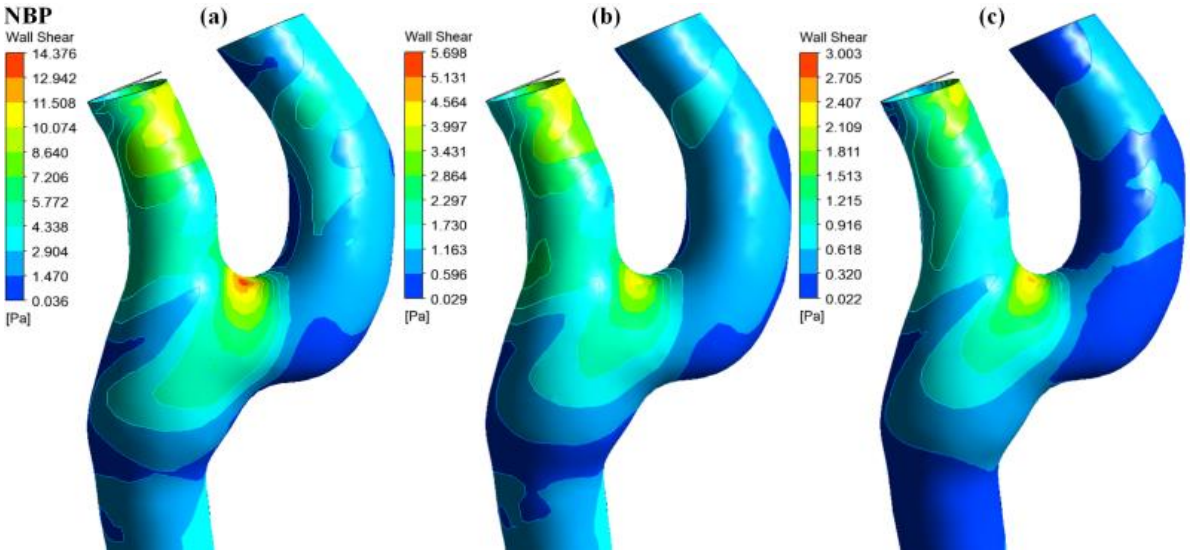

Figure 5-16: WSS contour in normal carotid artery subjected to NBP considering Carreau – Yasuda viscosity model, (a) Peak systole, (b) Early diastole, (c) Late diastole.

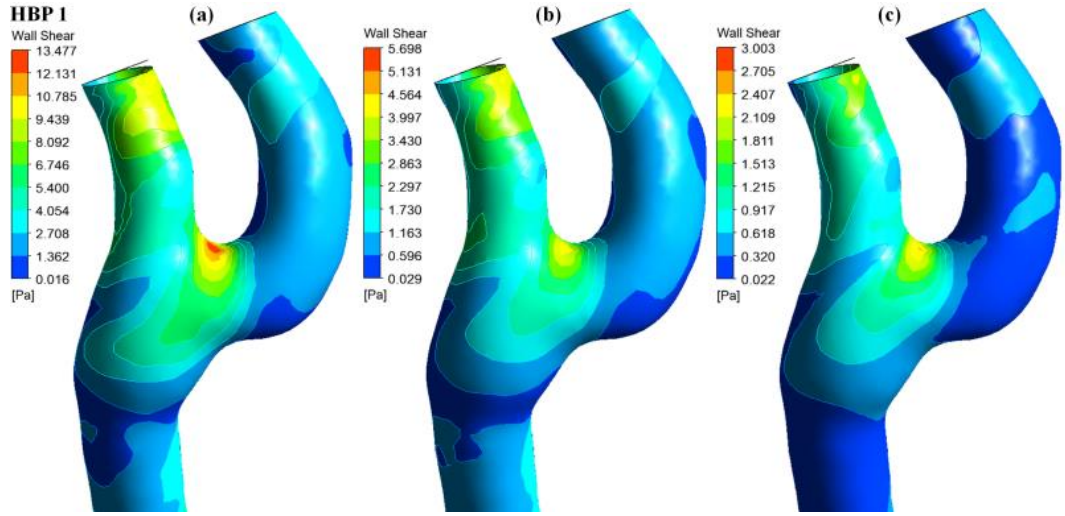

Figure 5-17: WSS contour in normal carotid artery subjected to HBP 1 considering Carreau – Yasuda viscosity model, (a) Peak systole, (b) Early diastole, (c) Late diastole.

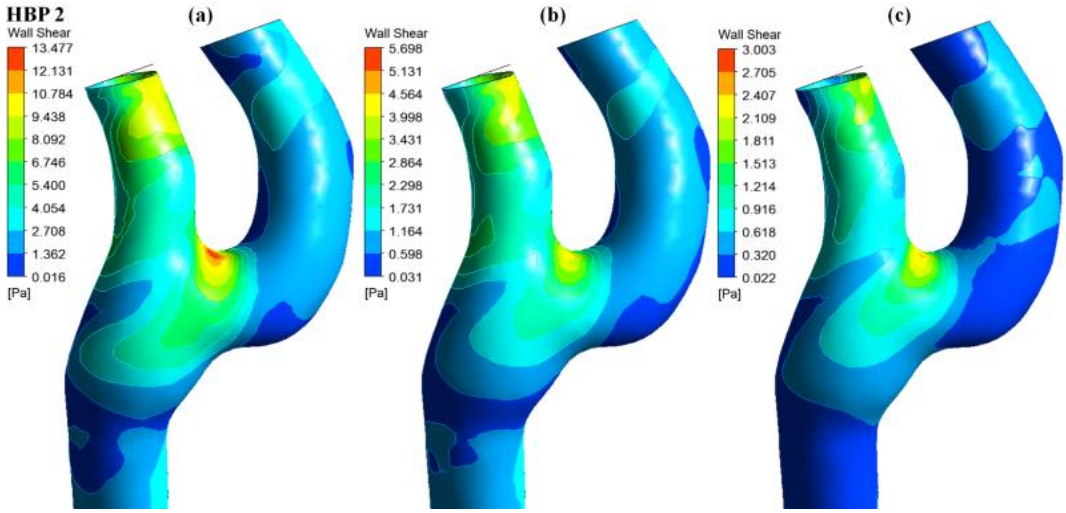

Figure 5-18: WSS contour in normal carotid artery subjected to HBP 2 considering Carreau – Yasuda viscosity model, (a) Peak systole, (b) Early diastole, (c) Late diastole.

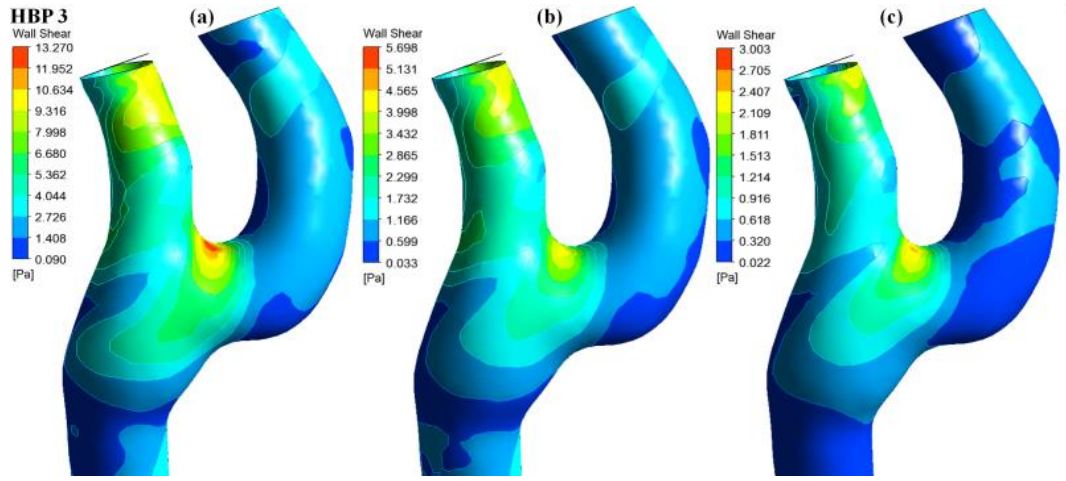

Figure 5-19: WSS contour in normal carotid artery subjected to HBP 3 considering Carreau – Yasuda viscosity model, (a) Peak systole, (b) Early diastole, (c) Late diastole.

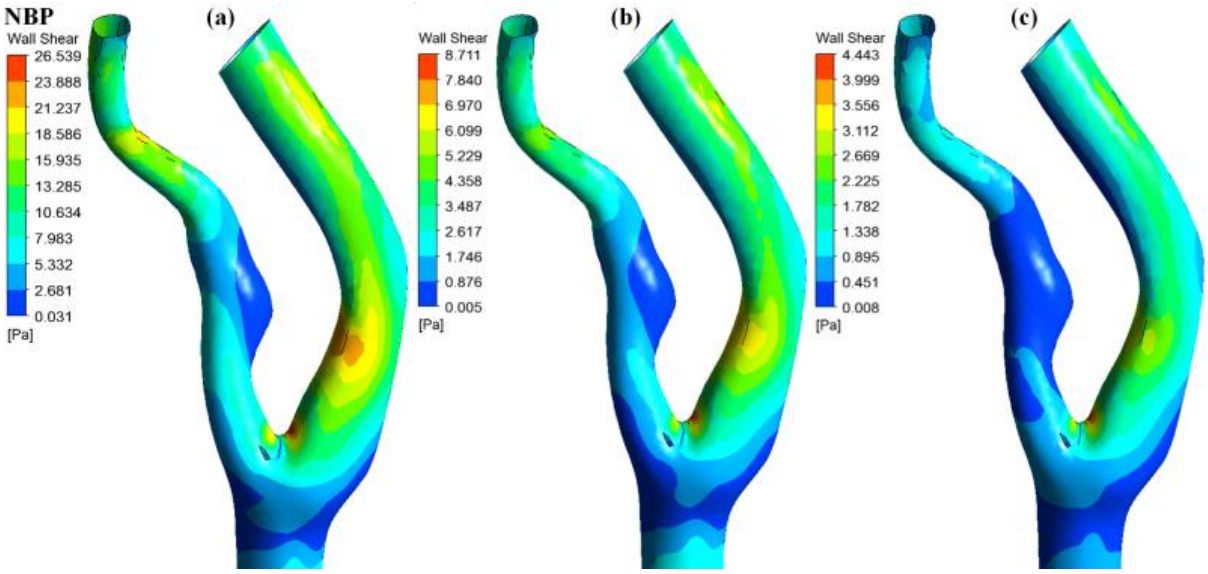

Figure 5-20: WSS contour in stenosed carotid artery subjected to NBP considering Newtonian model, (a) Peak systole, (b) Early diastole, (c) Late diastole.

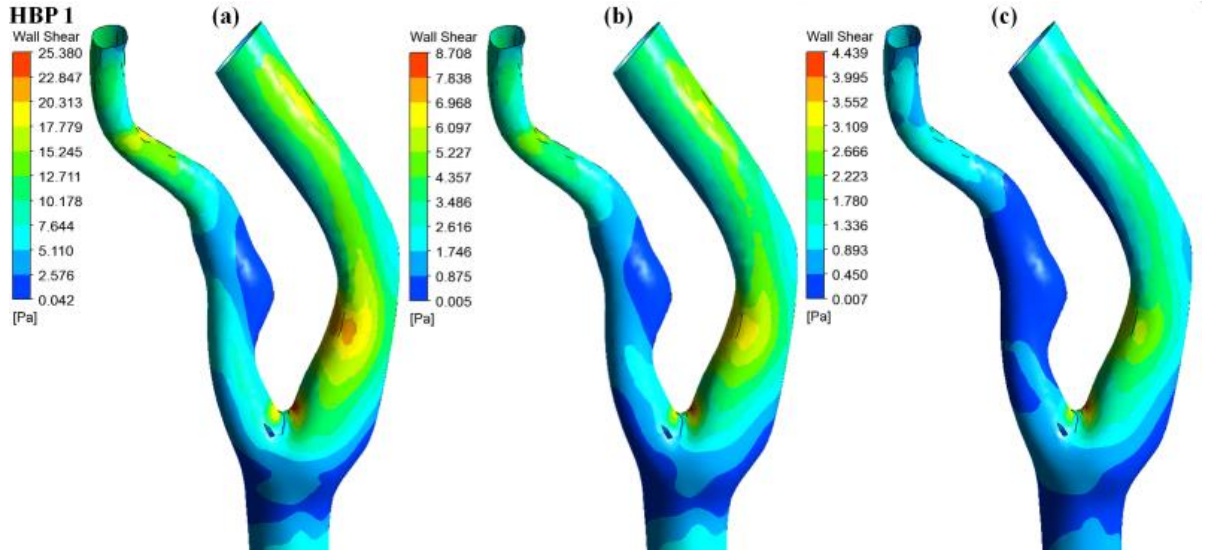

Figure 5-21: WSS contour in stenosed carotid artery subjected to HBP 1 considering Newtonian model, (a) Peak systole, (b) Early diastole, (c) Late diastole.

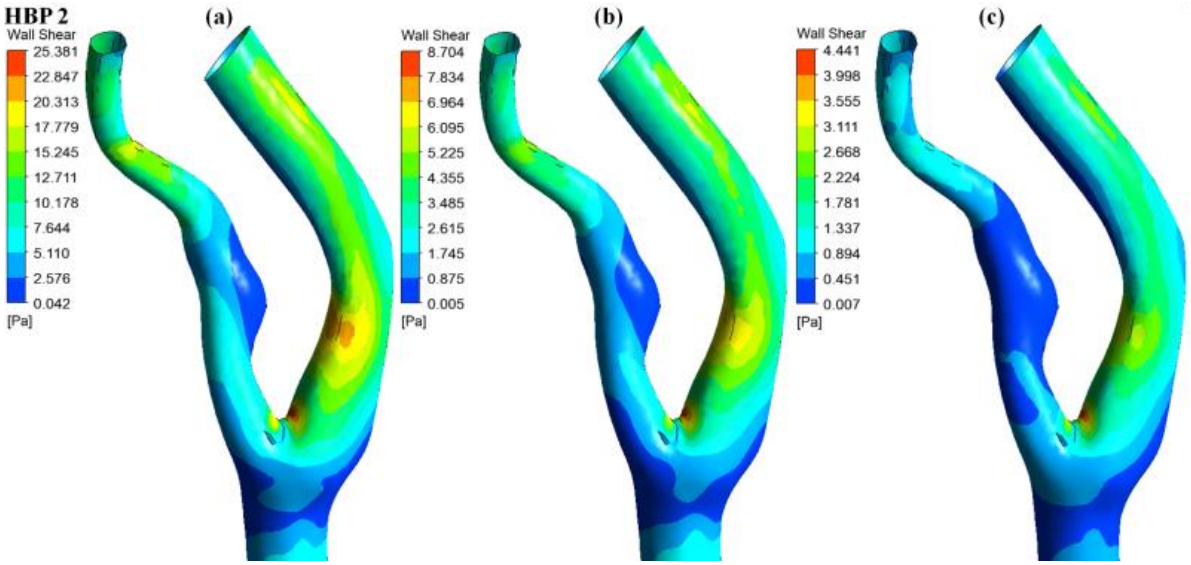

Figure 5-22: WSS contour in stenosed carotid artery subjected to HBP 2 considering Newtonian model, (a) Peak systole, (b) Early diastole, (c) Late diastole.

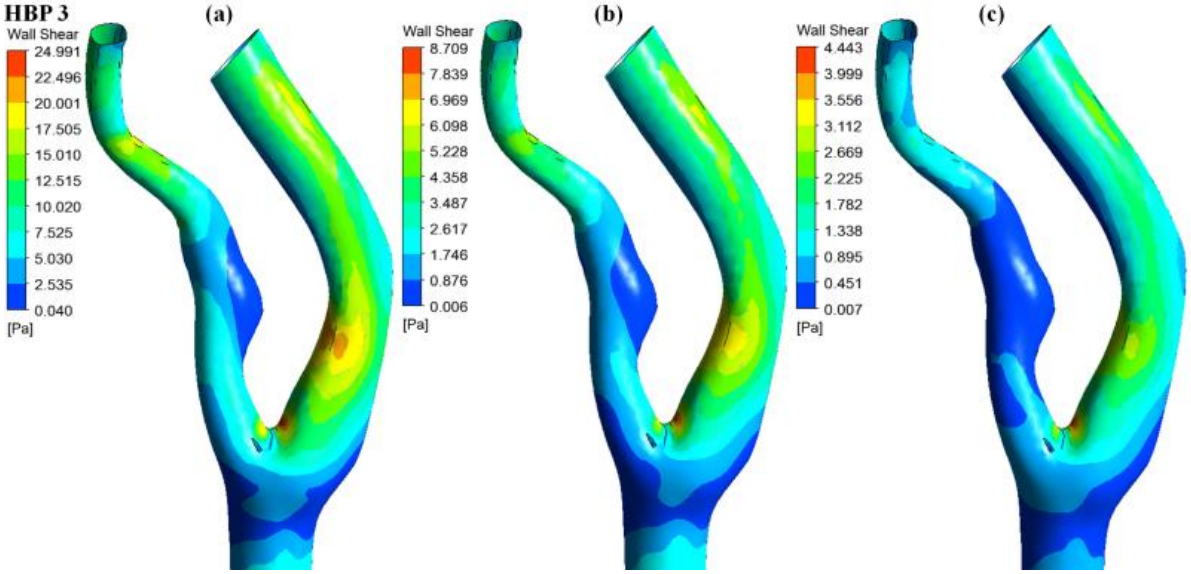

Figure 5-23: WSS contour in stenosed carotid artery subjected to HBP 3 considering Newtonian model, (a) Peak systole, (b) Early diastole, (c) Late diastole.

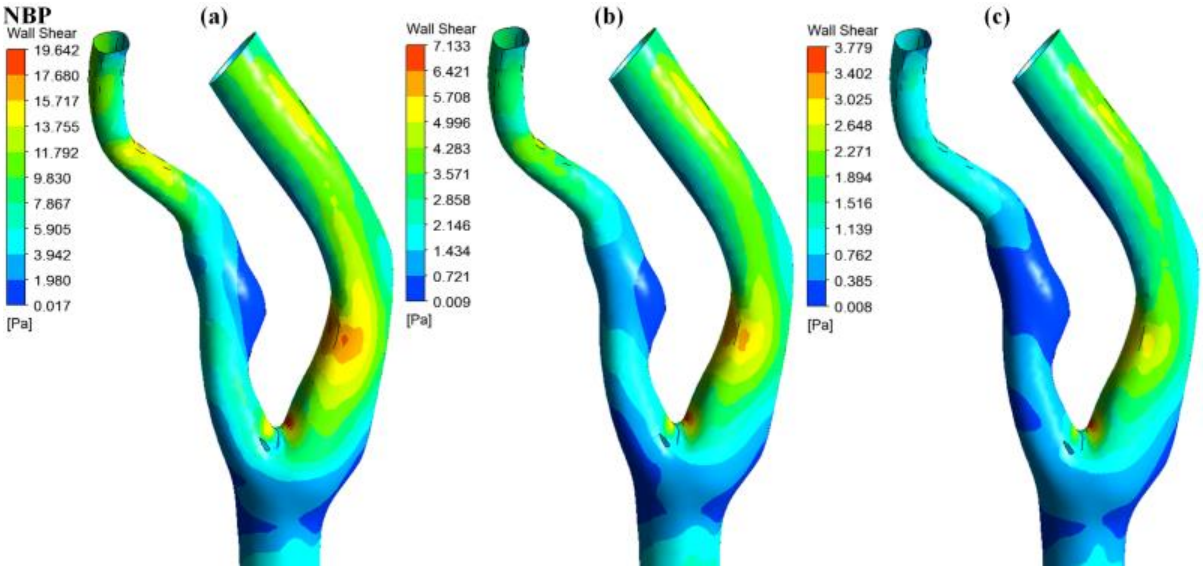

Figure 5-24: WSS contour in stenosed carotid artery subjected to NBP considering Carreau – Yasuda viscosity model, (a) Peak systole, (b) Early diastole, (c) Late diastole.

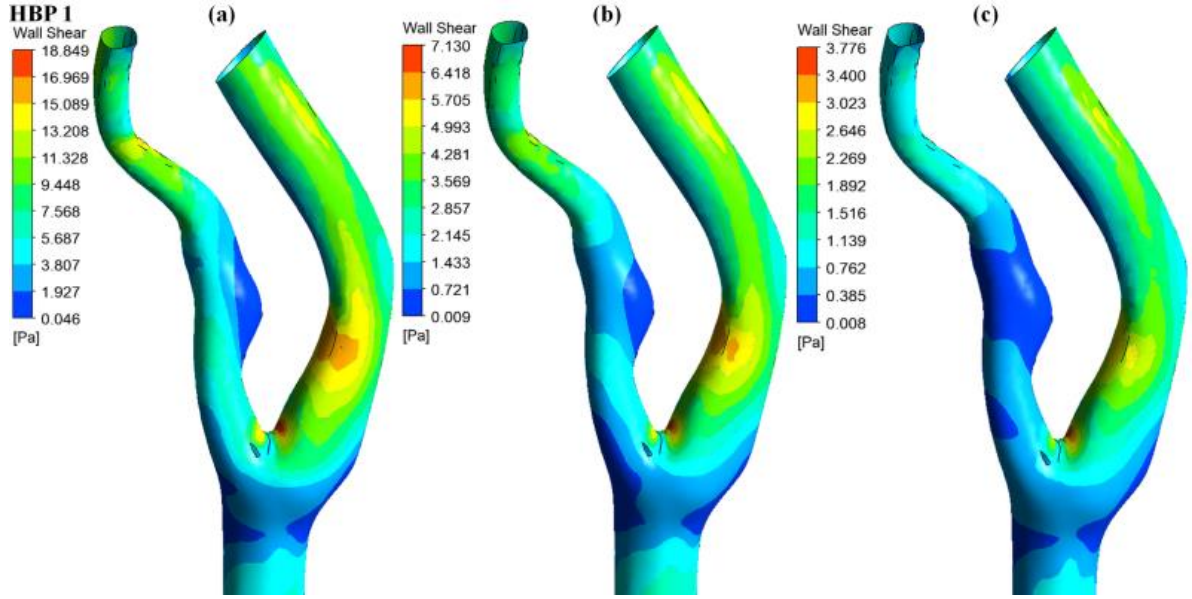

Figure 5-25: WSS contour in stenosed carotid artery subjected to HBP 1 considering Carreau – Yasuda viscosity model, (a) Peak systole, (b) Early diastole, (c) Late diastole.

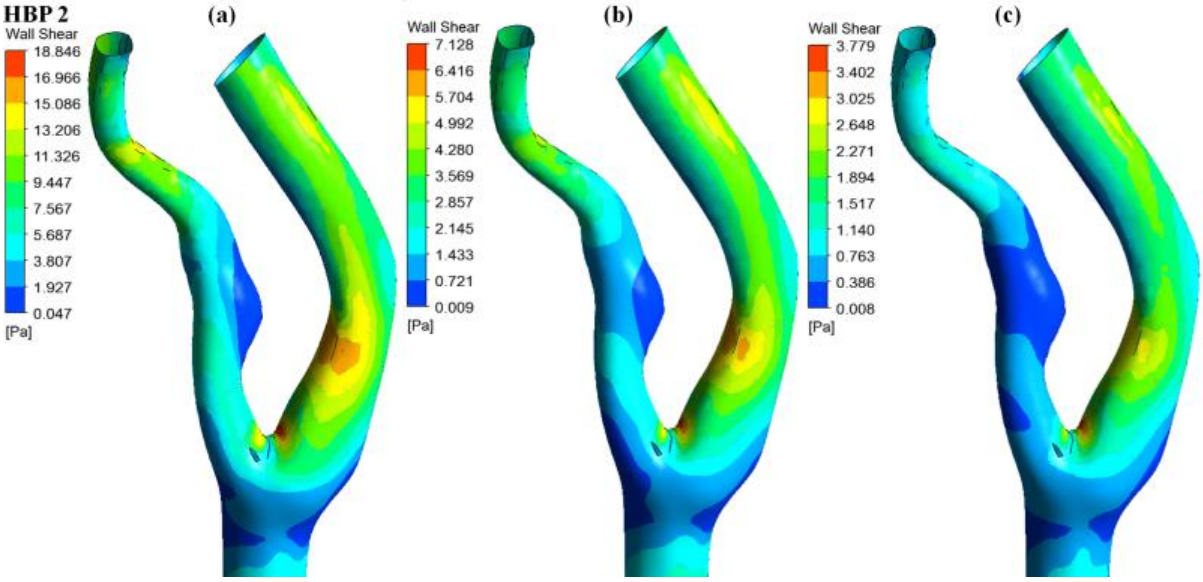

Figure 5-26: WSS contour in stenosed carotid artery subjected to HBP 2 considering Carreau – Yasuda viscosity model, (a) Peak systole, (b) Early diastole, (c) Late diastole.

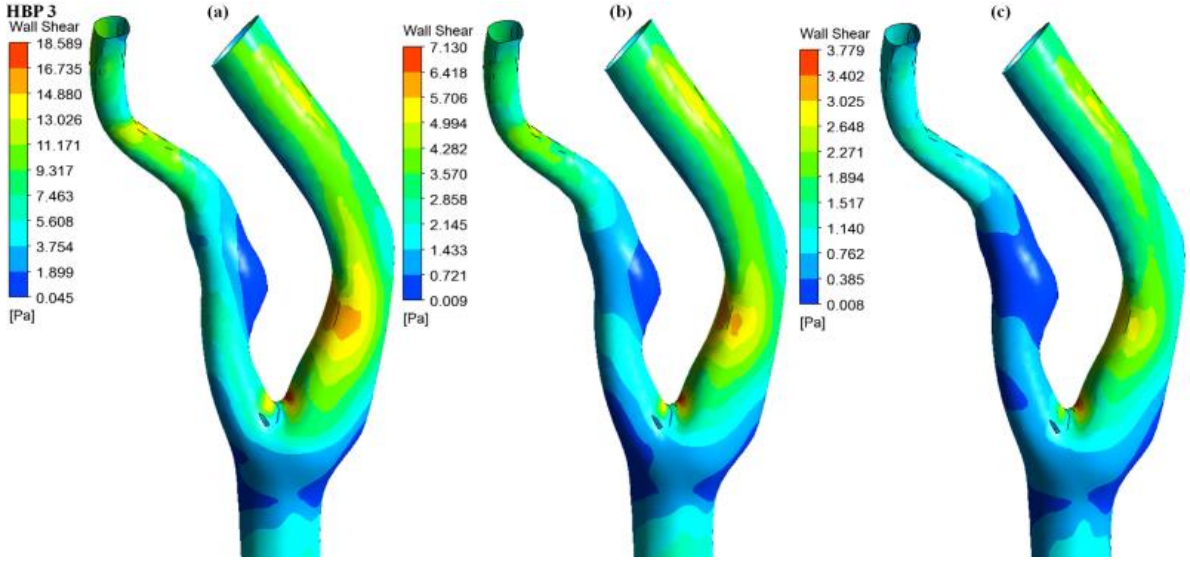

Figure 5-27: WSS contour in stenosed carotid artery subjected to HBP 3 considering Carreau – Yasuda viscosity model, (a) Peak systole, (b) Early diastole, (c) Late diastole.

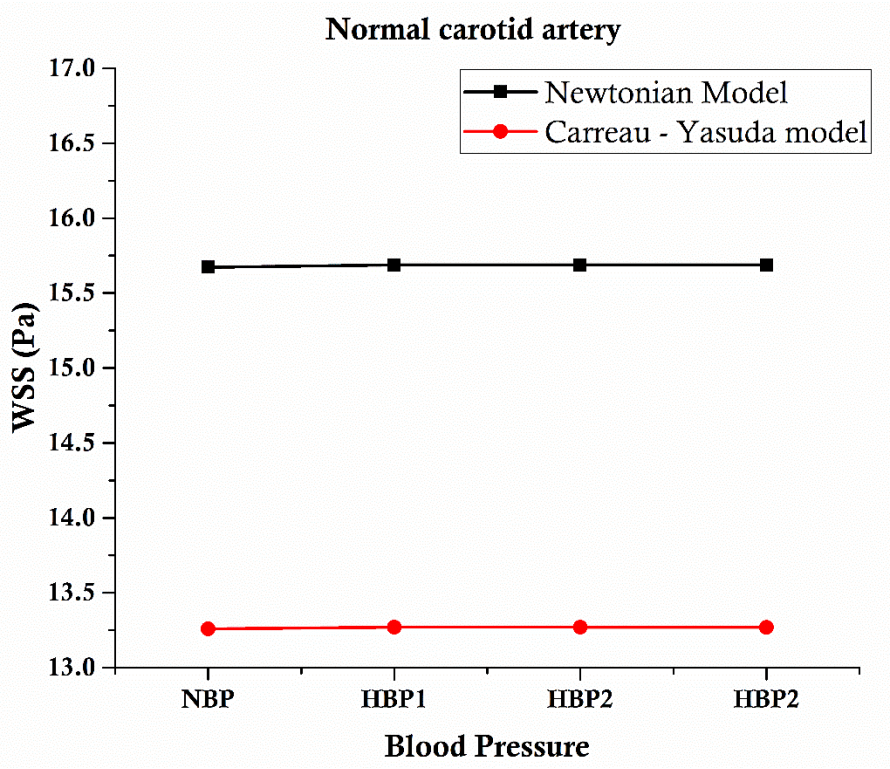

Figure 5-28: Comparision of maximum WSS at the wall of normal carotid artery

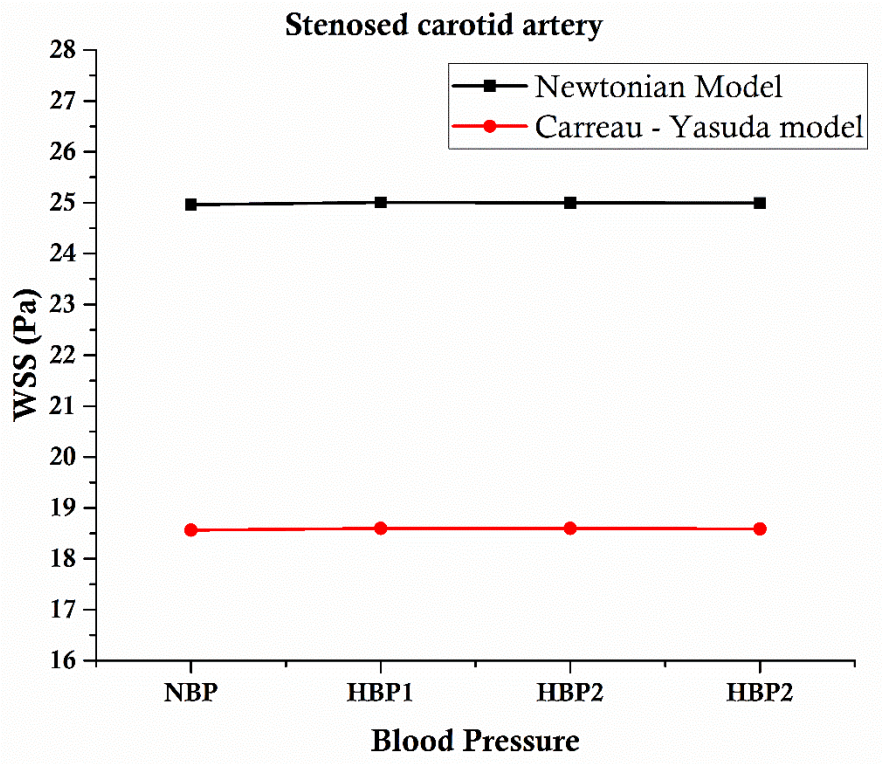

Figure 5-29: Comparison of maximum WSS at the wall of stenosed carotid artery

Traditionally, Newtonian approximation or blood was adopted in large vessels. However, the regions of low WSS in the arteries were associated with flow recirculations and plaque depoits. In such regions, the blood was flowing at very low velocities, and hence subjected to very low shear rates compared to other regions as observed in the WSS contours. In these regions the non – Newtonian effects must not be negletced. The Newtonian model cannot capture the increase viscosity in such low WSS regions and as a result, overestimates the shear rate and WSS. This could underestimate the risk of atherosclerosis. As seen in *Figure 5-28* and *Figure 5-29*, the WSS is the same for all blood pressures, for both normal and stenosed arteries. This is because of the lack of energy disspation in terms of wall expansion due to increased outlet pressure.

5.7.2 Velocity

Figure 5-30 to *Figure 5-33* shows velocity streamlines in normal carotid artery for Newtonian and the Carreau – Yasuda models respectively. The velocity streamlines show similar flow patterns for different blood pressures. This co relates to the same WSS magnitudes between blood pressures (NBP, HBP 1, HBP 2 and HBP 3). In all cases the blood flow until the bifurcation tip and divides into the ICA and ECA, and due to the geometry, it recirculated into the carotid bulb and the base of the ICA leading to low WSS in those regions. *Figure 5-34* to *Figure 5-37* shows the velocity streamlines in stenosed carotid artery model. Here the Newtonian model shows higher recirculation as compared to the Carreau – Yasuda model.

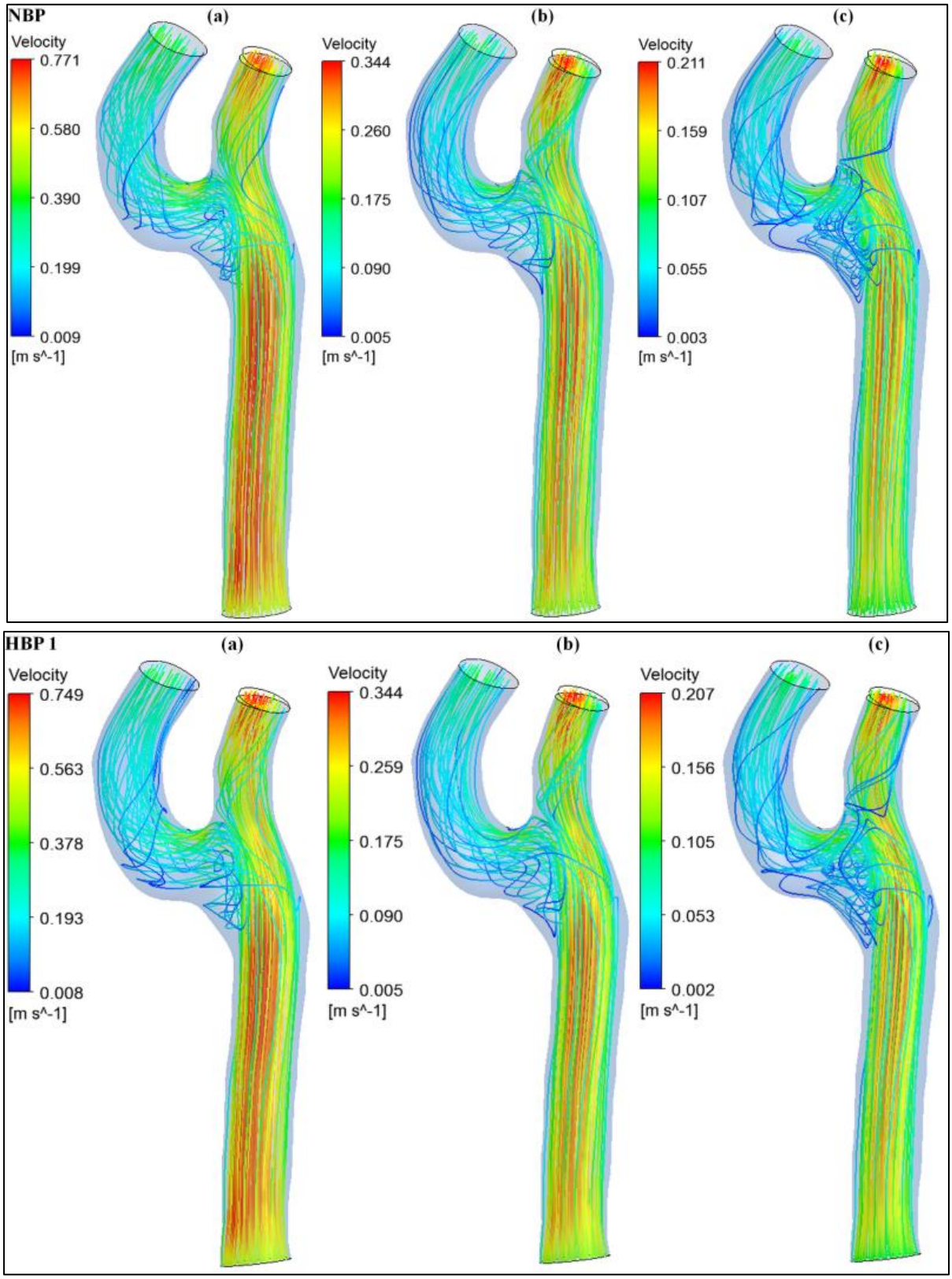

Figure 5-30: Velocity streamlines of normal carotid artery considering Newtonian model, (a) Peak Systole, (b) Early Diastole, (c) Late Diastole

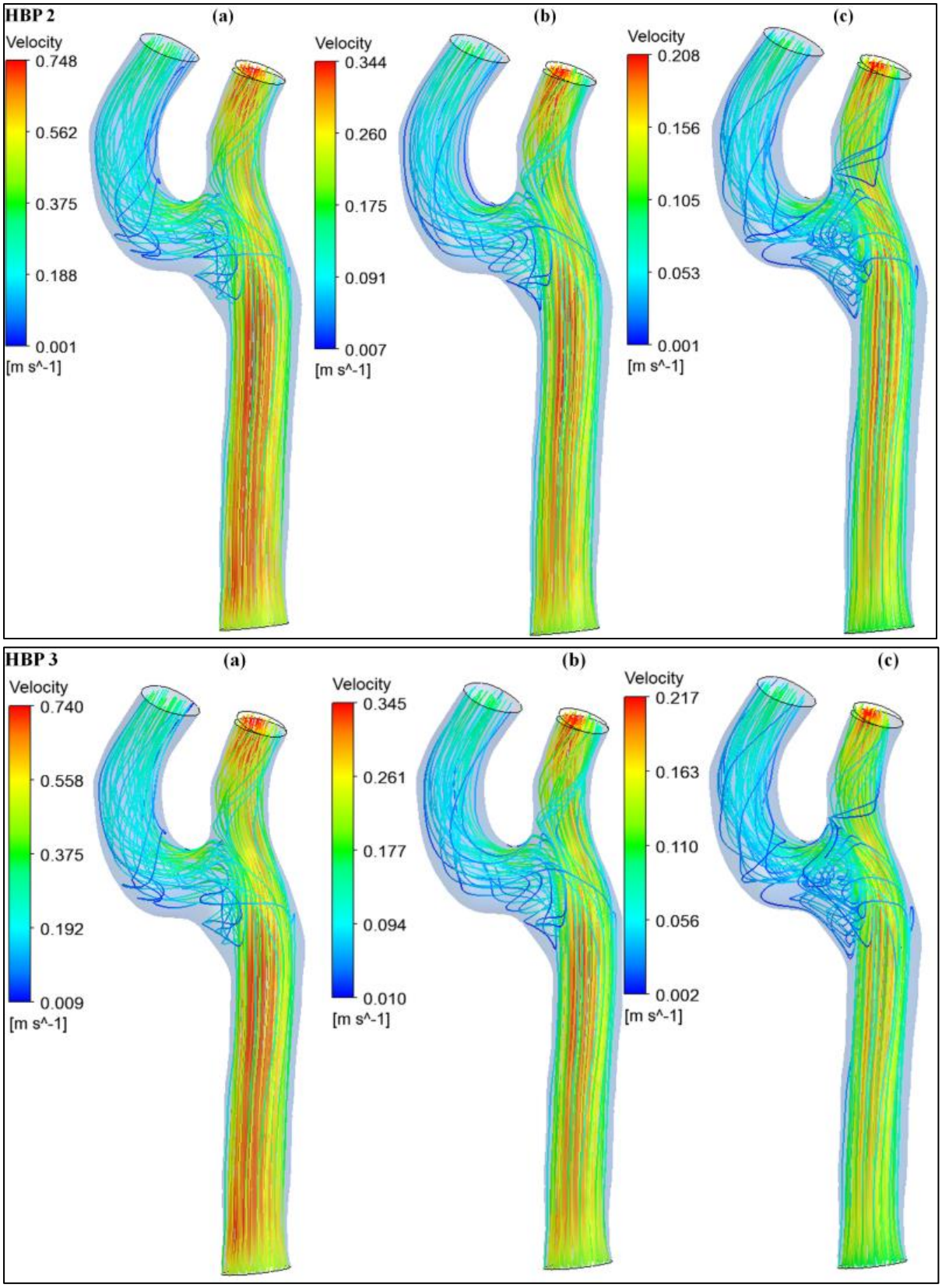

Figure 5-31: Velocity streamlines of normal carotid artery considering Newtonian model, (a) Peak Systole, (b) Early Diastole, (c) Late Diastole

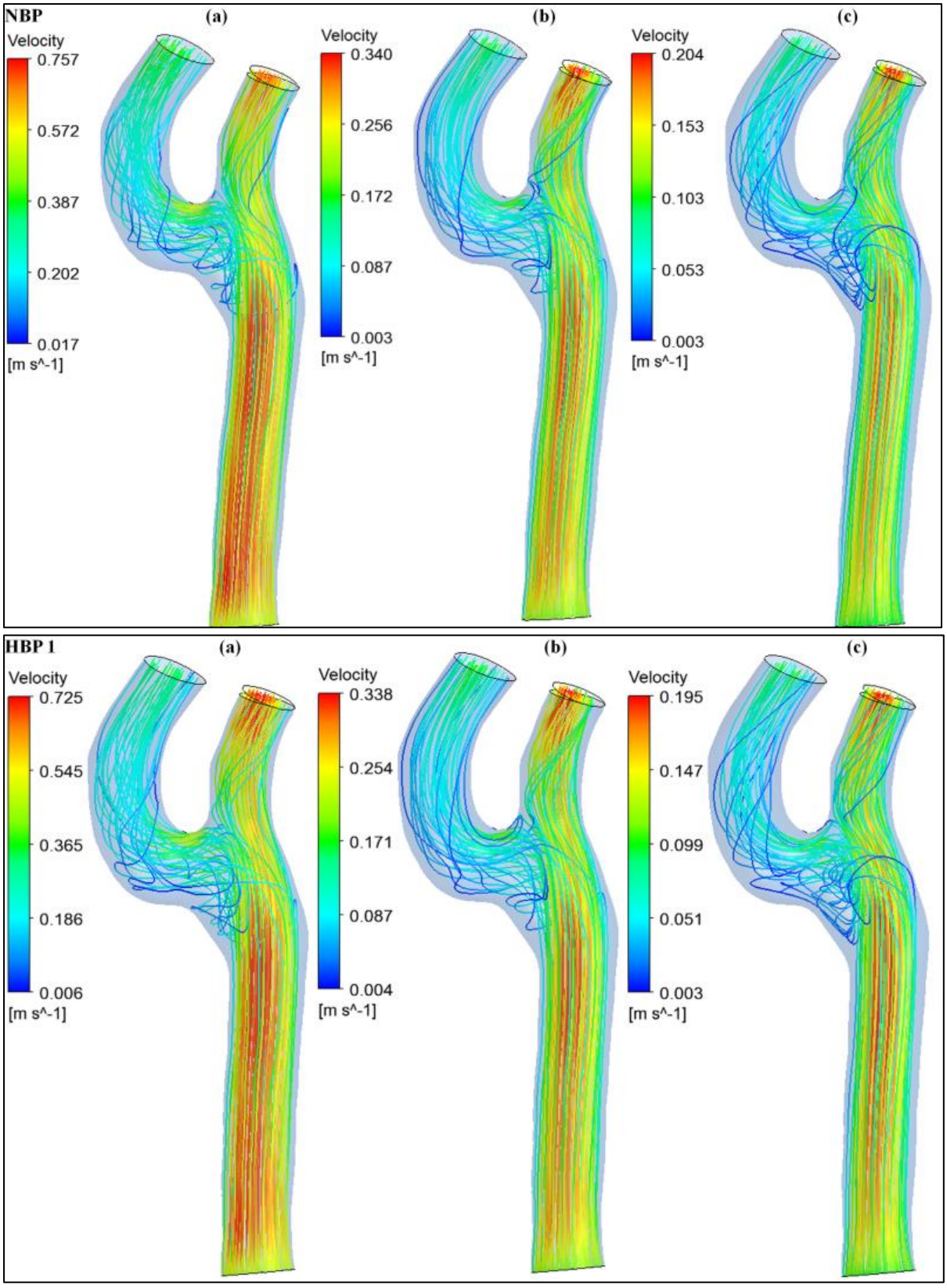

Figure 5-32: Velocity streamlines of normal carotid artery considering Carreau – Yasuda viscosity model, (a) Peak Systole, (b) Early Diastole, (c) Late Diastole

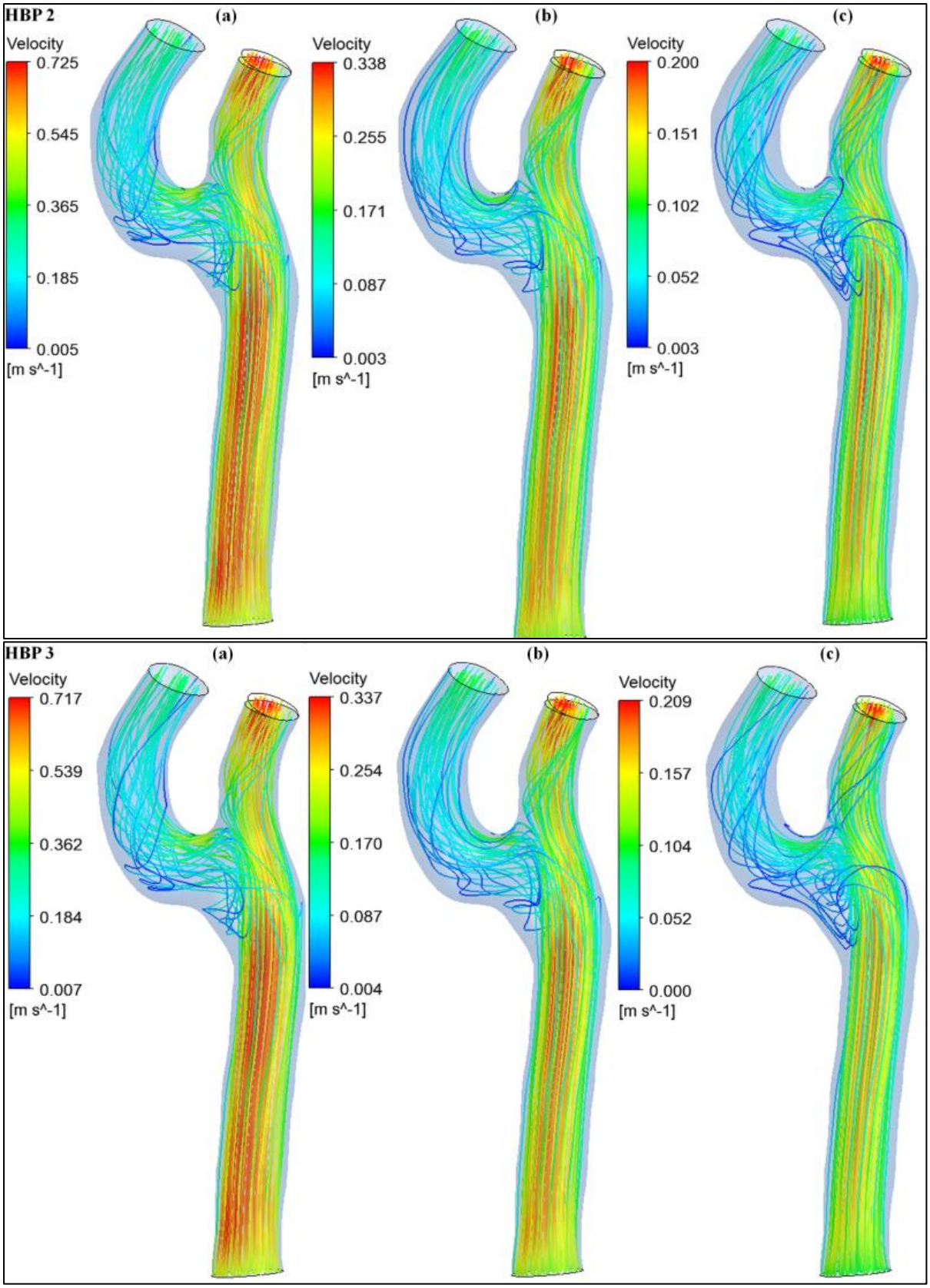

Figure 5-33: Velocity streamlines of normal carotid artery considering Carreau – Yasuda viscosity model, (a) Peak Systole, (b) Early Diastole, (c) Late Diastole

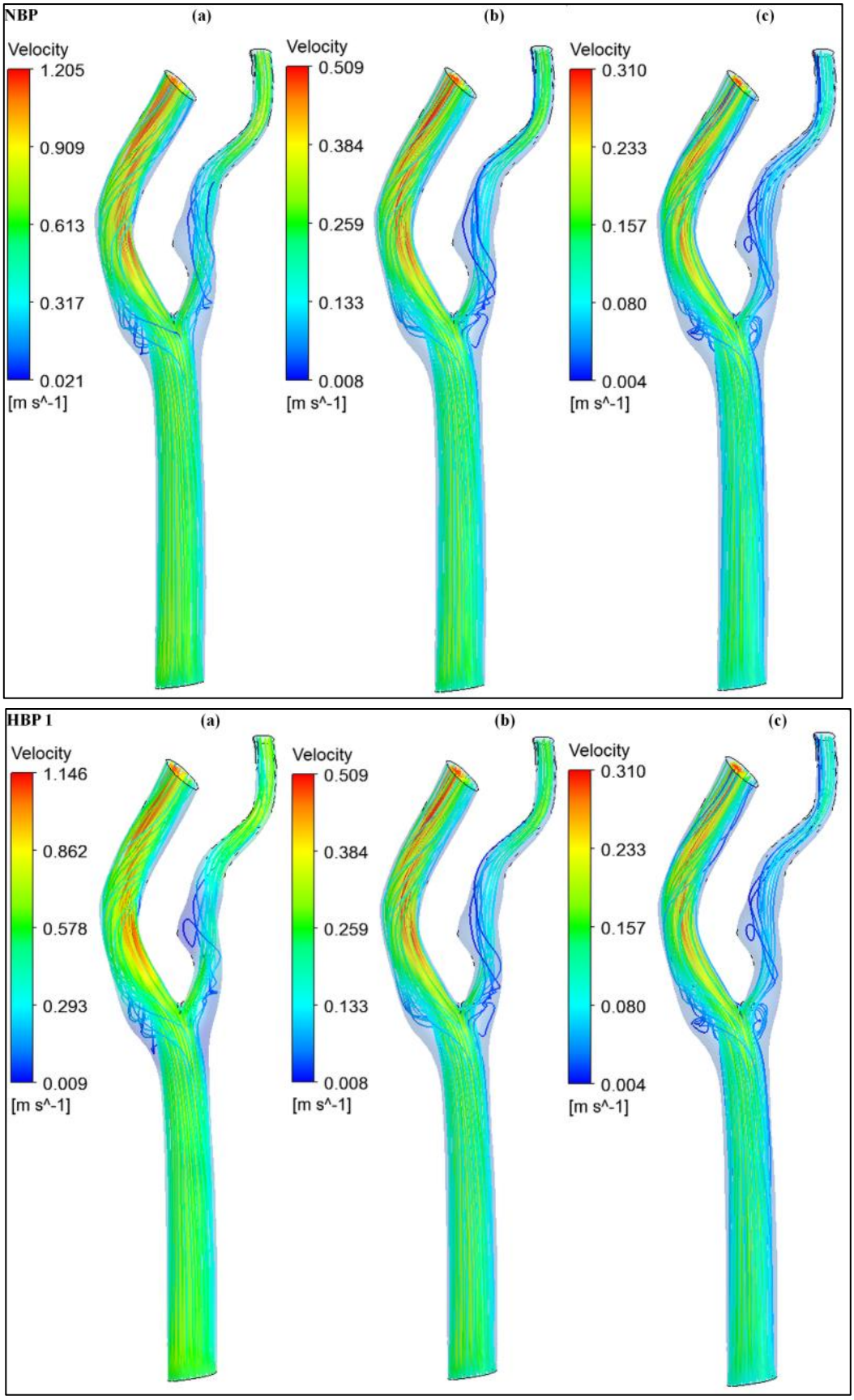

Figure 5-34: Velocity streamlines of stenosed carotid artery considering Newtonian model, (a) Peak Systole, (b) Early Diastole, (c) Late Diastole

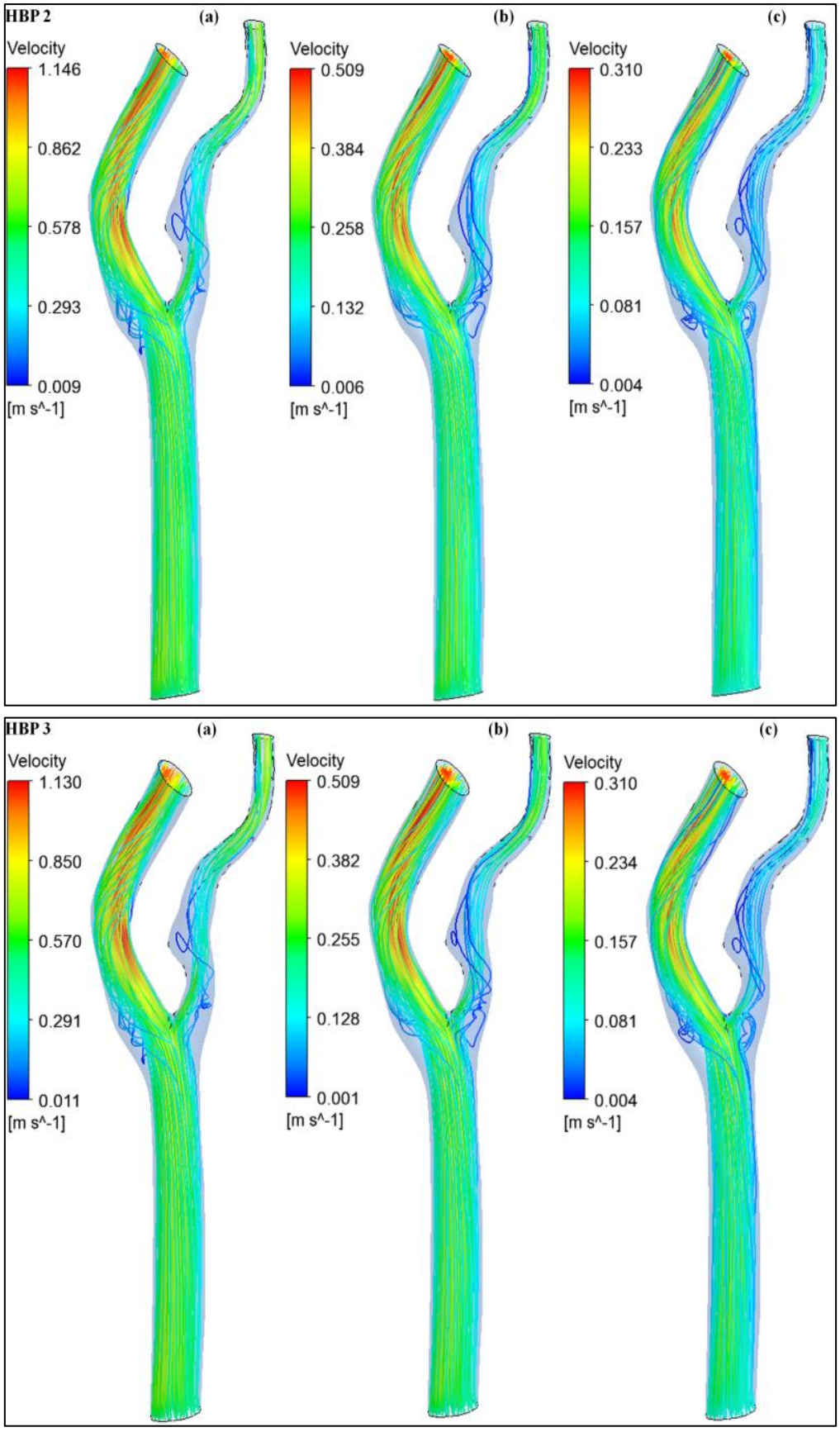

Figure 5-35: Velocity streamlines of stenosed carotid artery considering Newtonian model, (a) Peak Systole, (b) Early Diastole, (c) Late Diastole

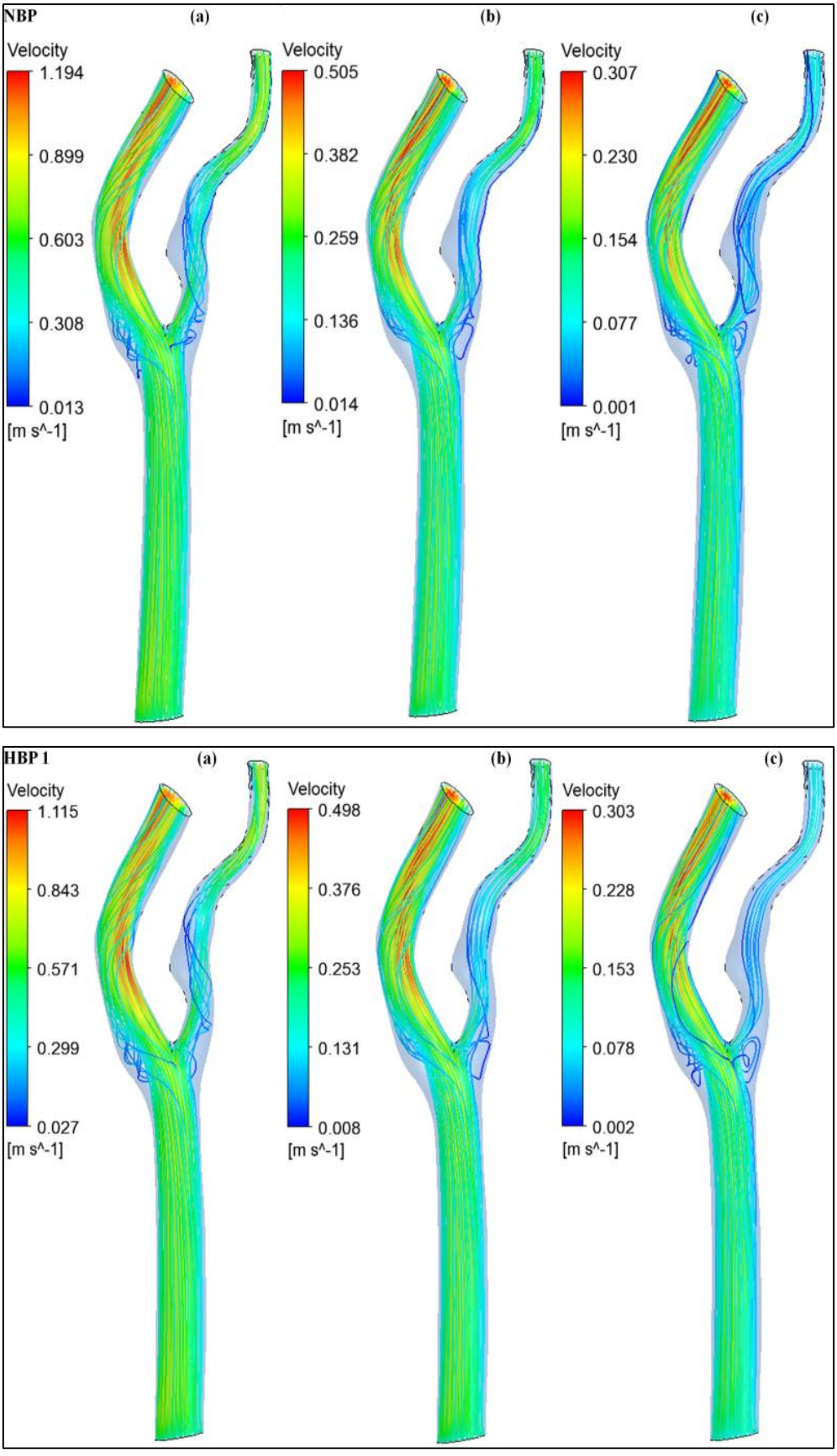

Figure 5-36: Velocity streamlines of stenosed carotid artery considering Carreau - Yasuda viscosity model, (a) Peak Systole, (b) Early Diastole, (c) Late Diastole

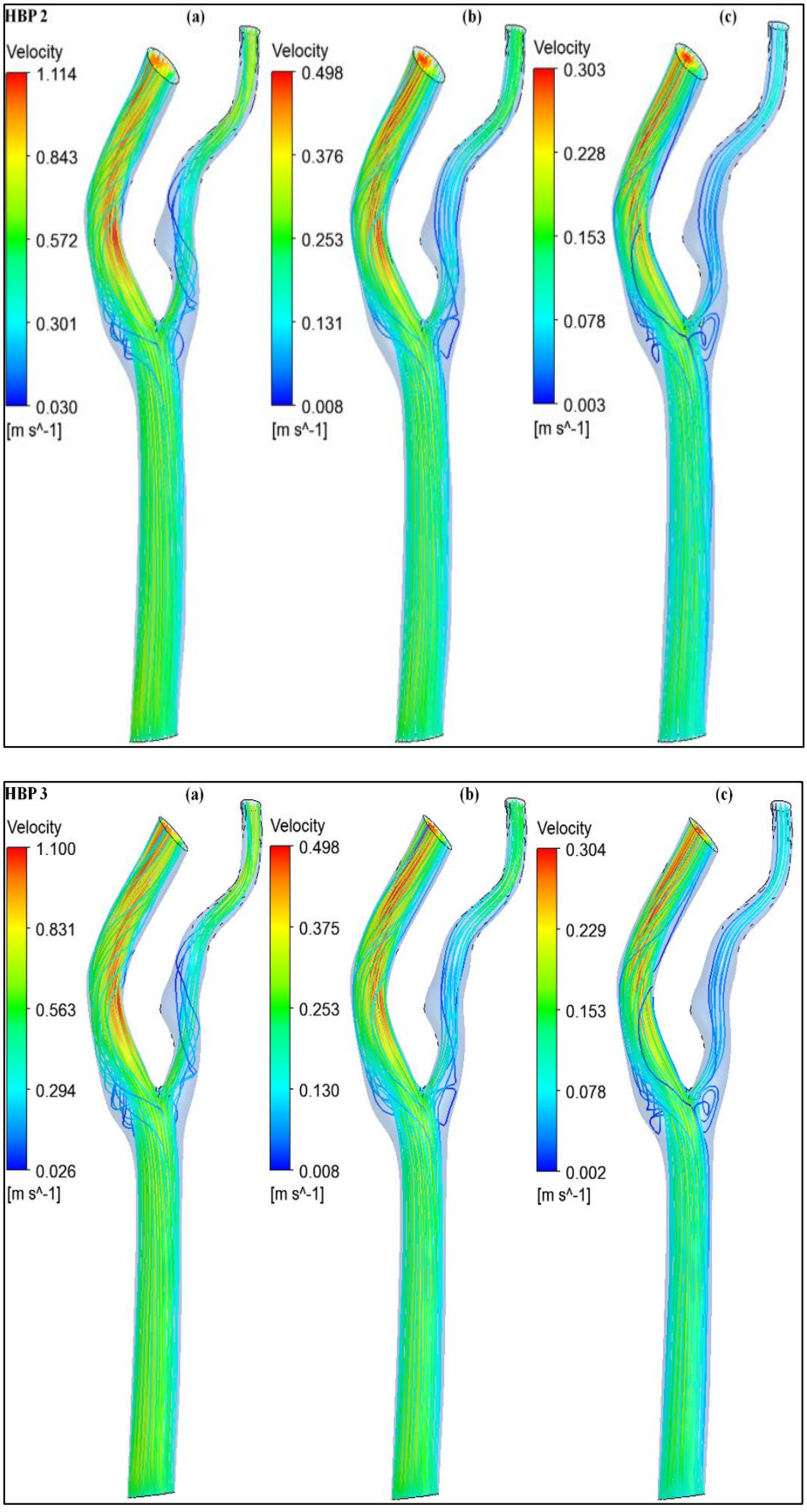

Figure 5-37: Velocity streamlines of stenosed carotid artery considering Carreau - Yasuda viscosity model, (a) Peak Systole, (b) Early Diastole, (c) Late Diastole

The maximum velocity in the carotid artery reduced with an increase in blood pressure due to higher peripheral resistance. In the normal carotid artery model, there were no significant differences between the viscosity models, but there was variation in the stenosed carotid artery model. This was because in a large artery, the consideration of Newtonian viscosity model was sufficient, whereas in a small artery or an artery with stenosis, the consideration of a non – Newtonian viscosity would be necessary [240].

Figure 5-38 shows the temporal variation of maximum velocity in normal and stenosed carotid artery model. It is evident that there is no significant variation between the viscosity models or the different blood pressure cases considered (NBP, HBP 1, HBP 2 and HBP 3).

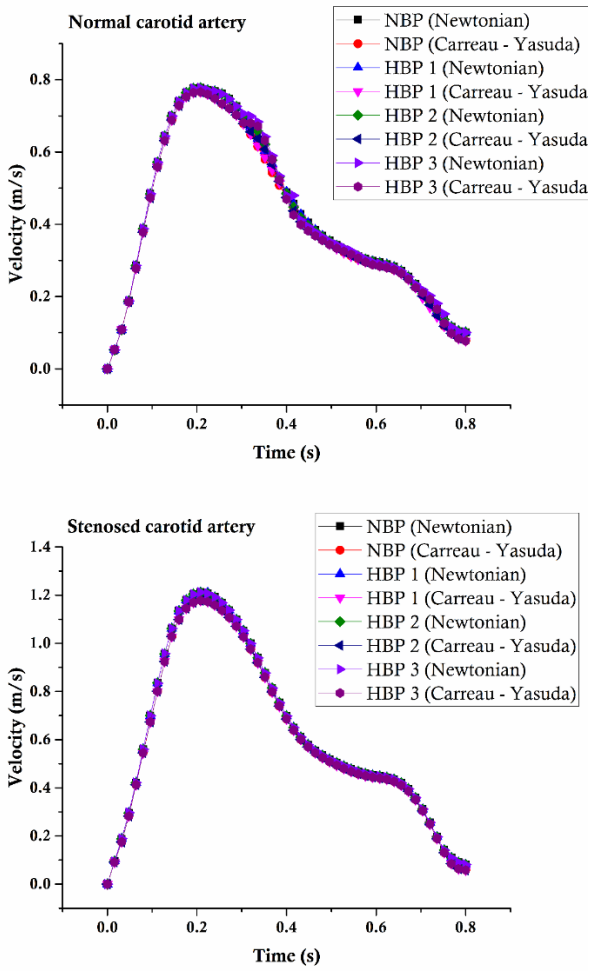

Figure 5-38: Temporal variation of maximum velocity

5.7.3 Oscillatory shear index.

Oscillatory shear index (OSI) shows oscillation of WSS vector in a cardiac cycle. Temporal variations of low and high shear stress were measured [252]. Magnitude of time average of wall shear stress vector, where time was averaged over one cardiac cycle T is defined as

$$\tau_{mean} = \left|\frac{1}{T}\int_0^T \tau_w dt\right| \tag{5.9}$$

Time average of wall shear stress magnitude is defined as

$$TAWSS = \frac{1}{T}\int_0^T |\tau_w| dt \tag{5.10}$$

Now, Oscillatory shear index is defined as

$$OSI = 0.5\left(1 - \frac{\left|\frac{1}{T}\int_0^T \tau_w dt\right|}{\frac{1}{T}\int_0^T |\tau_w| dt}\right) \tag{5.8}$$

It describes the cyclic variation of WSS from its major axial alignment and its values range from 0 in unidirectional flow regions to 0.5 in fully reversible flow regions.

Figure 5-39 shows the bar chart of OSI in stenosed and normal carotid artery using Newtonian and Carreau – Yasuda model respectively. Both the rheological models show similar behaviour with OSI of 0.085 for stenosed and 0.14 for normal carotid artery respectively. OSI does not change with increase in blood pressure supporting the velocity and WSS variations in previous sections.

Although CFD gives reasonable approximation on haemodynamic parameters such as WSS, velocity and OSI, it fails to predict the key haemodynamic parameters accurately when the blood pressure in increased. Irrespective of the outlet pressure, the rigid artery wall assumption, due to its high stiffness does not influence the haemodynamics. This was because the elastic artery absorbs the increased energy and deforms and changes in the flow behaviour. This motivates the study of FSI analysis of the carotid artery subjected to different blood pressures.

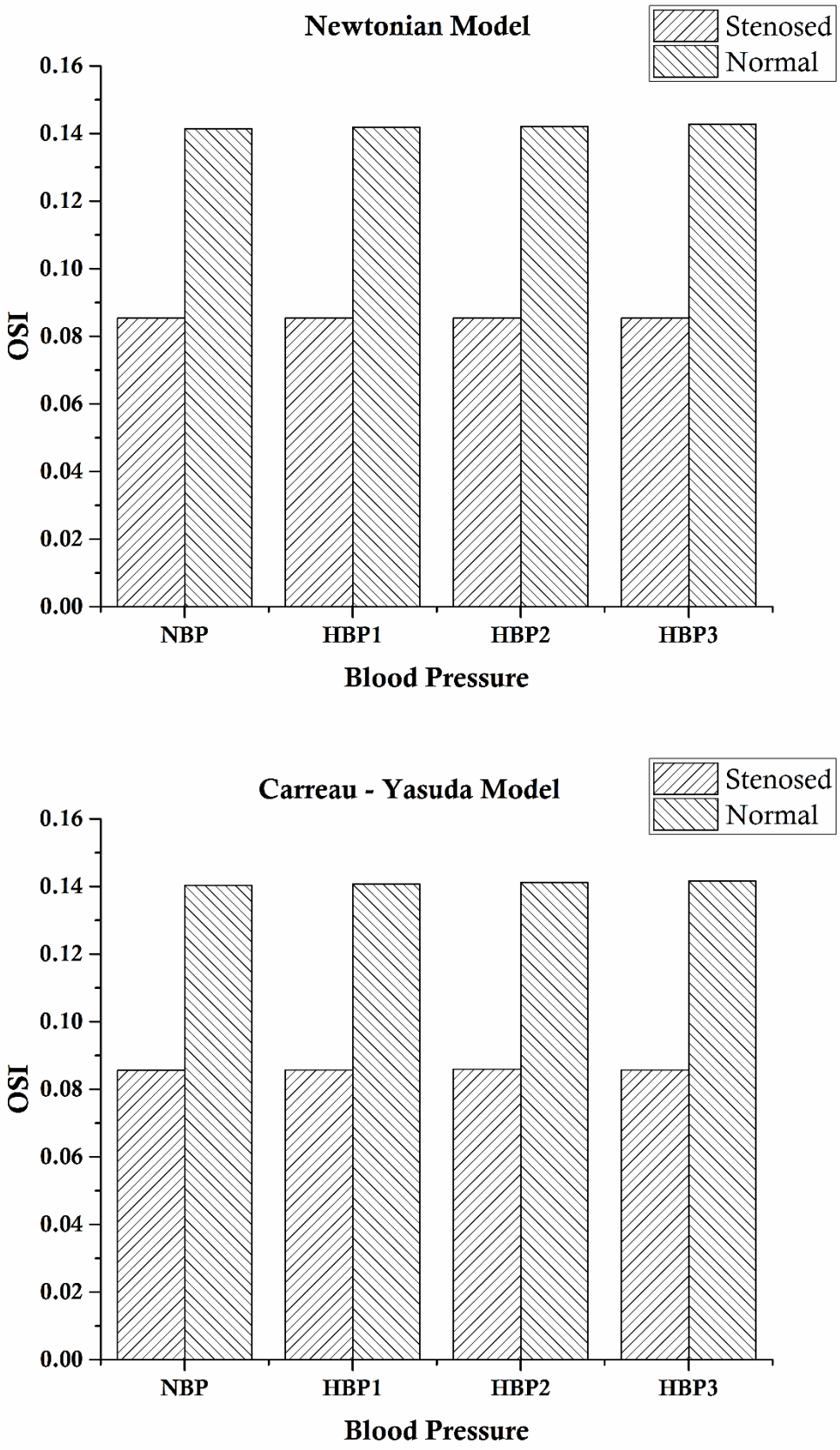

Figure 5-39: OSI in normal and stenosed carotid artery with blood as Newtonian fluid

Chapter 6 Fluid Structure Interaction study of normal and stenosed carotid artery

It is evident from many studies that atherosclerotic plaque is a location specific disease which occurs particularly at regions with complex flow caused by geometry variations such as bends or bifurcations [60]. However, the complexity associated with atherosclerosis and the effect of mechanical factors and blood pressure was not fully understood. Although WSS is a prime factor to stimulate endothelial cell response [253], understanding its variation due to wall deformation and identifying these flow patterns in vivo is very difficult.

In the previous chapter, image – based CFD studies were performed which also gives detailed flow patterns such as WSS which cannot be discovered from medical images. Indicators such as WSS and OSI are commonly used to equate atherosclerosis with disrupted flow.. However, in these studies arterial elasticity was ignored and was based on rigid wall assumptions.

In FSI approach, fluid and solid models were simultaneously solved and was of great interest for researchers because of its potential in predictive diagnosis [254]. This technique was widely used to model the abdominal aorta, carotid artery and cerebral aneurysm extensively. Torii et al [249] studied the effect of wall elasticity on a stenosed coronary artery and found significant differences in WSS magnitude between rigid and FSI models. This is confirmed by the analysis of the porcine coronary artery by Huo et al [104] where temporal wall shear stress gradient obtained by FSI model was less compared to rigid models.

In this study, FSI analysis of anatomically realistic normal and stenosed carotid artery model was performed to understand the effect of wall compliance and blood pressure on hemodynamic markers such as WSS, velocity and OSI. Such a study provide a better understanding to clinicians on the effect of blood pressure on normal and stenosed carotid artery and the difference between CFD which was seen in previous chapter and FSI.

6.1 Numerical validation

6.1.1 Pressure pulse propagation

Fluid structure interaction study on a straight elastic tube by Degroote et al [123] was used to validate the present analysis. A simple test case of wave propagation in an elastic tube was used. The dimensions of the geometry correspond to the approximate dimensions of the human aorta. Two-way FSI analysis was carried out using Ansys Structural and Ansys CFX solvers and the pressure wave propagation was simulated in 3D elastic tube of inner radius of 0.01 m and a tube thickness of 0.001 m. *Figure 6-1* shows the dimensions and boundary conditions and the mesh used in the study. The fluid and solid domains were meshed into 12240 and 35190 number of hexahedral elements respectively after grid independence study. The wall of the elastic tube was assumed to be linearly elastic with density of 1200 kg/m^3, elastic modulus of 300,000 N/m^2 and Poisson's ratio of 0.3. Fluid was assumed to be Newtonian with a density of 1000 kg/m^3 and dynamic viscosity of 0.003 Pa s. The inlet and outlet face of the solid model was fixed. Fluid and sold domain were at rest initially and the pressure pulse was applied at the inlet for 0.01 s with 0 traction at the outlet. The applied pressure was approximately 10 mmHg and was not the physiological pressure. However, it was used to check the wave propagation phenomenon for a short segment of elastic tube [120]. Total simulation time was 0.01 s, with a time step of 0.0001 s.

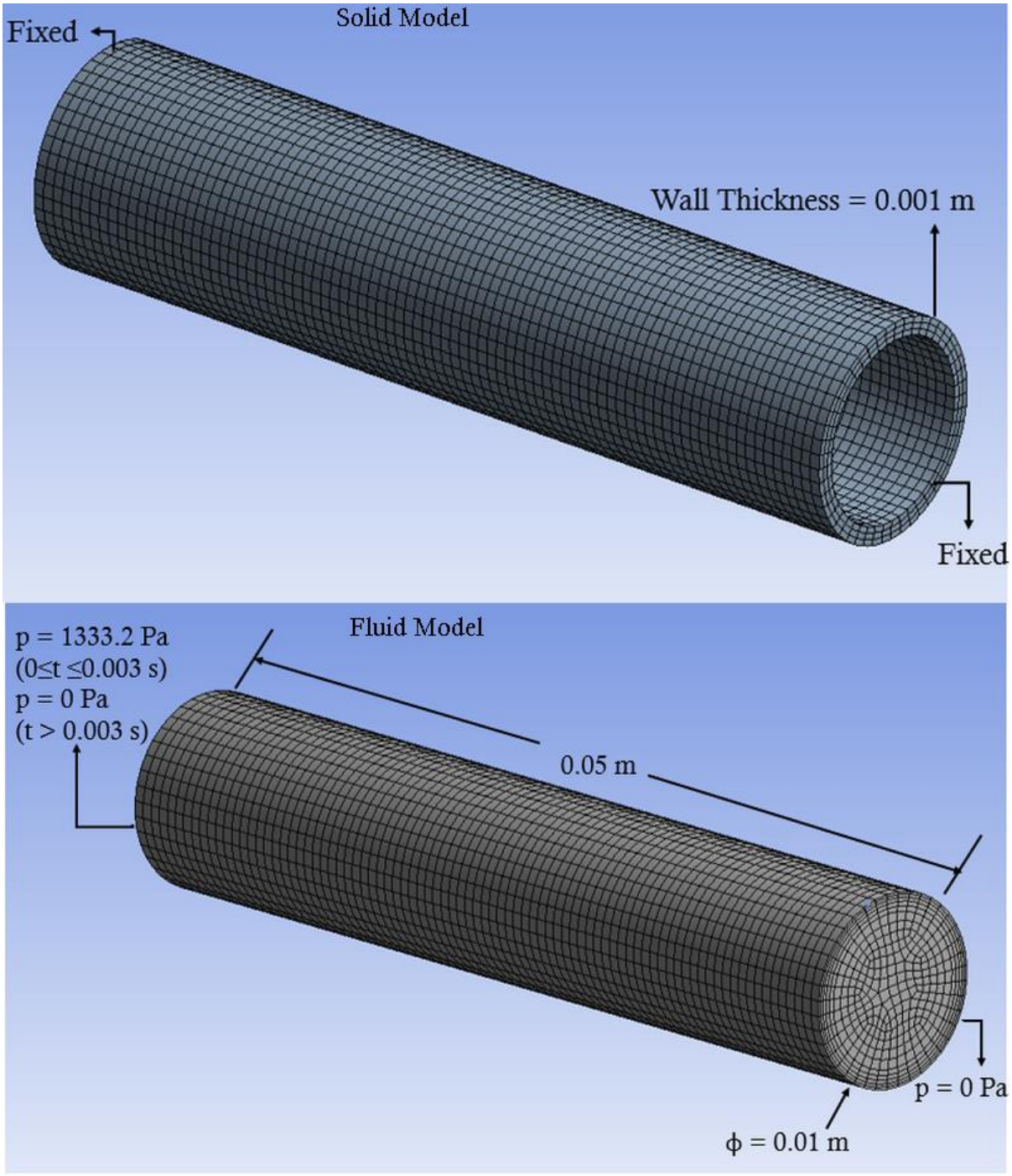

Figure 6-1: Solid and fluid meshed model showing geometry, mesh details, applied boundary conditions and dimensions

Figure 6-2 shows the comparison of wave propagating between present study and the study conducted by Degroote et al [123] at 2.5 ms, 5 ms, 7.5 ms and 10 ms. The maximum pressure is observed at the first 2.5 ms and this pressure pulse gradually propagates till the distal end.

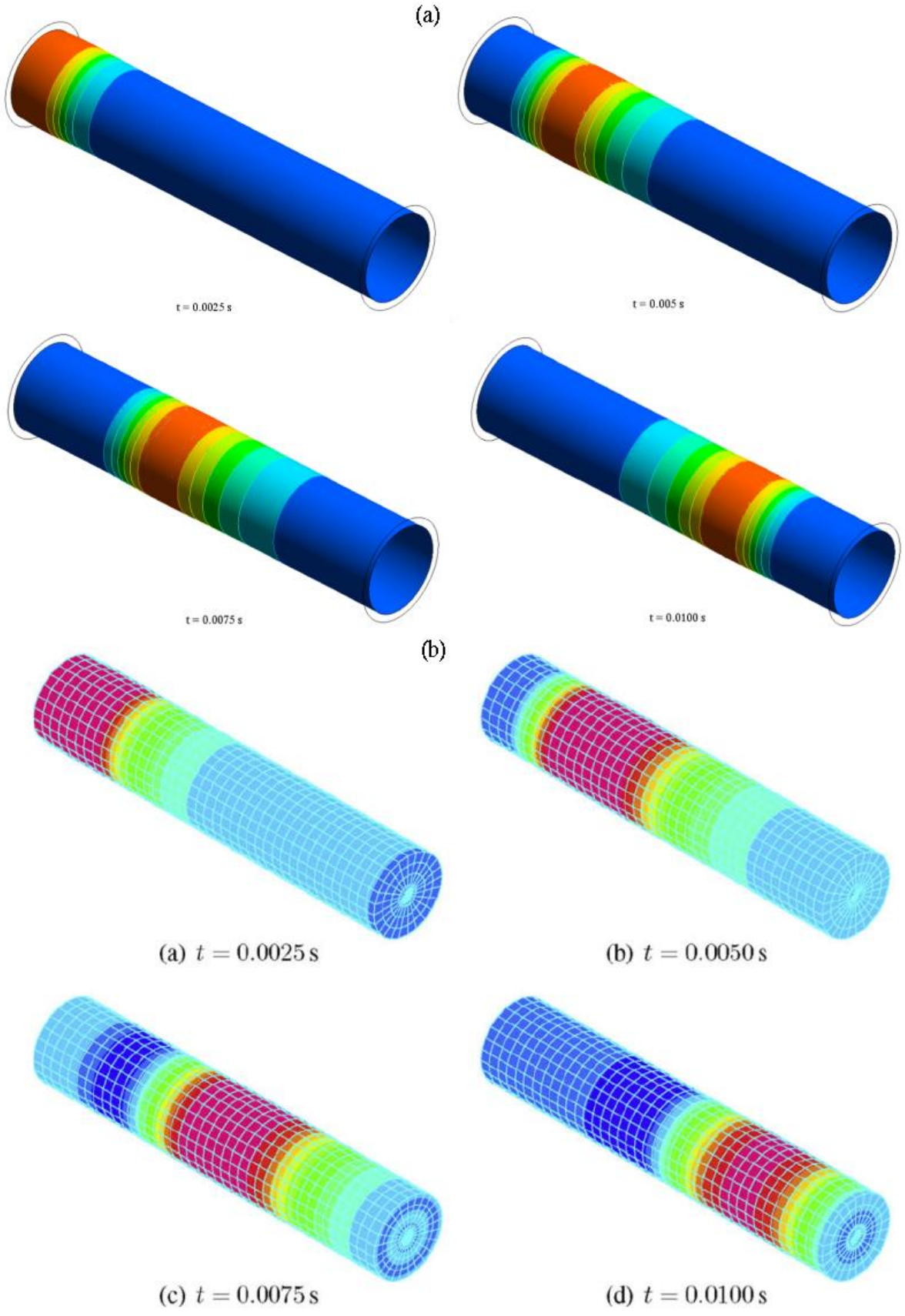

Figure 6-2: Pressure contours at 2.5 ms, 5 ms, 7.5 ms and 10 ms (a) Present study, (b) Degroote et al [123].

The pressure propagation was validated both qualitatively and quantitatively with the above literature. This validation was required to check the two – way FSI coupling capability in ANSYS.

6.1.2 Validation for physiological boundary condition

FSI analysis was validated for pulsatile flow by considering the physiological boundary condition as observed by Alberto Figueroa [131], where pulsatile flow was simulated through a simple straight tube representing carotid artery. The fluid model has a diameter of 6 mm and 126 mm long. The solid model has a wall thickness of 0.3 mm as shown in *Figure 6-3*.

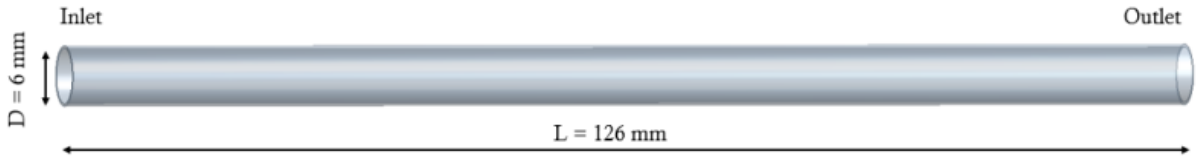

Figure 6-3: Geometric details of elastic tube model

Young's modulus and Poison's ration of the arterial model was taken as 4.07 MPa and 0.45 respectively, whereas fluid was considered as Newtonian with a density of 1000 kg/m^3 and dynamic viscosity of 0.004 Pa – s. The outlet and inlet face of the solid model was fixed, and the rest of the wall nodes could move in any direction due to the interaction with fluid flow. A pulsatile periodic wave form of three cardiac cycle was prescribed at the inlet. The total simulation time was 1.1 seconds with a parabolic profile as shown in *Figure 6-4*. For the outlets, resistance boundary conditions was applied as described by Irene [132], shown in *Figure 6-5*. Grid independence study was performed and an optimum mesh size of 17560 and 35680 elements for solid and fluid model respectively.

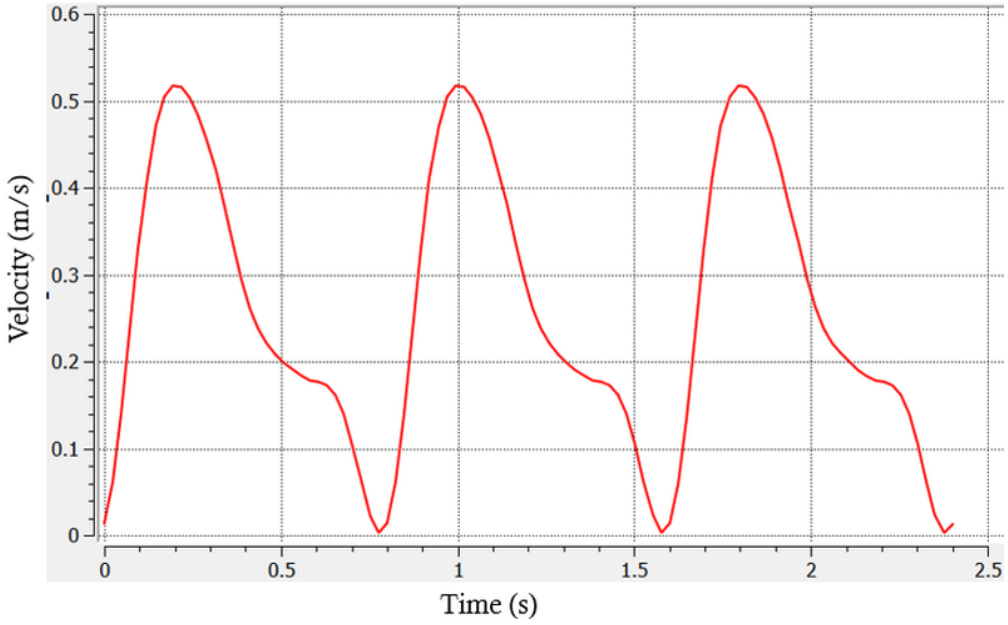

Figure 6-4: Inlet velocity profile

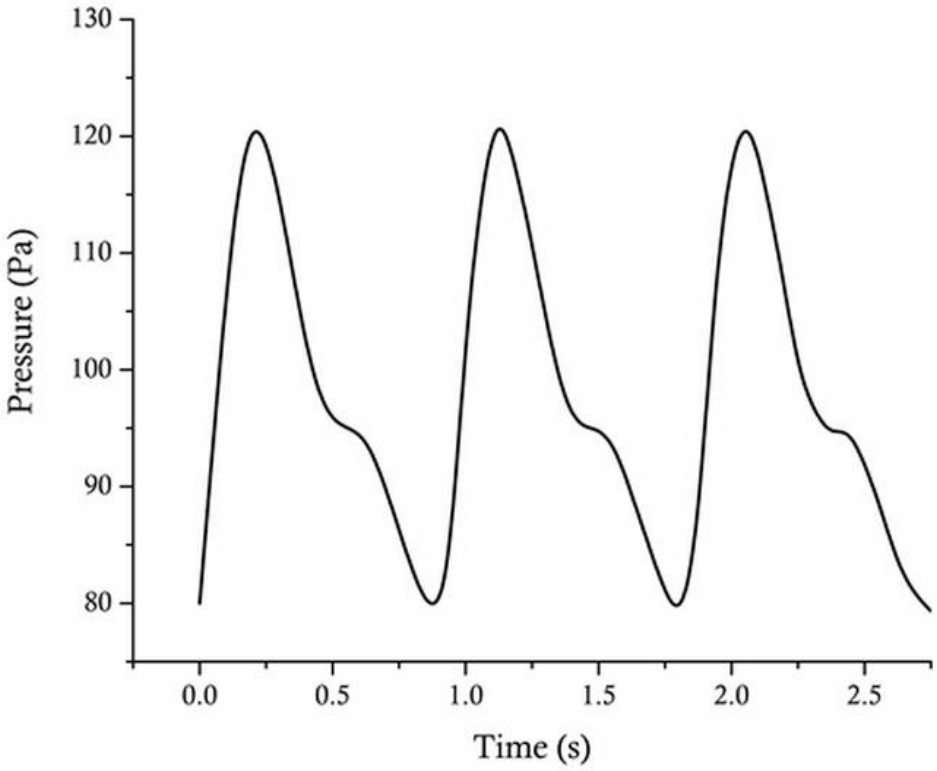

Figure 6-5: Outlet pressure waveform

A steady 2-way FSI is solved and the results were used as initial conditions for transient 2-way FSI analysis. Two sections, S1 and S2 at 6 mm from inlet and outlet was taken to capture the pressure profile, flow and displacement. These locations were selected as the

radial deformation was not affected by the constrained inlet and outlet faces of the solid model. *Figure 6-6* shows the radial deformation and pressure profiles and *Figure 6-7* shows the mass flow compared with Alberto Figueroa [131].

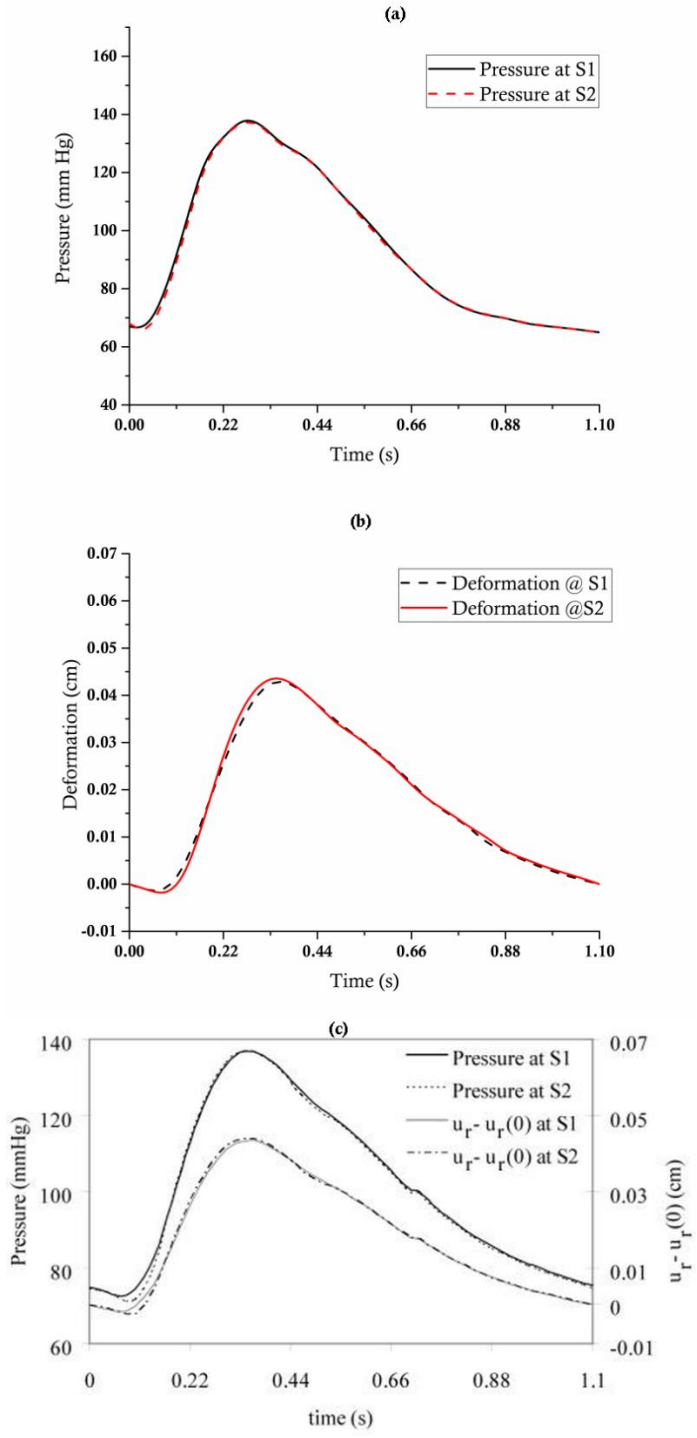

Figure 6-6: Pressure and deformation profile comparision (a) Present study, (b) Alberto Figueroa [131]

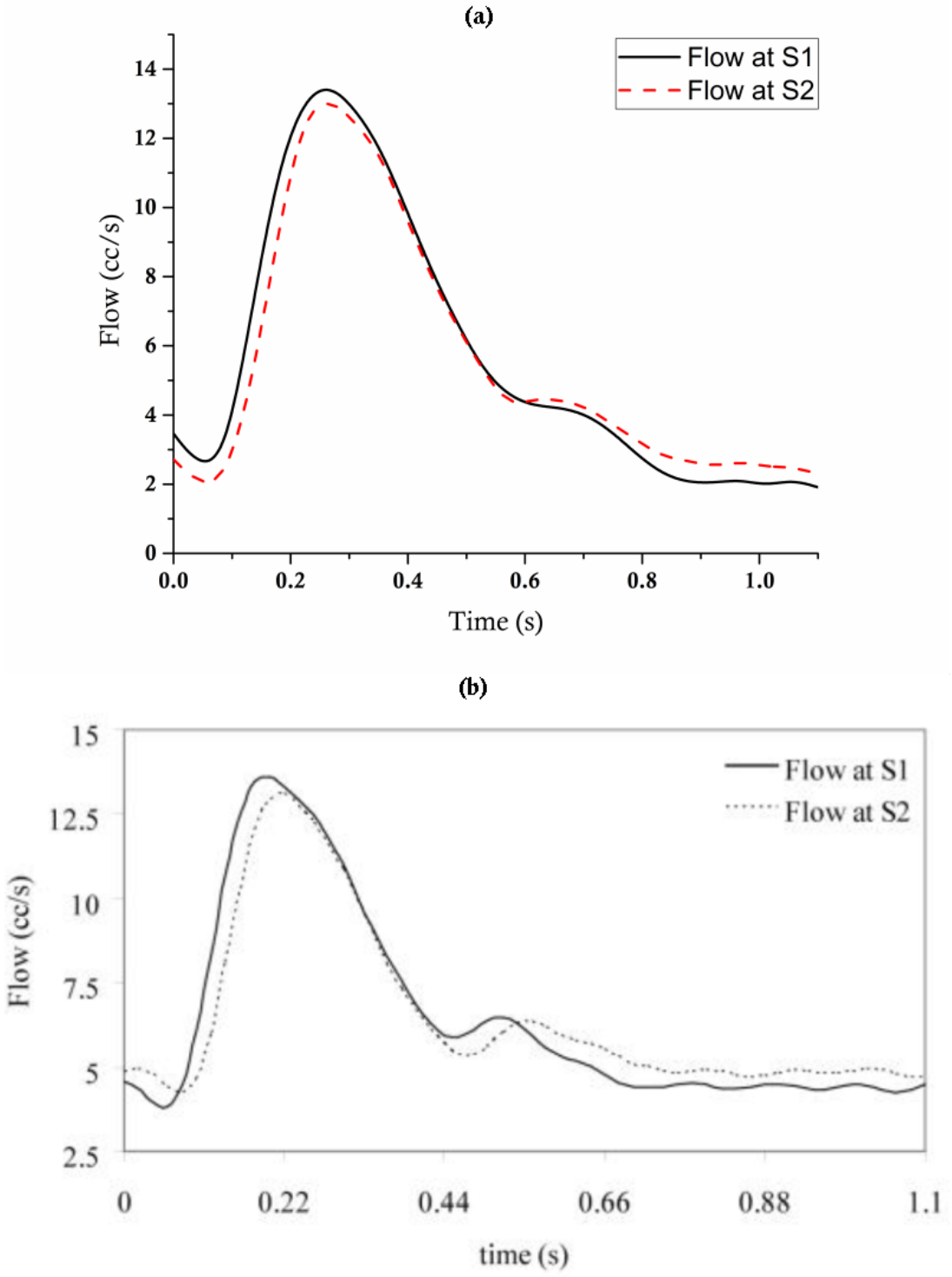

Figure 6-7: Mass flow variation between (a) present study, (b) Albertro Figueroa[131]

The maximum deformation is within 10% of the arterial diameter. Flow is maximum at peak systole when the deformation is maximum. The computed parametes show realistic

phase lag and wall ldeformation. There is significant phase lag between the mass flow rates at plane S1 and S2 and there is noticeable difference during systole and diastole since the outlet is comparatively large duing diastole because it receives extra flow that is stored during systole. This mass flow profile shows the ability of the artery to store the fluid during systolic phase and then release it during the diastolic phase of the cardiac cycle. Therefore, the obtained results, both qualitatively and quantitatively corresponds with the literature[131].

Wave speed was compared using Moens – Korteweg equation. The phase lag during peak systole between inlet and outlet flow was 0.024 seconds for 126 mm length of the tube, and wave speed produced was 5.25 m/s. The wave speed obtained by using Moens – Korteweg equation was 4.51 m/s. In this study the lag between the inlet and outlet was 0.022 seconds for 126 mm length and the corresponding wave speed using Moens – Korteweg equation was 5.68 m/s. Therefore, there was a close relationship between the wave speed obtained in this analysis and the literature [131].

6.2 Fluid structure interaction analysis on Normal carotid artery subjected to different blood pressures

Many researchers have explored FSI analysis in understanding haemodynamics of blood flow in both normal and stenosed carotid arteries. However, the effect of varying blood pressure on the same carotid artery in changing the flow behaviour was not understood. In this section, haemodynamics in a patient specific normal carotid artery was studied by changing the blood pressure, focussing on the understanding of haemodynamics in critical locations like the bifurcation. The significant changes observed in flow during change in blood pressure in normal carotid artery was discussed in this section.

6.2.1 Case description

In this study, a healthy normal carotid bifurcation is considered to evaluate the effect of blood pressure on haemodynamics. The geometry was generated based on data obtained by CT angio scan as described in section 5.4.2. The 3D CAD model was generated in CATIA based on the data exported from MIMICS. The FSI models are generated in ANSYS Workbench. The detailed methodology of model reconstruction was elaborated in Chapter 3. Temporal velocity and pressure waveform was applied at the inlet and the outlets respectively as shown in *Figure 5-8* and *Figure 5-9* and a sequentially coupled two – way transient FSI analysis was performed for three cardiac cycles and the results obtained at the third cycle was considered for the analysis. The models were meshed with ten node tetrahedral elements using patch conforming algorithm and quadratic element order. Inflation was defined in the fluid model to capture the boundary layer effects.

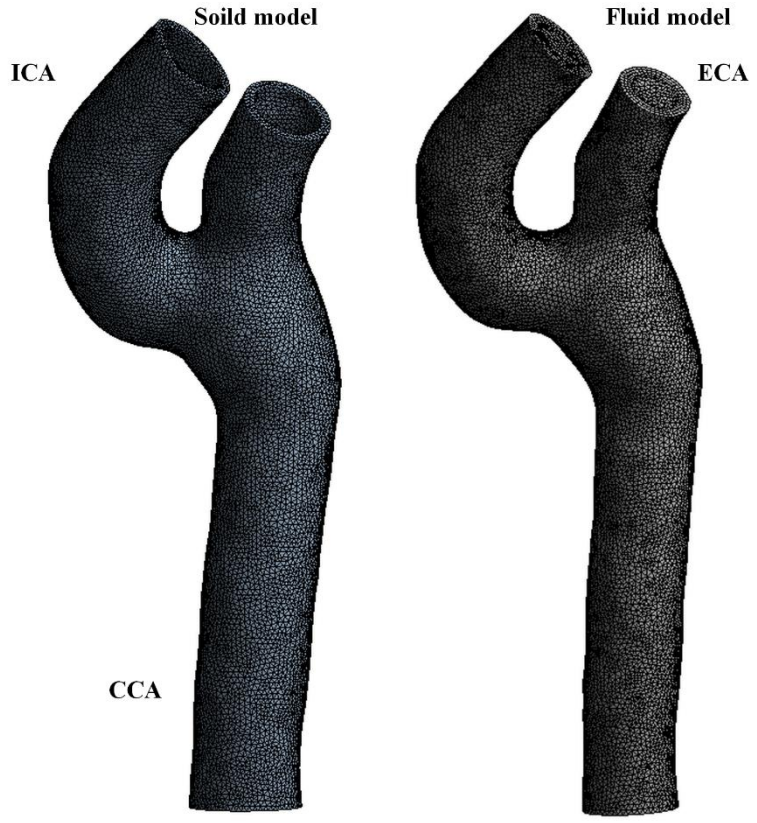

Figure 6-8: Meshed model used in the FSI analysis

6.2.2 Results and discussion

The variations in the flow behaviour during different blood pressures and blood viscosity models were investigated by considering critical hemodynamic parameters such as WSS, Velocity, deformation and Oscillatory shear index. The maximum changes occurred at peak systole, early and late diastole, and hence, these instants were considered to compare the flow behaviour [255]. The changes in the flow was enumerated and corresponding changes in WSS and OSI in normal carotid artery is highlighted in this section.

6.2.3 Grid Independence test

The fluid and solid models were discretized using 10 node tetrahedral elements and variation of Maximum WSS magnitude at the wall, Maximum velocity magnitude at the fluid domain and maximum wall deformation were noted at peak systole for different mesh size. Based on the grid independence test as shown in *Figure 6-9*, an optimum mesh size of 105963 solid and 323514 fluid elements are used in this analysis.

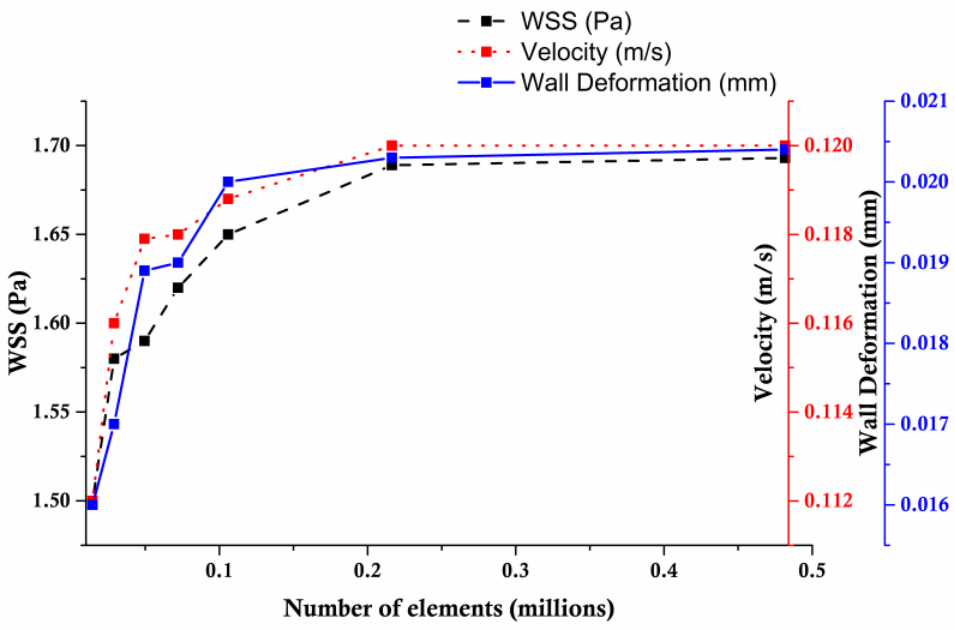

Figure 6-9: Grid independence study of normal carotid artery

6.2.4 Time step sensitivity test

Optimum timestep for FSI analysis was chosen based on time – step sensitivity test. Analysis was performed for 25, 50, 100 and 200 time steps with a step size of 0.032 s, 0.16 s, 0.008 s, and 0.004 s. Test was performed for NBP and outlet boundary condition and prescribed inlet velocity as shown in *Figure 5-9* is applied. Average velocity in the fluid domain and average WSS in the wall is plotted against different time steps as shown in *Figure 6-10*. Based on the above study, an optimum time step of 100 with a step size of 0.008 s was chosen in this study.

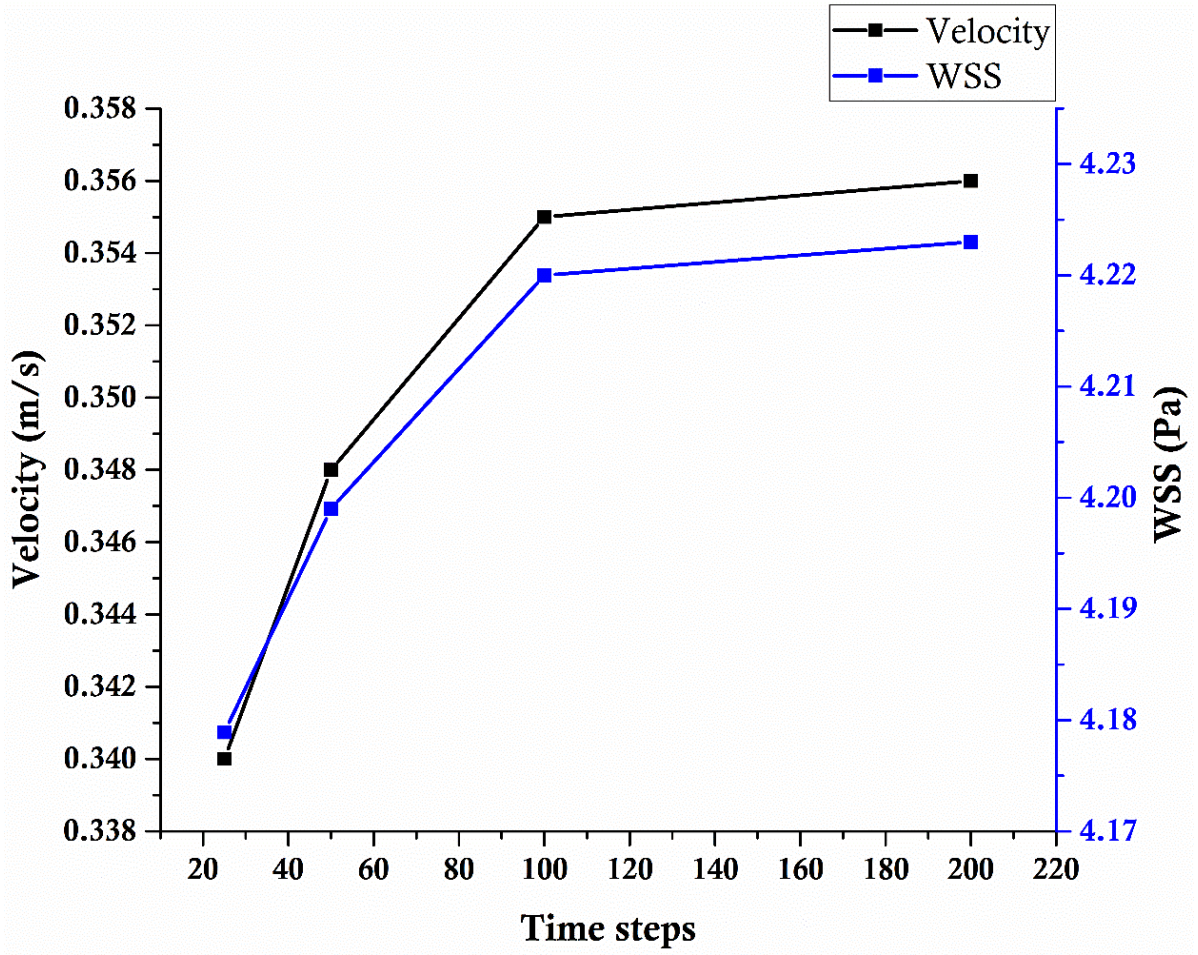

Figure 6-10: time step sensitivity test for normal carotid artery model

6.2.5 Velocity

Figure 6-11 shows the velocity streamlines of normal carotid artery model subjected to NBP by Newtonian and Carreau-Yasuda model considerations. Velocity magnitude was maximum at peak systole for both rheological models. At peak systole and early diastole, the position of the flow recirculation area was nearly identical, but at late diastole, at the base of ICA near the carotid sinus, the flow recirculation and low-velocity area were more chaotic. The difference between the viscosity models was also more prominent in this phase of the cardiac cycle as seen from *Figure 6-11*. The Newtonian model showed more chaotic flow whereas in the Carreau – Yasuda model, the flow was more laminar compared to the Newtonian model. This was justified as at low velocities the shear rate is low and the Newtonian model fails to capture the non – Newtonian flow behaviour in that flow regime and, at low velocities, the viscosity of blood was comparatively increased, and flow profiles were more laminar. This behaviour was not captured by the Newtonian model. At the bifurcation, the flow experiences a high-velocity gradient and reversed flow along the outer wall of ICA. This as due to the bifurcation of the CCA into ICA and ECA and the carotid sinus that is present in the outer wall region of the ICA causing flow recirculation in that region. *Figure 6-15* shows the variation of average velocity magnitude and from this, it can be established that the velocity magnitude does not vary significantly with blood viscosity models.

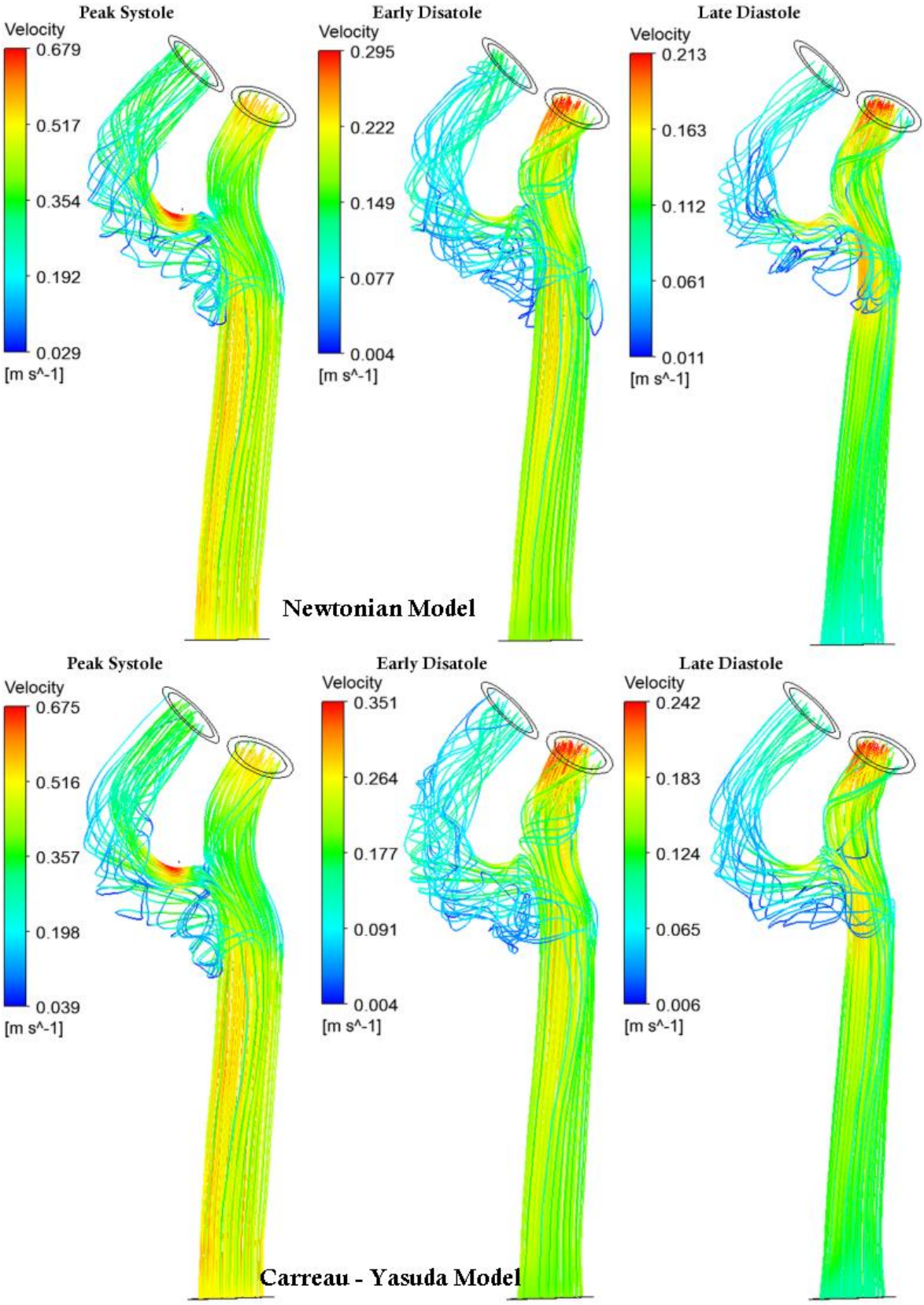

Figure 6-11: Velocity Streamlines for Normal blood pressure (NBP) considering Newtonian model and Carreau – Yasuda model.

Similar behaviour is observed with higher blood pressure cases viz., HBP 1, HBP 2 and HBP 3. *Figure 6-12* shows the velocity streamlines in normal carotid artery subjected to HBP 1 by using Newtonian and Carreau – Yasuda model. It can be seen that the Newtonian model shows higher recirculation when compared to the Carreau – Yasuda model. *Figure 6-13* and *Figure 6-14* shows the velocity streamlines for HBP 2 and HBP 3 respectively. The velocity streamlines tend to be more laminar compared to NBP, as the blood pressure increase. The flow seperation led to vortices and vortex shedding at elevated flow rates caused by increased flow momentum. Higher velocity was observed at peak systole, and flow separation occurred at the upper portion of the CCA due to bifurcation and increased diameter at the carotid sinus. The velocity magnitude was inversely proportional to blood pressure. This was attributed to higher peripheral resistance, which also contributed to a rise in arterial deformation due to blood pressure. Because of the geometry, where the ICA centreline was almost in line with the CCA, higher velocities was observed in the ECA relative to the ICA.

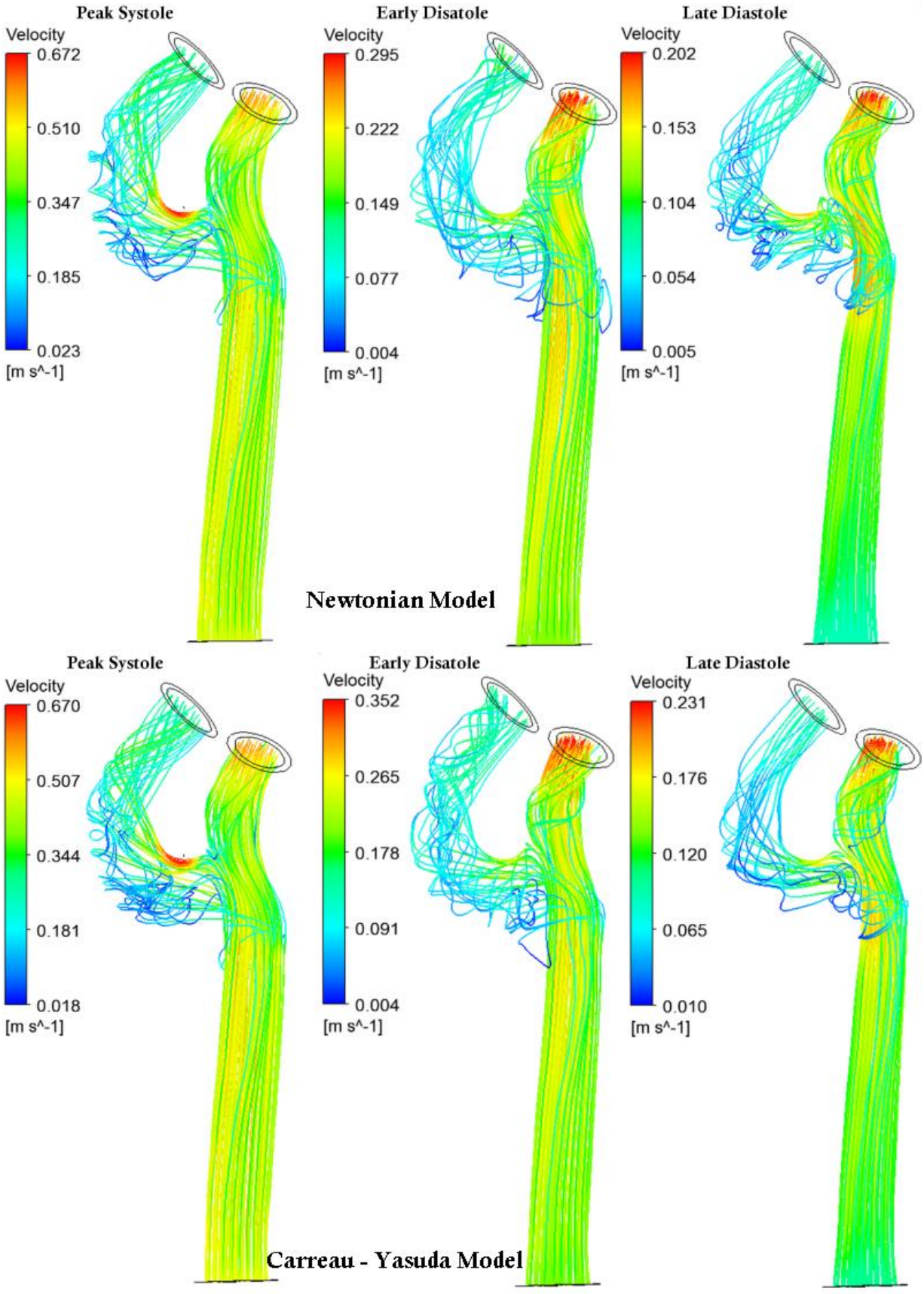

Figure 6-12: Velocity streamlines for Pre - hypertension (HBP 1) condition considering Newtonian and Carreau - Yasuda model

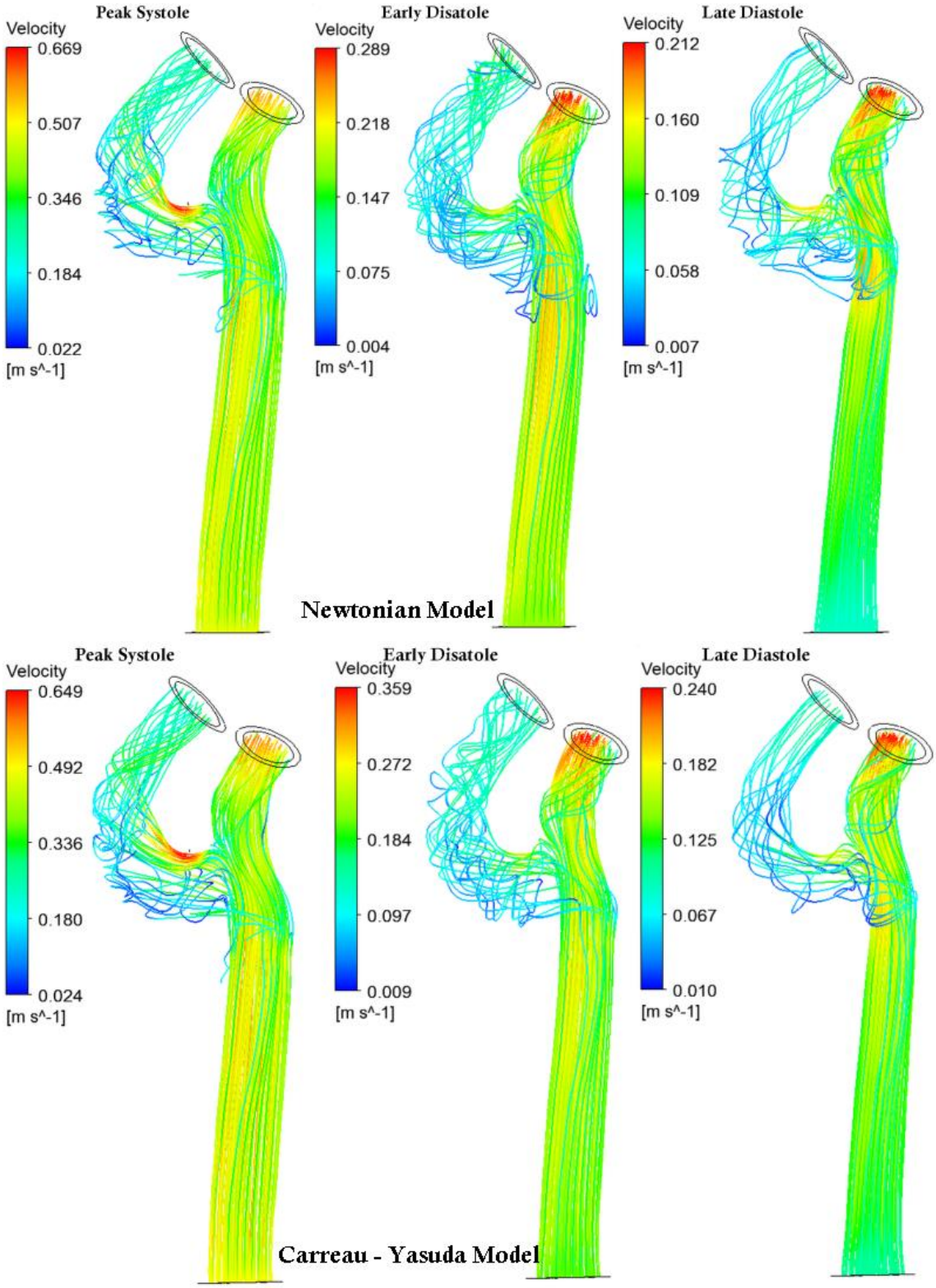

Figure 6-13: Velocity streamlines for stage 1 hypertension (HBP 2) condition considering Newtonian and Carreau - Yasuda model

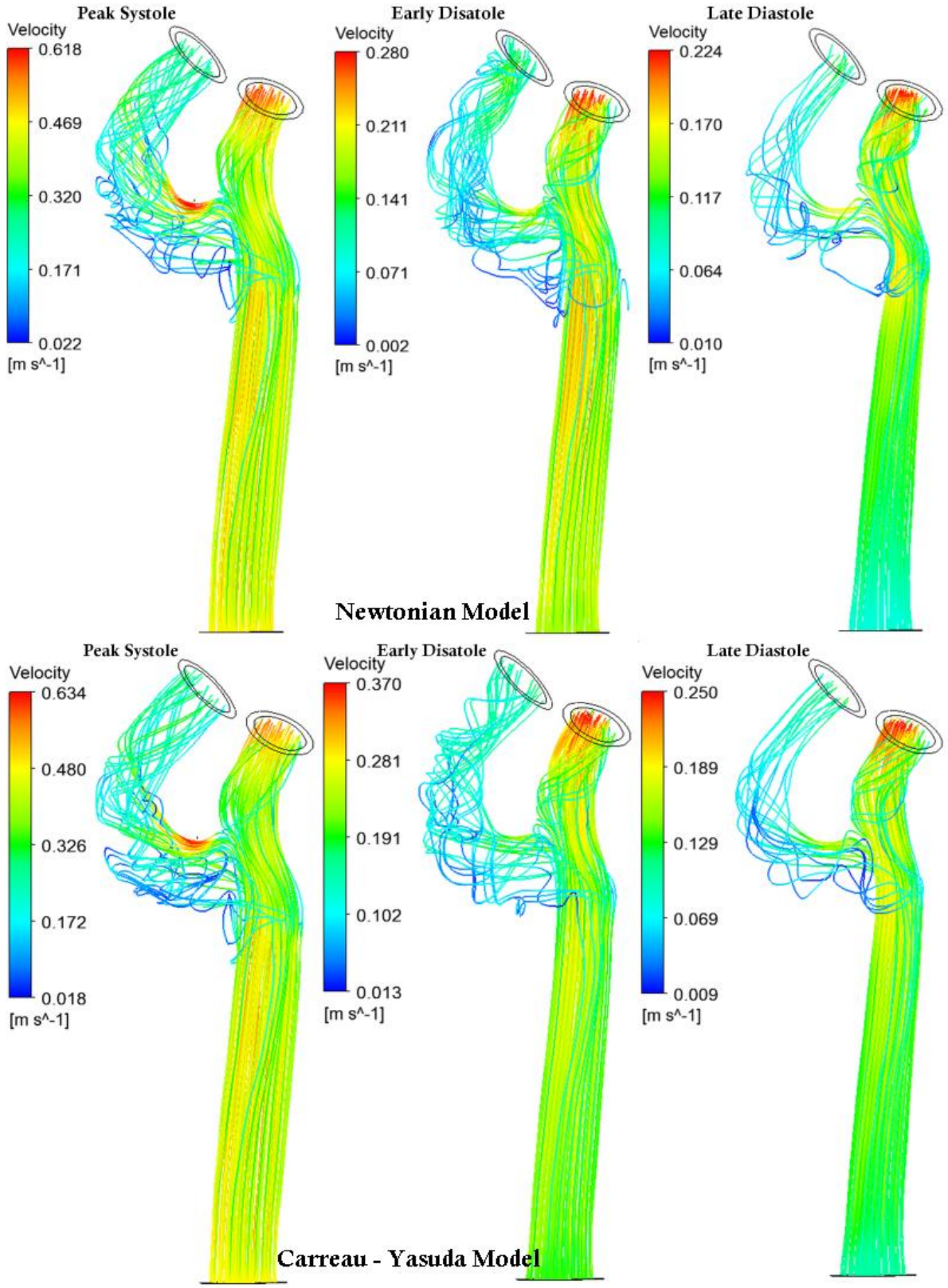

Figure 6-14: Velocity streamlines for stage 2 hypertension (HBP 3) condition considering Newtonian and Carreau - Yasuda model

Figure 6-15 shows the average velocity magnitude at different phases of the cardiac cycle considering different rheological model. With an increase in blood pressure, the magnitude of velocity is decreased, particularly at the peak systolic phase.

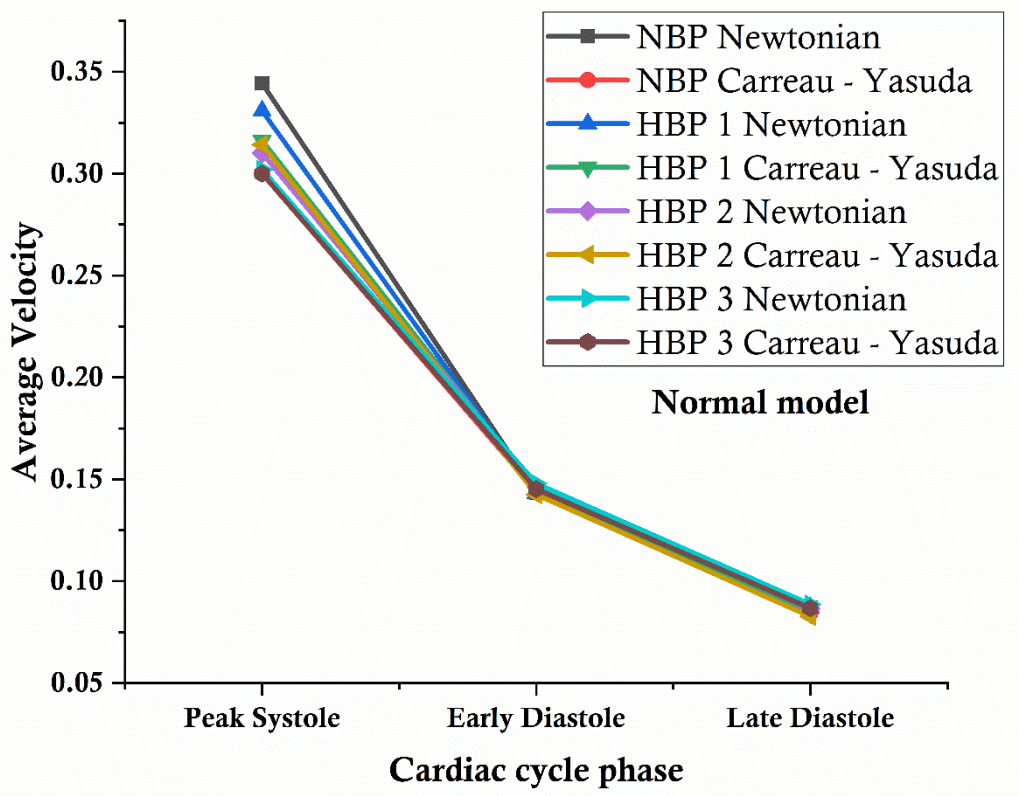

Figure 6-15: Average velocity magnitude in normal carotid artery at different phases of the cardiac cycle considering both Newtonian and Carreau – Yasuda model.

6.2.6 Wall Shear Stress

Wall shear stress is one of the most important haemodynamic parameter as it is directly related to arterial wall degeneration. *Figure 6-16 – Figure 6-19* show the WSS contours at the three phases of the cardiac cycle. In all the blood pressure cases, the Newtonian model significantly underestimates the WSS magnitude. *Figure 6-20* to *Figure 6-22* shows the bar chart highlighting the difference in WSS magnitude between the two viscosity models. The WSS magnitude is maximum for NBP and reduce with increase in blood pressure. At HBP

3, the lowest WSS magnitude was noted. In all cases, due to the high velocity gradient, the WSS was concentrated at the bifurcation point on the inner wall at the stagnation point. With the rise in blood pressure, the low WSS at the outer wall of the ICA at the bifurcation decreases, and compared to the Newtonian model, the Carreau-Yasuda model showed a difference of 38% average increase in WSS magnitude. The flow separation occurs at the base of the bifurcation near the carotid sinus at peak systole, and at late diastole lower WSS was along the outer wall of the ICA. At late diastole, where the flow recirculation was maximum, significantly lower WSS was observed. Because of elevated blood pressure, the drop in WSS was due to decreased flow rate and enlargement of the arterial wall.

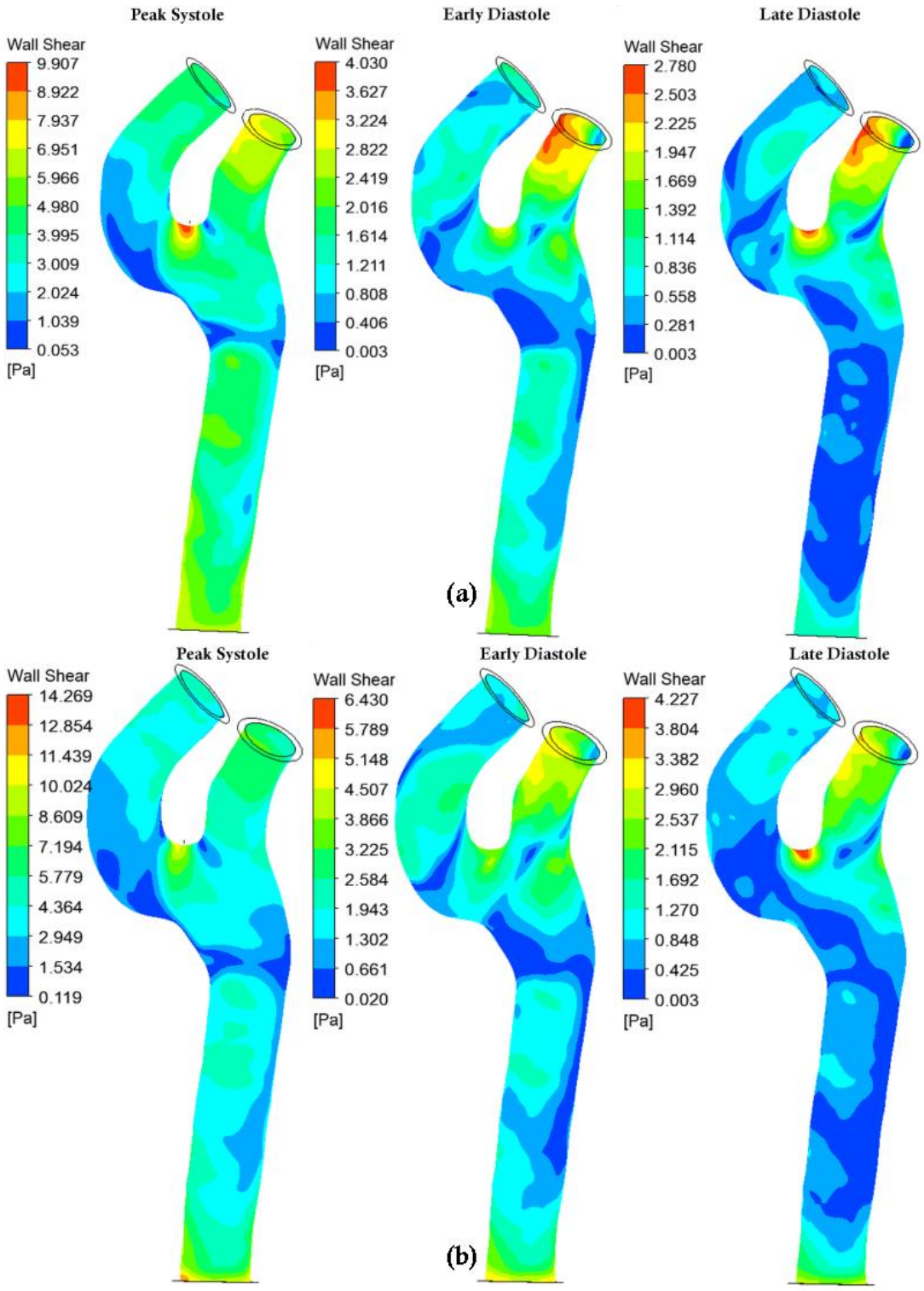

Figure 6-16: WSS contours for NBP (a) Newtonian model, (b) Carreau – Yasuda model.

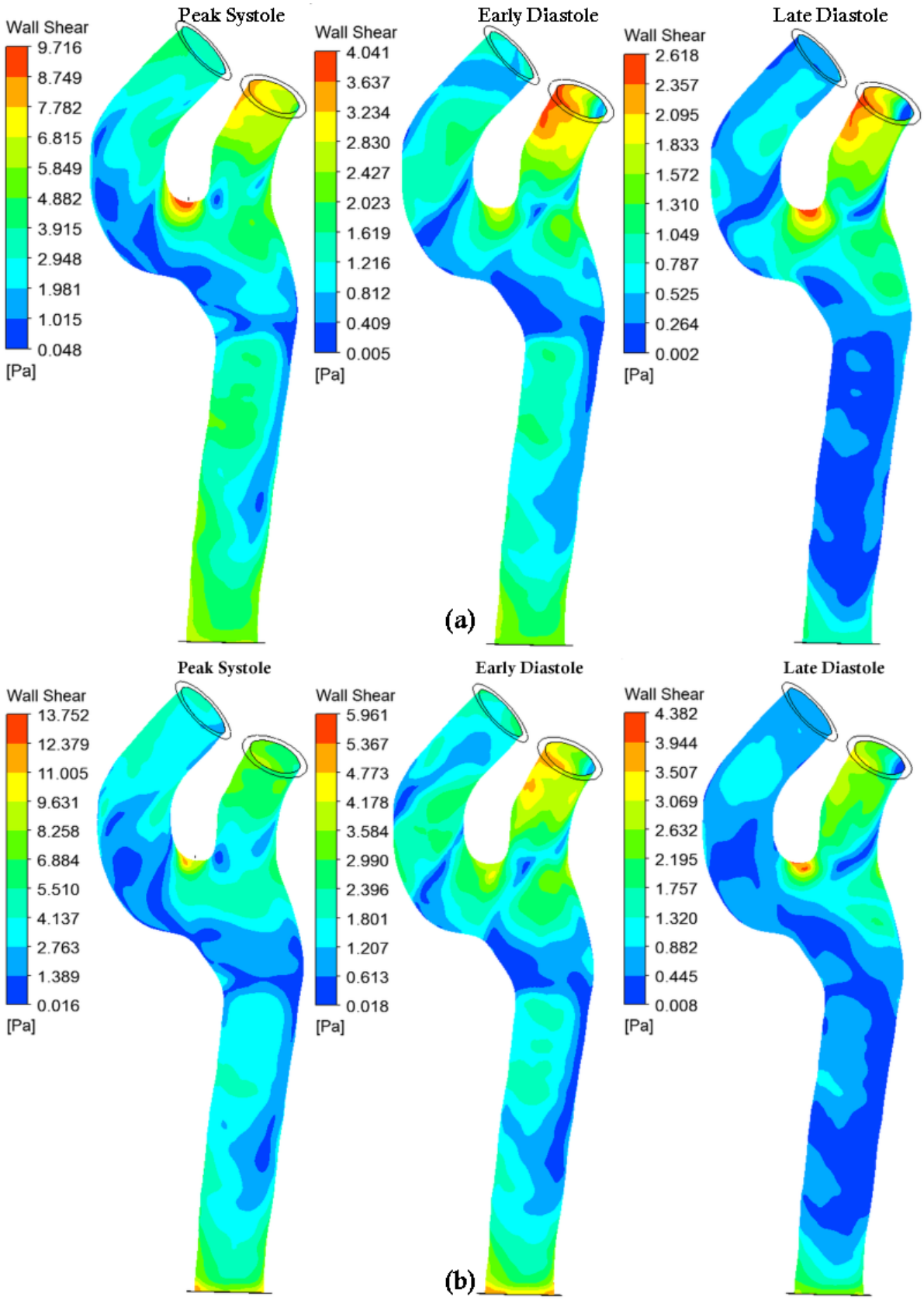

Figure 6-17: WSS contours for HBP 1 (a) Newtonian model, (b) Carreau – Yasuda model.

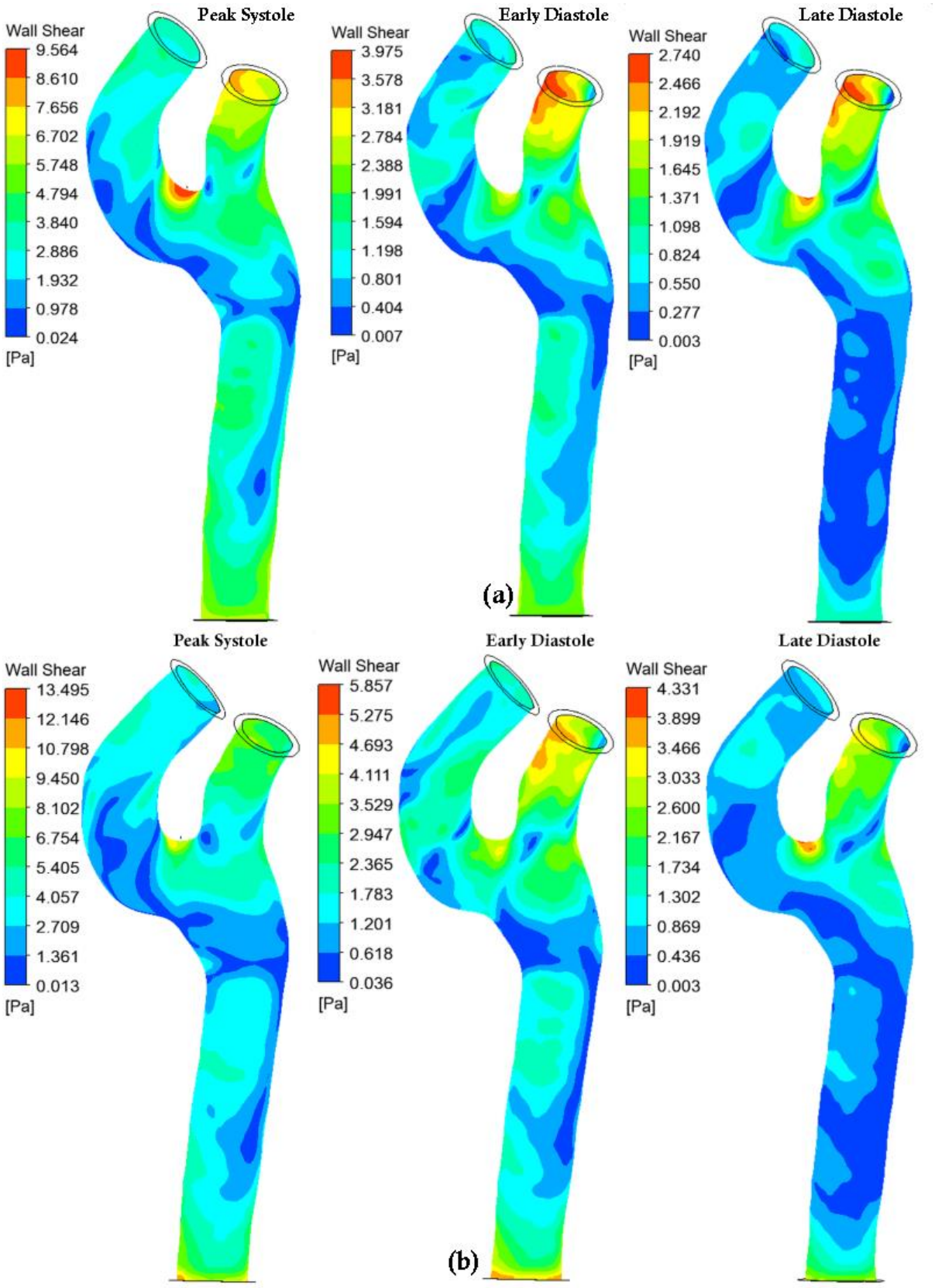

Figure 6-18: WSS contours for HBP 2 (a) Newtonian model, (b) Carreau – Yasuda model.

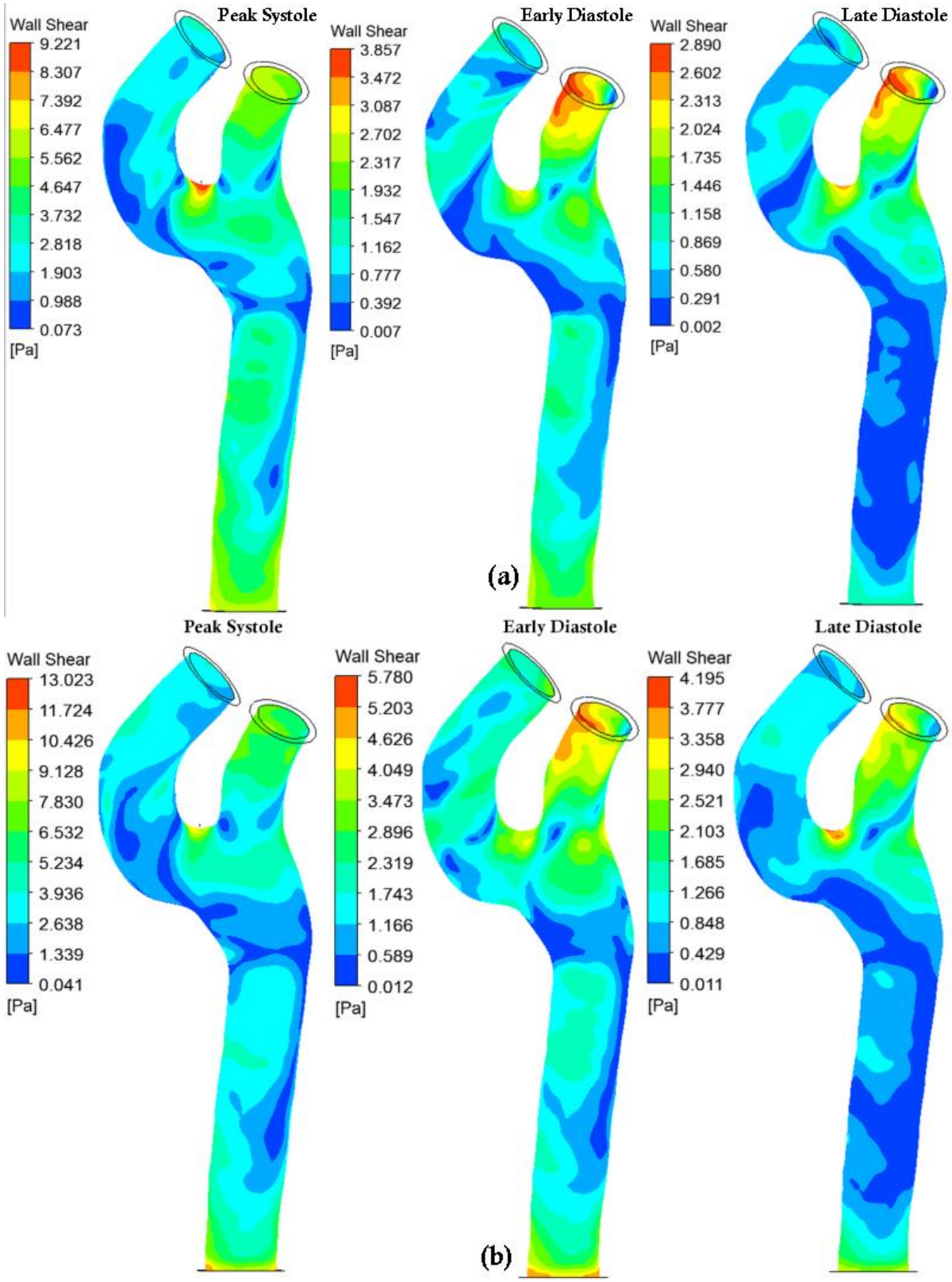

Figure 6-19:WSS contours for HBP 3 (a) Newtonian model, (b) Carreau – Yasuda model.

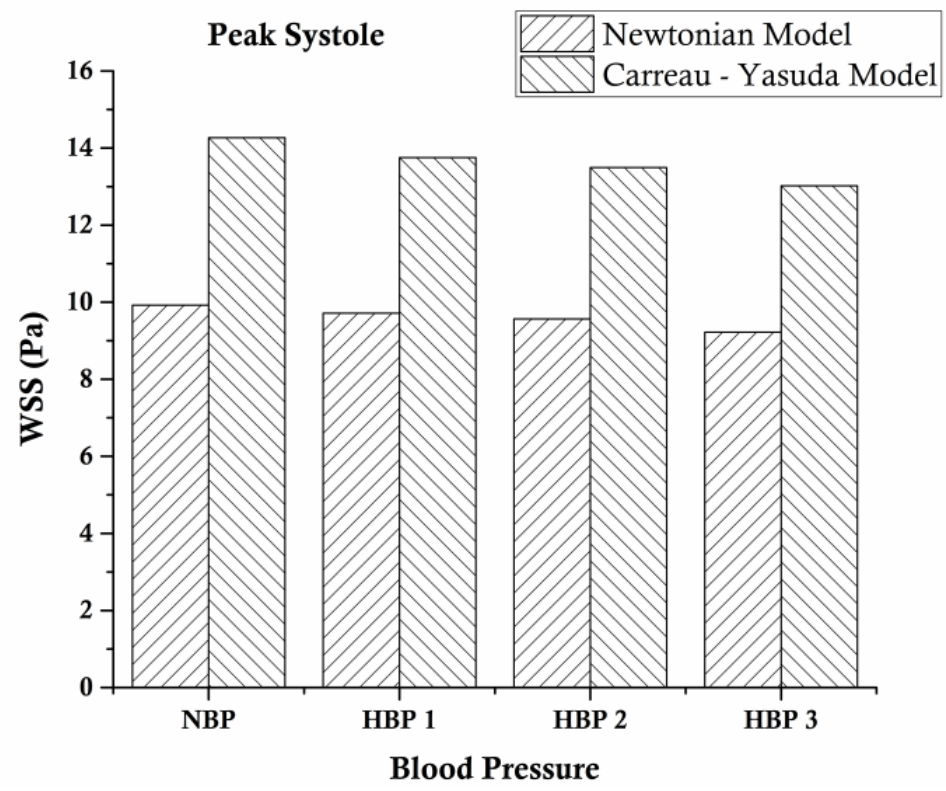

Figure 6-20: Bar chart showing WSS magnitude at peak systole

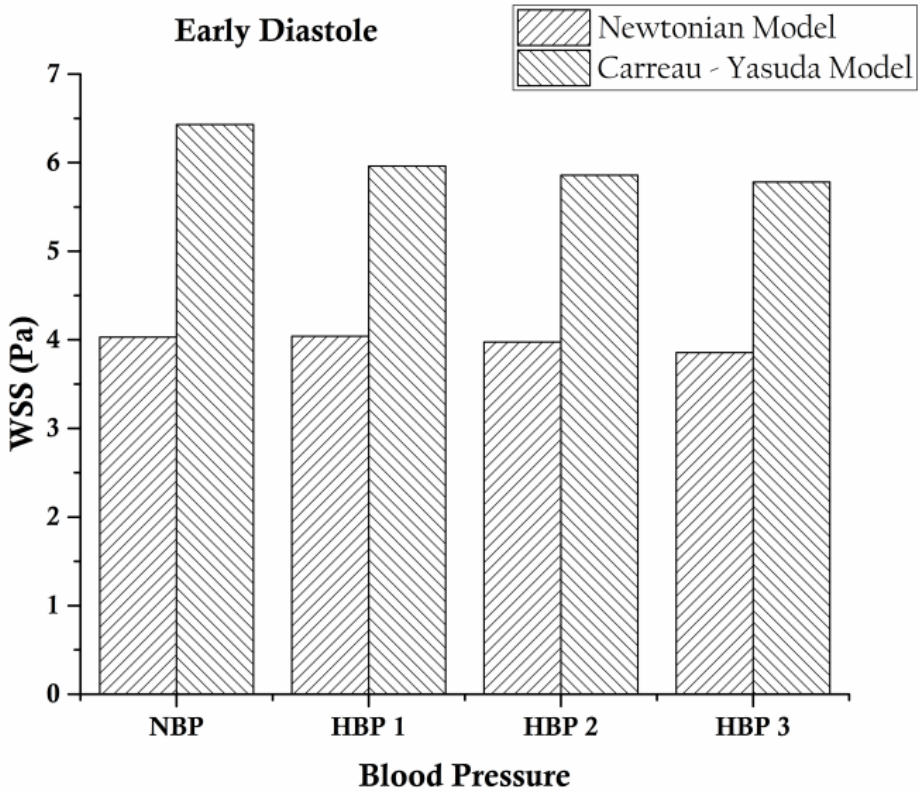

Figure 6-21: Bar chart showing WSS magnitude at Early diastole

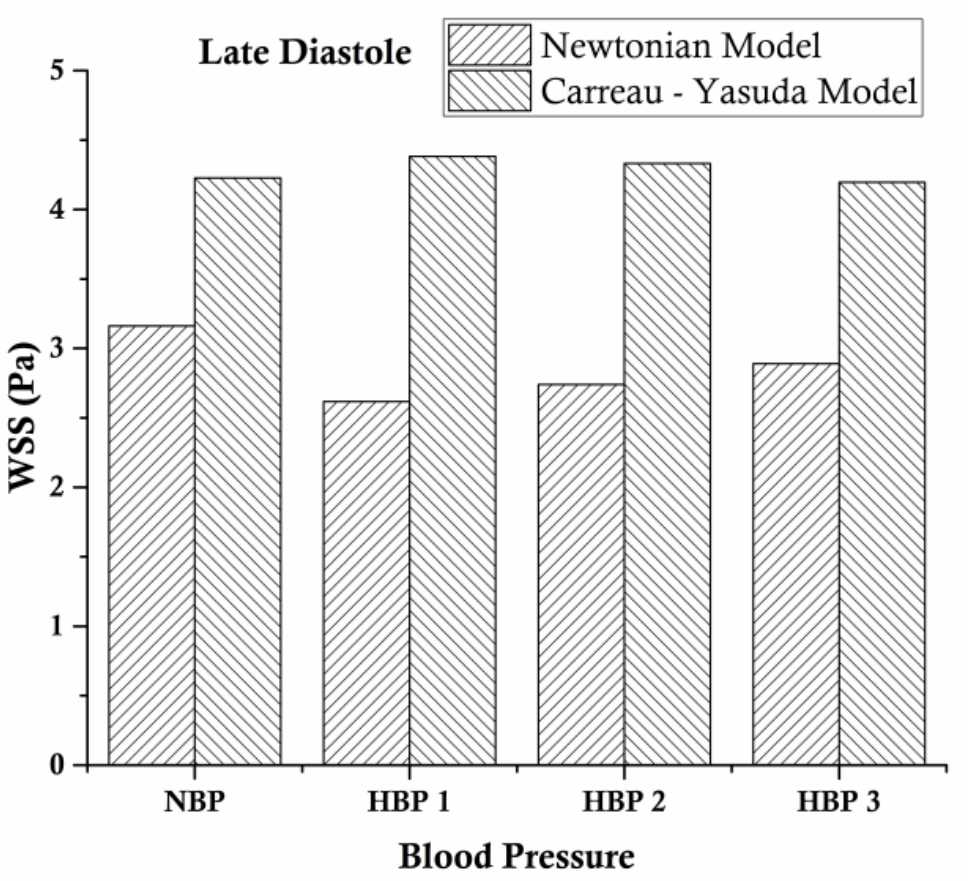

Figure 6-22: Bar chart showing WSS magnitude at late diastole

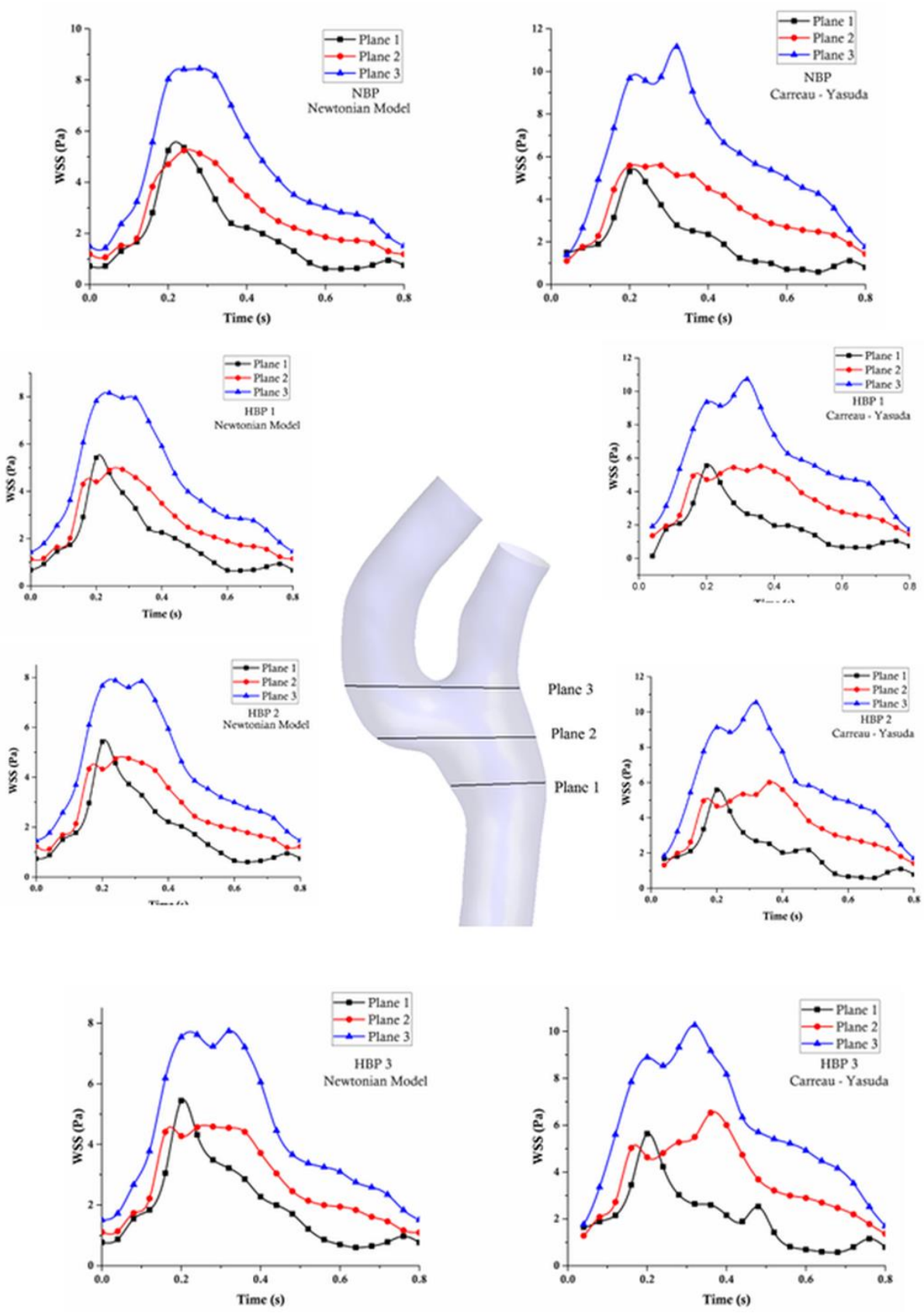

Figure 6-23: Temporal veriation of WSS magnitude at different planes.

6.2.7 Wall Deformation

Figure 6-24 to *Figure 6-27* shows the deformation of the arterial wall at different phases of the cardiac cycle for Newtonian and Carreau – Yasuda blood viscosity models. Here in the normal carotid artery, the deformation was maximum was at the bifurcation, mainly due to lower arterial stiffness caused by curvature. Generally, at the location where pressure is maximum, higher deformation is observed, especially at the apex of the bifurcation. The curvature of the bifurcation reduced the stiffness of the wall, and therefore, has high wall deformation [256].

The outer wall of the ICA, along with the bifurcation zone, was also subjected to moderate deformation. One of the potential causes of the development of atherosclerosis was low WSS along with greater wall deformation. There was no significant difference in the deformation magnitude between the viscosity models. Maximum deformation of 0.447 mm, 0.516 mm, 0.602 mm and 0.689 mm was observed at peak systole for NBP, HBP 1, HBP 2 and HBP 3 conditions respectively.

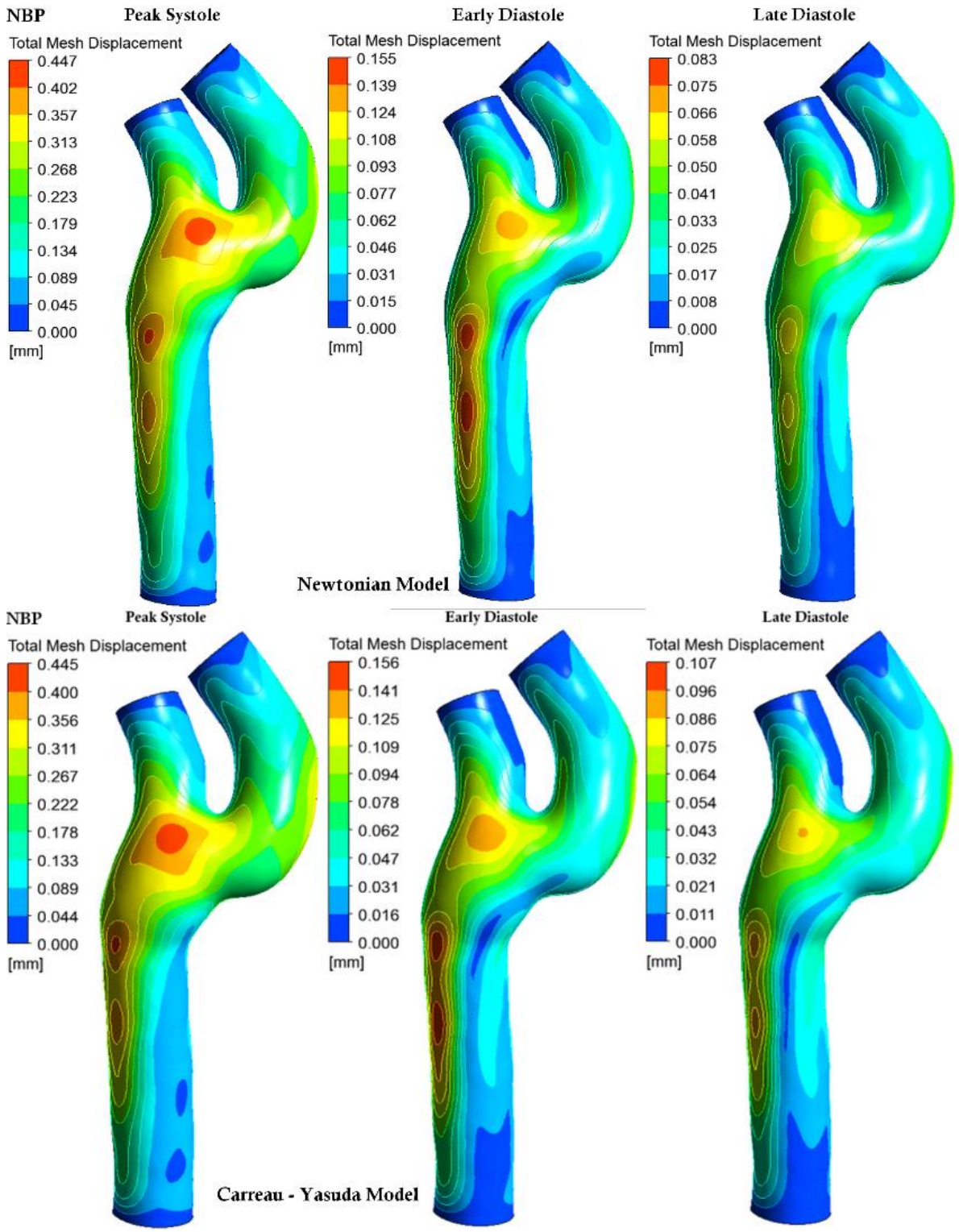

Figure 6-24: Arterial Wall deformation contours for NBP

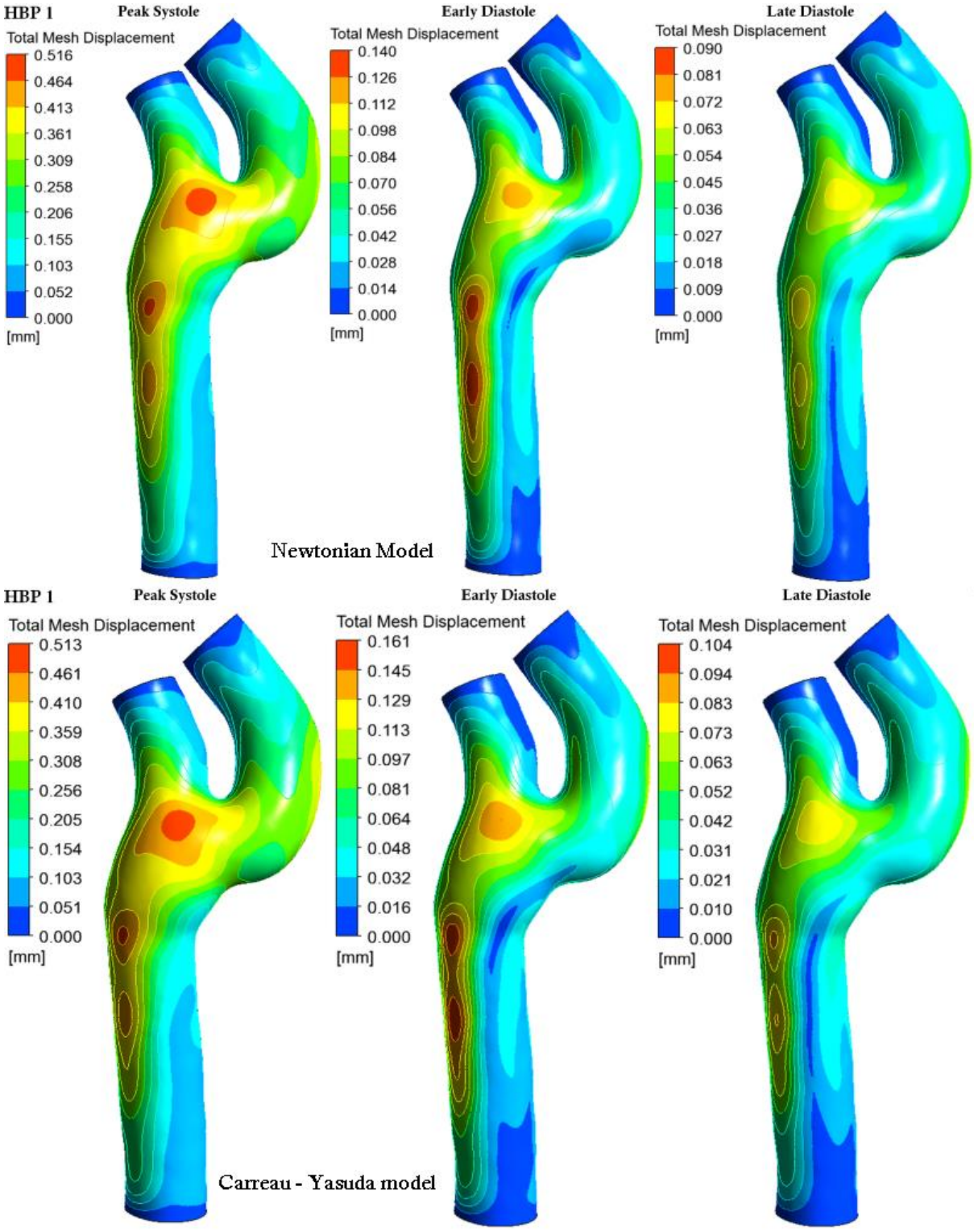

Figure 6-25: Wall deformation contours for HBP 1 condition.

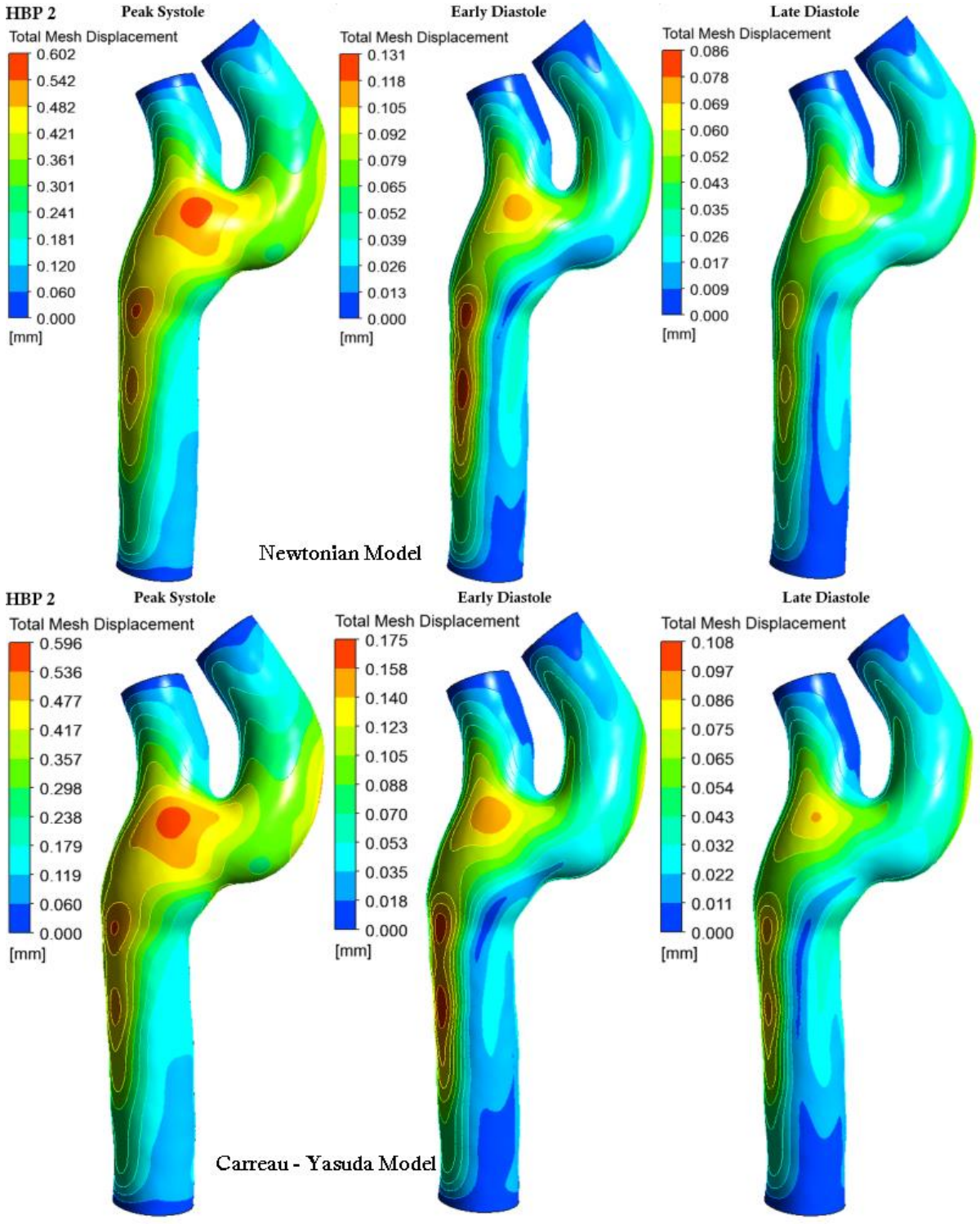

Figure 6-26: Wall deformation contours for HBP 1 condition.

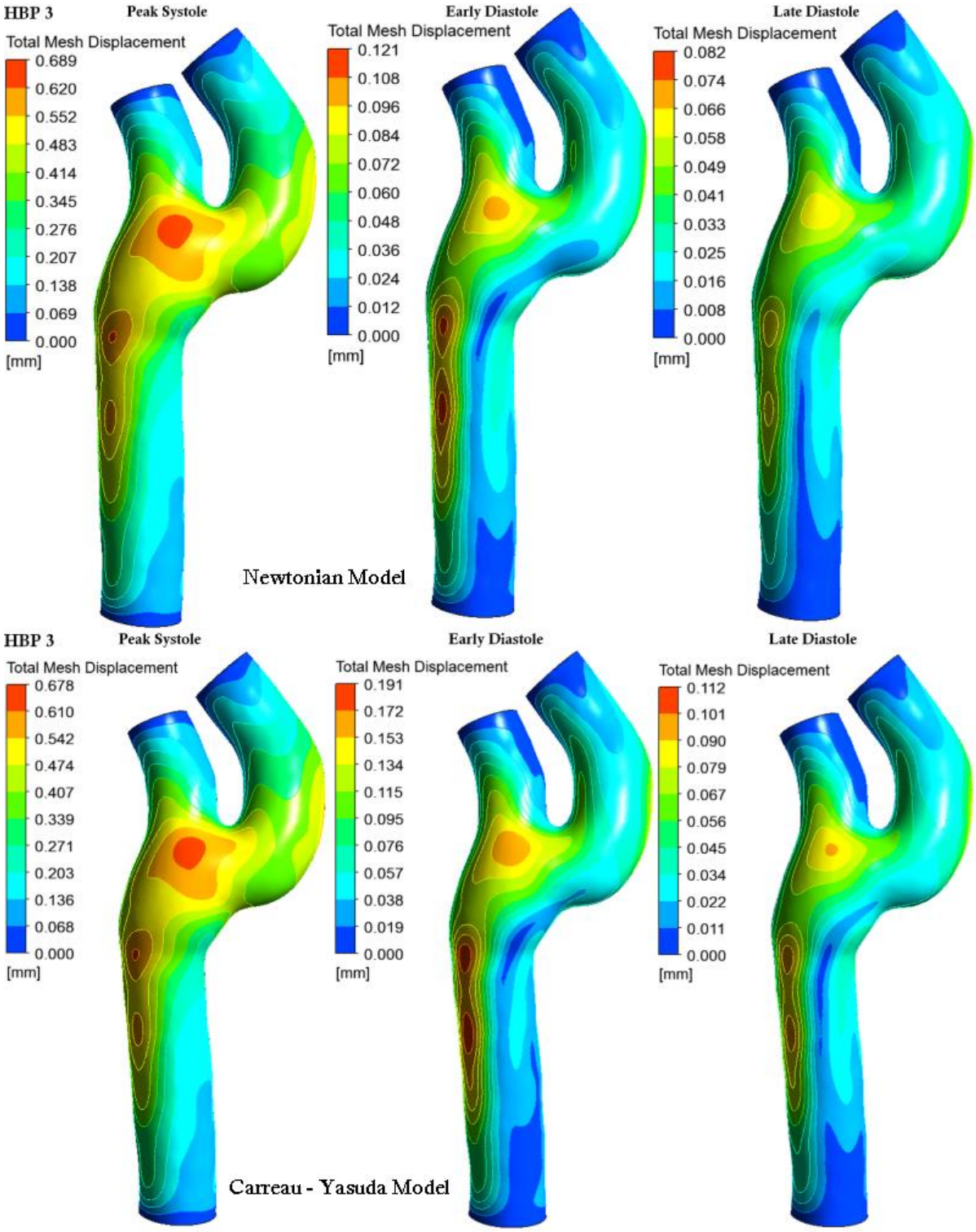

Figure 6-27: Wall deformation contours for HBP 3 condition.

6.2.8 Oscillatory Shear Index

The oscillatory shear index is a non-dimensional parameter used to evaluate the oscillatory behaviour of arterial flows. It gives the differences between average WSS and average WSS vector. Using these values, the OSI elucidates the WSS vector deflection from blood flow principal directions during cardiac cycle. Therefore, OSI is calculated as:

$$OSI = 0.5 \times \left(1 - \frac{\left|\int_0^T \overrightarrow{WSS} dt\right|}{\int_0^T |\overrightarrow{WSS}| dt}\right) \tag{6.1}$$

Where (0, T) is the time interval of the single cardiac cycle and $\overrightarrow{WSS}$ is the Wall shear stress defined as

$$WSS = -T_f n.\tau \tag{6.2}$$

Here T_f is the Cauchy stress tensor of the fluid $T_f = -pI + 2\mu(|D(\nabla u)|)D(\nabla u)$, n and τ are the unit outward normal and the unit tangential vector on the arterial wall Γ^w, respectively. OSI shows the time bound oscillations of the shear stress without taking into account the shear stress behaviour in an immediate neighbourhood of a specific point [257].

This parameter can be used to quantify the effect of oscillatory shears on the endothelial layer of the arterial wall. It elucidates the deflection of the WSS vector from the direction of blood flow during the cardiac cycle. It can vary from 0 for no cyclic variations to 0.5 for 180° deflection of the WSS [258].

Figure 6-28 shows the average OSI calculated over the wall for different blood pressure models considering both Newtonian and the Carreau – Yasuda model. The OSI does not vary with blood pressures or viscosity models. The average OSI is calculated at the wall

and is found to be 0.175, 0.180, 0.181 and 0.18 for NBP, HBP 1, HBP 2, and HBP 3 respectively for both viscosity models.

Figure 6-29 – *Figure 6-36* shows the OSI contours for different blood pressure conditions considering Newtonian and Carreau – Yasuda blood viscosity models. Emphasis was on OSI distribution during three phases of the cardiac cycle (Peak systole, early diastole and late diastole). It was evident from the figures that the OSI was maximum at the outer wall of the ICA near the carotid sinus, and at the base of the ECA which may be a likely location for development of plaque. The OSI distribution patterns were not significantly altered by varying the blood pressure and the viscosity models.

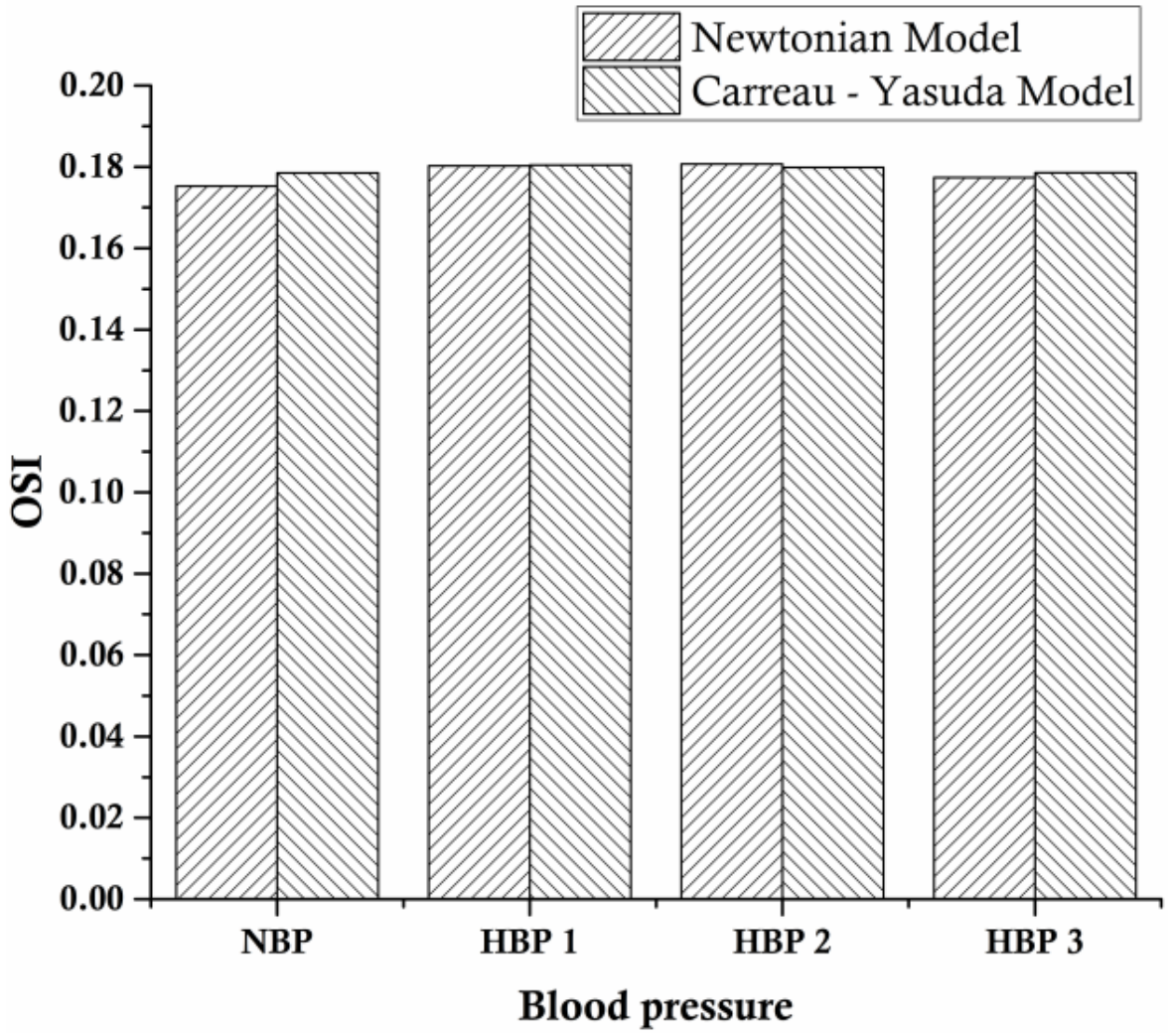

Figure 6-28: Average OSI for different blood pressure conditions for Newtonian and Carreau - Yasuda models

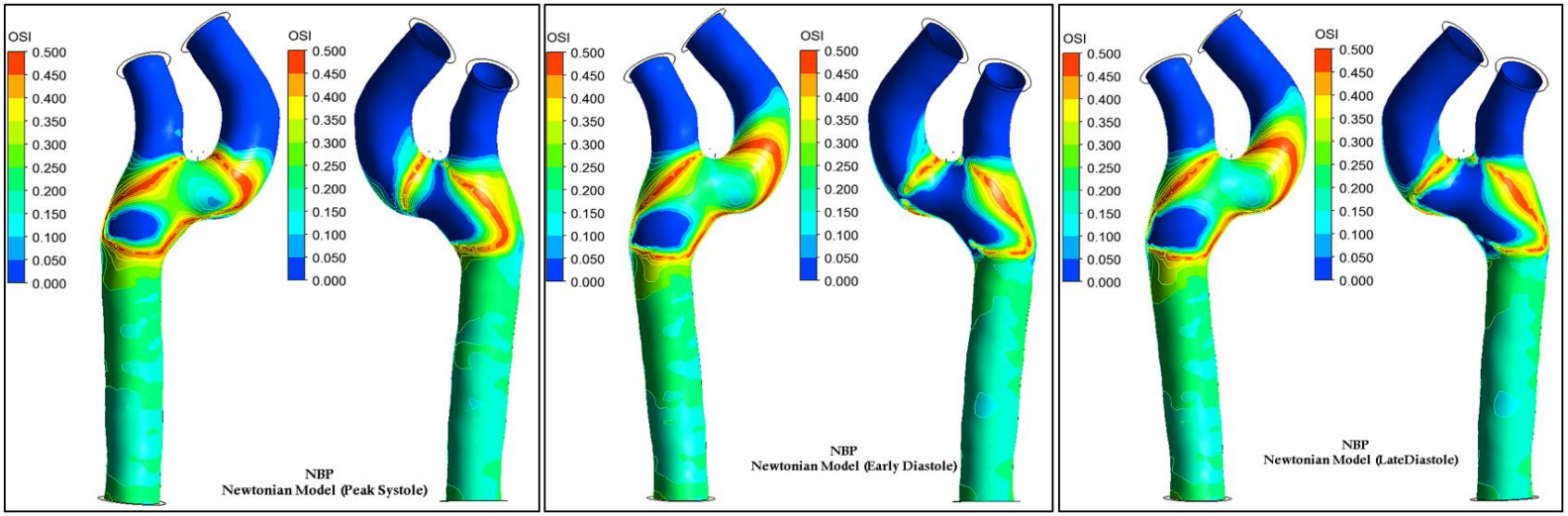

Figure 6-29: OSI contours for NBP considering Newtonian model

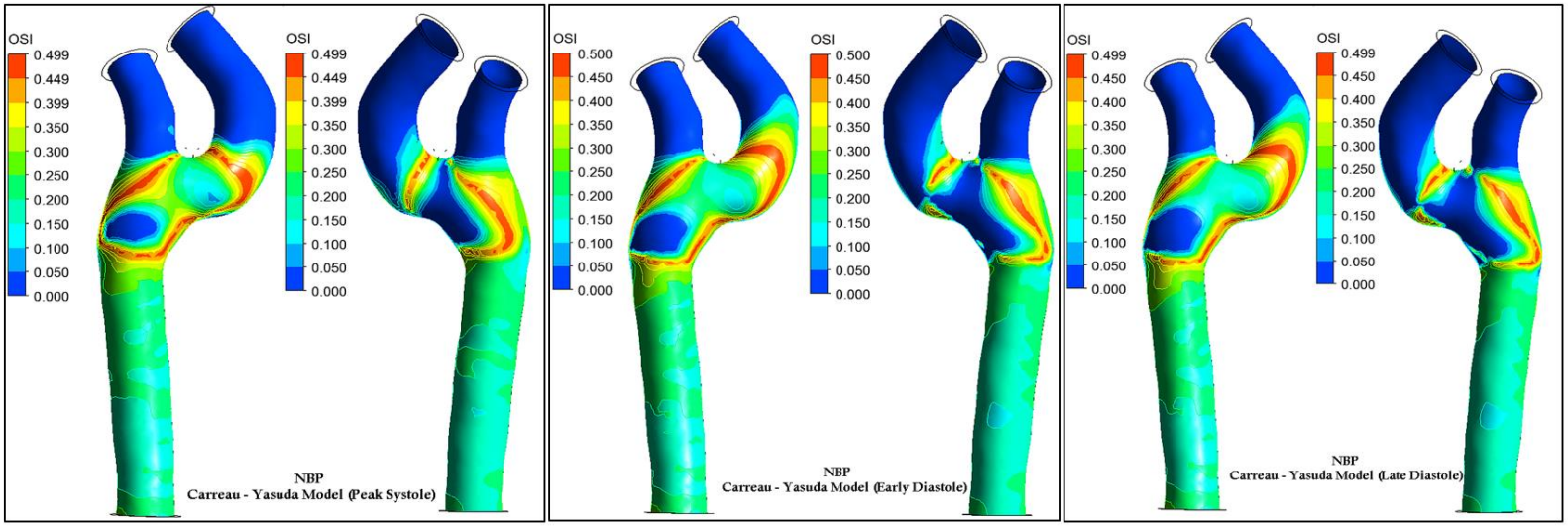

Figure 6-30: OSI contours for NBP considering Carreau – Yasuda model

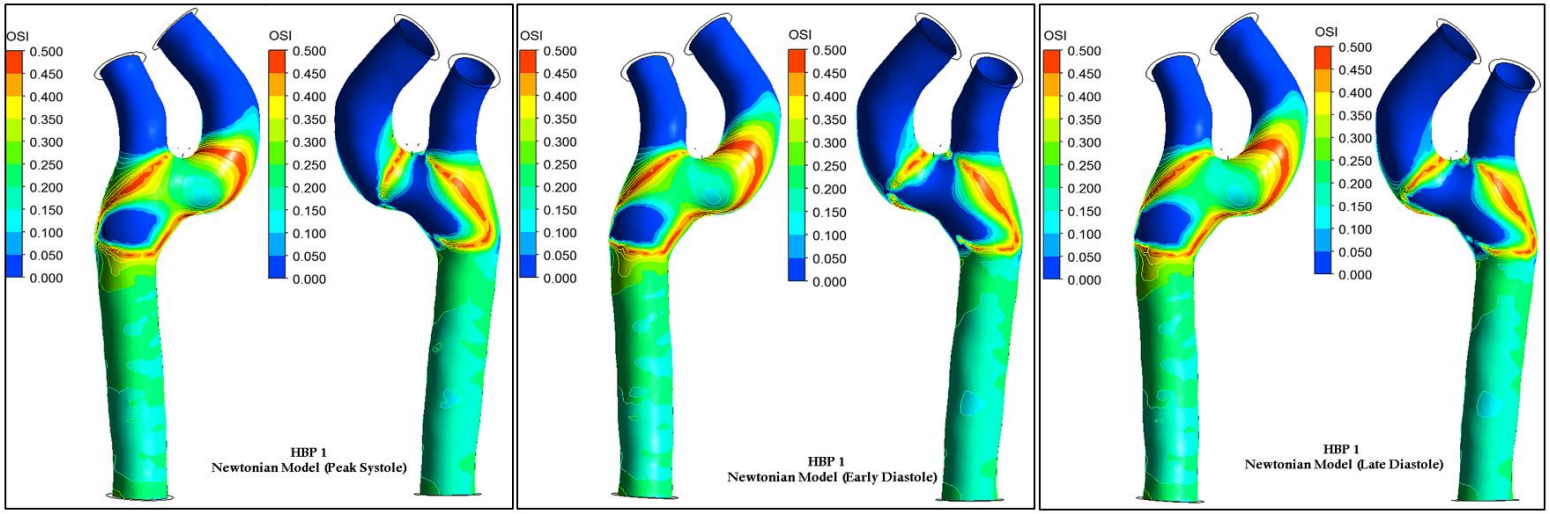

Figure 6-31: OSI contours for HBP 1 considering Newtonian model

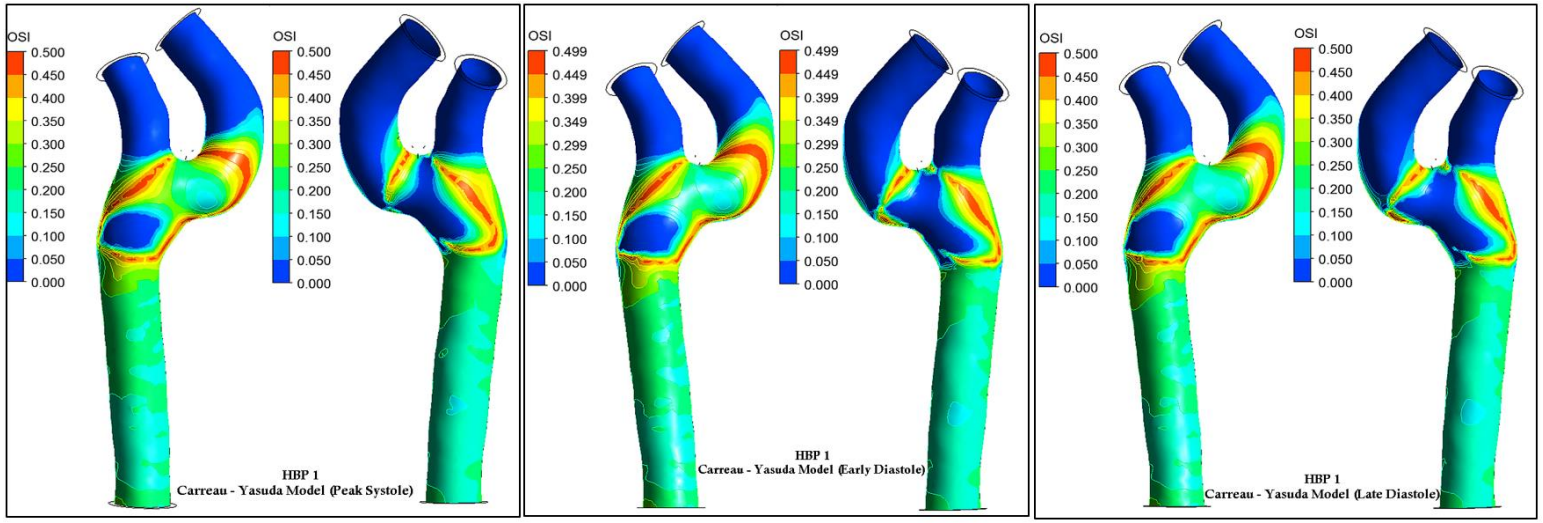

Figure 6-32: OSI contours for HBP 1 considering Careau – Yasuda model

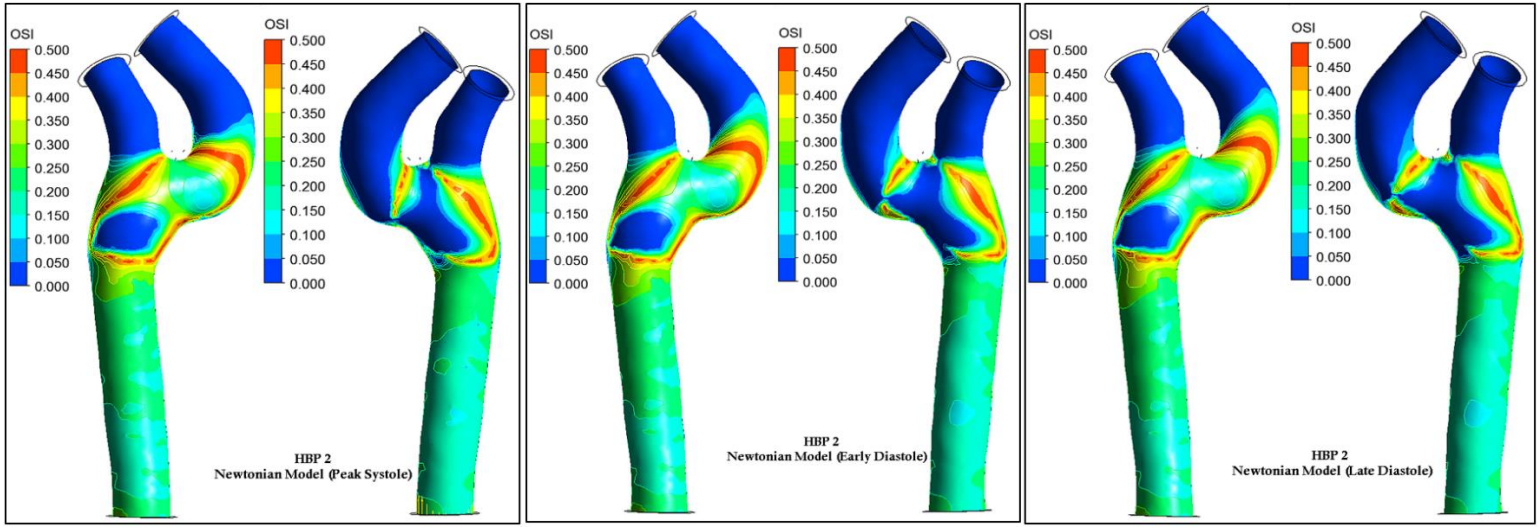

Figure 6-33: OSI contours for HBP 2 considering Newtonian model

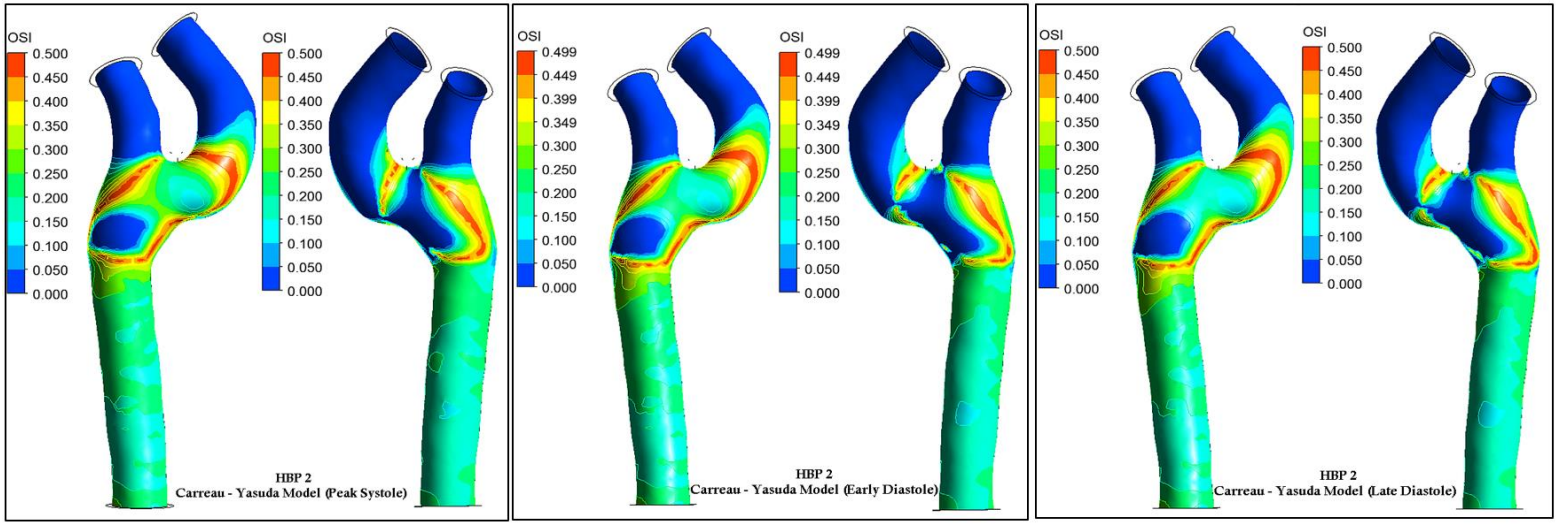

Figure 6-34: OSI contours for HBP 2 considering Carreau – Yasuda model

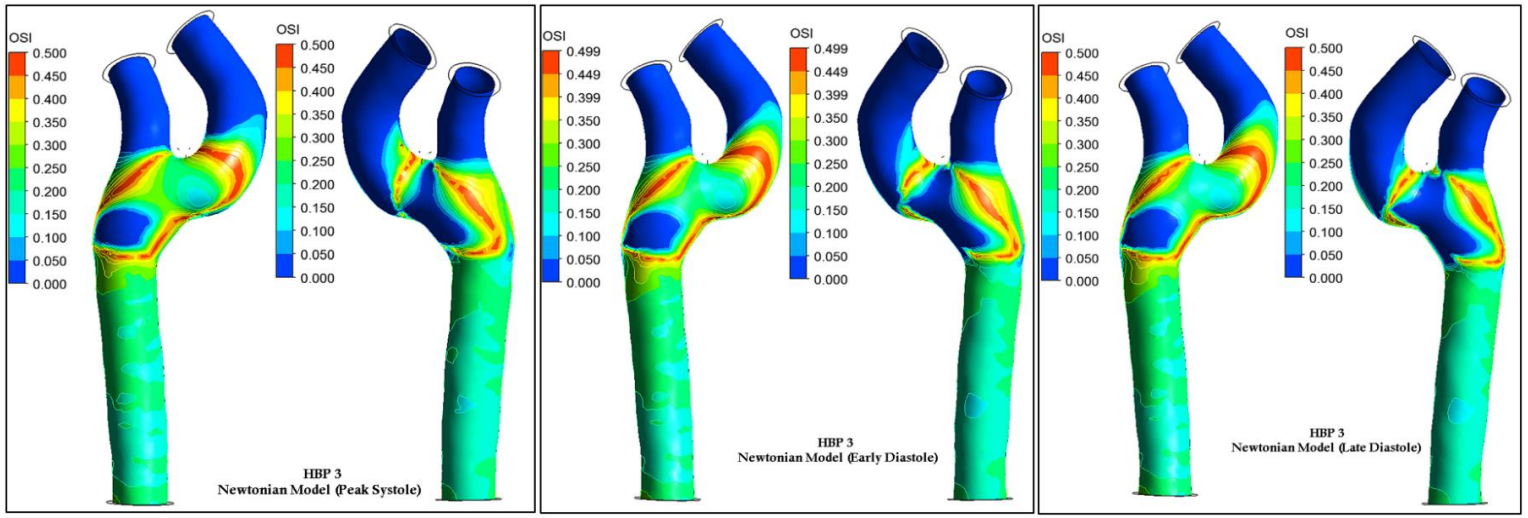

Figure 6-35: OSI contours for HBP 3 considering Newtonian model

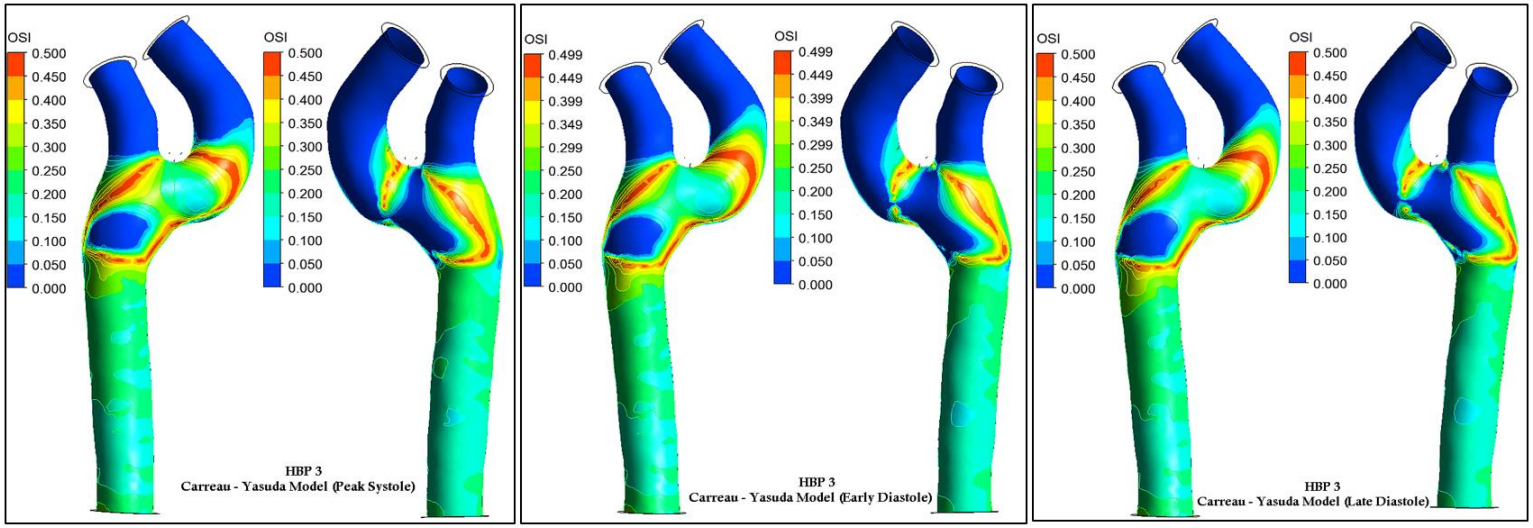

Figure 6-36: OSI contours for HBP 3 considering Carreau - Yasuda model

6.2.9 Helicity

Carotid artery haemodynamics is further elucidated by introducing helicity. Helicity is the property of a moving fluid representing the potential for helical flow to evolve (flow with a corkscrew-like pattern). Helicity is proportional to the strength and the amount of turning in the flow (i.e. vorticity) [259]. The harmful clinical significance of this hypotheses of the presence of helical flow in the umbilical portion of the portal vein have been elucidated by Sugimoto et al [260] who suggest that the dilation in the vessel and helical flow are characteristic signs indicating the proximal stenosis of the portal vein. In stenosed coronary arteries, helical patterns have also been observed at sites with increased vessel wall thickness [261]. The benificial role playes by the helical flow is also discussed in fluid dynamic studies in the aortic arch by Bogren et al [262] who observed the helical flow in normal subjects, while, Houston et al [263] found that the carotid atheromatous disease is associated with reduced systolic helical flow pattern in the aortic arch.

In three dimensional flows described by velocity vector field $V(s;t)$, The helicity H (t) of fluid flow is given as

$$H\ (s;t) = V(s;t) \cdot \omega(s;t) \tag{6.3}$$

Where V is the velocity and ω is the vorticity field of the flow.

Equation 6.4 states that, in flows with a rotational velocity field, helicity is maximum when velocity V and ω vectors lie in same direction, and helicity is null when velocity and vorticity vectors lie in orthogonal directions ($V.\omega = 0$).

Figure 6-37 and *Figure 6-38* shows helical flow regions captured at peak systolic phase of the cardiac cycle, mapped with vorticity vectors and OSI contour bands, by considering blood as Newtonian and Carreau – Yauda model respectively.

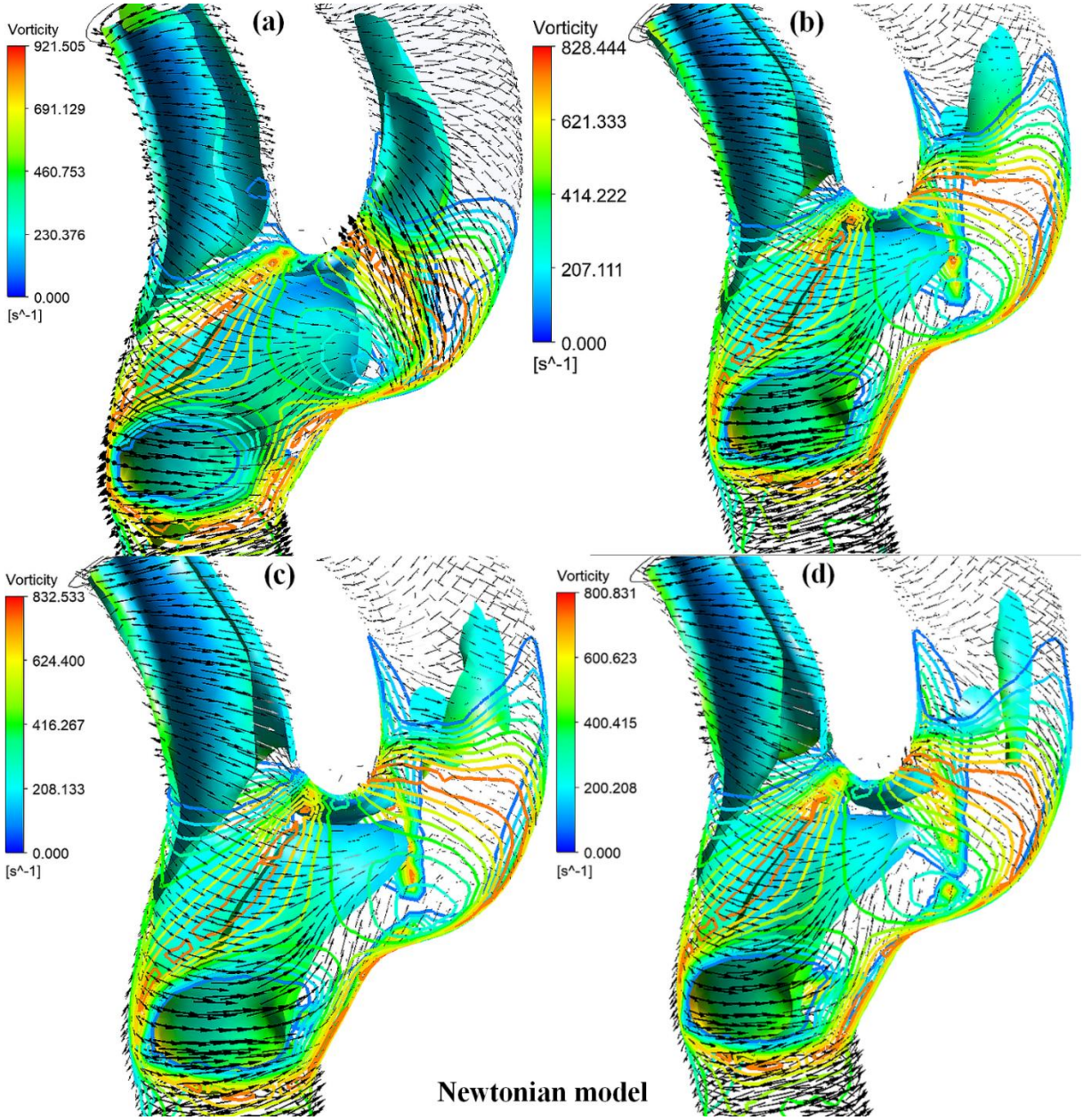

Figure 6-37: Voriticy vectors (black arrows) and iso – surface representing Helicty mapped with OSI bands in normal carotid artery model considering Newtonian model (a) NBP, (b) HBP 1, (c) HBP 2, and (c) HBP 3.

Due to rapid change in the direction of flow at the bifurcation, a vortex area was present at the outer wall of the ICA. Helicity mapped with vorticity vectors and OSI bands shows higher flow recirculation is observed where OSI is higher with low flow strength, which is higher at the inner wall of the ICA. Sicne the ECA is inline with the CCA, the helical strength is low as observed in the velocity streamlines. Although there is no qualitative

differences between the rheological models, the vorticity magnitude is higher in Carreau – Yasuda model compared to Newtonian model.

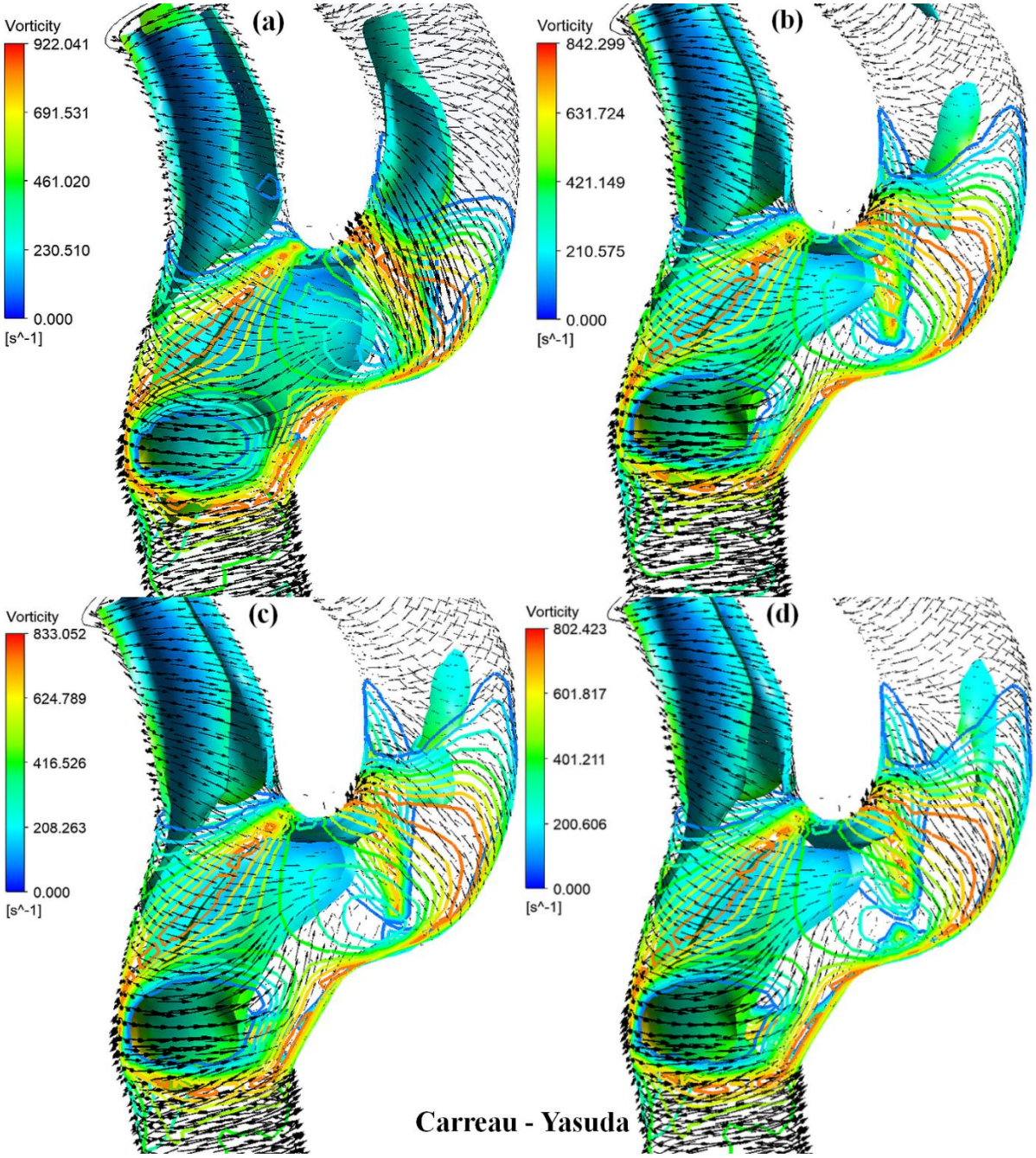

Figure 6-38: Voriticy vectors (black arrows) and iso – surface representing Helicty mapped with OSI bands in normal carotid artery model considering Carreau - Yasuda model (a) NBP, (b) HBP 1, (c) HBP 2, and (c) HBP 3.

Figure 6-39 shows temporal variation of average helicty in the flow domain of normal carotid artery model. The helicty strength is predominant in systolic phase of the cardiac cycle and reduces with increase in blood pressure. The helicty strength is reduced with

increased blood pressure indicating that the region of low WSS increases with blood pressure.

Figure 6-39

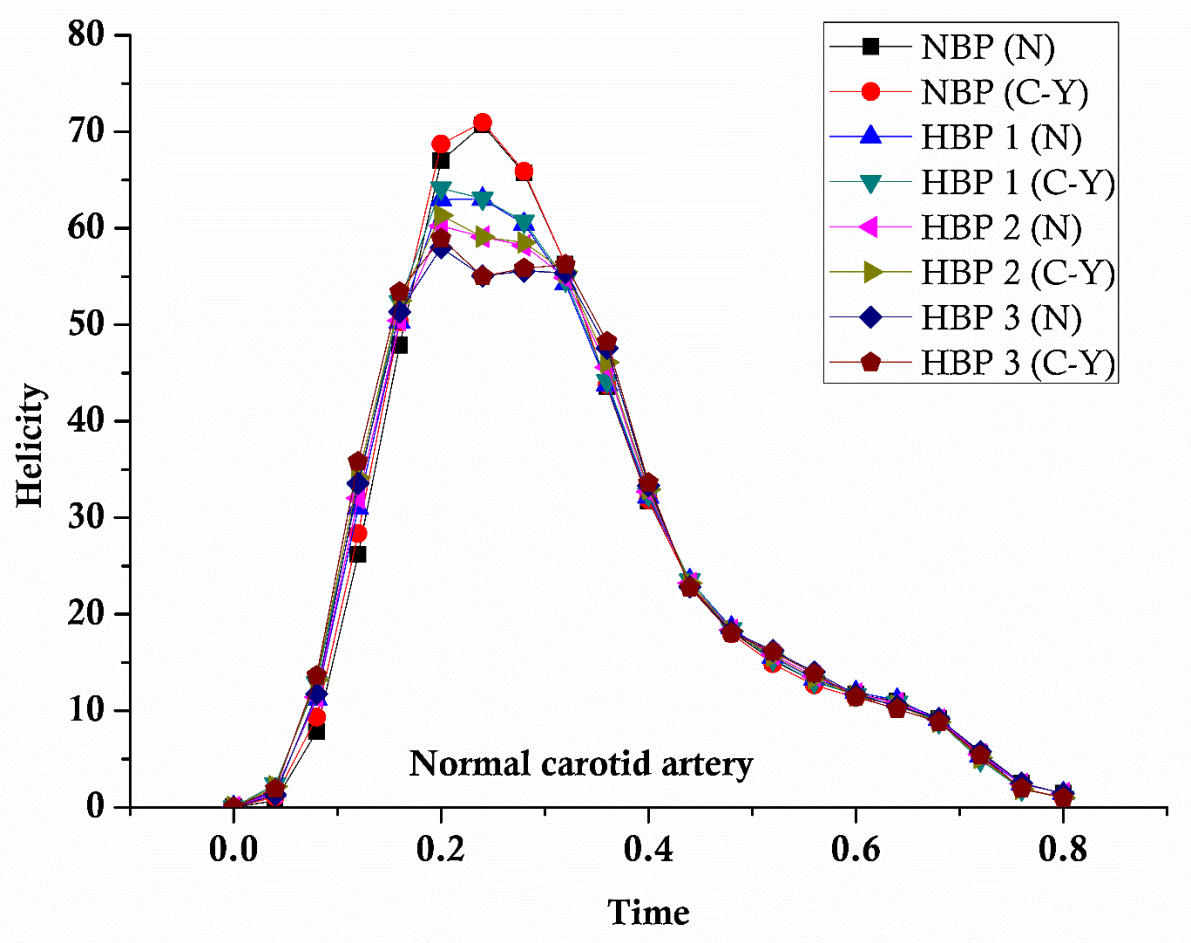

Figure 6-39: Temporal average helicity magnitude in normal carotid artery

Table 6-1 compares the average helicity magnitude at peak systole for different blood pressure conditions in normal carotid artery. The magnitude of helicity decreases with increased blood p127ressure indicating higher flow recirculation.

Table 6-1: Helicity (m/s^2) at peak systolic phase in normal carotid artery model

BP	Newtonian	Carreau – Yasuda
NBP	66.96	68.72
HBP 1	61.72	62.19
HBP 2	58.64	58.79
HBP 3	55.3	55.42

6.3 Fluid structure interaction analysis on Stenosed carotid artery subjected to different blood pressures

6.3.1 Case description

In this case, a stenosed carotid bifurcation model of a 60-year-old male, who had suffered multiple strokes was used. Here, a partial narrowing at the origin of the ECA was observed as shown in *Figure 6-40* with a normal ICA and CCA, with a 50% narrowing is diagnosed at the ECA root. The detailed methodology of model generation, meshing and applied boundary condition was described in section 6.2.1. *Figure 6-40* shows the meshed solid and fluid models used in the present study and the applied boundary conditions.

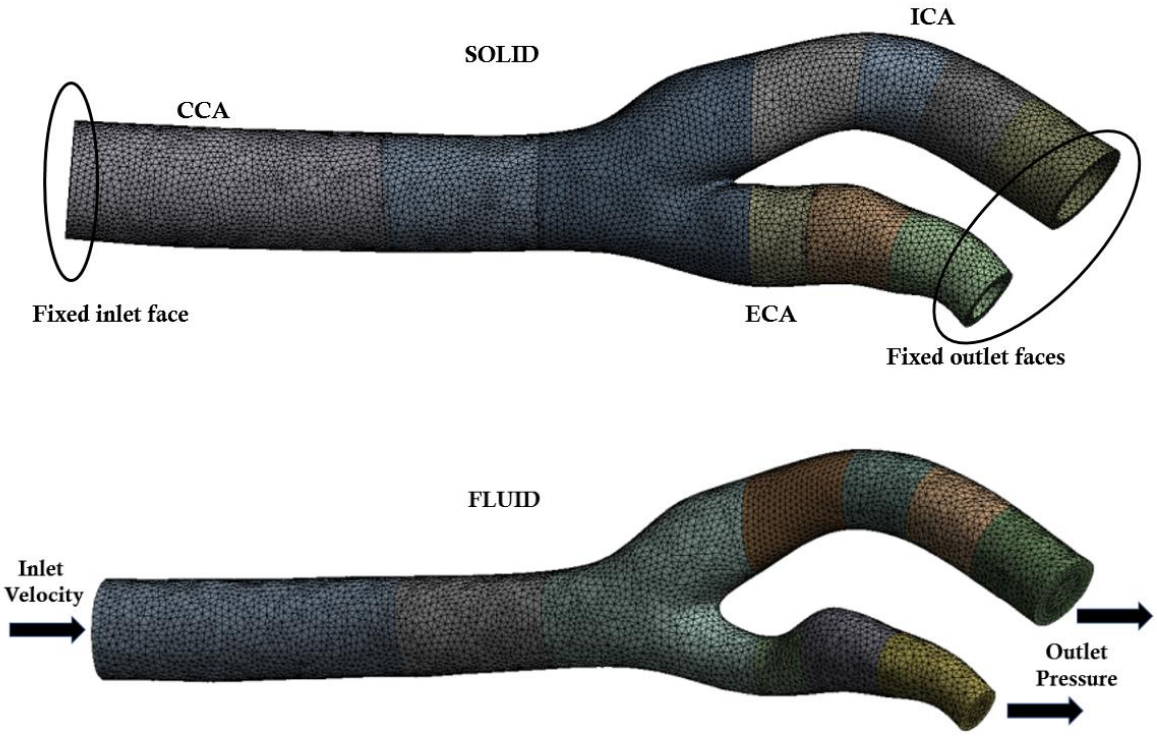

Figure 6-40: Meshed solid and fluid model with boundary condition details

6.3.2 Results and Discussion

In this section stenosed carotid artery was subjected to different blood pressures and analysis was performed by considering Newtonian and Carreau – Yasuda models. Hemodynamic parameters such as velocity, WSS, deformation and OSI was captured and compared. The difference in the hemodynamic parameter compared to normal artery was enumerated.

6.3.3 Grid independence

Grid independence study was carried out to determine optimum mesh size for the simulation. *Figure 6-41* shows the variation of average deformation, WSS and average velocity for different grid sizes. An optimum mesh size of 205938 and 215208 elements for structure and fluid respectively was chosen in the study.

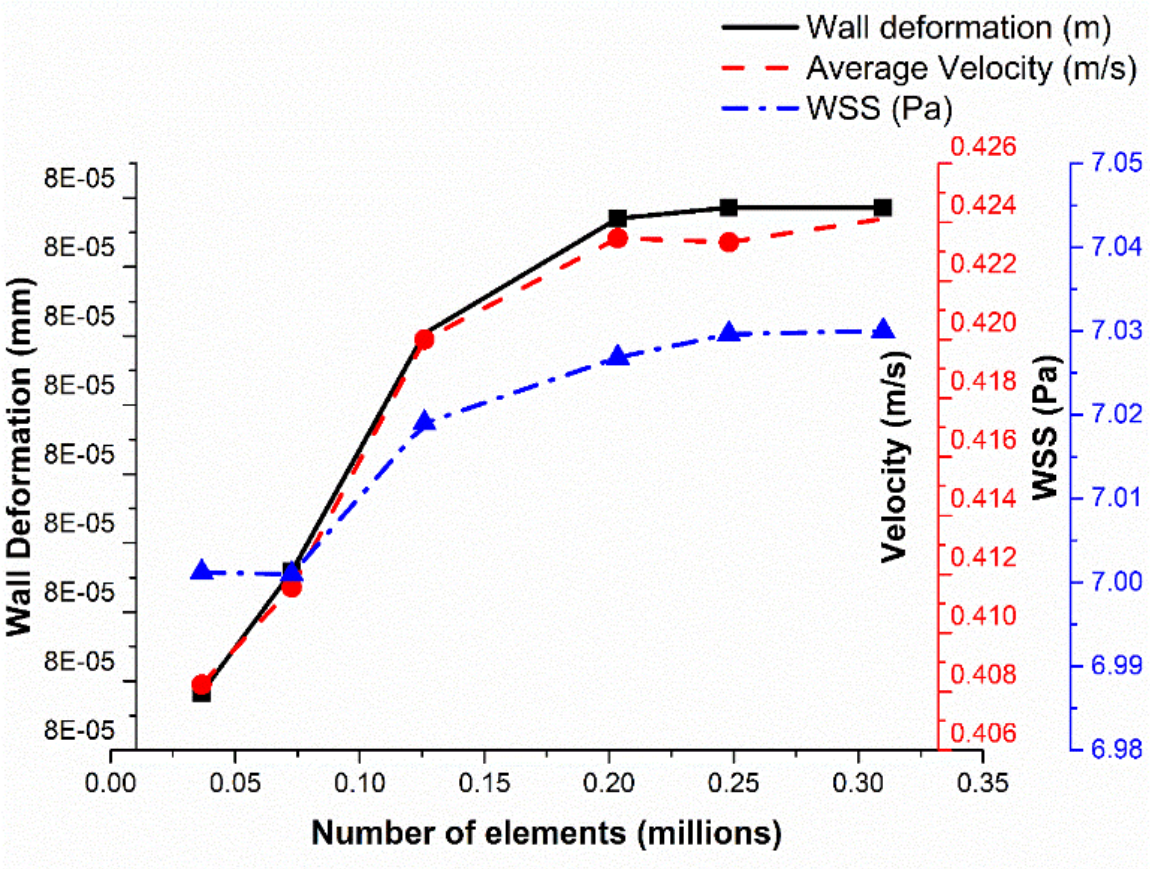

Figure 6-41: Grid independence plot for stenosed carotid artery model

6.3.4 Time step sensitivity test

Similar to normal model, Optimum timestep for FSI analysis was chosen based on time – step sensitivity test. Analysis was performed for 25, 50, 100 and 200 time steps with a step size of 0.032 s, 0.16 s, 0.008 s and 0.004 s. Test was performed for NBP and outlet boundary condition and prescribed inlet velocity as shown in *Figure 6-42* is applied. Average velocity in the fluid domain and average WSS in the wall was plotted against different time steps. Based on the above study, an optimum time step of 100 with a step size of 0.008 s was chosen in this study.

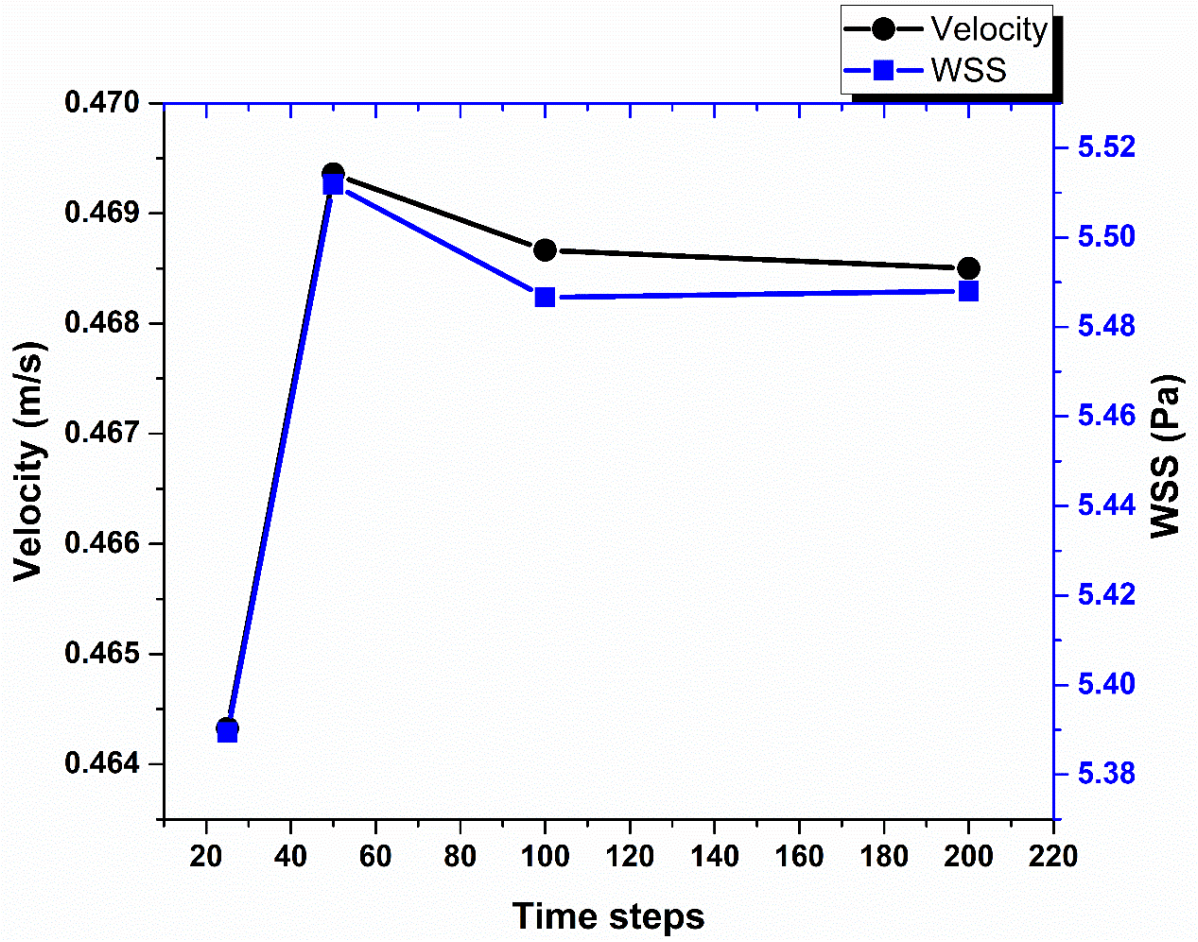

Figure 6-42: Time step sensitivity test for stenosed carotid artery model

6.3.5 Velocity

Figure 6-43 shows the variation of average velocity magnitude at different phases of the cardiac cycle considering both rheological models. The velocity was highest at NBP and gradually reduced with increase in the blood pressure due to the resistance offered at the outlets.

Figure 6-44 – Figure 6-47 shows the velocity streamlines for all the BP cases at different phases of the cardiac cycle. Except for small flow recirculation areas at the carotid sinus and post stenotic region in ECA, the flow was mostly uniform at peak systole, which is more prominent with the increase in blood pressure. The flow, however, turns chaotic post stenosis and the carotid sinus at the diastolic phase. In addition, the stenosis causes abrupt flow disruption in the downstream of the narrowed ECA, causing complex vortex formation. With an increase in blood pressure at peak systole, the amplitude of the velocity had decreased and it continued to increase at late diastole at the ICA. The flow recirculation area at late diastole was increased with higher blood pressure.

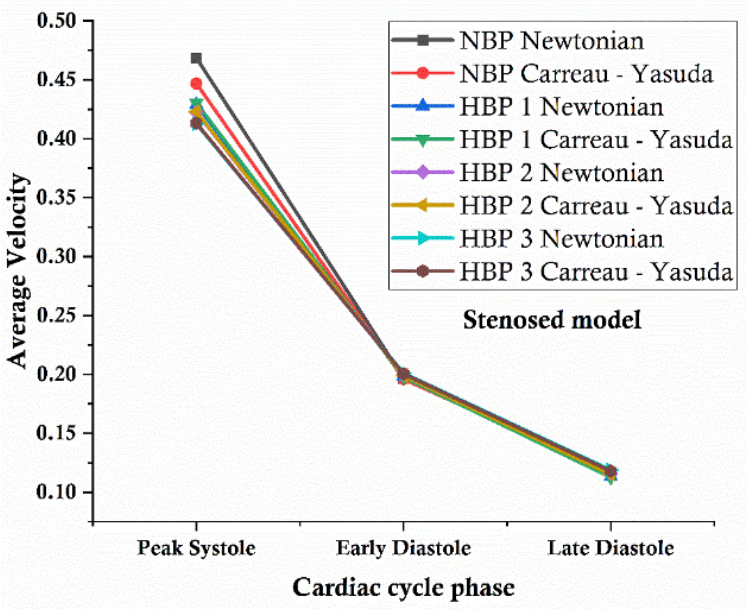

Figure 6-43: Average velocity magnitude in stenosed carotid artery at different phases of the cardiac cycle considering both Newtonian and Carreau – Yasuda model.

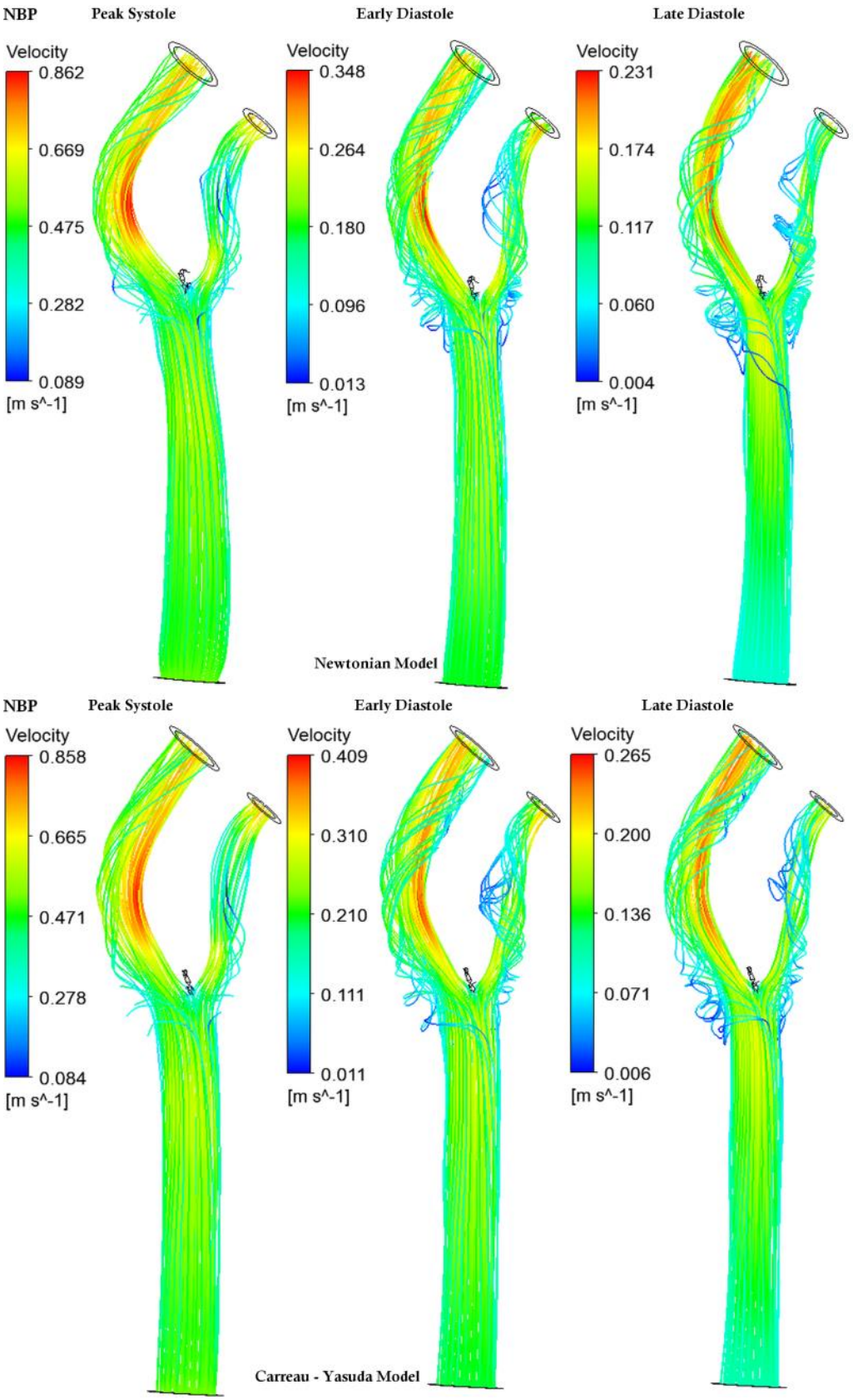

Figure 6-44: Velocity Streamlines for NBP

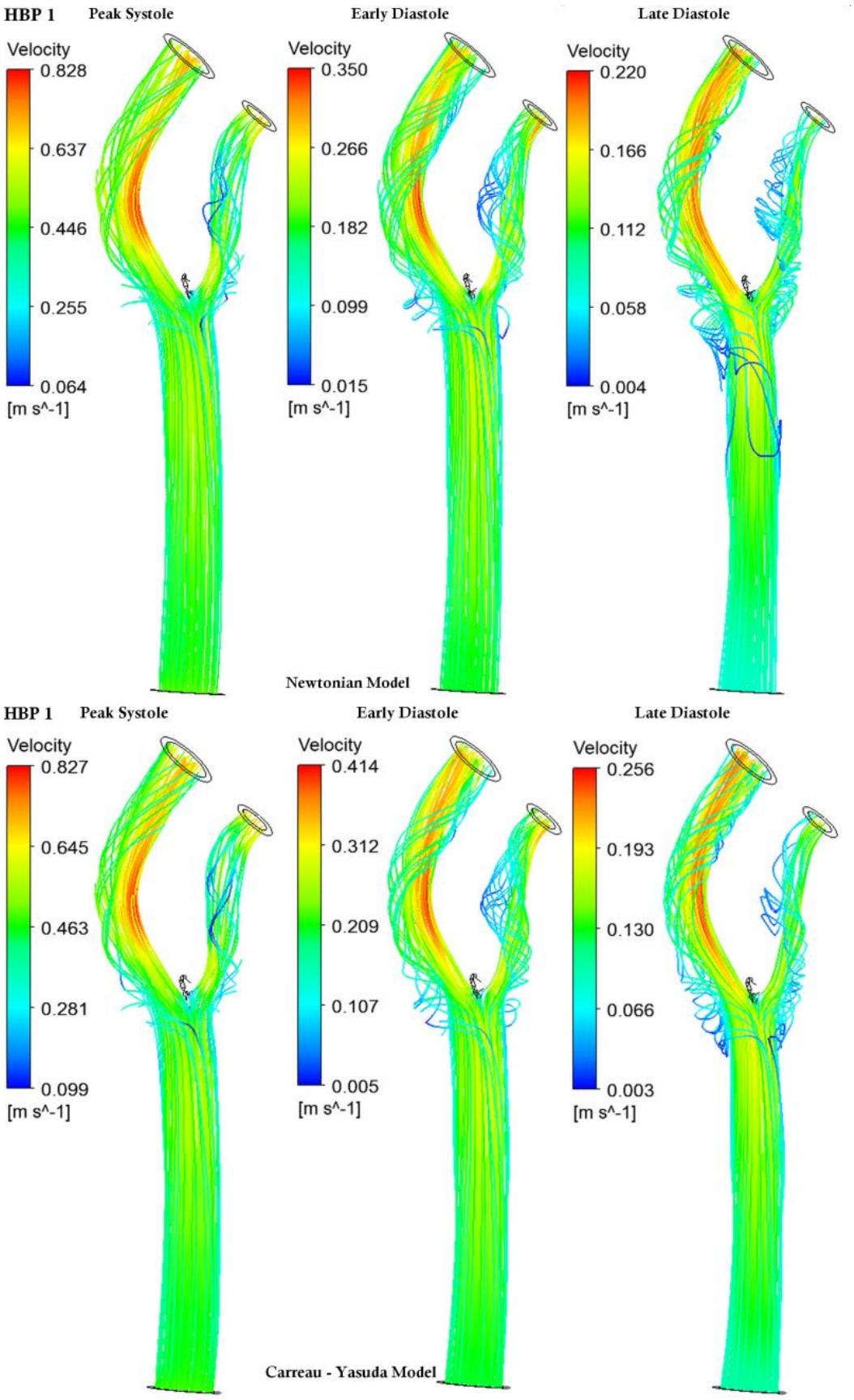

Figure 6-45: Velocity streamlines for HBP 1

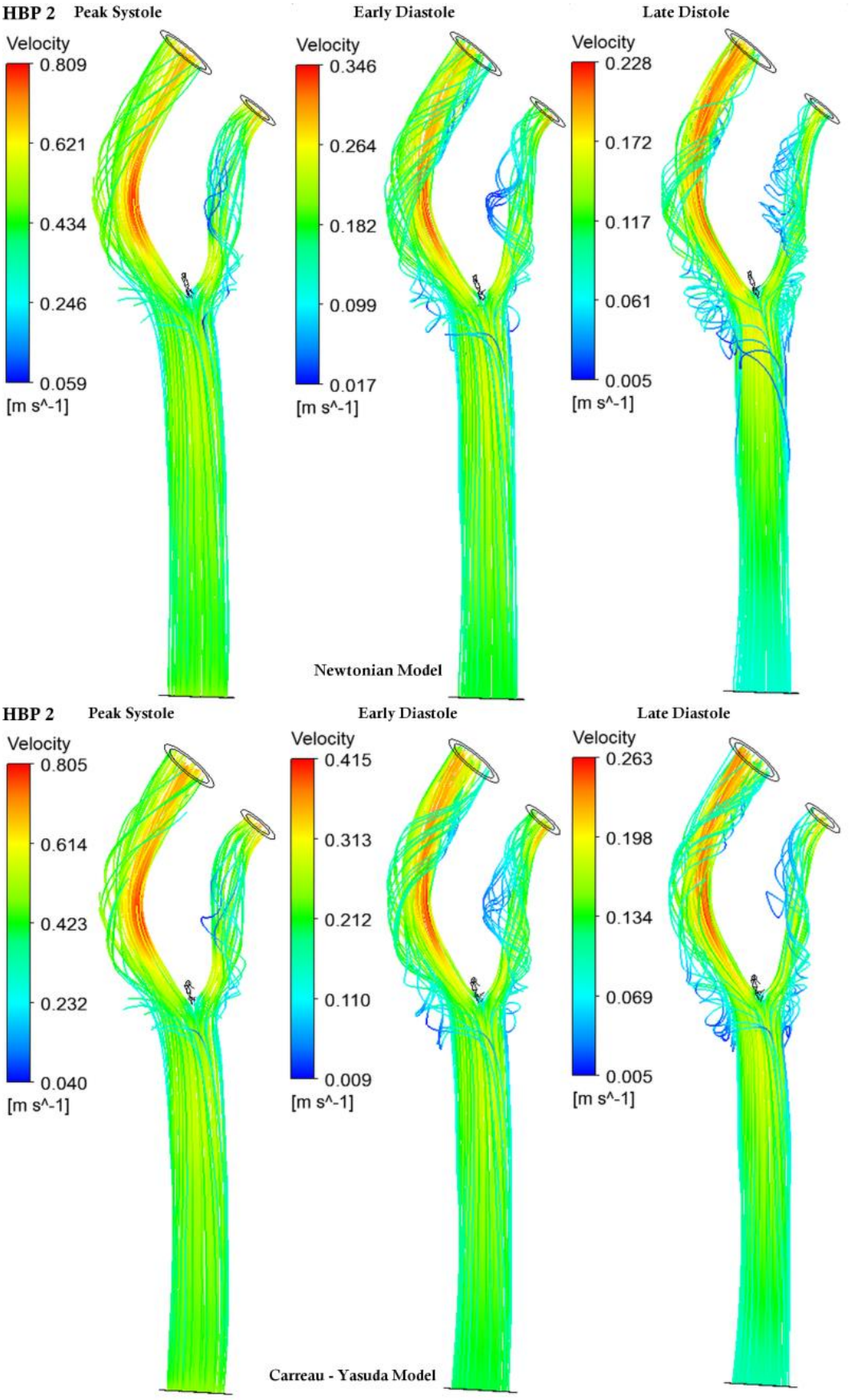

Figure 6-46: Velocity streamlines for HBP 2

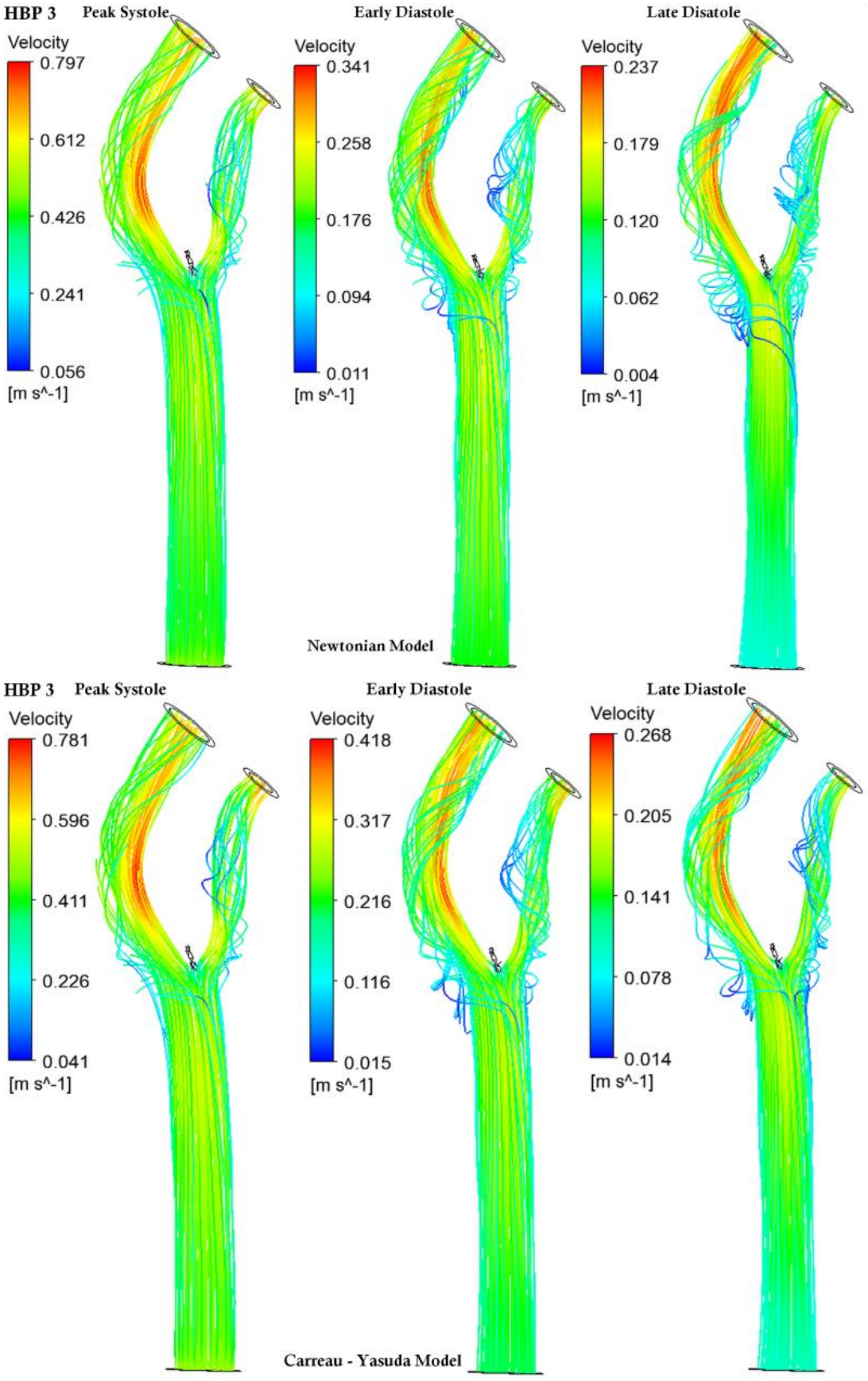

Figure 6-47: Velocity streamlines for HBP 3

6.3.6 Wall Shear Stress

Figure 6-48 to *Figure 6-51* shows the WSS contours for NBP, HBP 1, HBP 2 and HBP 3 at peak systole, early diastole and late diastole. Maximum WSS magnitude at peak systole for NBP, HBP 1, HBP 2 and HBP 3 were 10.147 Pa, 10.176 Pa, 9.858 Pa and 9.631 Pa respectively by considering Newtonian model whereas WSS magnitudes of 14.892 Pa, 14.166 pa, 13.809 Pa, and 13.390 Pa for NBP, HBP 1, HBP 2 and HBP 3 respectively were obtained by considering Carreau – Yasuda model. *Table 6-2* shows the WSS magnitude at different BP cases. With increasing blood pressure, the WSS magnitude rises and the WSS appears to concentrate primarily at the stenosis area at the bifurcation and at the inner wall of the ICA at late diastole. The WSS was concentrated mostly at the inner wall of the ICA in the curved region at the peak systole, while the low WSS region was predominant for all BP cases immediately after stenosis. At early diastole, the intensity of the low shear region increases and it extends across the inner wall of ECA at late diastole. The inner wall of the ECA at the bifurcation zone has traces of low WSS (> 2 Pa) with a significantly decreased effect of atherosclerosis progression. [264]. Moreover, WSS increased pre-stenosis at the neck of the stenosis at this stage. Low WSS was also observed in the carotid sinus and post stenosis regions of the ECA due to a sudden increase in diameter caused by flow recirculation. The development of atherosclerosis is induced by this low WSS (> 0.4 Pa).Although the locations of the high and low WSS regions are captured by Carreau – Yasuda model was like the Newtonian model, it was highly exaggerated by the Newtonian model as compared to the Carreau – Yasuda model. At the neck of the bifurcation below the carotid sinus, where there was maximum flow recirculation, was the low WSS region. Atherosclerosis progression and endothelial cell disorientation will probably be caused by low WSS at greater BP.[265].

Table 6-2: Maximum WSS magnitudes

BP	Maximum WSS (Pa)					
	Newtonian model			Carreau –Yasuda model		
	Peak Systole	Early Diastole	Late Diastole	Peak Systole	Early Diastole	Late Diastole
NBP	10.155	3.93	2.57	14.892	6.171	4.014
HBP 1	10.176	4.171	2.58	14.166	6.247	3.965
HBP 2	9.856	4.107	2.608	13.809	6.284	3.997
HBP 3	9.631	4.03	2.74	13.370	6.364	4.034

Figure 6-52 shows the temporal variation of WSS for different blood pressures and viscosity models. It can be observed that for NBP condition the WSS variation was proportional to the pressure variation in both Newtonian and Carreau – Yasuda model. However, for HBP 2 and HBP 3 conditions, the WSS behaves in an oscillatory fashion with a reduction in the WSS magnitude at peak systole. Behaviour may be due to strong resistance offered at the outlet due to higher blood pressures, significant WSS variation with time was observed showing low WSS values at peak systolic phase probably because of higher flow recirculation. The oscillatory behaviour was mainly observed in plane 3 region at the stenosis and post stenosis where there is sudden reduction and expansion in the diameter. These are the critical regions where atherosclerosis progression is observed.

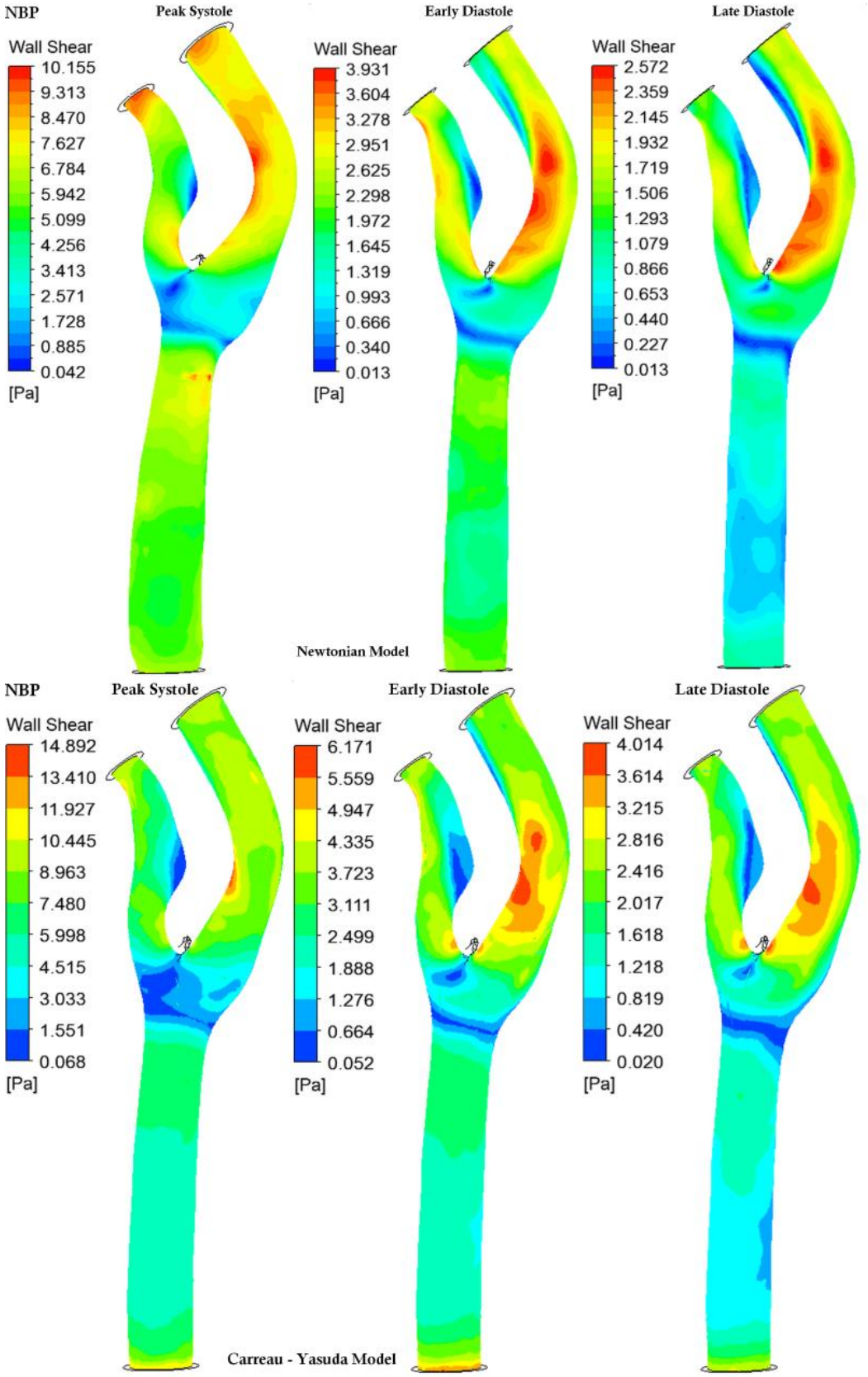

Figure 6-48: WSS contours for NBP

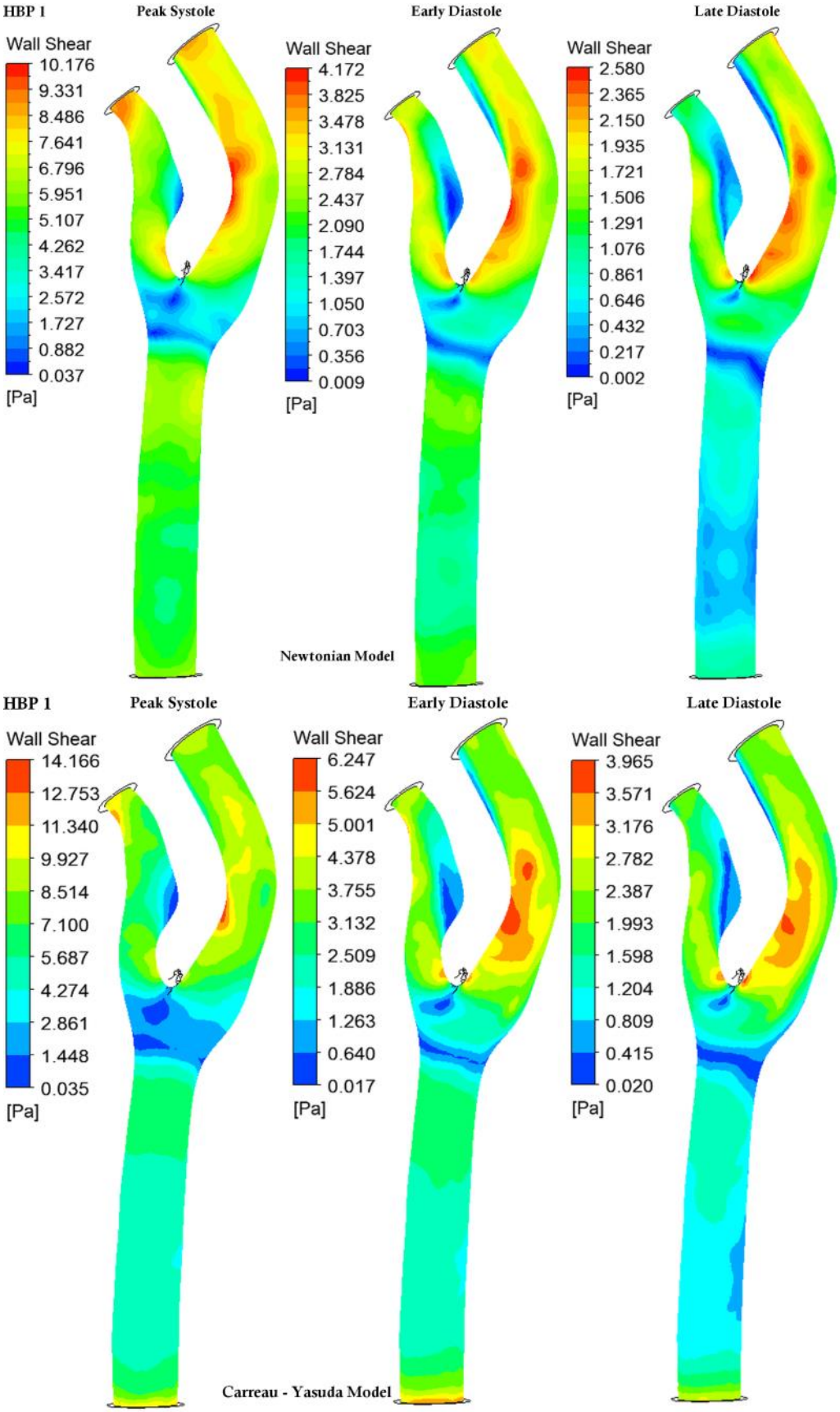

Figure 6-49: WSS contours for HBP 1

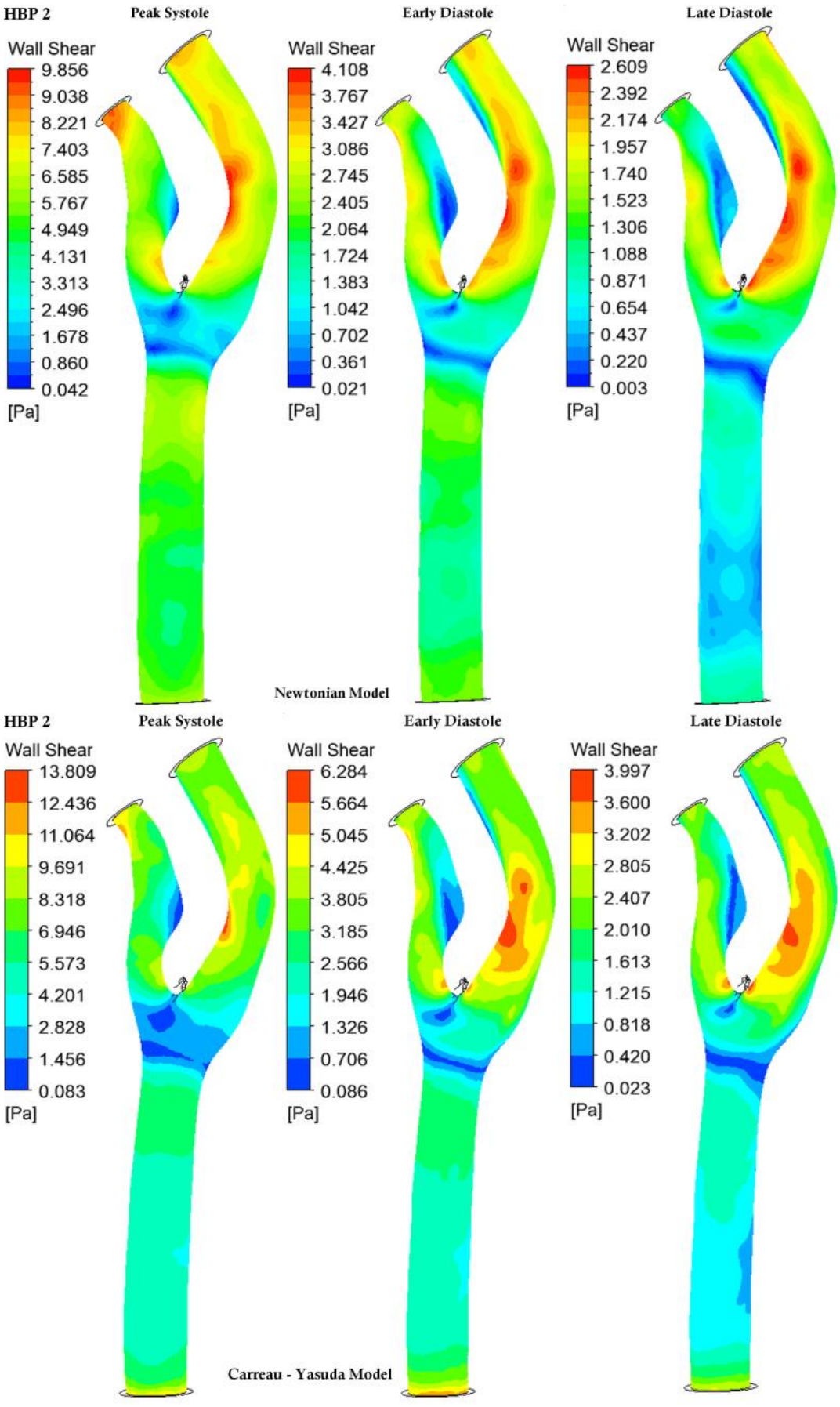

Figure 6-50: WSS contours for HBP 2

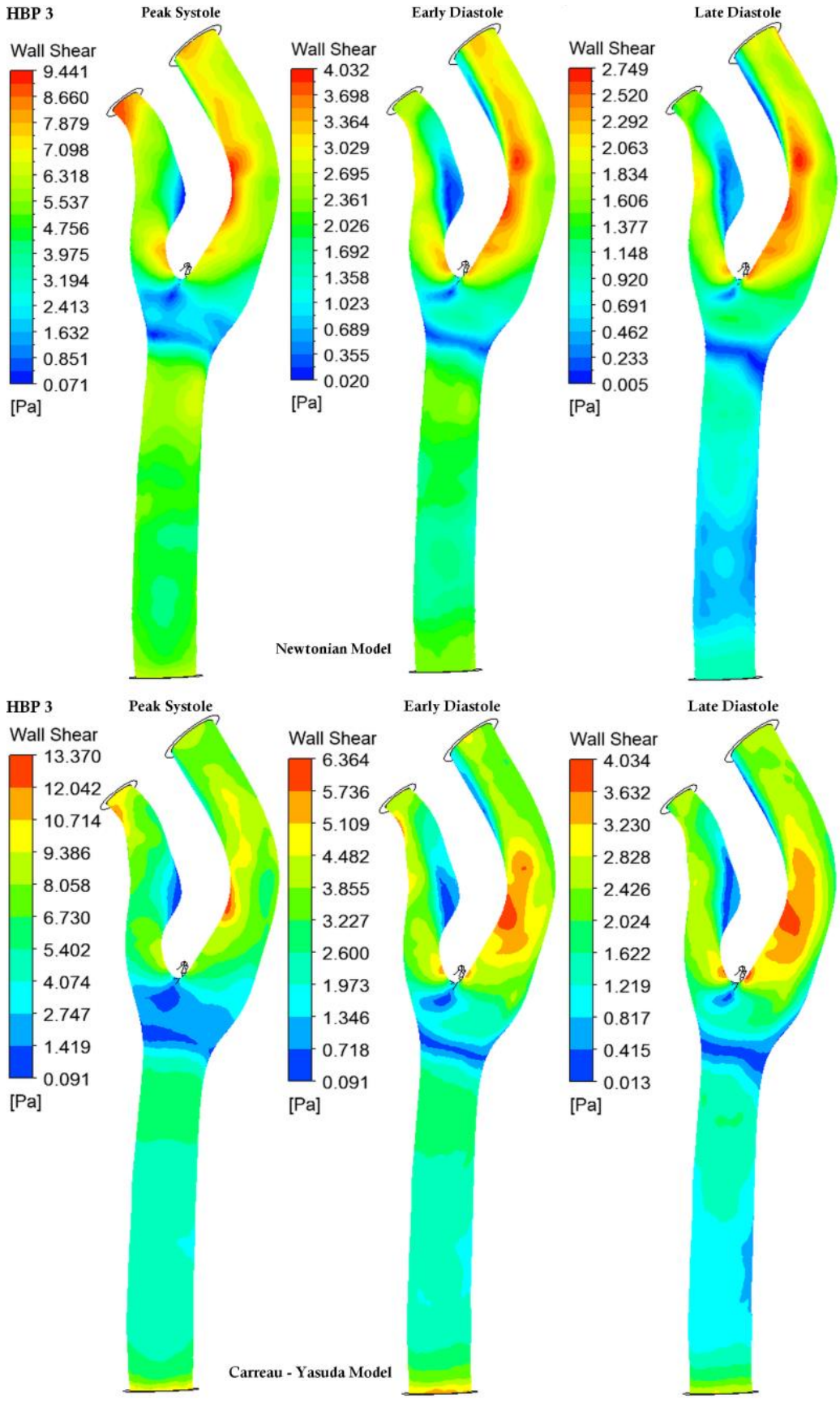

Figure 6-51: WSS contours for HBP 3

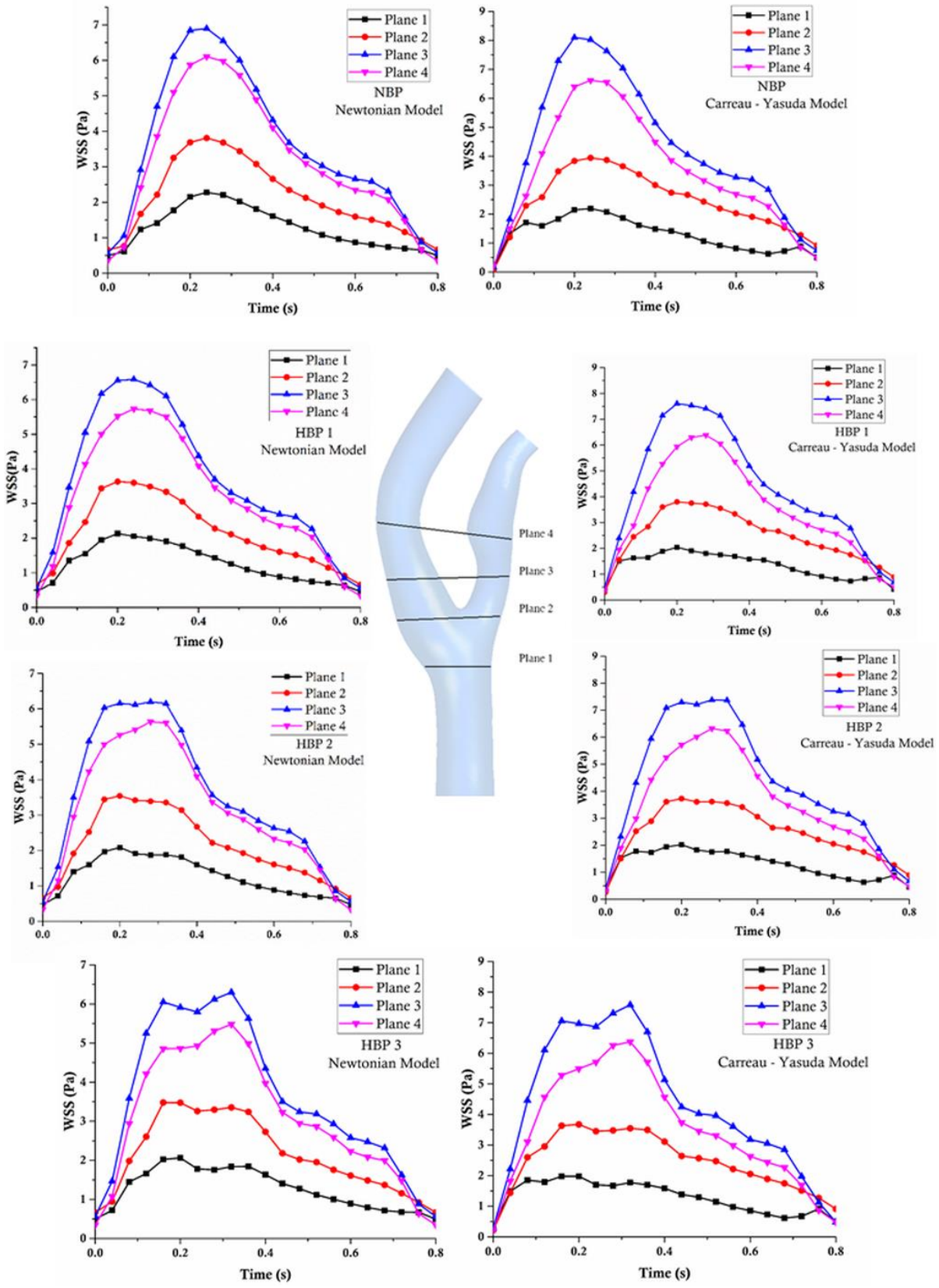

Figure 6-52: Temporal WSS variation at different planes considering Newtonian and Carreau – yasuda models for different blood pressures

6.3.7 Wall Deformation

Maximum arterial deformation occurred in the carotid bifurcation at peak systole, as seen for all BP conditions in *Figure 6-53* to *Figure 6-56*. It was observed that the location of maximum deformation was in the bifurcation region. Higher stiffness in the region of plaque accumulation at the root of the ECA, resulted in decreased elastic deformation. The reduced wall stiffness was localized around the ECA, resulting in decreased wall deformation around the stenosis site. Post stenotic deformation in the distal side of the ECA was another observation due to eccentric stenosis with a lower profile due to increased plaque stiffness. The partial flow restriction offered by the ECA diverts the flow through the ICA. However, the deformation had increased due to increased pressure in the upstream of the narrowed region to compensate the flow. Therefore, maximum deformation was observed at the peak systolic phase at the entrance of the ICA in the bifurcation region. As observed in published literature, the deformation profile was representative of normal carotid bifurcation.[12]. Among the rheological models considered in the analysis, there was no substantial difference in arterial deformation.

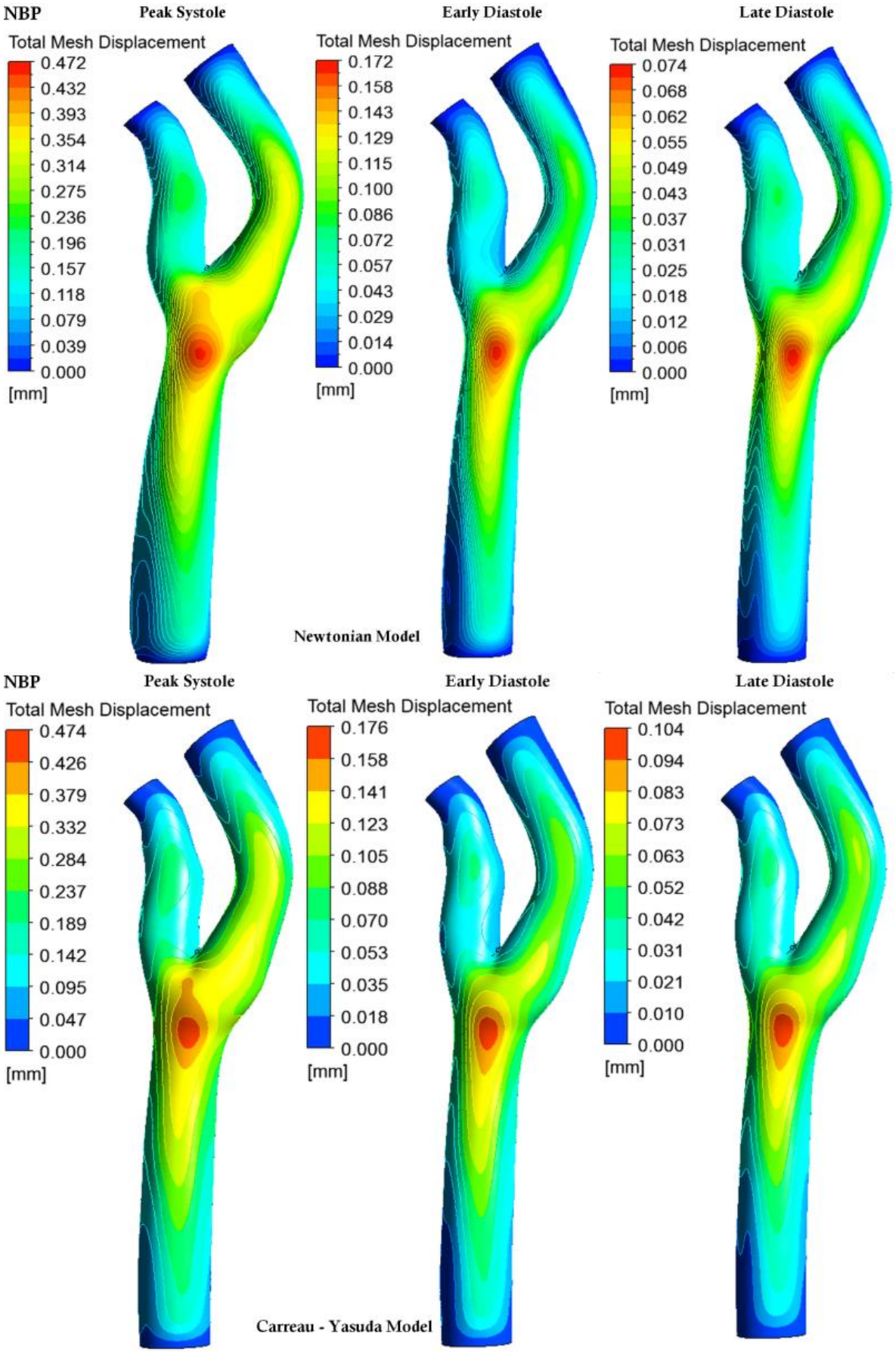

Figure 6-53: Deformation contours for NBP

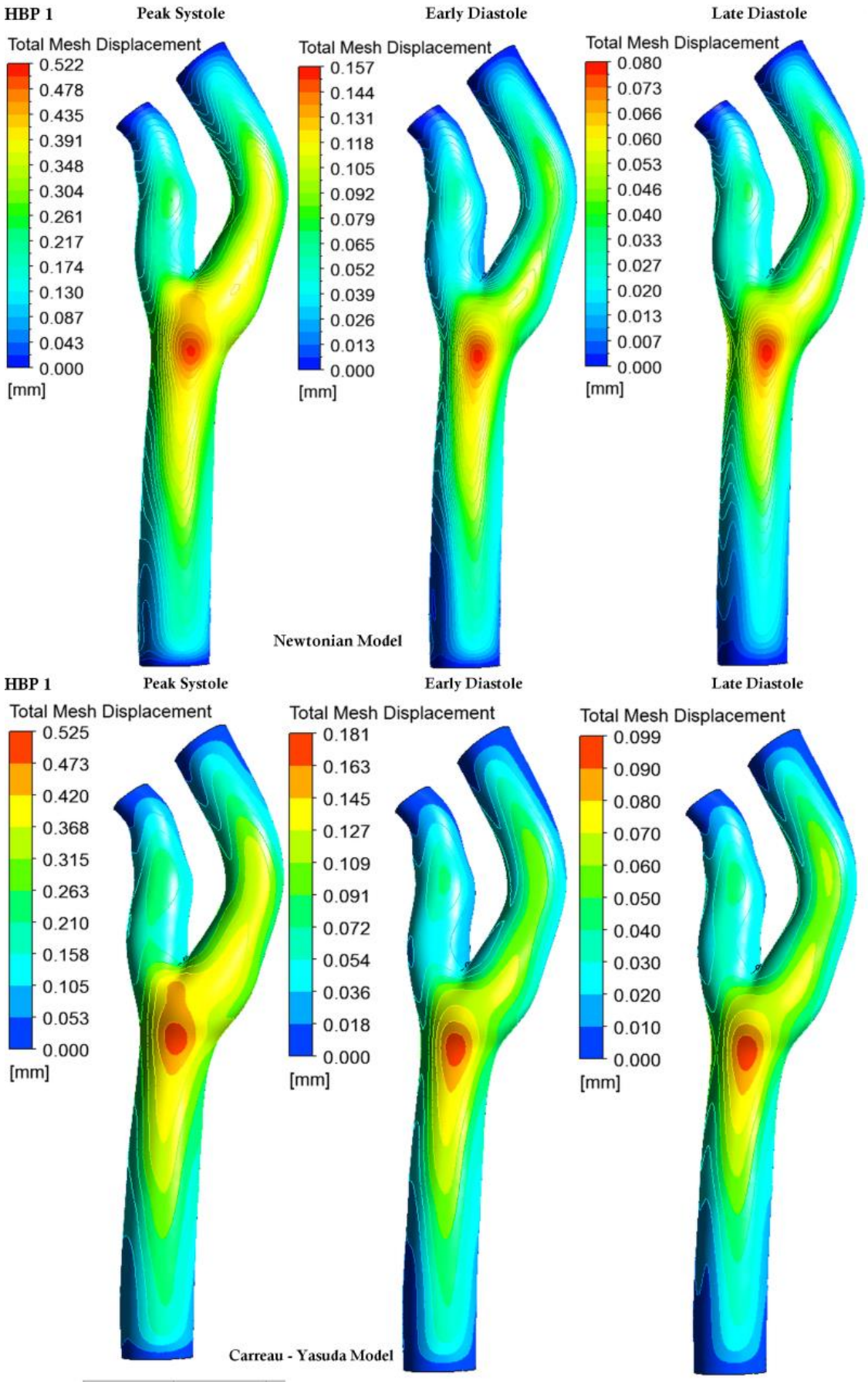

Figure 6-54: Deformation contours for HBP 1

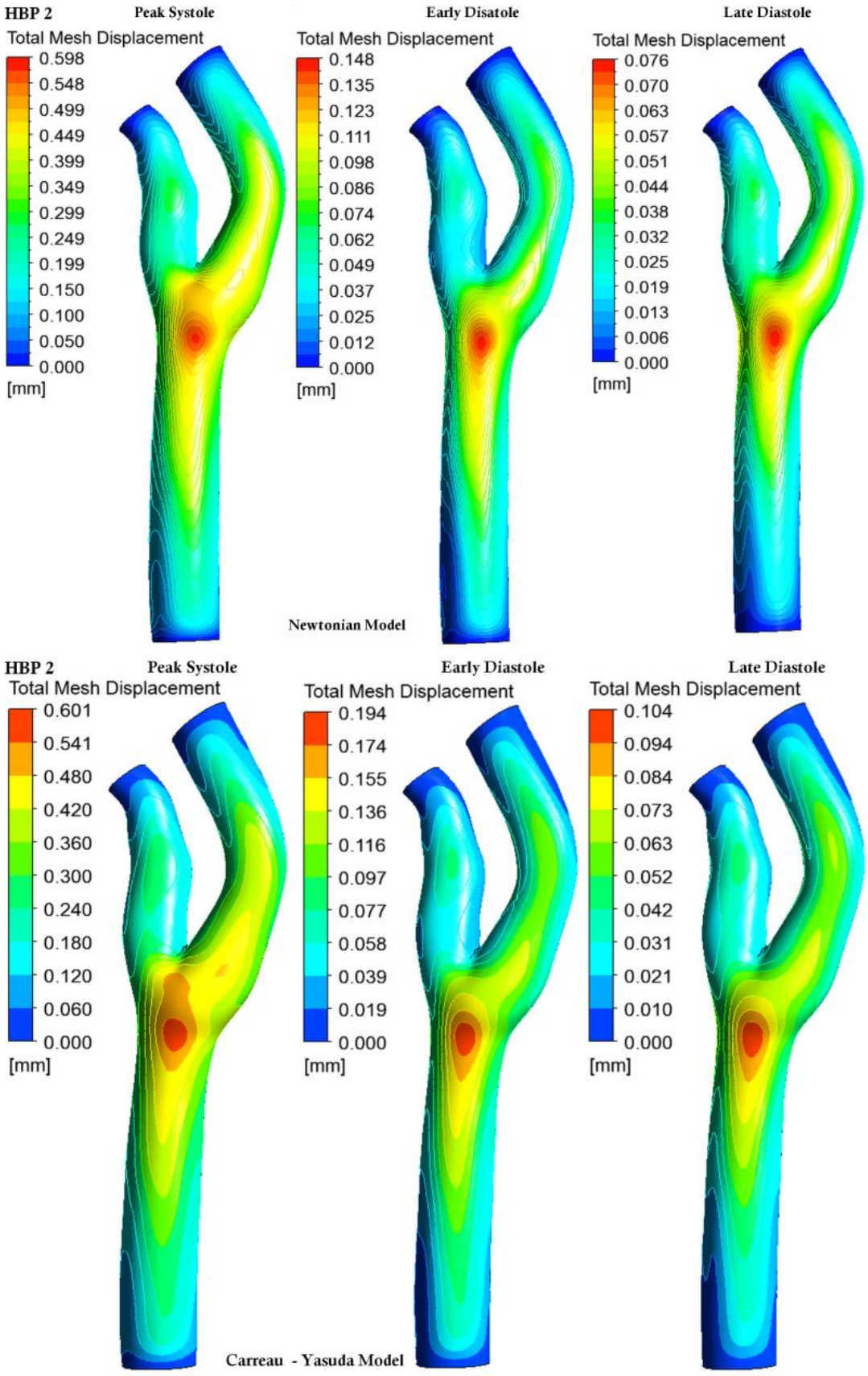

Figure 6-55: Deformation contours for HBP 2

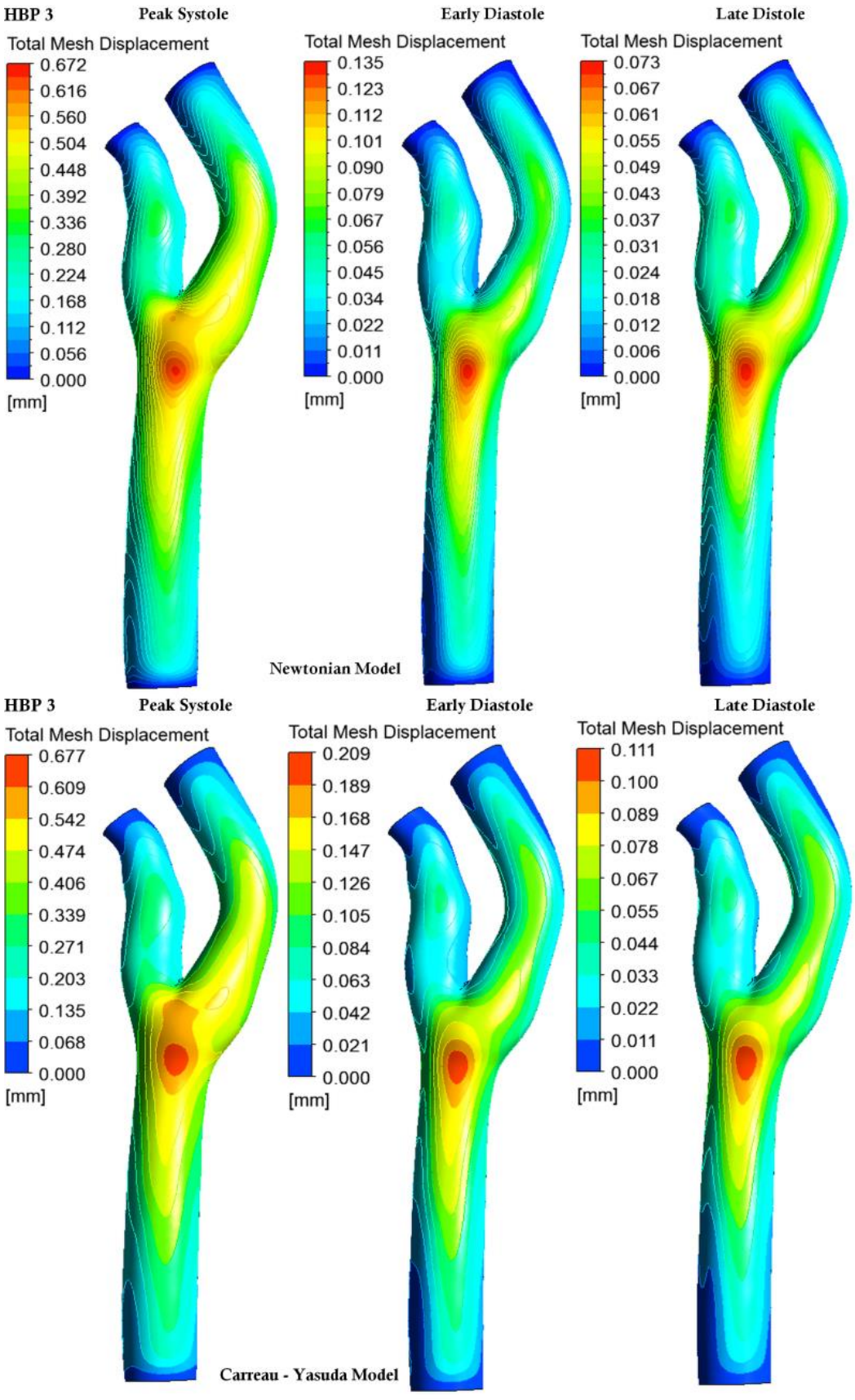

Figure 6-56: Deformation contours for HBP 3

6.3.8 Oscillatory Shear index

Figure 6-57 shows the average OSI in stenosed carotid artery subjected to different blood pressures. As observed with normal carotid artery, the OSI did not show significant variation with blood pressure. However, the OSI magnitude was significantly higher compared to the normal carotid artery. This indicates higher flow reversals in the stenosed artery due to sudden reduction and expansion of the artery resulting in flow reversals at different locations of the artery.

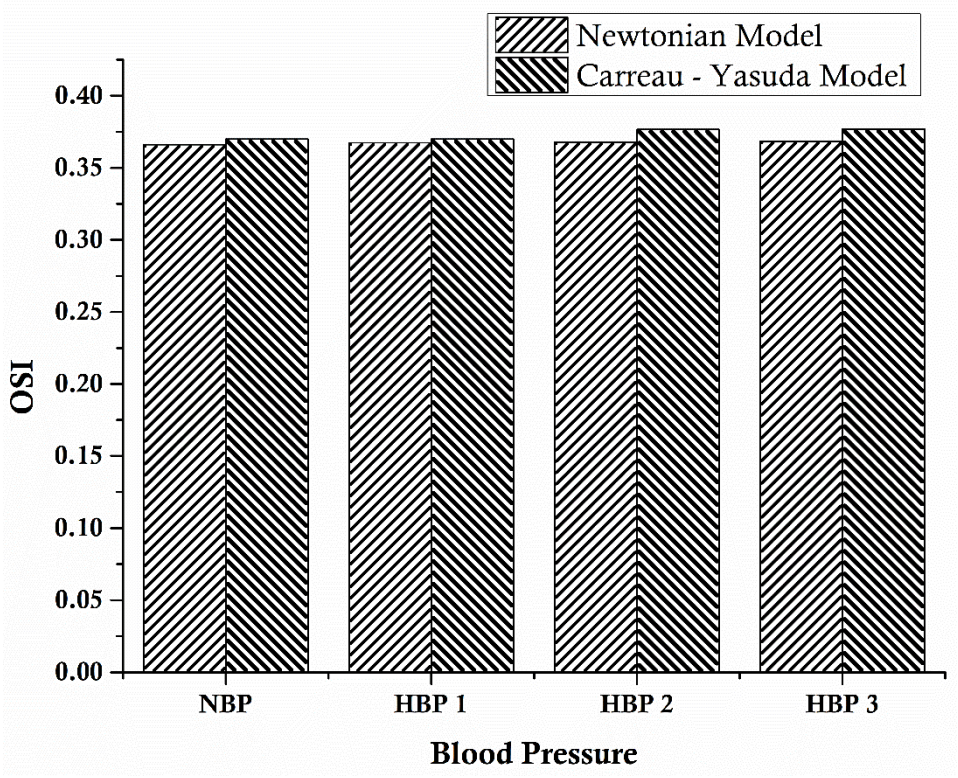

Figure 6-57: Average OSI for different blood pressure conditions for Newtonian and Carreau - Yasuda models

Figure 6-58 to *Figure 6-65* shows the OSI contours in the stenosed carotid artery subjected to different blood pressures by considering both Newtonian and Carreau – Yasuda models. It was evident that the OSI did not show any significant difference between the blood pressures and viscosity model. At peak systole the maximum OSI was observed at the inner wall of ICA extended towards the outer wall encircling the carotid sinus, and this

remains the same for all the phases of the cardiac cycle and for different blood pressures with minor movement towards the downstream at early and late diastole.

The higher OSI defines the regions of flow recirculation occurring in circular pattern at the outer wall of the ICA and distal inner wall of the ICA. The OSI contours emphasize that the elevated OSI tend to occur at the sites of impingement of flow and the mean WSS divergence regions at the distal end of recirculation zones. It was also predominant where reverse flow meets the dominant flow direction at the outer wall of the ECA below the stenosis. OSI was maximum in the regions where flow streamline meets along the front and back of the ICA and where there was a vortex formation adjacent to the wall as observed during the late diastole phase of the cardiac cycle. The Newtonian and Carreau – Yasuda viscosity models did not show significant difference in the OSI contours. The OSI distributions suggest the low magnitude of WSS was captured with the OSI. The OSI contours also show large variation among the two carotid artery models. For both models the high OSI was found near the inner wall of the ICA. The high level of OSI indicates detrimental flow condition and the regions with an OSI magnitude of >0.2 are prone to vascular dysfunction [252]. Additionally, the region near the outer wall of the ECA adjacent to the stenosis showed higher OSI compared to the normal carotid artery model.

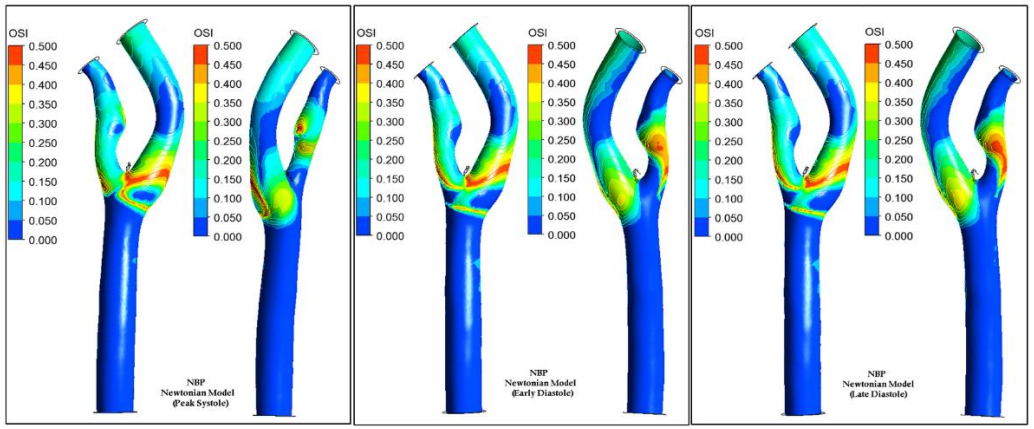

Figure 6-58: OSI contours for NBP considering Newtonian model

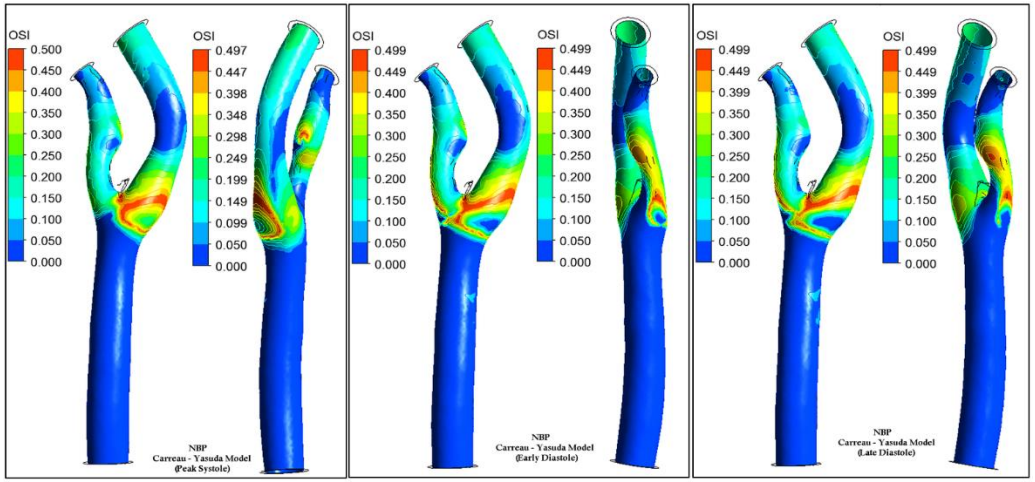

Figure 6-59: OSI contours for NBP considering Carreau – Yasuda model

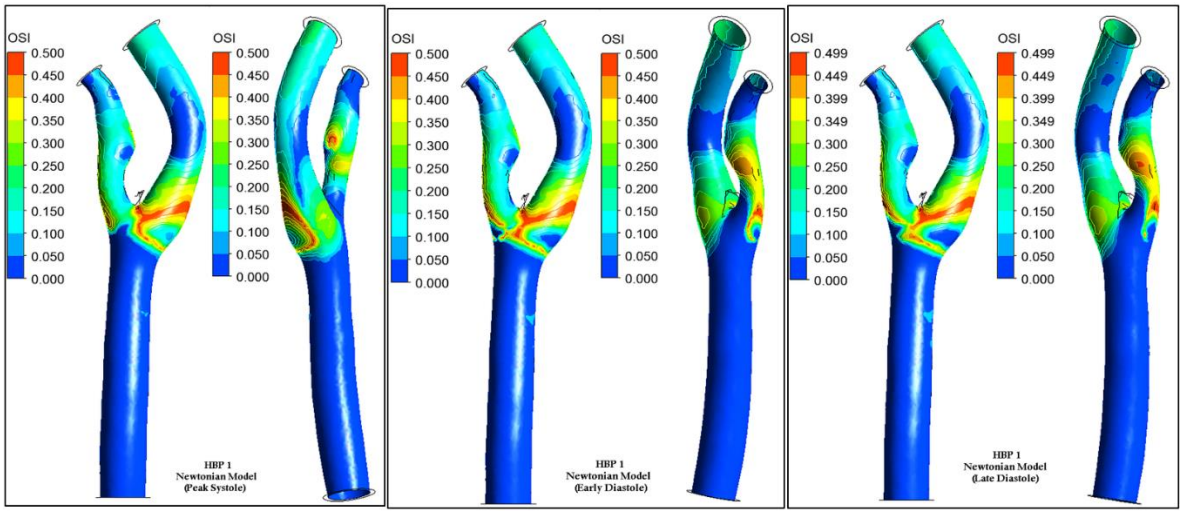

Figure 6-60: OSI contours for HBP 1 considering Newtonian model

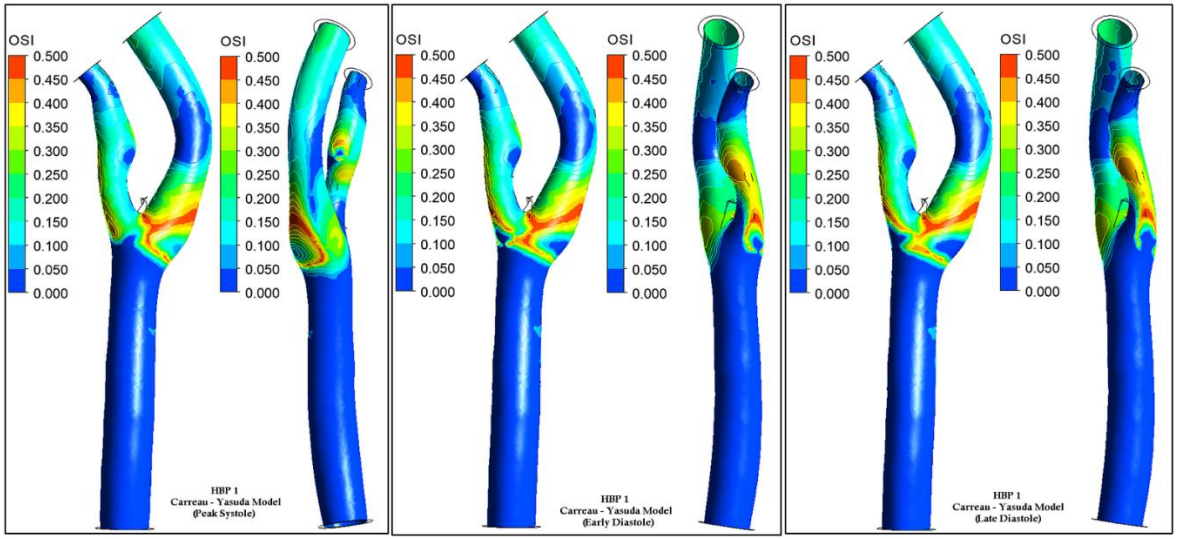

Figure 6-61: OSI contours for HBP 1 considering Carreau - Yasuda model

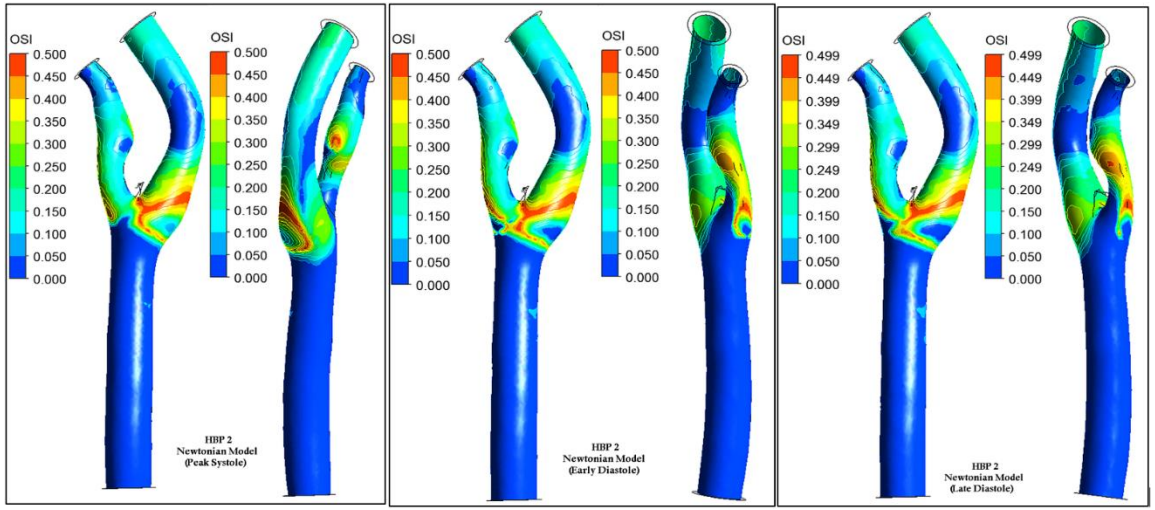

Figure 6-62: OSI contours for HBP 2 considering Newtonian model

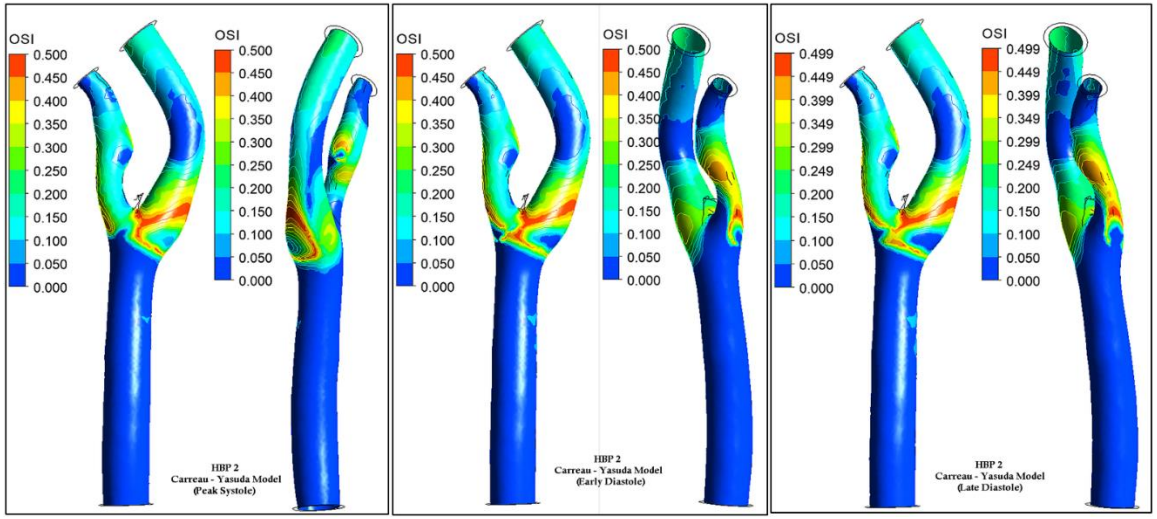

Figure 6-63: OSI contours for HBP 2 considering Carreau - Yasuda model

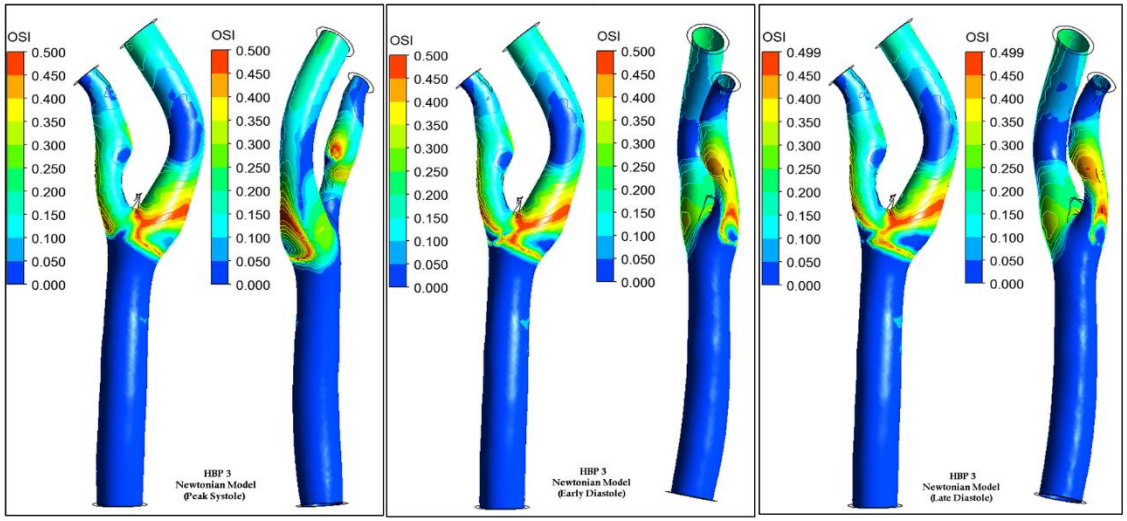

Figure 6-64: OSI contours for HBP 3 considering Newtonian model

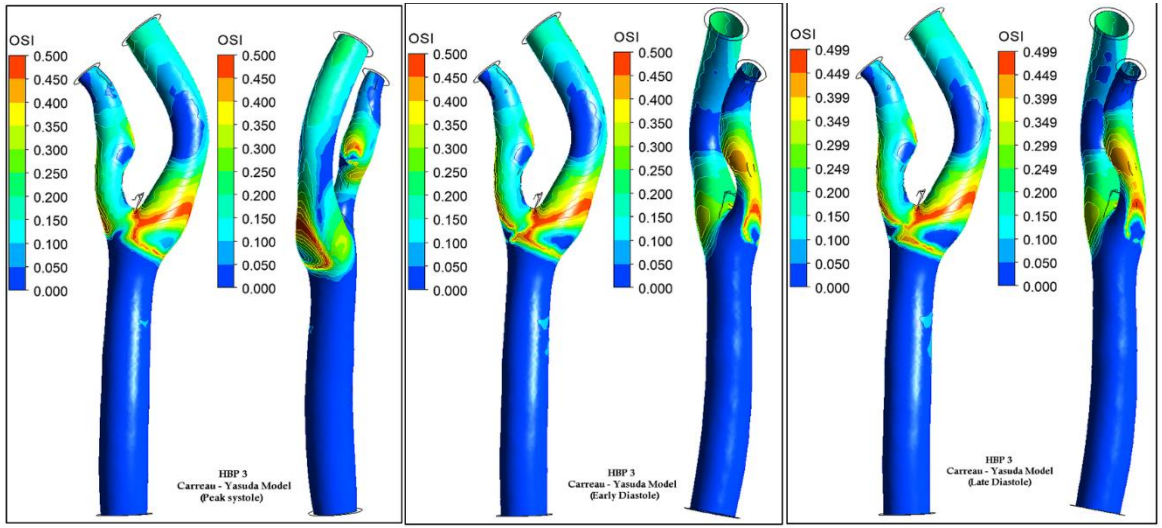

Figure 6-65: OSI contours for HBP 3 considering Carreau - Yasuda model

6.3.9 Helicity

Figure 6-66 and *Figure 6-67* shows the iso surface representing the helicity mapped with the vorticity vectors and OSI bands in stenosed carotid artery using Newtonian and Carreau – Yasuda model respectively.

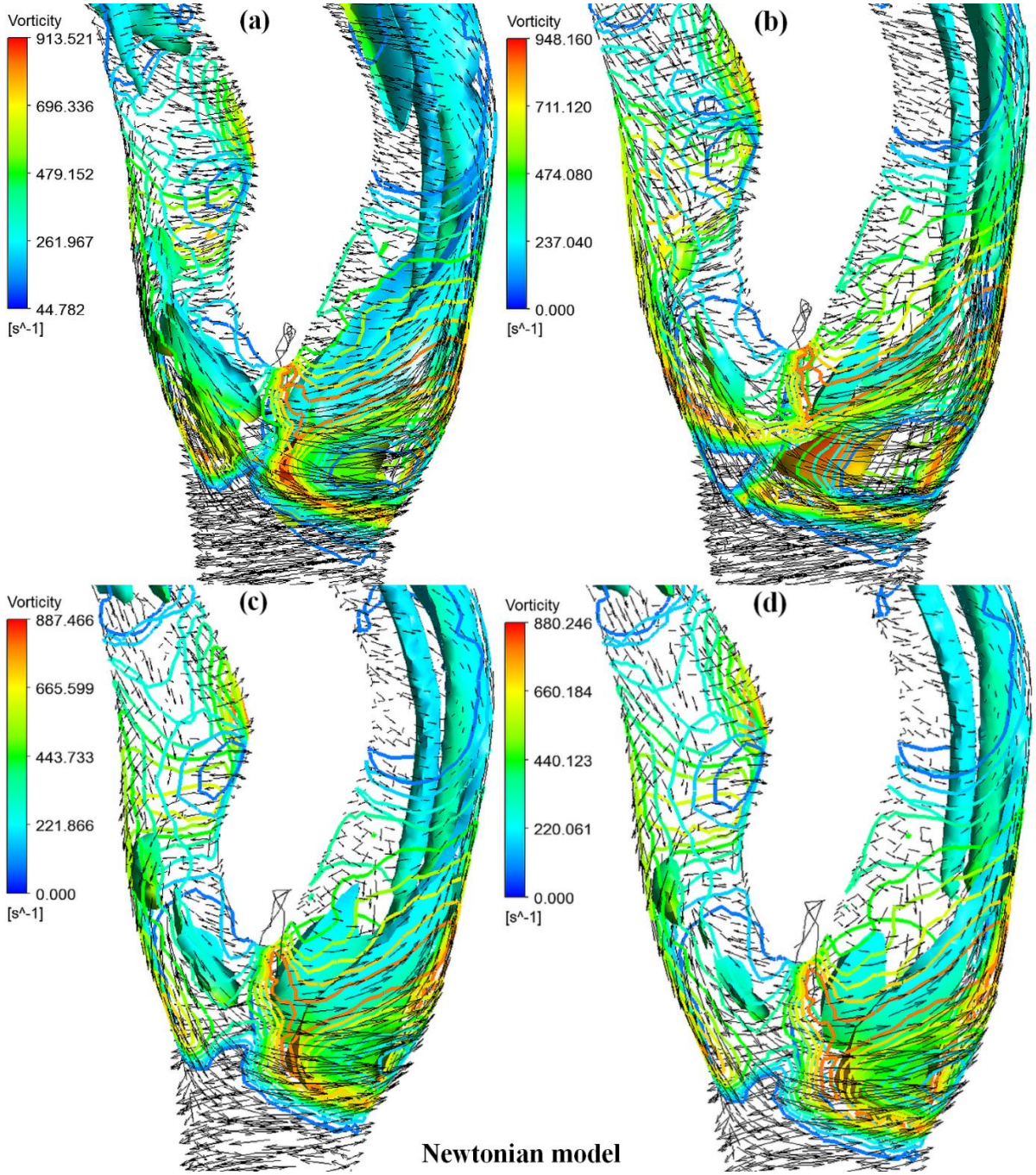

Figure 6-66: Voriticy vectors and iso – surface representing Helicty mapped with OSI bands in stenosed carotid artery model considering Newtonian model

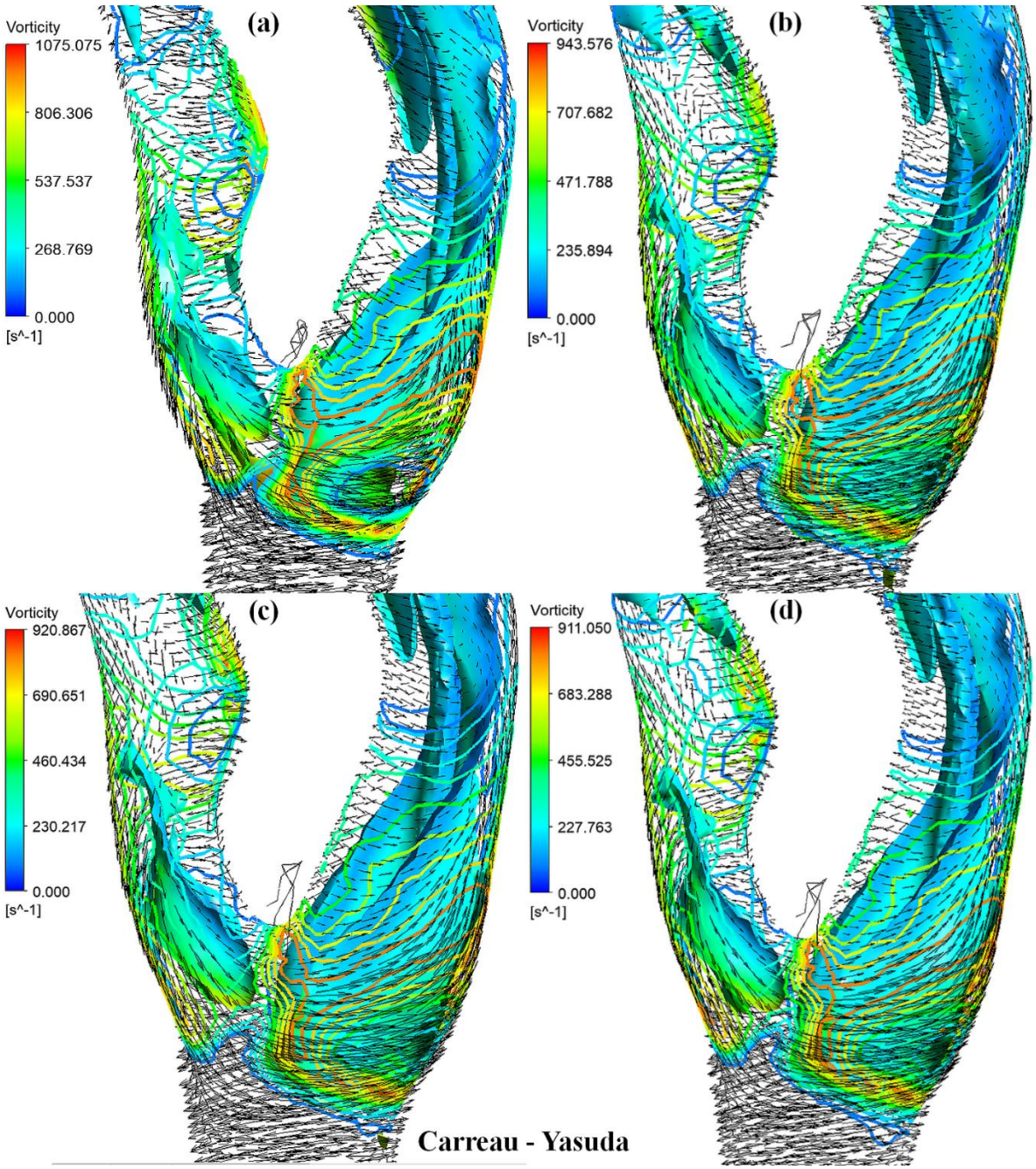

Figure 6-67: Voriticy vectors and iso – surface representing Helicty mapped with OSI bands in stenosed carotid artery model considering Carreau - Yasuda model

As observed in the figures, the helical strength is higher in the Carreau – yasuda model compared to the Newtonian model. The helicity is predominant at the carotid sinus and it reduces with increased blood pressure as indicated by the vorticity vectors. As the blood pressure increases, counter rotating helical structures is observed near the inner wall of the ICA and at the post stenotic region of the ECA, whose intenstity increases with increased

blood pressure. *Figure 6-68* shows the temporal variation of the helicity indicating reduced helicity with increased blood pressure.

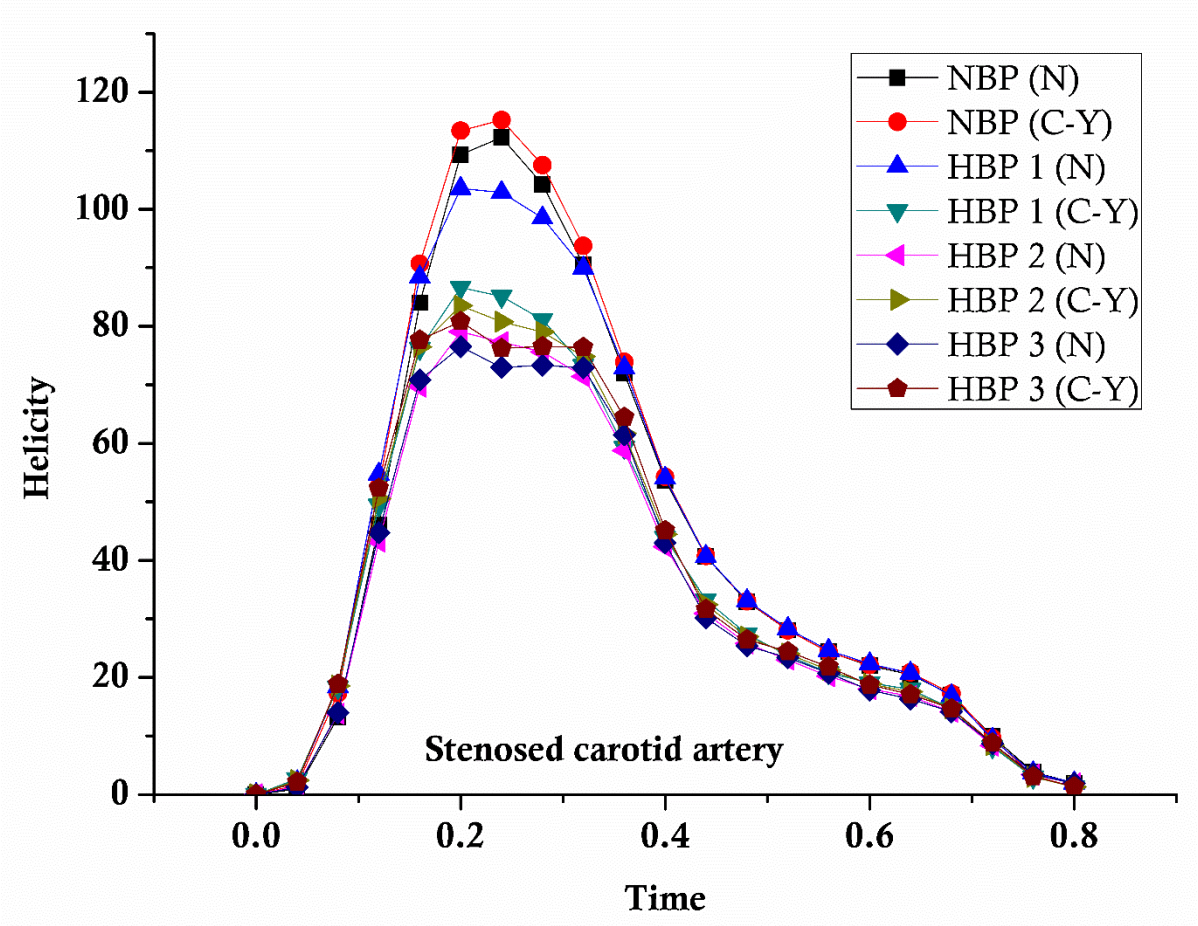

Figure 6-68: Temporal average helicity magnitude in stenosed carotid artery

Table 6-3 shows the comparision of average helicity magnitude at peak systole in stenosed carotid artery model for different blood pressure and rheology. Carreau – Yasuda model shows higher helicity compared to the Newtonian model by approximately 4% for all the blood pressure model.

Table 6-3: Helicity (m/s^2) at peak systolic phase in stenosed carotid artery model

BP	Newtoninan	Carreau - Yasuda
NBP	109.33	113.41
HBP 1	79.205	83.105
HBP 2	76.45	79.91
HBP 3	73.15	76.375

Chapter 7 Conclusions and Scope for future work

As highlighted in the introductory parts of the thesis, the main motivation of the research is to understand the effects of blood pressure and rheology on haemodynamics in stenosed and normal carotid artery.

The results generated from this research have contributed towards the better understanding of the influence of blood pressure and blood rheology on blood flow in the carotid artery bifurcation. The study also highlighted the contribution of the use of FSI in aiding the diagnosis of cardiovascular physiology in the normal and stenosed carotid artery.

The study can be classified into CFD simulation of patient-specific normal and stenosed carotid artery subjected to different blood pressure range, FSI simulation of a straight elastic tube, and FSI simulation of normal and stenosed carotid artery subjected to different blood pressures. In this study, the objectives were met satisfactorily and the results have contributed towards the understanding of the fundamentals of blood flow under different blood pressures and the advantage of using non – Newtonian model.

The outcome of this research was to provide an understanding of the effect of the physiological phenomenon of flow and compare the changes in haemodynamics of normal and stenosed carotid artery, by considering different blood pressures and blood viscosity models. The present study demonstrated the use of FSI analysis in visualizing the changes in haemodynamics which may have significant implications in medical diagnosis and may also be useful in planning clinical interventions.

The accuracy of the present analysis was validated by PIV measurements in literature and the flow patterns agreed satisfactorily with the published data. Compared with the PIV data, flow separation, and vortex generation due to abrupt changes in the cross-sections at the carotid sinus of the healthy model were successfully predicted by numerical simulation using a laminar model. The predicted velocities at all the sections were comparable to the published work. This study was used to validate the CFD results of ANSYS CFX software used. Therefore, the numerical configurations used in this study could provide satisfactory information on vascular flows.

A two – way transient coupled field analysis was validated using a benchmark simulation available in the literature. The results obtained matched satisfactorily with that of the literature and demonstrate the pulsatile flow behaviour through a segment of elastic tube representing the artery. Further, a validation study was performed considering realistic physiological boundary conditions for idealized common carotid artery segment and the obtained results agreed with the results in the literature. The pulsatile propagation of the wave, wall deformation, and flow rate agreed well with the literature. A wave speed test was also performed to validate the results which were in close agreement with the Moens – Korteweg equation.

Initially, numerical simulations were performed on normal and stenosed carotid artery model considering rigid wall conditions. The study was conducted considering different blood pressures and compared between Newtonian and Carreau – Yasuda viscosity models. In the normal carotid artery, the Newtonian model followed the flow profile at the distal end of the CCA as justified by the principle that the shear stress has a relationship with the velocity gradient. As the flow progressed towards the bifurcation, the sudden increase in the cross-sectional area reduced the flow velocity leading to flow recirculation zones. The Newtonian model failed to capture the unsteady flow variations in this region

as captured by the Carreau – Yasuda model. In the stenosed model, it could be noted that for the NBP condition, the WSS was proportional to the pressure variation. However, for HBP 2 and HBP 3 conditions, the WSS oscillated with a reduction in the WSS magnitude at peak systole at the neck of the stenosis. The WSS increased towards the downstream and maximum at the neck of the stenosis. The average WSS plots bring out the differences in temporal WSS variations for different BP cases. The normal BP had a proportionate variation compared to the pressure, as the BP increased the oscillatory behaviour was more evident.

The variation of WSS at different blood pressure ranges for both rigid and FSI models was observed and the rigid model predicted higher WSS magnitude compared to FSI for both normal and stenosed carotid artery models. While comparing the viscosity models, the Newtonian model predicted higher WSS in the rigid artery model by 19% for the normal artery model and 35% for the stenosed carotid artery model, whereas in FSI it gave lower WSS as compared to the Carreau – Yasuda model by 42% for normal artery model and 41% for the stenosed model.

The WSS contours in the normal carotid artery model considering both Newtonian and Carreau – Yasuda viscosity models showed a reduced WSS with an increase in the blood pressure due to increased deformation of the artery and increased peripheral resistance in the artery. Maximum WSS magnitude for NBP, HBP 1, HBP 2, and HBP 3 are 9.907 Pa, 9.716 Pa, 9.564 Pa, and 9.221 Pa respectively for the Newtonian model and 14.269 Pa, 13.752 Pa, 13.495 Pa, and 13.023 Pa for the Carreau – Yasuda model. The WSS was maximum at the divider wall of the bifurcation, and due to flow diversion, recirculation zones are generated at the outer wall of the ICA near carotid sinus which extends until the end of the curved ICA. The recirculation zone was more prominent in the Carreau – Yasuda model and extended towards the inner wall of the ICA.

Similarly, for the stenosed carotid artery, the Newtonian model gave 10.155 Pa, 10.176 Pa, 9.856 Pa, and 9.441 Pa for NBP, HBP 1, HBP 2, HBP 3 respectively by considering Newtonian model and WSS of 14.892 Pa, 14.166 Pa, 13.809 Pa, and 13.370 Pa by considering the Carreau – Yasuda model. The WSS magnitude decreased with increasing blood pressure and it tended to concentrate mainly near the stenosis region at the bifurcation and the inner wall of the ICA at the curved region, whereas the low WSS region was predominant immediately after the stenosis for all cases. Besides, at this instant WSS increased pre stenosis at the neck of the stenosis where the diameter was least. Low WSS was also observed at the carotid sinus and post stenosis regions due to flow recirculation caused by increased diameter. In the Carreau – Yasuda model, the behaviour was like the Newtonian model, however the low WSS region was more predominant at the base of the ECA and post stenosis. According to Fry [266], shear stress exceeding 40 Pa is critical to endothelial cells. Moreover, Ramstack et al [267] claimed that a shear stress magnitude of 100 Pa can result in detachment of the endothelial cell layer resulting in plaque rupture and for clots resulting in a stroke. It was safe to say based on the above results that there is no biomechanical damage to the endothelial layer of the arterial wall. As the stenosis was in the external carotid artery, its effect on the healthy branch was also greater due to the law of conservation of mass. The presence of stenosis in ECA makes the ICA a favourable location for the generation of stenosis because of the generation of flow recirculation at the carotid sinus. These observations led to a more concentrated qualitative measurement of WSS based descriptors on the arterial wall. Wall shear stress is a flow-driven parameter, therefore, the variation in blood pressure also governs the variation in the WSS. Since the flow was in the axial direction, the value of WSS was more in the axial direction compared to other directions. However, at high flow rates, the oscillatory behaviour of the WSS may be due to chaotic flow developed due to the

interaction of blood and the stenosed region of the arterial wall. Such interactions create unstable flow domains in the flow direction, leading to significant flow in a direction perpendicular to the direction of flow. Therefore, based on the WSS markers, the locations susceptible to secondary plaque accumulation can be evaluated.

Oscillatory shear index (OSI) is an index that explains the flow reversals and highlights the difference between average wall shear stress and average wall shear stress vector. Although the formation of plaque is dependent on many other factors, the oscillatory shear stress was more appropriate while dealing with oscillatory blood flow [183]. According to many experimental investigations [45], [264], [268], the plaque formation was at the location where there was the maximum shear oscillation. *Figure 6-29* to *Figure 6-36* shows OSI contours for normal carotid artery subjected to different blood pressures and *Figure 6-58* to *Figure 6-65* shows the OSI contours of the stenosed carotid artery for different blood pressures. The maximum OSI occurred near the external walls of the ICA and the opening of the bifurcation. These were the regions that are susceptible to plaque formation. The high shear stress on the wall and higher velocities were the factors that prevent plaque accumulation at the bifurcation apex. Meanwhile, studies have also found that flow separation, recirculation and low shear stress at the carotid sinus makes the area susceptible to plaque accumulation [256]. The low shear stress is the most important index which determines the development of atherosclerosis. Hence, the maximum OSI was seen in the regions where the WSS was low and there was high flow recirculation.

The thorough investigation of 2 different subject specific cases demonstrate the potential of numerical FSI simulations to understand the detailed haemodynamics in normal and diseased conditions, such as entry and exit of flow velocity near the stenosis, swirling of flow post stenosis and at the carotid sinus, post stenotic arterial wall deformations, WSS at the neck and across the stenosis and at the carotid sinus. All these variables are not

under the purview of imaging diagnostic techniques. Although accurate investigations are dependent on arterial wall, flow assumptions, boundary conditions, numerical approximations, FSI simulations with few approximations provide an overall flow pattern and haemodynamic behaviour similar to clinical observations. The numerical simulation of subject specific models for different blood pressures will certainly be useful in understanding the haemodynamic variations and possible outcomes.

The CFD and FSI simulations were conducted under physiological conditions to study the flow patterns in the carotid artery models subjected to different blood pressures. The flow patterns and the WSS distributions were discussed to enumerate the effects of the rheological models. A categorical difference between the WSS distributions of Newtonian and Carreau – Yasuda models was observed and as observed in the results, the more that blood shows shear thinning behaviour, the less the area of the bulb experiences back flow. The results show that the Newtonian model overestimates the extent of backflow zone. Hence, using the non – Newtonian model to mimic the behaviour of blood is required as blood has a significant shear thinning nature.

The Newtonian model fails to capture the unsteady flow variations in this region as captured by Carreau – Yasuda model. In the stenosed model, the WSS varies proportionately with the pressure. However, for higher blood pressures, the oscillatory behavior of the WSS is observed with a reduced WSS at peak systole at the neck of the stenosis. An increased WSS at the downstream is observed and it is maximum at the neck of the stenosis. The temporal plots bring out the differences in the WSS for different blood pressures. The variation of WSS is proportional to pressure for normal blood pressure. However, as the blood pressure increases the oscillatory behavior was more evident. With increased blood pressure, the WSS tends to reduce and it is concentrated mainly near the

stenosis region at the bifurcation near the inner wall of the ICA, whereas, the low WSS region is immediately after the stenosis for all the cases. However, at this instant, the WSS increases pre stenosis at the neck. Low WSS was also observed at the carotid sinus and post stenosis due to flow recirculation caused to increased arterial deformation. In the Carreau – Yasuda model, the behavior was similar to the Newtonian model, however, the low WSS region was more predominant at the base of the ECA and post stenosis. According to Fry [266], shear stress exceeding 40 Pa is critical to endothelial cells. Moreover, Ramstack et al [267] claimed that a shear stress magnitude of 100 Pa can result in detachment of the endothelial cell layer resulting in plaque rupture and for clots resulting in a stroke. It was safe to say based on the above results that there is no biomechanical damage to the endothelial layer of the arterial wall.

Since the stenosis was in ECA, its effect on the healthy ICA was greater due to the law of conservation of mass. The blocked ECA leads to higher flow recirculation in carotid sinus making it a favorable location for plaque deposits. These observations led to a more concentrated analysis of WSS based descriptors on the artery wall. WSS is a flow-driven quantity, therefore, the blood pressure also has a significant effect on it. Since the flow is axial, the WSS was higher in axial direction compared to other directions. However, at high flow rates, the oscillatory behavior was due to disturbed flow developed due to interaction between the stenosed region of the arterial wall and blood, creating unstable flow domains, leading to significant flow in the direction perpendicular to flow direction. Therefore, using the WSS markers, the location favorable to secondary plaque accumulation can be determined.

Meanwhile, studies have also found that flow separation, recirculation and low shear stress at the carotid sinus makes the area susceptible to plaque accumulation [256]. The low shear stress is the most important index which determines the development of

atherosclerosis. Hence, the maximum OSI was seen in the regions where the WSS was low and there was high flow recirculation. Moreover, this kind of investigation with detailed discussion on variations in flow behavior under the influence of different blood pressures and rheology offers the preliminary information for further studies to be used as diagnostic tool and planning of surgical interventions.

Helical flow naturally occurs throughout the arterial tree because of the geometric complexity of the vasculature and flow conditions [269]. The benefits of helical flow such as reduced flow disturbance which leads to disturbed shear is observed by researchers. The presence of helical flow may therefore protect the vasculature from atherosclerotic disease [270]. In this study the presence of helical flow in normal and stenosed carotid artery model is studied for different blood pressures and blood rheology models. The presence of helical flow is associated with oscillatory shear and it is observed that with increased blood pressure the helical intensity is reduced which indicated that the increased blood pressure can lead to disturbed shear leading to atherosclerotic lesion. The results exhibit high helical intensity and strong balance between helical structures coinciding with low distribution of oscillatory shear. This suggests that high helical intensity coupled with balanced helical structures is capable of suppressing the exposure to low or oscillatory shear. These observations are in agreement with Gallo et al [271] who observed that high helical intensity coupled with balanced helical structure can suppress areas of low or oscillatory shear in carotid bifurcation.

The three – dimensional CFD and FSI analysis revealed that increased blood pressure led to reduced maximum wall shear stress and higher recirculation zones in critical areas in the carotid artery that were captured by solving the flow field using three dimensional fully coupled FSI analysis. The major conclusions from the analysis are as follows,

1. The CFD (rigid wall assumption) analysis overestimates the WSS as compared to FSI analysis.
2. In FSI analysis, the WSS magnitude predicted by the Newtonian model is lower compaered to Carreau – yasuda model due to the shear thinning behaviour captured by the Carreau – Yasuda model.
3. The flow recirculation zone is mainly observed in the carotid sinus region in the normal carotid artery model, whereas in the stenosed carotid artery, it is also seen in the post stenotic region due to sudden increase in the cross-section regions, that correspond to low-WSS regions, as areas prone to atherosclerosis.
4. The oscillatory shear index is mainly model-specific, as there is no significant difference in the distribution between different blood pressure conditions.
5. The results show that the formation of atherosclerotic plaque in regions such as the posterior wall of the carotid sinus is high as the WSS is lower.
6. Helical intensity is higher in stenosed model compared to normal model, also the difference between the rheological model is more prominent in stenosed model compared to the normal model.

7.1 Recommendation for future work.

The present study assumed the arterial wall to be linearly elastic. However, physically the actual nature of the artery is viscoelastic. The FSI study by considering the anisotropic property of the artery can be performed to demonstrate its effect on haemodynamics.

In this study, the material property of the plaque is considered the same as the artery. The study can be further improved by considering the material properties of the plaque and artery separately. Also, the stiffness of the artery wall is assumed to be the same for different blood pressures. However, it is observed that at elevated blood pressures the

stiffness of the artery varies. It can be investigated further by incorporating varying stiffness of the artery corresponding to increasing blood pressure.

References

[1] C. Weber and H. Noels, "Atherosclerosis: Current pathogenesis and therapeutic options," *Nat. Med.*, vol. 17, no. 11, pp. 1410–1422, 2011.

[2] D. G. Harrison, "The shear stress of keeping arteries clear," *Nat. Med.*, vol. 11, no. 4, pp. 375–376, 2005.

[3] A. S. M. Khader, "Fluid-structure interaction of blood flow Through human arteries," Manipal Institute of Technology, Manipal, 2014.

[4] C. C. H. Klaus Ley, Yury I. Miller, "Monocyte and Macrophage Dynamics during Atherogenesis," *Arter. Thromb Vasc Biol*, vol. 31, no. 7, pp. 1506–1516, 2011.

[5] J. Dong, "Development of a haemodynamic model for improving clinical treatment of vascular disease," 2015.

[6] J. Yang *et al.*, "Wall shear stress in hypertensive patients is associated with carotid vascular deformation assessed by speckle tracking strain imaging," *Clin. Hypertens.*, vol. 20, no. 1, p. 10, 2014.

[7] R. Agarwal, V. K. Katiyar, and P. Pradhan, "A mathematical modeling of pulsatile flow in carotid artery bifurcation," *Int. J. Eng. Sci.*, vol. 46, no. 11, pp. 1147–1156, 2008.

[8] J. Janela, A. Moura, and A. Sequeira, "A 3D non-Newtonian fluid-structure interaction model for blood flow in arteries," *J. Comput. Appl. Math.*, vol. 234, no. 9, pp. 2783–2791, 2010.

[9] L.-S. Yao, M. Mamun Molla, and S. Ghosh Moulic, "Fully-Developed Circular-Pipe Flow of a Non-Newtonian Pseudoplastic Fluid," *Univers. J. Mech. Eng.*, vol. 1, no. 2, pp. 23–31, 2013.

[10] M. G. Rabby, A. Razzak, and M. M. Molla, "Pulsatile non-Newtonian blood flow through a model of arterial stenosis," *Procedia Eng.*, vol. 56, pp. 225–231, 2013.

[11] H. J. M. B. Michael Eliasziw, James Kennedy, Michael D Hill, Alastair M Buchan, "Early risk of stroke after a transient ischemic attack in patients with internal carotid artery disease," vol. 0, no. 0, pp. 1–6, 2017.

[12] M. Toloui, B. Firoozabadi, and M. S. Saidi, "A numerical study of the effects of blood rheology and vessel deformability on the hemodynamics of carotid bifurcation," *Sci. Iran.*, vol. 19, no. 1, pp. 119–126, 2012.

[13] M. M. Corrada *et al.*, "Age of onset of hypertension and risk of dementia in the oldest-old: The 90+ Study," *Alzheimer's Dement.*, vol. 13, no. 2, pp. 103–110, 2017.

[14] Y. Fan, W. Jiang, Y. Zou, J. Li, J. Chen, and X. Deng, "Numerical simulation of pulsatile non-Newtonian flow in the carotid artery bifurcation," *Acta Mech. Sin.*, vol. 25, no. 2, pp. 249–255, 2009.

[15] B. M. Johnston, P. R. Johnston, S. Corney, and D. Kilpatrick, "Non-Newtonian blood flow in human right coronary arteries: Steady state simulations," *J.*

Biomech., vol. 37, no. 5, pp. 709–720, 2004.

[16] J. Chen and X. Y. Lu, "Numerical investigation of the non-Newtonian blood flow in a bifurcation model with a non-planar branch," *J. Biomech.*, vol. 37, no. 12, pp. 1899–1911, 2004.

[17] F. J. H. Gijsen, E. Allanic, F. N. Van De Vosse, and J. D. Janssen, "The influence of the non-Newtonian properties of blood on the flow in large arteries: Unsteady flow in a 90°curved tube," *J. Biomech.*, vol. 32, no. 7, pp. 705–713, 1999.

[18] R. Tabrizchi and M. K. Pugsley, "Methods of blood flow measurement in the arterial circulatory system," *J. Pharmacol. Toxicol. Methods*, vol. 44, no. 2, pp. 375–384, 2000.

[19] N. Pomella, E. N. Wilhelm, C. Kolyva, J. González-Alonso, M. Rakobowchuk, and A. W. Khir, "Common Carotid Artery Diameter, Blood Flow Velocity and Wave Intensity Responses at Rest and during Exercise in Young Healthy Humans: A Reproducibility Study," *Ultrasound Med. Biol.*, vol. 43, no. 5, pp. 943–957, 2017.

[20] N. Riaz, S. L. Wolden, D. Y. Gelblum, and J. Eric, "HHS Public Access," vol. 118, no. 24, pp. 6072–6078, 2016.

[21] N. Vorobtsova, C. Chiastra, M. A. Stremler, D. C. Sane, F. Migliavacca, and P. Vlachos, "Effects of Vessel Tortuosity on Coronary Hemodynamics: An Idealized and Patient-Specific Computational Study," *Ann. Biomed. Eng.*, vol. 44, no. 7, pp. 2228–2239, 2016.

[22] B. Guerciotti *et al.*, "Computational study of the fluid-dynamics in carotids before and after endarterectomy," *J. Biomech.*, vol. 49, no. 1, pp. 26–38, 2016.

[23] D. Gallo, D. A. Steinman, P. B. Bijari, and U. Morbiducci, "Helical flow in carotid bifurcation as surrogate marker of exposure to disturbed shear," *J. Biomech.*, vol. 45, no. 14, pp. 2398–2404, 2012.

[24] J. Alastruey, N. Xiao, H. Fok, T. Schaeffter, and C. A. Figueroa, "On the impact of modelling assumptions in multi-scale, subject-specific models of aortic haemodynamics," *J. R. Soc. Interface*, vol. 13, no. 119, 2016.

[25] M. Cibis *et al.*, "Relation between wall shear stress and carotid artery wall thickening MRI versus CFD," *J. Biomech.*, vol. 49, no. 5, pp. 735–741, 2016.

[26] D. A. Steinman *et al.*, " Segment-specific associations between local haemodynamic and imaging markers of early atherosclerosis at the carotid artery: an in vivo human study ," *J. R. Soc. Interface*, vol. 15, no. 147, p. 20180352, 2018.

[27] F. Rikhtegar *et al.*, "Choosing the optimal wall shear parameter for the prediction of plaque location-A patient-specific computational study in human left coronary arteries," *Atherosclerosis*, vol. 221, no. 2, pp. 432–437, 2012.

[28] I. Marshall, P. Papathanasopoulou, and K. Wartolowska, "Carotid flow rates and flow division at the bifurcation in healthy volunteers," *Physiol. Meas.*, vol. 25, no. 3, pp. 691–697, 2004.

[29] Benjamin et al, *Heart Disease and Stroke Statistics—2019 Update: A Report From the*

American Heart Association, vol. 139, no. 10. 2019.

[30] P. M. Rothwell, R. Gibson, and C. P. Warlow, "Interrelation between plaque surface morphology and degree of stenosis on carotid angiograms and the risk of ischemic stroke in patients with symptomatic carotid stenosis," *Stroke*, vol. 31, no. 3, pp. 615–621, 2000.

[31] J. Bamford, P. Sandercock, M. Dennis, C. Warlow, and J. Burn, "Classification and natural history of clinically identifiable subtypes of cerebral infarction," *Lancet*, vol. 337, no. 8756, pp. 1521–1526, 1991.

[32] C. A. Taylor, T. J. R. Hughes, and C. K. Zarins, "Finite element modeling of blood flow in arteries," *Comput. Methods Appl. Mech. Eng.*, vol. 158, no. 1–2, pp. 155–196, 1998.

[33] C. Michiels, "Endothelial cell functions," *J. Cell. Physiol.*, vol. 196, no. 3, pp. 430–443, 2003.

[34] Y. S. Chatzizisis, A. U. Coskun, M. Jonas, E. R. Edelman, C. L. Feldman, and P. H. Stone, "Role of Endothelial Shear Stress in the Natural History of Coronary Atherosclerosis and Vascular Remodeling. Molecular, Cellular, and Vascular Behavior," *J. Am. Coll. Cardiol.*, vol. 49, no. 25, pp. 2379–2393, 2007.

[35] B. C. Traub, O. and Berk, "Laminar shear stress: Mechanisms by which endothelial cells transduce an atheroprotective force.," *Arterioscler. Throm- bosis, Vasc. Biol.*, vol. 18, no. 5, pp. 677–685, 1998.

[36] J. W. Yau, H. Teoh, and S. Verma, "Endothelial cell control of thrombosis," *BMC Cardiovasc. Disord.*, vol. 15, no. 1, pp. 1–11, 2015.

[37] J. E. Barbato and E. Tzeng, "Nitric oxide and arterial disease," *J. Vasc. Surg.*, vol. 40, no. 1, pp. 187–193, 2004.

[38] A. Woywodt, "Circulating endothelial cells: life, death, detachment and repair of the endothelial cell layer," *Nephrol. Dial. Transplant.*, vol. 17, no. 10, pp. 1728–1730, 2002.

[39] D. MICHAEL A. GIMBRONE, JR., JAMES N. TOPPER, TOBI NAGEL and A. G. G.-C. KEITH R. ANDERSON, "Endothelial Dysfunction, Hemodynamic Forces, and Atherogenesis," p. 11, 2001.

[40] J. Davignon and P. Ganz, "Role of endothelial dysfunction in atherosclerosis," *Circulation*, vol. 109, no. 23 SUPPL., 2004.

[41] T. Karino, "Microscopic structure of disturbed flows in the arterial and venous systems, and its implication in the localization of vascular diseases.," *Int. Angiol. a J. Int. Union Angiol.*, vol. 5, no. 4, pp. 297–313, 1986.

[42] T. Nagel, N. Resnick, C. F. Dewey Jr, and M. A. Gimbrone Jr, "Vascular endothelial cells respond to spatial gradients in fluid shear stress by enhanced activation of transcription factors," *Arterioscler. Thromb. Vasc. Biol.*, vol. 19, no. 8, pp. 1825–1834, 1999.

[43] D. P. Giddens, C. K. Zarins, and S. Glagov, "The role of fluid mechanics in the localization and detection of atherosclerosis," *J. Biomech. Eng.*, vol. 115, no. 4B,

pp. 588–594, 1993.

[44] T. Asakura and T. Karino, "Flow patterns and spatial distribution of atherosclerotic lesions in human coronary arteries.," *Circ. Res.*, vol. 66, no. 4, pp. 1045–1066, 1990.

[45] D. N. Ku, D. P. Giddens, C. K. Zarins, and S. Glagov, "Pulsatile flow and atherosclerosis in the human carotid bifurcation. Positive correlation between plaque location and low oscillating shear stress.," *Arterioscler. An Off. J. Am. Hear. Assoc. Inc.*, vol. 5, no. 3, pp. 293–302, 1985.

[46] C. G. Caro, J. M. Fitz-Gerald, and R. C. Schroter, "Arterial wall shear and distribution of early atheroma in man," *Nature*, vol. 223, no. 5211, p. 1159, 1969.

[47] A. Bhagyalakshmi and J. A. Frangos, "Mechanism of shear-induced prostacyclin production in endothelial cells," *Biochem. Biophys. Res. Commun.*, vol. 158, no. 1, pp. 31–37, 1989.

[48] G. M. Rubanyi, J. C. Romero, and P. M. Vanhoutte, "Flow-induced release of endothelium-derived relaxing factor," *Am. J. Physiol. Circ. Physiol.*, vol. 250, no. 6, pp. H1145--H1149, 1986.

[49] M. J. Kuchan and J. A. Frangos, "Shear stress regulates endothelin-1 release via protein kinase C and cGMP in cultured endothelial cells," *Am. J. Physiol. Circ. Physiol.*, vol. 264, no. 1, pp. H150--H156, 1993.

[50] A. M. Malek, G. H. Gibbons, V. J. Dzau, and S. Izumo, "Fluid shear stress differentially modulates expression of genes encoding basic fibroblast growth factor and platelet-derived growth factor B chain in vascular endothelium.," *J. Clin. Invest.*, vol. 92, no. 4, pp. 2013–2021, 1993.

[51] H. J. Hsieh, N. Q. Li, and J. A. Frangos, "Shear stress increases endothelial platelet-derived growth factor mRNA levels," *Am. J. Physiol. Circ. Physiol.*, vol. 260, no. 2, pp. H642--H646, 1991.

[52] M. A. Awolesi, W. C. Sessa, and B. E. Sumpio, "Cyclic strain upregulates nitric oxide synthase in cultured bovine aortic endothelial cells.," *J. Clin. Invest.*, vol. 96, no. 3, pp. 1449–1454, 1995.

[53] T. Iba and B. E. Sumpio, "Morphological response of human endothelial cells subjected to cyclic strain in vitro," *Microvasc. Res.*, vol. 42, no. 3, pp. 245–254, 1991.

[54] J. Liu and S. Agarwal, "Mechanical signals activate vascular endothelial growth factor receptor-2 to upregulate endothelial cell proliferation during inflammation," *J. Immunol.*, vol. 185, no. 2, pp. 1215–1221, 2010.

[55] B. O. Oluwole, W. Du, I. Mills, and B. E. Sumpio, "Gene regulation by mechanical forces," *Endothelium*, vol. 5, no. 2, pp. 85–93, 1997.

[56] B. E. Sumpio and M. D. Widmann, "Enhanced production of endothelium-derived contracting factor by endothelial cells subjected to pulsatile stretch.," *Surgery*, vol. 108, no. 2, pp. 277–281, 1990.

[57] B. E. Sumpio and A. J. Banes, "Prostacyclin synthetic activity in cultured aortic

endothelial cells undergoing cyclic mechanical deformation.," *Surgery*, vol. 104, no. 2, pp. 383–389, 1988.

[58] H. Wang, Y. Fan, Q. Huang, and X. Deng, "The effects of cyclic stretching on vascular endothelial cell orientation, division and proliferation," *J. Biomech.*, vol. 39, p. S581, 2006.

[59] J. H. Haga, Y.-S. J. Li, and S. Chien, "Molecular basis of the effects of mechanical stretch on vascular smooth muscle cells," *J. Biomech.*, vol. 40, no. 5, pp. 947–960, 2007.

[60] H. E. Barrett, K. Van der Heiden, E. Farrell, F. J. H. Gijsen, and A. C. Akyildiz, "Calcifications in atherosclerotic plaques and impact on plaque biomechanics," *J. Biomech.*, vol. 87, pp. 1–12, 2019.

[61] E. L. Teng and A. J. Engler, "Mechanical influences on cardiovascular differentiation and disease modeling," *Exp. Cell Res.*, vol. 377, no. 1, pp. 103–108, 2019.

[62] M. J. Thubrikar and F. Robicsek, "Pressure-induced arterial wall stress and atherosclerosis," *Ann. Thorac. Surg.*, vol. 59, no. 6, pp. 1594–1603, 1995.

[63] R. W. Alexander, "Hypertension and the pathogenesis of atherosclerosis: oxidative stress and the mediation of arterial inflammatory response: a new perspective," *Hypertension*, vol. 25, no. 2, pp. 155–161, 1995.

[64] K. S. Cunningham and A. I. Gotlieb, "The role of shear stress in the pathogenesis of atherosclerosis," *Lab. Investig.*, vol. 85, no. 1, p. 9, 2005.

[65] T. Ohashi and M. Sato, "Remodeling of vascular endothelial cells exposed to fluid shear stress: experimental and numerical approach," *Fluid Dyn. Res.*, vol. 37, no. 1, pp. 40–59, 2005.

[66] U. Landmesser, B. Hornig, and H. Drexler, "Endothelial function: a critical determinant in atherosclerosis?," *Circulation*, vol. 109, no. 21_suppl_1, pp. II--27, 2004.

[67] A. V Dokunin, "A modification of the method of differential manometry for registration of the volume velocity of the blood flow," *Bull. Exp. Biol. Med.*, vol. 46, no. 5, pp. 1414–1417, 1958.

[68] C. Barfod, N. Akgören, M. Fabricius, U. Dirnagl, and M. Lauritzen, "Laser-Doppler measurements of concentration and velocity of moving blood cells in rat cerebral circulation," *Acta Physiol. Scand.*, vol. 160, no. 2, pp. 123–132, 1997.

[69] H. Bitterman, V. Brod, G. Weisz, D. Kushnir, and N. Bitterman, "Effects of oxygen on regional hemodynamics in hemorrhagic shock," *Am. J. Physiol. Circ. Physiol.*, vol. 271, no. 1, pp. H203--H211, 1996.

[70] N. Iida, "Different flow regulation mechanisms between celiac and mesenteric vascular beds in conscious rats," *Hypertension*, vol. 25, no. 2, pp. 260–265, 1995.

[71] J. Urdzik, T. Bjerner, A. Wanders, F. Duraj, U. Haglund, and A. Norén, "Magnetic resonance imaging flowmetry demonstrates portal vein dilatation subsequent to oxaliplatin therapy in patients with colorectal liver metastasis," *Hpb*,

vol. 15, no. 4, pp. 265–272, 2013.

[72] A. M. Elhawary and C. C. Pang, "Renal vascular and tubular actions of calcitonin gene-related peptide: effect of NG-nitro-L-arginine methyl ester.," *J. Pharmacol. Exp. Ther.*, vol. 273, no. 1, pp. 56–63, 1995.

[73] Y. He and R. Tabrizchi, "Effects of niflumic acid on $α$1-adrenoceptor-induced vasoconstriction in mesenteric artery in vitro and in vivo in two-kidney one-clip hypertensive rats," *Eur. J. Pharmacol.*, vol. 328, no. 2–3, pp. 191–199, 1997.

[74] Z. Chen *et al.*, "Noninvasive imaging of in vivo blood flow velocity using optical Doppler tomography," *Opt. Lett.*, vol. 22, no. 14, pp. 1119–1121, 1997.

[75] U. K. M. Decking *et al.*, "High-resolution imaging reveals a limit in spatial resolution of blood flow measurements by microspheres," *Am. J. Physiol. Circ. Physiol.*, vol. 287, no. 3, pp. H1132--H1140, 2004.

[76] P. A. Clingan and M. H. Friedman, "The effect of celiac and renal artery outflows on near-wall velocities in the porcine iliac arteries," *Ann. Biomed. Eng.*, vol. 28, no. 3, pp. 302–308, 2000.

[77] S. W. Day and J. C. McDaniel, "PIV measurements of flow in a centrifugal blood pump: steady flow," *J. Biomech. Eng.*, vol. 127, no. 2, pp. 244–253, 2005.

[78] B. K. Bharadvaj, R. F. Mabon, and D. P. Giddens, "Steady flow in a model of the human carotid bifurcation. Part I—Flow visualization," *J. Biomech.*, vol. 15, no. 5, pp. 349–362, 1982.

[79] M. Conti, C. Long, M. Marconi, R. Berchiolli, Y. Bazilevs, and A. Reali, "Carotid artery hemodynamics before and after stenting: A patient specific CFD study," *Comput. Fluids*, vol. 141, pp. 62–74, 2016.

[80] C. V Nguyen and J. C. Wells, "Direct Measurement of Fluid Velocity Gradients at a Wall by PIV Image Processing with Stereo Reconstruction 1 . Measuring Interfacial Gradients 2 . Near-Wall Image Gradiometry," *Society*, vol. 9, no. 2, pp. 199–208, 2006.

[81] C. K. Zarins, D. P. Giddens, B. K. Bharadvaj, V. S. Sottiurai, R. F. Mabon, and S. Glagov, "Carotid bifurcation atherosclerosis. Quantitative correlation of plaque localization with flow velocity profiles and wall shear stress.," *Circ. Res.*, vol. 53, no. 4, pp. 502–514, 1983.

[82] V. Peiffer, S. J. Sherwin, and P. D. Weinberg, "Does low and oscillatory wall shear stress correlate spatially with early atherosclerosis? A systematic review," *Cardiovasc. Res.*, vol. 99, no. 2, pp. 242–250, Jul. 2013.

[83] K. Perktold and M. Resch, "Numerical flow studies in human carotid artery bifurcations: basic discussion of the geometric factor in atherogenesis," *J. Biomed. Eng.*, vol. 12, no. 2, pp. 111–123, 1990.

[84] B. K. Lee *et al.*, "Hemodynamic effects on atherosclerosis-prone coronary artery: wall shear stress/rate distribution and impedance phase angle in coronary and aortic circulation," *Yonsei Med. J.*, vol. 42, no. 4, pp. 375–383, 2001.

[85] J. G. Myers, J. A. Moore, M. Ojha, K. W. Johnston, and C. R. Ethier, "Factors

influencing blood flow patterns in the human right coronary artery," *Ann. Biomed. Eng.*, vol. 29, no. 2, pp. 109–120, 2001.

[86] X. He and D. N. Ku, "Pulsatile flow in the human left coronary artery bifurcation: average conditions," *J. Biomech. Eng.*, vol. 118, no. 1, pp. 74–82, 1996.

[87] S.-W. Lee, L. Antiga, and D. A. Steinman, "Correlations among indicators of disturbed flow at the normal carotid bifurcation," *J. Biomech. Eng.*, vol. 131, no. 6, p. 61013, 2009.

[88] M. Lei, C. Kleinstreuer, and G. A. Truskey, "Numerical investigation and prediction of atherogenic sites in branching arteries," *J. Biomech. Eng.*, vol. 117, no. 3, pp. 350–357, 1995.

[89] B. Ene-Iordache and A. Remuzzi, "Disturbed flow in radial-cephalic arteriovenous fistulae for haemodialysis: low and oscillating shear stress locates the sites of stenosis," *Nephrol. Dial. Transplant.*, vol. 27, no. 1, pp. 358–368, 2011.

[90] G.-Y. Suh *et al.*, "Quantification of particle residence time in abdominal aortic aneurysms using magnetic resonance imaging and computational fluid dynamics," *Ann. Biomed. Eng.*, vol. 39, no. 2, pp. 864–883, 2011.

[91] I. E. Vignon-Clementel, C. A. Figueroa, K. E. Jansen, and C. A. Taylor, "Outflow boundary conditions for 3D simulations of non-periodic blood flow and pressure fields in deformable arteries," *Comput. Methods Biomech. Biomed. Engin.*, vol. 13, no. 5, pp. 625–640, 2010.

[92] N. M. Maurits, G. E. Loots, and A. E. P. Veldman, "The influence of vessel wall elasticity and peripheral resistance on the carotid artery flow wave form: A CFD model compared to in vivo ultrasound measurements," *J. Biomech.*, vol. 40, no. 2, pp. 427–436, 2007.

[93] H. C. Groen *et al.*, "MRI-based quantification of outflow boundary conditions for computational fluid dynamics of stenosed human carotid arteries," *J. Biomech.*, vol. 43, no. 12, pp. 2332–2338, 2010.

[94] F. J. Gijsen, F. N. van de Vosse, and J. D. Janssen, "The influence of the non-Newtonian properties of blood on the flow in large arteries: steady flow in a carotid bifurcation model," *J. Biomech.*, vol. 32, no. 6, pp. 601–8, 1999.

[95] C. M. Schirmer and A. M. Malek, "Patient based computational fluid dynamic characterization of carotid bifurcation stenosis before and after endovascular revascularization," *J. Neurointerv. Surg.*, vol. 4, no. 6, pp. 448–454, 2012.

[96] A. K. Chaniotis, L. Kaiktsis, D. Katritsis, E. Efstathopoulos, I. Pantos, and V. Marmarellis, "Computational study of pulsatile blood flow in prototype vessel geometries of coronary segments," *Phys. Medica*, vol. 26, no. 3, pp. 140–156, 2010.

[97] M. Tambasco and D. A. Steinman, "Path-dependent hemodynamics of the stenosed carotid bifurcation," *Ann. Biomed. Eng.*, vol. 31, no. 9, pp. 1054–1065, 2003.

[98] K. W. Lee, N. B. Wood, and X. Y. Xu, "Ultrasound image-based computer model of a common carotid artery with a plaque," *Med. Eng. Phys.*, vol. 26, no. 10, pp. 823–840, 2004.

[99] J. Tu, K. K. L. Wong, S. C. P. Cheung, R. Beare, and T. Phan, "Analysis of patient-specific carotid bifurcation models using computational fluid dynamics," *J. Med. Imaging Heal. Informatics*, vol. 1, no. 2, pp. 116–125, 2011.

[100] Y. Fan, W. Jiang, Y. Zou, J. Li, J. Chen, and X. Deng, "Numerical simulation of pulsatile non-Newtonian flow in the carotid artery bifurcation," *Acta Mech. Sin. Xuebao*, vol. 25, no. 2, pp. 249–255, 2009.

[101] A. D. Michaels and K. Chatterjee, "Angioplasty versus bypass surgery for coronary artery disease," *Circulation*, vol. 106, no. 23, pp. e187--e190, 2002.

[102] F. J. H. Gijsen *et al.*, "A new imaging technique to study 3-D plaque and shear stress distribution in human coronary artery bifurcations in vivo," *J. Biomech.*, vol. 40, no. 11, pp. 2349–2357, 2007.

[103] J. V. Soulis, T. M. Farmakis, G. D. Giannoglou, and G. E. Louridas, "Wall shear stress in normal left coronary artery tree," *J. Biomech.*, vol. 39, no. 4, pp. 742–749, 2006.

[104] Y. Huo, J. S. Choy, M. Svendsen, A. K. Sinha, and G. S. Kassab, "Effects of vessel compliance on flow pattern in porcine epicardial right coronary arterial tree," *J. Biomech.*, vol. 42, no. 5, pp. 594–602, 2009.

[105] R. Torii *et al.*, "Fluid--structure interaction analysis of a patient-specific right coronary artery with physiological velocity and pressure waveforms," *Commun. Numer. Methods Eng.*, vol. 25, no. 5, pp. 565–580, 2009.

[106] D. Tang *et al.*, "3D MRI-based anisotropic FSI models with cyclic bending for human coronary atherosclerotic plaque mechanical analysis," *J. Biomech. Eng.*, vol. 131, no. 6, p. 61010, 2009.

[107] B. M. Johnston, P. R. Johnston, S. Corney, and D. Kilpatrick, "Non-Newtonian blood flow in human right coronary arteries: steady state simulations," *J. Biomech.*, vol. 37, no. 5, pp. 709–720, 2004.

[108] K. Perktold and G. Rappitsch, "Computer simulation of local blood flow and vessel mechanics in a compliant carotid artery bifurcation model," *J. Biomech.*, vol. 28, no. 7, pp. 845–856, 1995.

[109] J. R. Cebral, P. J. Yim, R. Löhner, O. Soto, H. Marcos, and P. L. Choyke, "New methods for computational fluid dynamics modeling of carotid artery from magnetic resonance angiography," in *Medical Imaging 2001: Physiology and Function from Multidimensional Images*, 2001, vol. 4321, pp. 177–187.

[110] K. W. Lee and X. Y. Xu, "Modelling of flow and wall behaviour in a mildly stenosed tube," *Med. Eng. Phys.*, vol. 24, no. 9, pp. 575–586, 2002.

[111] S. Tada and J. M. Tarbell, "A computational study of flow in a compliant carotid bifurcation--stress phase angle correlation with shear stress," *Ann. Biomed. Eng.*, vol. 33, no. 9, pp. 1202–1212, 2005.

[112] S. A. Urquiza, P. J. Blanco, M. J. Vénere, and R. A. Feijóo, "Multidimensional modelling for the carotid artery blood flow," *Comput. Methods Appl. Mech. Eng.*, vol. 195, no. 33–36, pp. 4002–4017, 2006.

[113] E. Shaik, "Numerical simulations of blood flow in arteries using fluid-structure interactions," Wichita State University, 2007.

[114] M. X. Li, J. J. Beech-Brandt, L. R. John, P. R. Hoskins, and W. J. Easson, "Numerical analysis of pulsatile blood flow and vessel wall mechanics in different degrees of stenoses," *J. Biomech.*, vol. 40, no. 16, pp. 3715–3724, 2007.

[115] S. W. Cho, S. W. Kim, M. H. Sung, K. C. Rou, and H. S. Ryou, "Fluid-structure interaction analysis on the effects of vessel material properties on blood flow characteristics in stenosed arteries under axial rotation," *Korea Aust. Rheol. J.*, vol. 23, no. 1, pp. 7–16, 2011.

[116] A. Quaini, "Algorithms for fluid-structure interaction problems arising in hemodynamics," Ecole Polytechnique Federale De Lausanne, Suisse, 2009.

[117] J. Degroote, "Development of algorithms for the partitioned simulation of strongly coupled fluid-structure interaction problems," Ghent University, 2010.

[118] S. H. Lee, H. G. Choi, and J. Y. Yool, "Finite element simulation of blood flow in a flexible carotid artery bifurcation," *J. Mech. Sci. Technol.*, vol. 26, no. 5, pp. 1355–1361, 2012.

[119] M. Toloui, B. Firoozabadi, and M. S. Saidi, "A numerical study of the effects of blood rheology and vessel deformability on the hemodynamics of carotid bifurcation," *Sci. Iran.*, vol. 19, no. 1, pp. 119–126, 2012.

[120] L. Formaggia, J.-F. Gerbeau, F. Nobile, and A. Quarteroni, "On the coupling of 3D and 1D Navier--Stokes equations for flow problems in compliant vessels," *Comput. Methods Appl. Mech. Eng.*, vol. 191, no. 6–7, pp. 561–582, 2001.

[121] E. Jarvinen, M. Lyly, J. Ruokolainen, and P. Raback, "Three-dimensional fluid-structure interaction modeling of blood flow in elastic arteries," *ECCOMAS CFD, Swansea, United Kingdom*, 2001.

[122] T. Fukui *et al.*, "Effect of wall motion on arterial wall shear stress," *J. Biomech. Sci. Eng.*, vol. 2, no. 2, pp. 58–68, 2007.

[123] J. Degroote, K.-J. Bathe, and J. Vierendeels, "Performance of a new partitioned procedure versus a monolithic procedure in fluid--structure interaction," *Comput. Struct.*, vol. 87, no. 11–12, pp. 793–801, 2009.

[124] R. S. Salzar, M. J. Thubrikar, and R. T. Eppink, "Pressure-induced mechanical stress in the carotid artery bifurcation: a possible correlation to atherosclerosis," *J. Biomech.*, vol. 28, no. 11, pp. 1333–1340, 1995.

[125] Z. Teng *et al.*, "3D critical plaque wall stress is a better predictor of carotid plaque rupture sites than flow shear stress: an in vivo MRI-based 3D FSI study," *J. Biomech. Eng.*, vol. 132, no. 3, p. 31007, 2010.

[126] M. Oshima, R. Torii, T. Kobayashi, N. Taniguchi, and K. Takagi, "Finite element simulation of blood flow in the cerebral artery," *Comput. Methods Appl. Mech. Eng.*, vol. 191, no. 6–7, pp. 661–671, 2001.

[127] T. Deschamps, P. Schwartz, D. Trebotich, P. Colella, D. Saloner, and R. Malladi, "Vessel segmentation and blood flow simulation using level-sets and embedded

boundary methods," in *International Congress Series*, 2004, vol. 1268, pp. 75–80.

[128] J. Cebral, M. A. Castro, R. Löhner, J. E. Burgess, R. Pergolizzi, and C. M. Putman, "Recent developments in patient-specific image-based modeling of hemodynamics," *Mec. Comput.*, vol. 23, pp. 1471–1482, 2004.

[129] P. L. Rinderu, E. T. Rinderu, L. Gruionu, and C. Bratianu, "A FEM study of aortic hemodynamics in the case of stenosis," *Acta Bioeng. Biomech.*, vol. 4, pp. 526–527, 2003.

[130] G. Tabor, D. Tame, F. Pierron, P. G. Young, A. Watkinson, and J. Thompson, "Patient-specific arterial flow simulation with additional geometric elements," 2006.

[131] C. A. Figueroa, "A coupled-momentum method to model blood flow and vessel deformation in human arteries: applications in disease research and simulation-based medical planning," Stanford University Stanford, CA, 2006.

[132] I. E. Vignon-Clementel, "A coupled multidomain method for computational modeling of blood flows [Ph. D. dissertation]." Stanford University, Mechanical Engineering Department, 2006.

[133] E. Järvinen, P. Råback, M. Lyly, and J.-P. Salenius, "A method for partitioned fluid--structure interaction computation of flow in arteries," *Med. Eng. Phys.*, vol. 30, no. 7, pp. 917–923, 2008.

[134] H. J. Kim, C. A. Figueroa, T. J. R. Hughes, K. E. Jansen, and C. A. Taylor, "Augmented Lagrangian method for constraining the shape of velocity profiles at outlet boundaries for three-dimensional finite element simulations of blood flow," *Comput. Methods Appl. Mech. Eng.*, vol. 198, no. 45–46, pp. 3551–3566, 2009.

[135] P. Reymond, "Pressure and flow wave propagation in patient-specific models of the arterial tree." Ecole Polytechnique Federale De Lausanne, Suisse., 2011.

[136] H. F. Younis *et al.*, "Hemodynamics and wall mechanics in human carotid bifurcation and its consequences for atherogenesis: Investigation of inter-individual variation," *Biomech. Model. Mechanobiol.*, vol. 3, no. 1, pp. 17–32, 2004.

[137] T. E. Tezduyar *et al.*, "Modelling of fluid--structure interactions with the space--time finite elements: Arterial fluid mechanics," *Int. J. Numer. Methods Fluids*, vol. 54, no. 6–8, pp. 901–922, 2007.

[138] T. E. Tezduyar, K. Takizawa, C. Moorman, S. Wright, and J. Christopher, "Multiscale sequentially-coupled arterial FSI technique," *Comput. Mech.*, vol. 46, no. 1, pp. 17–29, 2010.

[139] T. E. Tezduyar, S. Sathe, M. Schwaab, and B. S. Conklin, "Arterial fluid mechanics modeling with the stabilized space--time fluid--structure interaction technique," *Int. J. Numer. Methods Fluids*, vol. 57, no. 5, pp. 601–629, 2008.

[140] K. Takizawa *et al.*, "Patient-specific arterial fluid--structure interaction modeling of cerebral aneurysms," *Int. J. Numer. Methods Fluids*, vol. 65, no. 1–3, pp. 308–323, 2011.

[141] M. Toma, A. Krdey, S. Takagi, and M. OSHIMA, "Strongly coupled fluid-structure interaction cardiovascular analysis with the effect of peripheral network,"

SEISAN KENKYU, vol. 63, no. 3, pp. 339–344, 2011.

[142] M.-C. Hsu and Y. Bazilevs, "Blood vessel tissue prestress modeling for vascular fluid--structure interaction simulation," *Finite Elem. Anal. Des.*, vol. 47, no. 6, pp. 593–599, 2011.

[143] D. Tang *et al.*, "3D MRI-based multicomponent FSI models for atherosclerotic plaques," *Ann. Biomed. Eng.*, vol. 32, no. 7, pp. 947–960, 2004.

[144] D. Tang *et al.*, "A negative correlation between human carotid atherosclerotic plaque progression and plaque wall stress: in vivo MRI-based 2D/3D FSI models," *J. Biomech.*, vol. 41, no. 4, pp. 727–736, 2008.

[145] S. A. Kock *et al.*, "Mechanical stresses in carotid plaques using MRI-based fluid--structure interaction models," *J. Biomech.*, vol. 41, no. 8, pp. 1651–1658, 2008.

[146] D. Tang *et al.*, "Sites of rupture in human atherosclerotic carotid plaques are associated with high structural stresses: an in vivo MRI-based 3D fluid-structure interaction study," *Stroke*, vol. 40, no. 10, pp. 3258–3263, 2009.

[147] C. Yang *et al.*, "In VivoIVUS-Based 3-D Fluid--Structure Interaction Models With Cyclic Bending and Anisotropic Vessel Properties for Human Atherosclerotic Coronary Plaque Mechanical Analysis," *IEEE Trans. Biomed. Eng.*, vol. 56, no. 10, pp. 2420–2428, 2009.

[148] J. R. Leach, V. L. Rayz, B. Soares, M. Wintermark, M. R. K. Mofrad, and D. Saloner, "Carotid atheroma rupture observed in vivo and FSI-predicted stress distribution based on pre-rupture imaging," *Ann. Biomed. Eng.*, vol. 38, no. 8, pp. 2748–2765, 2010.

[149] H. Gao, "Carotid plaque stress analysis by fluid structure interaction based on in-vivo MRI: Implications to plaque vulnerability assessment," 2010.

[150] N. Aristokleous *et al.*, "Head posture influences the geometric and hemodynamic features on the healthy human carotid bifurcation," in *2012 IEEE 12th International Conference on Bioinformatics & Bioengineering (BIBE)*, 2012, pp. 727–731.

[151] L. Antiga, "Patient-specific modeling of geometry and blood flow in large arteries," *Politec. di Milano*, 2002.

[152] B. N. Steele, M. S. Olufsen, and C. A. Taylor, "Fractal network model for simulating abdominal and lower extremity blood flow during resting and exercise conditions," *Comput. Methods Biomech. Biomed. Engin.*, vol. 10, no. 1, pp. 39–51, 2007.

[153] Y. Papaharilaou *et al.*, "Effect of head posture on the healthy human carotid bifurcation hemodynamics," *Med. Biol. Eng. Comput.*, vol. 51, no. 1–2, pp. 207–218, 2013.

[154] D. A. Steinman, "Image-based computational fluid dynamics modeling in realistic arterial geometries," *Ann. Biomed. Eng.*, vol. 30, no. 4, pp. 483–497, 2002.

[155] L. Antiga, M. Piccinelli, L. Botti, B. Ene-Iordache, A. Remuzzi, and D. A. Steinman, "An image-based modeling framework for patient-specific computational hemodynamics," *Med. Biol. Eng. Comput.*, vol. 46, no. 11, p. 1097,

2008.

[156] K. R. Moyle, L. Antiga, and D. A. Steinman, "Inlet conditions for image-based CFD models of the carotid bifurcation: is it reasonable to assume fully developed flow?," *J. Biomech. Eng.*, vol. 128, no. 3, pp. 371–379, 2006.

[157] E. J. Bekkers and C. A. Taylor, "Multiscale vascular surface model generation from medical imaging data using hierarchical features," *IEEE Trans. Med. Imaging*, vol. 27, no. 3, pp. 331–341, 2008.

[158] P. B. Bijari, L. Antiga, and D. A. Steinman, "Reliability of vascular geometry factors derived from clinical MRA," in *Medical Imaging 2009: Visualization, Image-Guided Procedures, and Modeling*, 2009, vol. 7261, p. 72612X.

[159] C. J. Slager *et al.*, "True 3-dimensional reconstruction of coronary arteries in patients by fusion of angiography and IVUS (ANGUS) and its quantitative validation," *Circulation*, vol. 102, no. 5, pp. 511–516, 2000.

[160] F. J. H. Gijsen *et al.*, "A new imaging technique to study 3-D plaque and shear stress distribution in human coronary artery bifurcations in vivo," *J. Biomech.*, vol. 40, no. 11, pp. 2349–2357, 2007.

[161] "ITK - Segmentation & Registration Toolkit." [Online]. Available: https://itk.org/. [Accessed: 09-Aug-2019].

[162] "SimTK: Welcome." [Online]. Available: https://simtk.org/. [Accessed: 09-Aug-2019].

[163] "vmtk - the Vascular Modelling Toolkit." [Online]. Available: http://www.vmtk.org/vmtkscripts/vmtksurfacetonumpy.html. [Accessed: 09-Aug-2019].

[164] O. Sahni, J. Müller, K. E. Jansen, M. S. Shephard, and C. A. Taylor, "Efficient anisotropic adaptive discretization of the cardiovascular system," *Comput. Methods Appl. Mech. Eng.*, vol. 195, no. 41–43, pp. 5634–5655, 2006.

[165] D. A. Steinman, "Image-based computational fluid dynamics modeling in realistic arterial geometries," *Ann. Biomed. Eng.*, vol. 30, no. 4, pp. 483–497, 2002.

[166] L. Botti, M. Piccinelli, B. Ene-Iordache, A. Remuzzi, and L. Antiga, "An adaptive mesh refinement solver for large-scale simulation of biological flows," *Int. j. numer. method. biomed. eng.*, vol. 26, no. 1, pp. 86–100, 2010.

[167] K. M. Tse, P. Chiu, H. P. Lee, and P. Ho, "Investigation of hemodynamics in the development of dissecting aneurysm within patient-specific dissecting aneurismal aortas using computational fluid dynamics (CFD) simulations," *J. Biomech.*, vol. 44, no. 5, pp. 827–836, 2011.

[168] C. A. Taylor and D. A. Steinman, "Image-based modeling of blood flow and vessel wall dynamics: applications, methods and future directions," *Ann. Biomed. Eng.*, vol. 38, no. 3, pp. 1188–1203, 2010.

[169] C. G. Caro, J. M. Fitz-Gerald, and R. C. Schroter, "Atheroma and arterial wall shear-Observation, correlation and proposal of a shear dependent mass transfer mechanism for atherogenesis," *Proc. R. Soc. London. Ser. B. Biol. Sci.*, vol. 177, no. 1046, pp. 109–133, 1971.

[170] M. H. Friedman, G. M. Hutchins, C. B. Bargeron, O. J. Deters, and F. F. Mark, "Correlation between intimal thickness and fluid shear in human arteries," *Atherosclerosis*, vol. 39, no. 3, pp. 425–436, 1981.

[171] D. E. M. Palmen, F. J. H. Gijsen, F. N. de Vosse, and J. D. Janssen, "Diagnosing minor stenoses in carotid artery bifurcation models using the disturbed velocity," *J. Vasc. Investig.*, vol. 3, no. 1, pp. 26–41, 1997.

[172] K. Perktold and D. Hilbert, "Numerical simulation of pulsatile flow in a carotid bifurcation model," *J. Biomed. Eng.*, vol. 8, no. 3, pp. 193–199, 1986.

[173] C. C. M. Rindt, A. A. Van Steenhoven, J. D. Janssen, R. S. Reneman, and A. Segal, "A numerical analysis of steady flow in a three-dimensional model of the carotid artery bifurcation," *J. Biomech.*, vol. 23, no. 5, pp. 461–473, 1990.

[174] C. C. M. Rindt, A. A. Van Steenhoven, J. D. Janssen, and G. Vossers, "Unsteady entrance flow in a 90 curved tube," *J. Fluid Mech.*, vol. 226, pp. 445–474, 1991.

[175] Y. I. Cho and K. R. Kensey, "Effects of the non-Newtonian viscosity of blood on flows in a diseased arterial vessel. Part 1: Steady flows," *Biorheology*, vol. 28, no. 3–4, pp. 241–262, 1991.

[176] K. Perktold, R. O. Peter, M. Resch, and G. Langs, "Pulsatile non-Newtonian blood flow in three-dimensional carotid bifurcation models: a numerical study of flow phenomena under different bifurcation angles," *J. Biomed. Eng.*, vol. 13, no. 6, pp. 507–515, 1991.

[177] C. M. Rodkiewicz, P. Sinha, and J. S. Kennedy, "On the application of a constitutive equation for whole human blood," *J. Biomech. Eng.*, vol. 112, no. 2, pp. 198–206, 1990.

[178] J. P. Baaijens, J. D. Janssen, and others, "Numerical analysis of steady generalized Newtonian blood flow in a 2D model of the carotid artery bifurcation.," *Biorheology*, vol. 30, no. 1, pp. 63–74, 1993.

[179] P. D. Ballyk, D. A. Steinman, and C. R. Ethier, "Simulation of non-Newtonian blood flow in an end-to-side anastomosis.," *Biorheology*, vol. 31, no. 5, pp. 565–86.

[180] D. N. Ku and D. Liepsch, "The effects of non-Newtonian viscoelasticity and wall elasticity on flow at a 90 bifurcation," *Biorheology*, vol. 23, no. 4, pp. 359–370, 1986.

[181] D. Liepsch and S. T. Moravec, "Pulsatile flow of non-Newtonian fluid in distensible models of human arteries," *Biorheology*, vol. 21, no. 4, pp. 571–586, 1984.

[182] H. A. González and N. O. Moraga, "On predicting unsteady non-Newtonian blood flow," *Appl. Math. Comput.*, vol. 170, no. 2, pp. 909–923, 2005.

[183] M. Jahangiri, M. Saghafian, and M. R. Sadeghi, "Effects of non-Newtonian behavior of blood on wall shear stress in an elastic vessel with simple and consecutive stenosis," *Biomed. Pharmacol. J.*, vol. 8, no. 1, pp. 123–131, 2015.

[184] Y. Fung, *Biomechanics: mechanical properties of living tissues*. Springer Science & Business Media, 2013.

[185] M. M. Molla and M. C. Paul, "LES of non-Newtonian physiological blood flow in a model of arterial stenosis," *Med. Eng. Phys.*, vol. 34, no. 8, pp. 1079–1087, 2012.

[186] H. K. Huh, H. Ha, and S. J. Lee, "Effect of non-Newtonian viscosity on the fluid-dynamic characteristics in stenotic vessels," *Exp. Fluids*, vol. 56, no. 8, p. 167, 2015.

[187] S. Kefayati, J. S. Milner, D. W. Holdsworth, and T. L. Poepping, "In vitro shear stress measurements using particle image velocimetry in a family of carotid artery models: effect of stenosis severity, plaque eccentricity, and ulceration," *PLoS One*, vol. 9, no. 7, p. e98209, 2014.

[188] N. A. Buchmann, C. Atkinson, M. C. Jeremy, and J. Soria, "Tomographic particle image velocimetry investigation of the flow in a modeled human carotid artery bifurcation," *Exp. Fluids*, vol. 50, no. 4, pp. 1131–1151, 2011.

[189] J. Chen and X.-Y. Lu, "Numerical investigation of the non-Newtonian pulsatile blood flow in a bifurcation model with a non-planar branch," *J. Biomech.*, vol. 39, no. 5, pp. 818–832, 2006.

[190] H. K. Huh, H. Ha, and S. J. Lee, "Effect of non-Newtonian viscosity on the fluid-dynamic characteristics in stenotic vessels," *Exp. Fluids*, vol. 56, no. 8, pp. 1–12, 2015.

[191] M. Y. Yousif, D. W. Holdsworth, and T. L. Poepping, "A blood-mimicking fluid for particle image velocimetry with silicone vascular models," *Exp. Fluids*, vol. 50, no. 3, pp. 769–774, 2011.

[192] A. L. DiCarlo, D. W. Holdsworth, and T. L. Poepping, "Study of the effect of stenosis severity and non-Newtonian viscosity on multidirectional wall shear stress and flow disturbances in the carotid artery using particle image velocimetry," *Med. Eng. Phys.*, vol. 65, pp. 8–23, 2019.

[193] M. Iasiello, K. Vafai, A. Andreozzi, and N. Bianco, "Analysis of non-Newtonian effects within an aorta-iliac bifurcation region," *J. Biomech.*, vol. 64, pp. 153–163, 2017.

[194] R. B. Bird, R. C. Armstrong, and O. Hassager, "Dynamics of polymeric liquids. Vol. 1: Fluid mechanics," 1987.

[195] F. J. Walburn and D. J. Schneck, "A constitutive equation for whole human blood," *Biorheology*, vol. 13, no. 3, pp. 201–210, 1976.

[196] A. Razavi, E. Shirani, and M. R. Sadeghi, "Numerical simulation of blood pulsatile flow in a stenosed carotid artery using different rheological models," *J. Biomech.*, vol. 44, no. 11, pp. 2021–2030, 2011.

[197] A. Sharifi and H. Niazmand, "Analysis of flow and LDL concentration polarization in siphon of internal carotid artery: Non-Newtonian effects," *Comput. Biol. Med.*, vol. 65, pp. 93–102, 2015.

[198] A. Zaman, N. Ali, M. Sajid, and T. Hayat, "Effects of unsteadiness and non-Newtonian rheology on blood flow through a tapered time-variant stenotic artery," *AIP Adv.*, vol. 5, no. 3, p. 37129, 2015.

[199] C. Vlachopoulos, K. Aznaouridis, and C. Stefanadis, "Prediction of cardiovascular events and all-cause mortality with arterial stiffness: a systematic review and meta-analysis," *J. Am. Coll. Cardiol.*, vol. 55, no. 13, pp. 1318–1327, 2010.

[200] G. Mancia *et al.*, "2013 ESH/ESC guidelines for the management of arterial hypertension: the Task Force for the Management of Arterial Hypertension of the European Society of Hypertension (ESH) and of the European Society of Cardiology (ESC)," *Blood Press.*, vol. 22, no. 4, pp. 193–278, 2013.

[201] H. Aatola *et al.*, "Simplified definitions of elevated pediatric blood pressure and high adult arterial stiffness," *Pediatrics*, vol. 132, no. 1, pp. e70--e76, 2013.

[202] M. Cecelja and P. Chowienczyk, "Dissociation of aortic pulse wave velocity with risk factors for cardiovascular disease other than hypertension: a systematic review," *Hypertension*, vol. 54, no. 6, pp. 1328–1336, 2009.

[203] H. Aatola *et al.*, "Lifetime risk factors and arterial pulse wave velocity in adulthood: the cardiovascular risk in young Finns study," *Hypertension*, vol. 55, no. 3, pp. 806–811, 2010.

[204] S. P. Glasser and D. K. Arnett, "Vascular stiffness and the" chicken-or-the-egg" question," *Hypertension*, vol. 51, no. 2, p. 177, 2008.

[205] R. R. Townsend *et al.*, "Recommendations for improving and standardizing vascular research on arterial stiffness: a scientific statement from the American Heart Association," *Hypertension*, vol. 66, no. 3, pp. 698–722, 2015.

[206] B. M. Kaess *et al.*, "Aortic stiffness, blood pressure progression, and incident hypertension," *Jama*, vol. 308, no. 9, pp. 875–881, 2012.

[207] S. S. Najjar *et al.*, "Pulse wave velocity is an independent predictor of the longitudinal increase in systolic blood pressure and of incident hypertension in the Baltimore Longitudinal Study of Aging," *J. Am. Coll. Cardiol.*, vol. 51, no. 14, pp. 1377–1383, 2008.

[208] H. Takase *et al.*, "Brachial-ankle pulse wave velocity predicts increase in blood pressure and onset of hypertension," *Am. J. Hypertens.*, vol. 24, no. 6, pp. 667–673, 2011.

[209] T. Koivistoinen *et al.*, "Pulse wave velocity predicts the progression of blood pressure and development of hypertension in young adults," *Hypertension*, vol. 71, no. 3, pp. 451–456, 2018.

[210] K. Jesionek and M. Kostur, "Low-density lipoprotein accumulation within the right coronary artery walls for physiological and hypertension conditions," *Biosystems*, vol. 177, pp. 39–43, 2019.

[211] B. Bronte-Stewart and R. H. Heptinstall, "The relationship between experimental hypertension and cholesterol-induced atheroma in rabbits," *J. Pathol. Bacteriol.*, vol. 68, no. 2, pp. 407–417, 1954.

[212] G. E. Wakerlin, W. G. Moss, J. P. Kiely, M. G. Fein, and M. F. Kejikawa, "Effect of experimental renal hypertension on experimental thiouracil-cholesterol atherosclerosis in dogs," *Circ. Res.*, vol. 5, no. 4, pp. 426–434, 1957.

[213] A. V Chobanian *et al.*, "The seventh report of the joint national committee on prevention, detection, evaluation, and treatment of high blood pressure: the JNC 7 report," *Jama*, vol. 289, no. 19, pp. 2560–2571, 2003.

[214] Y. Wang and Q. J. Wang, "The prevalence of prehypertension and hypertension among US adults according to the new joint national committee guidelines: new challenges of the old problem," *Arch. Intern. Med.*, vol. 164, no. 19, pp. 2126–2134, 2004.

[215] S. Lewington, "Prospective studies collaboration. Age-specific relevance of usual blood pressure to vascular mortality: a meta-analysis of individual data for one million adults in 61 prospective studies," *Lancet*, vol. 360, pp. 1903–1913, 2002.

[216] J. J. Wentzel, Y. S. Chatzizisis, F. J. H. Gijsen, G. D. Giannoglou, C. L. Feldman, and P. H. Stone, "Endothelial shear stress in the evolution of coronary atherosclerotic plaque and vascular remodelling: current understanding and remaining questions," *Cardiovasc. Res.*, vol. 96, no. 2, pp. 234–243, 2012.

[217] C. K. Zarins, D. P. Giddens, B. K. Bharadvaj, V. S. Sottiurai, R. F. Mabon, and S. Glagov, "Carotid bifurcation atherosclerosis. quantitative correlation of plaque localization with flow velocity profiles and wall shear stress," *Circ. Re- search*, vol. 53, no. 4, pp. 502–514, 1983.

[218] V. Peiffer, S. J. Sherwin, and P. D. Weinberg, "Does low and oscillatory wall shear stress correlate spatially with early atherosclerosis? A systematic review," *Cardiovasc. Res.*, vol. 99, no. 2, pp. 242–250, Jul. 2013.

[219] C. Wang, B. M. Baker, C. S. Chen, and M. A. Schwartz, "Endothelial cell sensing of flow direction," *Arterioscler. Thromb. Vasc. Biol.*, vol. 33, no. 9, pp. 2130–2136, 2013.

[220] Y. Mohamied, E. M. Rowland, E. L. Bailey, S. J. Sherwin, M. A. Schwartz, and P. D. Weinberg, "Change of direction in the biomechanics of atherosclerosis," *Ann. Biomed. Eng.*, vol. 43, no. 1, pp. 16–25, 2015.

[221] A. Arzani and S. C. Shadden, "Characterizations and correlations of wall shear stress in aneurysmal flow," *J. Biomech. Eng.*, vol. 138, no. 1, p. 14503, 2016.

[222] U. Morbiducci *et al.*, "A rational approach to defining principal axes of multidirectional wall shear stress in realistic vascular geometries, with application to the study of the influence of helical flow on wall shear stress directionality in aorta," *J. Biomech.*, vol. 48, no. 6, pp. 899–906, 2015.

[223] A. Chakraborty *et al.*, "Impact of bi-axial shear on atherogenic gene expression by endothelial cells," *Ann. Biomed. Eng.*, vol. 44, no. 10, pp. 3032–3045, 2016.

[224] M. A. Balafar, A. R. Ramli, M. I. Saripan, and S. Mashohor, "Review of brain MRI image segmentation methods," *Artif. Intell. Rev.*, vol. 33, no. 3, pp. 261–274, 2010.

[225] Materialise®, "Mimics Student Edition Course Book," *Mimics® Student Ed. Course B.*, p. 83, 2015.

[226] J. H. Stein, "Carotid intima-media thickness and vascular age: you are only as old as your arteries look," *J. Am. Soc. Echocardiogr.*, vol. 17, no. 6, pp. 686–689, 2004.

[227] M.-Y. Rhee, H.-Y. Lee, and J. B. Park, "Measurements of arterial stiffness: methodological aspects," *Korean Circ. J.*, vol. 38, no. 7, pp. 343–350, 2008.

[228] H. N. Hodis *et al.*, "The role of carotid arterial intima-media thickness in predicting clinical coronary events," *Ann. Intern. Med.*, vol. 128, no. 4, pp. 262–269, 1998.

[229] I. Ansys, "ANSYS meshing user's guide," *vol*, vol. 15317, pp. 724–746, 2010.

[230] C. F. X. Ansys, "Release 11.0: ANSYS CFX-Solver theory guide," *ANSYS Inc., USA*, 2010.

[231] S. Patankar, *Numerical heat transfer and fluid flow*. CRC press, 2018.

[232] W. Q. Wang and Y. Yan, "Strongly coupling of partitioned fluid--solid interaction solvers using reduced-order models," *Appl. Math. Model.*, vol. 34, no. 12, pp. 3817–3830, 2010.

[233] W. A. Wall, C. Förster, M. Neumann, and E. Ramm, "Advances in fluid-structure interaction," 2006.

[234] R. Kamakoti and W. Shyy, "Fluid--structure interaction for aeroelastic applications," *Prog. Aerosp. Sci.*, vol. 40, no. 8, pp. 535–558, 2004.

[235] N. Buchmann, "Development of Particle Image Velocimetry for In-Vitro Studies of Arterial Haemodynamics," 2010.

[236] Z. Ding, K. Wang, J. Li, and X. Cong, "Flow field and oscillatory shear stress in a tuning-fork-shaped model of the average human carotid bifurcation," *J. Biomech.*, vol. 34, no. 12, pp. 1555–1562, 2001.

[237] I. E. Vignon-Clementel, C. Alberto Figueroa, K. E. Jansen, and C. A. Taylor, "Outflow boundary conditions for three-dimensional finite element modeling of blood flow and pressure in arteries," *Comput. Methods Appl. Mech. Eng.*, vol. 195, no. 29–32, pp. 3776–3796, 2006.

[238] N. M. Maurits, G. E. Loots, and A. E. P. Veldman, "The influence of vessel wall elasticity and peripheral resistance on the carotid artery flow wave form: a CFD model compared to in vivo ultrasound measurements," *J. Biomech.*, vol. 40, no. 2, pp. 427–436, 2007.

[239] K. T. Nguyen, C. D. Clark, T. J. Chancellor, and D. V. Papavassiliou, "Carotid geometry effects on blood flow and on risk for vascular disease," *J. Biomech.*, vol. 41, no. 1, pp. 11–19, 2008.

[240] D. A. Steinman, "Assumptions in modelling of large artery hemodynamics," in *Modeling of physiological flows*, Springer, 2012, pp. 1–18.

[241] A. De Waele, "Viscometry and plastometry," *Oil Color Chem Assoc J*, vol. 6, pp. 33–88, 1923.

[242] V. L. Rayz and S. A. Berger, "Computational modeling of vascular hemodynamics," in *Computational Modeling in Biomechanics*, Springer, 2010, pp. 171–206.

[243] M. M. Cross, "Rheology of non-Newtonian fluids: A new flow equation for

pseudoplastic systems," *J. Colloid Sci.*, vol. 20, no. 5, pp. 417–437, 1965.

[244] A. Europe, "ANSYS CFX-Solver Modelling Guide," *ANSYS Eur.*, 2009.

[245] H. Gharahi, B. A. Zambrano, D. C. Zhu, J. K. DeMarco, and S. Baek, "Computational fluid dynamic simulation of human carotid artery bifurcation based on anatomy and volumetric blood flow rate measured with magnetic resonance imaging," *Int. J. Adv. Eng. Sci. Appl. Math.*, vol. 8, no. 1, pp. 46–60, 2016.

[246] S. Madhavan and E. M. C. Kemmerling, "The effect of inlet and outlet boundary conditions in image-based CFD modeling of aortic flow," *Biomed. Eng. Online*, vol. 17, no. 1, p. 66, 2018.

[247] T. Du, D. Hu, and D. Cai, "Outflow boundary conditions for blood flow in arterial trees," *PLoS One*, vol. 10, no. 5, p. e0128597, 2015.

[248] P. Xu *et al.*, "Assessment of boundary conditions for CFD simulation in human carotid artery," *Biomech. Model. Mechanobiol.*, vol. 17, no. 6, pp. 1581–1597, 2018.

[249] R. Torii, M. Oshima, T. Kobayashi, K. Takagi, and T. E. Tezduyar, "Fluid--structure interaction modeling of blood flow and cerebral aneurysm: significance of artery and aneurysm shapes," *Comput. Methods Appl. Mech. Eng.*, vol. 198, no. 45–46, pp. 3613–3621, 2009.

[250] Y. Ohhara *et al.*, "Investigation of blood flow in the external carotid artery and its branches with a new 0D peripheral model," *Biomed. Eng. Online*, vol. 15, no. 1, p. 16, 2016.

[251] F. Ghalichi and X. Deng, "Turbulence detection in a stenosed artery bifurcation by numerical simulation of pulsatile blood flow using the low-Reynolds number turbulence model," *Biorheology*, vol. 40, no. 6, pp. 637–654, 2003.

[252] Z. Chen *et al.*, "Vascular remodelling relates to an elevated oscillatory shear index and relative residence time in spontaneously hypertensive rats," *Sci. Rep.*, vol. 7, no. 1, pp. 1–10, 2017.

[253] S. S. Dhawan *et al.*, "Shear stress and plaque development," *Expert Rev. Cardiovasc. Ther.*, vol. 8, no. 4, pp. 545–556, 2010.

[254] M. Heil and A. L. Hazel, "Fluid-structure interaction in internal physiological flows," *Annu. Rev. Fluid Mech.*, vol. 43, pp. 141–162, 2011.

[255] L. Kornet, A. P. G. Hoeks, J. Lambregts, and R. S. Reneman, "Mean wall shear stress in the femoral arterial bifurcation is low and independent of age at rest," *J. Vasc. Res.*, vol. 37, no. 2, pp. 112–122, 2000.

[256] S. Z. Zhao *et al.*, "Blood flow and vessel mechanics in a physiologically realistic model of a human carotid arterial bifurcation," *J. Biomech.*, vol. 33, no. 8, pp. 975–984, 2000.

[257] A. Hundertmark-Zaušková and M. Lukáčová-Medviďová, "Numerical study of shear-dependent non-Newtonian fluids in compliant vessels," *Comput. Math. with Appl.*, vol. 60, no. 3, pp. 572–590, 2010.

[258] J. V Soulis, O. P. Lampri, D. K. Fytanidis, and G. D. Giannoglou, "Relative

residence time and oscillatory shear index of non-Newtonian flow models in aorta," in *2011 10th International Workshop on Biomedical Engineering*, 2011, pp. 1–4.

[259] U. Morbiducci, R. Ponzini, M. Grigioni, and A. Redaelli, "Helical flow as fluid dynamic signature for atherogenesis risk in aortocoronary bypass. A numeric study," *J. Biomech.*, vol. 40, no. 3, pp. 519–534, 2007.

[260] H. Sugimoto, T. Kaneko, and A. Nakao, "Poststenotic dilatation and helical flow in the umbilical portion of the portal vein," *J. Hepatol.*, vol. 36, no. 5, p. 704, 2002.

[261] G. Van Langenhove, J. J. Wentzel, R. Krams, C. J. Slager, J. N. Hamburger, and P. W. Serruys, "Helical velocity patterns in a human coronary artery: a three-dimensional computational fluid dynamic reconstruction showing the relation with local wall thickness," *Circulation*, vol. 102, no. 3, pp. e22--e24, 2000.

[262] H. G. Bogren and M. H. Buonocore, "4D magnetic resonance velocity mapping of blood flow patterns in the aorta in young vs. elderly normal subjects," *J. Magn. Reson. Imaging An Off. J. Int. Soc. Magn. Reson. Med.*, vol. 10, no. 5, pp. 861–869, 1999.

[263] J. G. Houston, S. J. Gandy, D. G. Sheppard, J. B. Dick, J. J. F. Belch, and P. A. Stonebridge, "Two-dimensional flow quantitative MRI of aortic arch blood flow patterns: Effect of age, sex, and presence of carotid atheromatous disease on prevalence of spiral blood flow," *J. Magn. Reson. Imaging An Off. J. Int. Soc. Magn. Reson. Med.*, vol. 18, no. 2, pp. 169–174, 2003.

[264] A. M. Malek, S. L. Alper, and S. Izumo, "Hemodynamic shear stress and its role in atherosclerosis," *Jama*, vol. 282, no. 21, pp. 2035–2042, 1999.

[265] A. Kumar *et al.*, "Low coronary wall shear stress is associated with severe endothelial dysfunction in patients with nonobstructive coronary artery disease," *JACC Cardiovasc. Interv.*, vol. 11, no. 20, pp. 2072–2080, 2018.

[266] D. L. Fry, "Acute vascular endothelial changes associated with increased blood velocity gradients," *Circ. Res.*, vol. 22, no. 2, pp. 165–197, 1968.

[267] J. M. Ramstack, L. Zuckerman, and L. F. Mockros, "Shear-induced activation of platelets," *J. Biomech.*, vol. 12, no. 2, pp. 113–125, 1979.

[268] D. De Wilde, B. Trachet, G. De Meyer, and P. Segers, "The influence of anesthesia and fluid--structure interaction on simulated shear stress patterns in the carotid bifurcation of mice," *J. Biomech.*, vol. 49, no. 13, pp. 2741–2747, 2016.

[269] X. Liu, A. Sun, Y. Fan, and X. Deng, "Physiological significance of helical flow in the arterial system and its potential clinical applications," *Ann. Biomed. Eng.*, vol. 43, no. 1, pp. 3–15, 2015.

[270] C. G. Caro, N. J. Cheshire, and N. Watkins, "Preliminary comparative study of small amplitude helical and conventional ePTFE arteriovenous shunts in pigs," *J. R. Soc. interface*, vol. 2, no. 3, pp. 261–266, 2005.

[271] D. Gallo, D. A. Steinman, P. B. Bijari, and U. Morbiducci, "Helical flow in carotid bifurcation as surrogate marker of exposure to disturbed shear," *J. Biomech.*, vol. 45, no. 14, pp. 2398–2404, 2012.